Imperial College of Science, Technology and Medicine
University of London

The Ultrasonic Nondestructive Evaluation of Welds in Plastic Pipes

by

Che Wan Chan

A thesis submitted to the University of London
for the degree of Doctor of Philosophy

Department of Mechanical Engineering
Imperial College of Science, Technology and Medicine
London SW7

March 1996

BIBL. LONDIN. UNIV.

Abstract

The use of plastic as a pipe material for the transportation of potable water has increased over the last few years due to the improvements made to the material properties which have resulted in light, tough materials. In order to join the pipes together, two of the main welding technologies used are butt-fusion welding and electrofusion welding. At present, very limited quality assurance is carried out on such welded joints. Given that failures can occur due to the welding not being performed adequately, a nondestructive inspection technique is highly desirable.

Ultrasonics has been chosen as the tool to be used for the inspection. The approach of the studies is to assess the feasibility of several ultrasonic techniques with the aim of choosing the most appropriate for further development.

The likely failure in plastic water pipes is due to the slow brittle growth of a crack to a size which leads to fracture. The critical crack sizes required to cause failure in 50 years have been calculated using the theory of fracture mechanics.

For the butt-fusion weld, a technique using Lamb waves is investigated. In order to decide which mode(s) to use, dispersion curves were predicted and were verified experimentally. Studies were also carried out experimentally and using finite element analysis to assess the feasibility of using a low attenuation Lamb mode for defect detection. The results obtained were promising, indicating that a Lamb wave technique could be used for defect detection in plastic pipes. The practical implementation of the Lamb wave technique is discussed. Possible dry coupled transducers for exciting Lamb waves in pipes have been investigated and are described.

For the electrofusion weld, two techniques are assessed. The first is based on normal incidence inspection and was found to work extremely well although inspection times were long. The second technique uses Lamb waves and a finite element analysis was used to assess its feasibility. Although such a technique has potential in low damping materials such as steel, its use is very limited in plastics due to the high attenuation and low reflectivity from defects. Therefore, the normal incidence technique is the recommended method for electrofusion welds. The implementation of such a technique can be carried out using commercial systems currently available and by tailoring the system to use the appropriate transducers.

Acknowledgements

I would like to thank Dr Peter Cawley for his large contribution in supervising and providing guidance for this project. My warmest regards go to all my colleagues in the Nondestructive Testing Lab for their invaluable assistance: David Alleyne, Mike Lowe, Brian Pavlokovic, Bruce Drinkwater, Mark Evans, Keith Vine, Paul Wilcox, Brent Zeller, Michel Castaings and Tom Pialucha.

My thanks go out to WRc and EPSRC for their financial support and to Gary Sandilands at WRc for his useful guidance.

Last but not least, I would like to thank my family and friends for the support, help and understanding they have given me throughout my degree.

Contents

Abstract 2
Acknowledgements 3
Contents 4
List of Tables 8
List of Figures 9
Nomenclature 16

CHAPTER 1
INTRODUCTION

1.1 Overview 18
1.2 Evaluation of a Nondestructive Testing (NDT) Technique 19
1.3 Outline of Thesis 22

CHAPTER 2
CRITICAL DEFECT SIZE: A FRACTURE MECHANICS APPROACH

2.1 Introduction 26
2.2 Current Evaluation Tests for Long Term Performance 28
2.3 Fracture Mechanics Concepts 29
2.3.1 Introduction 29
2.3.2 Linear Elastic Fracture Mechanics (LEFM) 29
2.3.2.1 Introduction 29
2.3.2.2 The Energy Balance Approach 30
2.3.2.3 The Stress Intensity Factor Approach 31
2.3.2.4 Slow Crack Growth in Polymers 34
2.4 Determination of Critical Defect Sizes in Polyethylene Pipe 36
2.4.1 Introduction 36
2.4.2 Theory 37
2.4.2.1 Effects of Cracks on Net Section Yielding 37
2.4.2.2 Slow Crack Growth Model 38
2.4.3 Application of Theoretical Model 40
2.4.3.1 Initial Assumptions 40
2.4.3.2 Determination of Final Crack Size, a_f 42

2.4.3.3 Determination of Critical (Initial) Crack Size to Cause Failure in 50 years 45
2.5 Conclusions 46

CHAPTER 3
ACOUSTIC PROPERTIES OF POLYETHYLENE

3.1 Introduction 57
3.2 Longitudinal Bulk Wave Properties 57
3.2.1 Longitudinal Bulk Wave Velocity 57
3.2.2 Longitudinal Bulk Wave Attenuation 58
3.3 Shear Bulk Wave Properties 59
3.3.1 Shear Bulk Wave Velocity 59
3.3.2 Shear Bulk Wave Attenuation 60
3.4 Ultrasonic Examination of Weld Region 61
3.5 Conclusions 61

CHAPTER 4
NORMAL INCIDENCE INSPECTION OF ELECTROFUSION WELDS

4.1 Introduction 73
4.2 Focused Transducer C-Scanning 74
4.2.1 Introduction 74
4.2.2 Initial Scans 75
4.2.3 Effect of Spot Size and Frequency 77
4.2.4 Comparison of Scanning from Inside and Outside of Pipe 78
4.3 Discussion and Conclusions 79

CHAPTER 5
PLATE WAVE INSPECTION OF ELECTROFUSION WELDS

5.1 Introduction 97
5.2 Theory of Plate Waves 97
5.3 Overview of Problem 101
5.4 Analysis 102
5.4.1 Dispersion Curves 102
5.4.2 Numerical Simulations of Stepped Plate 103
5.4.3 Numerical Simulations of Lamb Wave-Defect Interaction 107

5.4.4 Discussion of Results 108
5.5 Conclusions 110

CHAPTER 6
LAMB WAVE PROPAGATION IN ATTENUATIVE MEDIA

6.1 Introduction 124
6.2 Attenuation Model 125
6.3 The Effect of Material Attenuation on Dispersion Curves 128
6.3.1 Zero Attenuation Case 129
6.3.2 Half Attenuation Case 131
6.3.3 Full Attenuation Case 134
6.3.4 Four Times Attenuation Case 135
6.4 Experimental Verification of Dispersion Curve Predictions 135
6.5 Practical Considerations 140
6.6 Conclusions 141

CHAPTER 7
AN INVESTIGATION INTO THE USE OF DRY COUPLED TRANSDUCERS FOR THE EXCITATION OF LAMB WAVES IN PIPES

7.1 Introduction 163

Part One: The Effect of Transducer Layout on the Efficiency of Lamb Wave Excitation

7.2 Lamb Mode Selection 165
7.3 The Effect of Transducer Positioning on the Pipe 167
7.3.1 Number of Elements 167
7.3.2 Axial Misalignment of Transducers 168
7.3.3 Circumferential Misalignment of Transducers 172
7.3.4 Non-Uniform Excitation Amplitude of Transducers 172
7.4 Summary of Transducer Placement and Consistency Requirements 173

Part Two: The Design of Piezoelectric Transducers for the Excitation of Lamb Waves in Pipes

7.5 Introduction 174
7.6 Expansional Piezoelectric Elements 175
7.6.1 Components of a Transducer 175

7.6.2 Effect of Backing 175
7.6.3 Effect of Shim Thickness 181
7.6.4 Effect of Loading Position of the Transducer on the Pipe 182
7.7 Shear Piezoelectric Elements 183
7.7.1 Effect of Backing 183
7.7.2 Effect of Loading Position of the Transducer on the Pipe 183
7.8 Summary of the Design of Dry-Coupled Piezoelectric Transducers for Lamb Wave Excitation in Pipes 184
7.9 Conclusions 185

CHAPTER 8
THE DETECTABILITY OF BUTT-FUSION WELD DEFECTS USING LAMB WAVES

8.1 Introduction 223
8.2 Choice of Configuration 224
8.3 Transmission Coefficient Measurements and FE Predictions 226
8.4 Discussion of Results 229
8.5 Conclusions 231

CHAPTER 9
CONCLUSIONS

9.1 Review of Thesis 246
9.2 Recommendations 249

APPENDIX 250

REFERENCES 252

List of Tables

Table 2.1	Slow crack growth data for Rigidex 002-40	40
Table 2.2	Parameters from limiting pipe cases used for slow crack growth analysis	41
Table 2.3	Critical crack sizes for net section yielding	44
Table 2.4	Critical crack sizes for unstable fracture	44
Table 2.5	Critical crack sizes and nature of failure	45
Table 2.6	Critical crack sizes for failure in 50 years	45
Table 4.1	Details of the focused transducers used for C-scanning	76
Table 5.1	Overall reflection ratio of reflected Lamb waves from a delamination for different configurations of input and reception Lamb modes	109
Table 6.1	Comparison of predicted and measured group velocities and attenuations for the s_2 mode	138
Table 6.2	Comparison of predicted and measured group velocities and attenuations for modes s_3 and a_4	140
Table 7.1	Properties of various backing materials	178
Table 7.2	Comparison of frequencies of maximum response from time marching FE analysis with natural frequencies from eigenvalue analysis	180
Table 8.1	Bulk property measurements for MDPE grade used in defect studies	225
Table 8.2	Comparison of predicted and measured group velocities and attenuation of s_2 mode	225
Table 8.3	Effect of slot starting position on the reflection coefficient from slots	229

List of Figures

Figure 1.1	Diagram of a butt-fusion joint	24
Figure 1.2	Diagram of an electrofusion joint	25
Figure 2.1	Example of a typical stress rupture plot	48
Figure 2.2	Example of a regression line for predicting 50 year failure stress	49
Figure 2.3	Fracture modes encountered in fracture mechanics analysis	50
Figure 2.4	Crack in an infinite plate	51
Figure 2.5	Comparison of stress rupture performance between TUB 124 HPPE and Rigidex 002-40	52
Figure 2.6	An example of a net section yield curve	53
Figure 2.7	Crack types used for slow crack growth analysis	54
Figure 2.8	Net section yield curves for edge, centre and semi-circular cracks	55
Figure 2.9	Stress rupture life vs. initial crack size for Rigidex 002-40	56
Figure 3.1	Schematic of specimens cut from orthogonal planes in polyethylene pipe	63
Figure 3.2	Schematic of a typical set-up used for velocity and attenuation measurement	64
Figure 3.3	Typical response of a polyethylene plate	65
Figure 3.4	Bulk longitudinal wave phase velocity variation with frequency	66
Figure 3.5	Schematic of reflection and transmission of waves used for attenuation calculation	67
Figure 3.6	Bulk longitudinal wave attenuation variation with frequency	68
Figure 3.7	Schematic of experimental set-up used for measurements involving shear waves	69
Figure 3.8	Bulk shear wave phase velocity variation with frequency	70

Figure 3.9	Bulk shear wave attenuation variation with frequency	71
Figure 3.10	Specimens used for examining the effect of the weld material ..... on ultrasound	72
Figure 4.1	Conventional normal incidence inspection	81
Figure 4.2	Schematic of C-scan system	82
Figure 4.3	Cross sectional views of flat bottom hole samples	83
Figure 4.4	Cross sectional views of samples used for inserting defects ..... along the weld interface	84
Figure 4.5	Scanning of electrofusion flat bottom hole joint with gate ..... placed over reflection from the wires	85
Figure 4.6	Diagram showing the position of the transducer face relative to .. the wires	86
Figure 4.7	Scanning of electrofusion flat bottom hole joint when gate ..... placed over reflection from the defect	87
Figure 4.8	Radiograph showing electrofusion joint with three 4mm flat ..... bottomed holes	88
Figure 4.9	Effect of wires on received signal from the joint	89
Figure 4.10	Scanning of electrofusion joint containing five 2mm flat ..... bottom holes	90
Figure 4.11	Scanning of electrofusion joint containing two 4mm flat ..... bottom holes using 1MHz transducer	91
Figure 4.12	Scanning of electrofusion joint containing two 4mm flat ..... bottom holes using 5MHz transducer	92
Figure 4.13	C-scan of joint containing an 8mm diameter aluminium circular . reflector using a 1MHz transducer	93
Figure 4.14	Effect of larger spacing between wires and weld interface on ..... the signal received by the transducer	94
Figure 4.15	Effect of scanning from inside and outside of pipe	95
Figure 4.16	Comparison of scans between a good joint and a joint ..... containing mud paste	96
Figure 5.1	Lamb wave inspection in a plate containing a defect	111

Figure 5.2	Modes shapes of zero order modes at low frequency-thickness	112
Figure 5.3	Geometries used in FE analysis	113
Figure 5.4	Geometry and co-ordinate system for stepped plate	114
Figure 5.5	Time domain responses (y-direction) of monitored point at 150mm from L-end of plate	115
Figure 5.6	Time domain responses (y-direction) of monitored point at 250mm from R-end of plate	116
Figure 5.7	Frequency and wavenumber spectra for t_2=2.5mm	117
Figure 5.8	Reflection ratios (y direction) vs. frequency	118
Figure 5.9	Transmission ratios (y direction) vs. frequency	119
Figure 5.10	Strain energy ratios of the various Lamb waves for t_2=3mm	120
Figure 5.11	Diagram showing extent and positions of the delamination used in FE modelling	121
Figure 5.12	FE analysis of delamination in a 2mm plate	122
Figure 5.13	Reflection ratio and shear stress vs. position of delamination through plate thickness for a_0 mode	123
Figure 5.14	Reflection ratio vs. frequency of a_0 mode for four positions of delamination through plate thickness	123
Figure 6.1	Bulk wave properties for HPPE used in Lamb wave studies	142
Figure 6.2	Phase velocity dispersion curves for different levels of attenuation	143
Figure 6.3	Group velocity dispersion curves for different levels of attenuation	144
Figure 6.4	Investigation of partial wave amplitudes for longitudinal and shear cut-off modes	145
Figure 6.5	Phase velocity dispersion curves highlighting the plateauing regions	146
Figure 6.6	Attenuation dispersion curves	147
Figure 6.7	Dispersion curve tracing in region of abrupt phase velocity change	148

Figure 6.8	Inspection of mode shapes near joining points of two asymmetric modes for zero attenuation case	149
Figure 6.9	Inspection of mode shapes near joining points of two asymmetric modes for the case of half attenuation	150
Figure 6.10	Phase velocity dispersion curves for a HPPE fluid-plate	151
Figure 6.11	Phase velocity dispersion curves showing point chosen for mode shape study	151
Figure 6.12	Displacement mode shapes of longitudinal asymptotic mode indicated in Fig.6.11 for different attenuation values	152
Figure 6.13	Dispersion curves and mode shapes for s_2 mode	153
Figure 6.14	Schematic diagram of set-up used for Lamb wave measurements	155
Figure 6.15	Details of input signal for excitation of s_2 mode	156
Figure 6.16	Schematic diagram showing the measurement sequence for monitoring Lamb waves along a HPPE plate	157
Figure 6.17	Time domain history of received signal	158
Figure 6.18	Dispersion curves and mode shapes for modes s_3 and a_4	159
Figure 6.19	Details of input signal for excitation of s_3 and a_4 modes	161
Figure 6.20	Time domain history of received signal	162
Figure 7.1	Expansional and shear piezoelectric transducers	187
Figure 7.2	Dispersion curves for an 89mm diameter, 5.5mm thick steel pipe	188
Figure 7.3	Mode shapes for L(0,2) mode at 70kHz	189
Figure 7.4	Diagram of set-up of transducers on a pipe and possible excited modes for 8 perfect transducers	190
Figure 7.5	Diagram showing axial misalignment of a transducer	191
Figure 7.6	Harmonic spectra for 8 transducers around the pipe	192
Figure 7.7	Axial wavenumber spectrum when a single transducer is misaligned by 1mm	193

Figure 7.8	Details of FE model used to analyse Lamb wave propagation in steel pipe	194
Figure 7.9	Harmonic number FE responses for different harmonic numbers	195
Figure 7.10	Time domain response when 8 ideal transducers are used	197
Figure 7.11	Time domain responses for a single transducer axially misaligned	198
Figure 7.12	Graph of baseline ratio vs. axial misalignment distance	199
Figure 7.13	Diagram showing a circumferentially misaligned transducer	200
Figure 7.14	Harmonic spectra when 1 transducer is circumferentially misaligned	201
Figure 7.15	Graph of baseline ratio vs. circumferential misalignment distance	202
Figure 7.16	Harmonic spectra when the amplitude of one transducer differs from the rest	203
Figure 7.17	Graph of baseline ratio vs. % amplitude difference from an ideal transducer	204
Figure 7.18	Schematic showing the outline and dimensions of the FE model used for looking at the response of a free expansional transducer	205
Figure 7.19	Details of excitation input	206
Figure 7.20	Response of an unbacked, freely supported transducer	207
Figure 7.21	Displacement mode shapes of an unbacked transducer with free boundary conditions	208
Figure 7.22	Schematic showing the outline and dimensions of the FE model used for looking at the response of an expansional transducer	209
Figure 7.23	Response of an unbacked transducer coupled to a steel block	210
Figure 7.24	Schematic of a transducer with backing showing dimensions used for FE model	211
Figure 7.25	Response of transducer edge with various backings	212

Figure 7.26 Bending modes of a transducer 213

Figure 7.27 Schematic showing outline of FE model of backed transducer on a steel pipe 214

Figure 7.28 Time domain responses for various backing thicknesses on an expansional transducer 215

Figure 7.29 Time domain responses on steel pipe using expansional transducers with various shim thicknesses 216

Figure 7.30 Time domain responses on steel pipe using expansional transducers for different contact areas 217

Figure 7.31 Time domain responses showing the phase shift when either end of the expansional transducer contacts the pipe 218

Figure 7.32 Time domain response on pipe using shear transducers for various backing thicknesses 219

Figure 7.33 Time domain responses on steel pipe using shear transducers for different contact areas 220

Figure 7.34 Time domain responses showing no phase shift when either end of the shear transducer contacts the pipe 221

Figure 7.35 Experimental results showing effect of contact position on generated Lamb mode L(0,2) 222

Figure 8.1 Dispersion curves for MDPE 233

Figure 8.2 Measurement sequence for monitoring Lamb waves along an MDPE plate 234

Figure 8.3 Reflection measurement using two transducers 235

Figure 8.4 Possible ray paths for backwards propagating waves 236

Figure 8.5 Reflection measurement using a single transducer 237

Figure 8.6 Transmission coefficient measurements of slotted plates 238

Figure 8.7 Measured transmission coefficient variation with depth of slot 239

Figure 8.8 Dispersion curves and mode shapes for s_2 mode 240

Figure 8.9 FE analysis of slots in plate 242

Figure 8.10 FE results for transmission and reflection coefficients 243

Figure 8.11 Starting positions for slots in plate 244

Figure 8.12 Cross sectional views of an infinite and finite defect in a plate 245

Nomenclature

a	Crack length, radius of transducer
A	Amplitude
a_0, a_1, a_2, ...	Asymmetric Lamb modes, subscript denotes mode number
α	Attenuation coefficient
c	Wave velocity
c_g	Group velocity
COD	Crack opening displacement
c_{ph}	Phase velocity
d	Plate thickness
δ_c	Critical crack opening displacement
∇	Gradient operator
E	Young's modulus
f	Frequency (Hz)
F(a,b)	Flexural modes in a pipe, arguments refer to classification of mode
G	Strain energy release rate
G_c	Critical strain energy release rate
i	$\sqrt{(-1)}$
k	Real part of wavenumber
k	Wavenumber vector
K	Stress intensity factor
K_c	Slow crack growth stress intensity factor
K_{Ic}	Fracture toughness
L	Denotes longitudinal wave
L(a,b)	Longitudinal modes in a pipe, arguments refer to classification of mode
λ	Wavelength
n	Harmonic number, mode number
υ	Poisson's ratio
ω	Frequency (rad/s)
ϕ	Scalar potential
ψ	Vector potential
r	Radial distance from crack tip
R	Fracture resistance, radius of curvature of transducer
R_{ab}	Reflection coefficient from medium a to medium b
ρ	Density
S	Denotes shear wave

SDR	Standard dimension ratio (ratio of minimum mean outer diameter to minimum wall thickness for a pipe)
s_0, s_1, s_2, ...	Symmetric Lamb modes, subscript denotes mode number
σ	Stress
t	Time, thickness
τ	Stress rupture lifetime
T_{ab}	Transmission coefficient from medium a to medium b
u	Displacement vector
U	Energy
x	Cartesian coordinate
y	Cartesian coordinate
Y	LEFM shape factor
z	Cartesian coordinate
Z	Acoustic impedance
λ, λ', μ, μ'	Lamé constants

CHAPTER 1

Introduction

1.1 Overview

Over the last few years, the use of plastic pipes in the water industry has increased as a direct result of their improved chemical and mechanical properties as well as the ease with which they can be manufactured and transported. These factors mean that they are now being considered as real alternatives to traditional pipe materials such as cast iron and steel.

Two common types of weld used for the joining of plastic water pipes are the butt-fusion weld and the electrofusion weld. The butt-fusion weld has been around for some time and the welding process is achieved by firstly planing the ends of the two pipes to be joined. A heater plate is then brought into contact with the ends and these ends are consequently heated. After a certain period, the heater plate is removed and the pipe ends are brought together to form the weld (Fig.1.1). The electrofusion weld is a relatively new type of weld. Here, the ends of two pipes are inserted into a sleeve or coupler. Moulded into the coupler is a copper wire and upon application of an electric current, the wire serves as a heat source for heating the contact region between the coupler and the pipe leading to the formation of a weld (Fig.1.2). Note that the pipes themselves are not welded to each other. The electrofusion weld was primarily introduced for pipes that needed repairing because of the easier welding process (less bulky equipment).

At present no standard method exists for the inspection of welds in plastic water pipes after they have been made. For butt-fusion welds, an inspection of the weld bead is often carried out to determine whether the weld has been made according to the specifications laid out by the pipe manufacturers. However, this test cannot reveal the existence of defects within the weld. Although there are strict guidelines for the welding procedure, the conditions under which contractors have to work can often be unforgiving (Marshall, Ingham et al. (1995)) . Such conditions could lead to the weld becoming contaminated prior to or even during the welding process by foreign entities such as mud, leaves or water and could eventually lead to failure of the weld.

The pressure in plastic water pipes is generally relatively low (WAA Sewers and Water Mains Committee: Materials and Standards (1987)) and as a result pipes do not tend to fail immediately unless there are major defects in the weld (e.g. large areas of incomplete fusion). These welds can usually be identified immediately by high pressure testing before the pipes are allowed to go into service (Gimmler, Farrage et al (1994)). The major concern for these welds is the problem of slow crack growth (Sandilands and Bowman (1986)). This is the phenomenon whereby small cracks in the weld region can grow in a brittle manner at relatively slow rates under the application of a small static stress. Given that there is potential for small cracks to develop during the welding process it is therefore possible for these small defects to cause failure at a future date.

There are British Standards covering the expected lifetime of plastic pipes (50 years) (WAA Sewers and Water Mains Committee: Materials and Standards (1987)) and tests on individual sample pipes can be carried out. However, on welds, this is a problem given that the quality of each weld can vary dramatically as it is dependent on the welder and the environment. Improved quality assurance of welds in plastic pipes is therefore an area in need of further investigation. A non-destructive testing method is clearly desirable for inspecting the welds before they are buried in the ground and this forms the basis for this thesis. Given the abundance of non-destructive testing techniques available, the first task is to decide on an appropriate technique.

1.2 Evaluation of a Nondestructive Testing (NDT) Technique

In the field of NDT there are numerous methods capable of detecting defects in materials. The principal techniques which can be applied to plastic materials (i.e. this rules out techniques involving electric and magnetic fields) are listed below and a description of each is given.

- Visual/Penetrants (dye and fluorescent)
- Radiography (X and Gamma rays)
- Thermography
- Ultrasonics

Visual \Penetrants

Visual inspection is probably the simplest and most widely used of all NDT methods. The method involves inspecting the testpiece by eye and the efficiency of this method

is largely dependent on the degree of surface preparation and on the lighting conditions. Given that the defects have to be visible for this method to work, this means that it is only appropriate for gross surface defects. By applying a penetrant to a test surface, the contrast of surface breaking defects with the background colour increases. Penetrants are basically coloured liquids which flow into surface breaking cracks. After an appropriate interval, excess penetrant is removed. Penetrant left within cracks bleeds onto the surface and this bleeding is increased by applying a white powder developer. The white powder also helps to improve contrast. Both these methods may be used for detecting defects which extend to the surface. However, given that not all flaws will be surface breaking these methods have very limited use for this project.

Radiography

Radiography is the branch of NDT which employs X or Gamma rays (Bryant and McIntire (1985)). These rays are propagated through the testpiece and whenever they encounter a flaw there will usually be a drop in energy absorption due to the absence of material. This change in absorption can be detected by a radiographic film placed at the end of the testpiece. This technique works well when the rays are propagated along the plane of a crack where the amount of material removed is large. This means that radiography should be able to detect defects in butt-fusion welds, where flaws tend to lie in a plane parallel to the propagation direction of the X-rays. If the crack plane is normal to the rays, there will be a negligible change in absorption in the direction of propagation of the rays due to the mass of the material being essentially constant and hence flaws of this nature will not show up on the radiographic film. As a result, we would not expect this technique to succeed for electrofusion welds where the flaws are likely to lie in a plane normal to the direction of propagation of the X-rays. Radiography therefore works best for volumetric defects because of the difference in density between the defects and the parent material. Given that a radiographic film is usually required (a T.V screen can also be used for real time imaging), a permanent record is obtained. The radiographic film needs to be developed and therefore instant results are not possible although films do exist which have developers built in. One of the main disadvantages with radiography is that systems are very expensive. In addition, and probably more importantly, there is always a health hazard associated with such a method. For these reasons, even though radiography could potentially be used for butt-fusion welds, this method was not pursued further.

Thermography

The principle behind thermography is that if heat is applied to one side of a testpiece, the spatial heat flux distribution on either surface will be governed by the homogeneity of the specimen (i.e. if there are any flaws), the diffusivity (related to the thermal conductivity and the specific heat capacity) and the time (Vavilov and Taylor (1982)). By monitoring this heat flux distribution with time, it is possible to ascertain the size and position of flaws. Single sided inspection is therefore possible with this method. The main problem with this method in plastics is that because plastics are relatively poor conductors of heat, the time taken for heat to flow through the specimen is likely to be long. A consequence of this is that temperature changes are likely to be very small and as a result the temperature changes caused by the presence of a defect may not be discernible. This method would therefore not be effective for this project.

Ultrasonics

This method is based on the principle that ultrasound incident on a flaw will interact with that flaw (Krautkramer and Krautkramer (1983)). As a result, a reflection will occur. In addition, some of the incident energy may be transmitted across the flaw. Depending on how big the reflected or transmitted signal is or how long it takes for the ultrasound to reach a receiver, it is possible to determine the size and position of the flaw. This method works best for planar flaws which lie perpendicular to the ultrasonic rays (i.e. opposite to radiography) but can also be used to detect flaws which are inclined to the direction of propagation of the rays. Single sided inspection is implicit when a reflected signal is being monitored. For plastics, one of the potential barriers to be overcome is the problem of material attenuation where the amplitude of waves decrease with propagation distance. However, given that the attenuation is dependent on the frequency of the ultrasound and on the propagation distance, it may be possible to select appropriate frequencies and propagation distances such that attenuation is minimised. Therefore, given that there is scope for ultrasonics to be used for measuring defects in different planes of orientation (i.e. for the butt-fusion and electrofusion welds), and also that the cost of ultrasonic systems is generally somewhat less than those of the previous two methods, ultrasonics was chosen as the method to be investigated for the NDT of welds in polyethylene pipes.

1.3 Outline of Thesis

This thesis presents an investigation into the use of ultrasonics for the inspection of welds in polyethylene water pipes. The aim of the inspection is to detect the presence of a certain size of defect immediately after they have been welded on site (i.e. before they are buried), the size of the defect being determined by fracture mechanics analysis.

The second chapter employs fracture mechanics to determine the slow crack growth critical defect sizes for butt-fusion and electrofusion welds, these critical defect sizes corresponding to a 50 year lifetime of the weld.

In Chapter 3 the measured acoustic properties of the two polyethylenes used in this project are presented. These are the properties of bulk longitudinal and bulk shear waves.

Chapter 4 presents an investigation of a normal incidence inspection technique for electrofusion joints. This concentrates primarily on the use of a focused probe C-scanning system.

A feasibility study of a potentially quicker alternative to the normal incidence technique is presented in Chapter 5. This technique involves the use of plate or Lamb waves where the direction of propagation of the insonifying waves is in the same plane as the potential defects. Dispersion curves are required and are presented.

In Chapter 6, the subject of Lamb waves in highly attenuative media such as polyethylene is looked at for plate geometry. The emphasis is on determining how the dispersion curves of a highly attenuative material compare with those where no attenuation exists. By studying the dispersion curves, we can determine whether low attenuation modes exist. If so, there is potential for these modes to be used for the Lamb wave inspection of butt-fusion welds.

In pipe structures, pipe modes could be used for defect detection. However, a large number of modes can exist when only one mode is required. Chapter 7 therefore looks at the question of how a single mode can be excited. This involves reducing the chances of other modes being excited by making sure factors such as transducer misalignment are minimised. In the same chapter, we go on to investigate two types of dry coupled transducers which could be used for exciting the chosen mode.

In Chapter 8, we present experimental and numerical results on the reflectivity/transmissibility of Lamb waves from simulated weld defects. The aim of this chapter is to determine whether Lamb waves could be used for defect detection in butt-fusion welds in polyethylene pipes.

The main conclusions of this thesis are then presented in Chapter 9.

1 Diagram of a butt-fusion joint

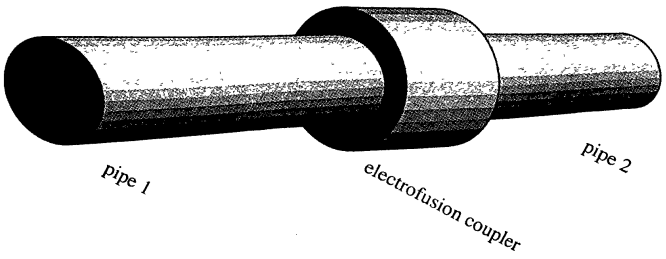


Fig.1.2 Diagram of an electrofusion joint

CHAPTER 2

Critical Defect Size: A Fracture Mechanics Approach

2.1 Introduction

The performance of welded pipes is very much determined by the quality of the welds. In an ideal situation, the strength of all welds would be identical and at least equal to the strength of the pipe. In reality, even though the welding process is fairly automated, this is not the case. If the welding process is not performed under clean conditions then dirt/water could become trapped at the weld interface thereby creating an area where there is a lack of fusion. Such imperfections can lead to failure of the weld by the growth of a defect to a size which leads to fracture. Therefore, information concerning the sizes of defects is advantageous so that suspect welds can be identified and removed. The identification of defective pipes can be performed using a suitable NDT technique. Sandilands and Bowman (1986) have examined the effect of defect size on pipe lifetime performance. Using a similar approach, acceptable defect sizes which will not lead to premature pipe failure can be evaluated.

A conventional method of assessing the performance of polyethylene pipes is to conduct stress rupture testing. In these tests, pipes are subjected to different constant pressures and at each pressure, the time to failure is recorded. The results are displayed on a log stress against log time scale, producing a stress rupture curve (Gray, Mallinson et al. (1981)). A typical plot is shown in Fig.2.1. From the stress rupture curve, three separate regions can be identified. Region 1 occurs at high stress levels and at short times. The failure mode in this region is ductile: the applied stresses are so high that yielding takes place on a large scale. In region 2, the stresses are much lower and the failure times significantly longer. The failure mode here is brittle fracture (or stress cracking) and occurs by the propagation of a crack originating from surface flaws, inclusions or voids in the pipe wall. In the intermediate region known as the 'knee', both modes can be found to exist and this region represents the transition from a ductile mode of failure to a brittle mode of failure. At a temperature of 20°C, the knee is very rarely seen due to the long times required for it to appear. An increase in temperature reduces the time required for the stress cracking mechanism to take place (Fig.2.1).

In the water industry, the loading of water pipes is not very severe. As a result, the stresses encountered in the pipes tend to lie in the brittle region of the stress rupture curve (Sandilands and Bowman (1986)). The mode of failure is therefore likely to be brittle fracture, with failure occurring at relatively large time scales. The subject of long term brittle fracture (or slow crack growth) is therefore the topic of interest in this chapter.

There are several inherent problems associated with the constant pressure test. In terms of finance, investment has to be made for equipment, and materials costs are likely to be high given that a large number of tests have to be carried out for reliable results to be obtained. Furthermore, tests are likely to last for long periods of time, possibly years if we want to observe the behaviour in the brittle region. Often, only the ductile region of the stress rupture curve can be generated because of time limitations, and this is particularly true at lower temperatures such as 20°C. In industry, to ascertain information concerning the long term performance at such temperatures, data is extrapolated to 50 years using predictions of 'knees' from high temperature tests (Marshall, Taylor et al. (1982)). A stress level is then determined which forms the basis for calculating an appropriate design stress.

Having identified the limitations with the constant pressure test, it would be desirable if short term tests using simple specimens can be used to predict long term performance. This approach is well suited to the application of fracture mechanics. Fracture mechanics has been used to study the failure behaviour of polyethylene pipes by at least two British research laboratories (Gray, Mallinson et al. (1981), Greig (1981)). The main attraction of fracture mechanics is that it offers considerable savings, both in financial terms and time. In terms of time alone, it can be the difference between several months and several years.

Initially, plastic water pipes in Britain were generally made of a grade of polyethylene known as Rigidex 002-50 (manufactured by BP Chemicals Ltd.). However, over the last few years a new grade known as TUB 124 HPPE (manufactured by Solvay, Belgium) has been introduced to the water pipe industry. Very little slow crack growth data has been published for this material to date so very little is known about its long term performance characteristics. However, work involving a similar material to Rigidex 002-50 has been carried out and crack growth data exists for this material (Rigidex 002-40). This material is used for gas distribution pipes. Data sheets exist for the above materials and a comparison between the two Rigidex materials show that their mechanical properties are similar. For this reason, it can be assumed for the

purposes of this chapter that the two Rigidex grades are the same and hence any future reference to the 002-40 grade will imply the 002-50 grade.

Given that failures of in-service pipes can be very costly, knowledge concerning their long term performance is crucial. In order to achieve this, the theory of fracture mechanics will be used to determine the critical defect sizes which could lead to failure of a pipe in a given time (50 years) for the two grades mentioned. Once this has been achieved, a basis on which to devise an appropriate non-destructive testing method for detecting defects which are larger than those found from the fracture mechanics analysis can be evaluated.

2.2 Current Evaluation Tests for Long Term Performance

At present, a specification exists for polyethylene pressure pipes for cold potable water (WAA Sewers and Water Mains Committee, (1987)). In this specification, details are provided for tests to ascertain the long term performance of polyethylene pipes: the long term hydrostatic strength at 20°C test and the slow crack growth resistance test.

The long term hydrostatic strength test is conducted over the range 10-10,000 hours and all failures have to be ductile bursts. A linear regression analysis of log stress against log time to failure is then performed to enable the 50 year strength to be estimated. The value that this stress should be is 8.3MPa. This value is based on a design stress of 5MPa with a safety factor of 1.66. Fig.2.2 shows an illustration of a regression line. An implicit assumption of the test is that over the 50 year period, the mode of failure is consistently ductile. Therefore, a drawback of such a test is that it only measures the pipe's long term ductile strength and yields no information concerning the long term resistance of the pipe to brittle failure.

The slow crack growth resistance test consists essentially of loading a notched pipe. The test pipe is then either taken to failure or the test discontinued at 500 hours, whichever is the sooner. Any sign of unstable crack propagation in the failed test piece is deemed unacceptable. Once again, the test does not really measure the long term performance of the pipe.

2.3 Fracture Mechanics Concepts

2.3.1 Introduction

Fracture mechanics is the general term used to describe the theory which attempts to quantify fracture phenomena in already cracked bodies under applied loads. The theory of fracture mechanics originates from Griffith (1920). His underlying assumption was that all materials contained flaws, an assumption which is fairly realistic. Furthermore, he proposed that the strength of a material could be characterised as the energy per unit area required to produce new surfaces and hence to propagate a crack. In 1948, Irwin (1948) used a stress analysis approach to fracture mechanics and introduced the now familiar subject of linear elastic fracture mechanics (LEFM), whereby the state of stress at the crack tip could be characterised by the fracture parameter G (energy release rate) and K (stress intensity factor).

The more recent advances have been made during the sixties. Wells (1961) suggested a crack opening displacement approach and Rice (1968) presented his J-integral. These two approaches fall into the category of elastic-plastic fracture mechanics.

All of the above approaches, although arrived at in different ways, share the same underlying philosophy: fracture is imminent when the characteristic parameter reaches a certain value, this value being known as the fracture toughness. The decision of which of these to adopt depends on the material being analysed (i.e. whether plasticity effects can be neglected). As the mode of failure of interest in this project is of a brittle nature, the approach adopted is that of linear elastic fracture mechanics which will now be discussed.

2.3.2 Linear Elastic Fracture Mechanics (LEFM)

2.3.2.1 Introduction

LEFM is the most developed and used of the various fracture mechanics approaches. A complete review of the theory can be found in various texts (e.g. Broek (1974), Ewalds (1986)). The underlying assumption of LEFM is that the body under investigation behaves elastically. However, the theory is acceptable for materials which exhibit plasticity provided the plasticity is localised around the crack tip. Two approaches exist in the LEFM regime, the Energy Balance Approach and the Stress Intensity Factor Approach. We have decided to use the Stress Intensity Factor

approach owing to its relative ease of application and the fact that it has been used successfully in the past to study crack propagation in polymers (e.g. Williams (1984)). Nevertheless, a brief review of the energy balance approach will be presented as this approach forms the foundation of fracture mechanics.

2.3.2.2 The Energy Balance Approach

The energy balance approach is based on the work of Griffith (1920). He proposed that all bodies contained cracks and that unstable fracture would take place if the strain energy released for incremental crack growth was at least equal to the energy absorbed in creating new crack surfaces (ignoring kinetic energy of the material and the external work applied). Mathematically, this can be expressed as:

$$\frac{d}{da}(U_r - U_s) \geq 0 \qquad (2.1)$$

where U_r is the strain energy released due to crack extension, U_s is the energy required to create two new surfaces and a is the crack length.

Griffith analysed the case of glass (a linear elastic material) so that the strain energy released could be calculated using elastic theory and the energy absorbed could be equated to the work done against surface tension. He found that the calculated surface energy was greater than that obtained by experiment. This discrepancy was attributed to the plastic work done in creating new surfaces, a contribution that was neglected in Griffith's theory. Irwin (1948) took this plasticity into account and consequently redefined the energy absorption to include the work done in plastic deformation.

He went on to define the energy release rate G as:

$$G = \frac{dU_r}{da} \qquad (2.2)$$

and the fracture resistance R as:

$$R = \frac{dU_s}{da} \qquad (2.3)$$

and said that unstable fracture would occur when G reached a critical value $G_c(=R)$. If the plastic zone was sufficiently small, G could still be evaluated from an elastic analysis. In addition, it was proposed that G_c was a material property.

By using the work of Inglis (1913), Griffith defined the energy release rate at fracture initiation, G_c, for an infinite plate:

$$G_c = \frac{\pi\sigma_c^2 a}{E} = R \qquad (2.4)$$

where σ_c is the stress at fracture. This is the condition for fracture of materials which exhibit limited plasticity. Using equation (2.1), it is possible to derive expressions for G in terms of measurable parameters such as load and compliance and therefore we have a way of determining the value of G.

2.3.2.3 The Stress Intensity Factor Approach

This approach is based on a stress analysis of the region in the vicinity of the crack tip. Developed by Irwin (1957), it uses Westergaard's (1939) stress function solutions to arrive at expressions for the elastic stress field near the crack tip in an elastic body. There are three main ways in which a body can be loaded:

i) Mode I - also known as the opening mode. This mode is associated with local displacement in which the crack surfaces move directly apart normal to the plane of the crack (Fig.2.3a),

ii) Mode II - also known as the edge-sliding mode. This mode is characterised by displacements in which the crack surfaces slide over each other perpendicular to the leading edge of the crack (Fig.2.3b).

iii) Mode III - also known as the tearing mode. This mode finds the crack surfaces sliding with respect to one another parallel to the leading edge (Fig.2.3c).

The equations for the stress fields are given as:

$$\sigma_{ij} = \frac{K_n}{\sqrt{2\pi r}} f_{ij}(\theta) + \text{non singular terms in r} \qquad (2.5)$$

where σ_{ij} is the stress in the i direction acting on the j plane, K_n is a constant which gives the magnitude of the elastic stress field under mode n loading, r is the radial distance away from the crack, θ is the angle from the horizontal plane and $f_{ij}(\theta)$ is a function of θ specific to the mode concerned.

It can be seen from equation (2.5) that the stress becomes singular at the crack tip itself (r=0) and hence the singular term will dominate very close to the crack tip. The magnitude of the stress field is then described by K_n. For most practical applications, mode I is by far the dominant mode of loading. For an infinite cracked plate of centre crack length 2a shown in Fig.2.4, K_I is given by:

$$K_I = \sigma\sqrt{\pi a} \qquad (2.6)$$

Therefore, stress fields can be characterised using a single parameter. The only parameter which distinguishes one crack from another is K. As K_I describes the state of state of stress near the crack tip, it is not unrealistic to assume that fracture will occur when K_I reaches a critical value K_{Ic}, known as the critical stress intensity factor or fracture toughness. This is indeed what Irwin proposed. This situation is analogous to the loading of a specimen; when the stress in the specimen reaches the yield stress, the specimen will yield.

For real materials with finite yield stresses, the high theoretical stresses near the crack tip will exceed the yield stress. This means that a finite plastic zone will develop at the crack tip and there will be a redistribution of stresses in order to maintain equilibrium. However, Liu (1965) showed that if the plastic zone was small compared to a certain region of the stress field dominated by K, then the elastic stress field would be unaffected by stress redistribution. Under such conditions, termed 'small scale yielding', the parameter K can still be used to characterise fracture.

Irwin's original assumption that non-singular stress terms could be omitted near the crack tip, from equation (2.5), has come under closer investigation. Rice (1974) demonstrated that one of the non-singular stress terms did not in fact vanish at the crack tip. This stress is known as the 'T' stress and is dependent on the geometry and mode of loading. Larsson and Carlsson (1973) did experimental work on four different geometries of specimen: centre-cracked tension, double edge-cracked tension, compact tension and single edge-cracked three point bend. They showed that the three point bend specimen gave by far the lowest value of T. Furthermore, they noted that increasing T in the positive direction produced smaller plastic zones

whereas increasing T in the negative direction resulted in larger plastic zones, at the same K level. Therefore, K_c levels may be affected by the 'T' stress if the fracture event is largely dependent on the plastic zone. The 'T' stress can account for the variation in the performance of different fracture toughness test specimens. Because of the small plastic zone (and hence large constraint), the bend specimen is much preferred in fracture toughness testing.

Thickness effects in fracture toughness testing are also very important. Irwin (1960) found that K_c (or G_c) depended strongly on specimen thickness below some minimum value of thickness and that above this value, K_c was independent of thickness and could hence be considered a material property. This variation can be explained by considering the failure mode:

i) Plane stress - failure occurring in a plate where there is unconstrained through-thickness plastic deformation,

ii) Plane strain - failure occurring in a plate where there is triaxial constraint.

When the thickness is large enough, 'plane strain' conditions prevail along the crack front and the measured thickness independent K_c is called the 'plane strain fracture toughness, K_{Ic}' which is believed to represent the lower limit of material toughness.

For different crack geometries, equation (2.6) is modified to a general equation:

$$K_I = Y\sigma\sqrt{\pi a} \qquad (2.7)$$

where Y is a factor known as the LEFM shape factor and in general is a function of a/w (w is the width of the specimen) and the mode of loading. The LEFM shape factor accounts for the geometry of the body in which the crack lies. LEFM shape factors for different geometries can be found in handbooks by Rooke and Cartwright (1975) and Tada, Paris et al. (1985). For the infinite crack case under mode I loading, Y=1.

Therefore, by knowing the fracture toughness and the LEFM shape factor, predictions can be made to determine whether fracture in a body will occur.

2.3.2.4 Slow Crack Growth in Polymers

Given that polymers are viscoelastic, using LEFM to predict their behaviour may appear somewhat dubious. However, Williams (1987) argued that polymers are essentially linear and only slightly viscoelastic, so that standard LEFM could be used to characterise the fracture behaviour of polymers. Indeed, Williams (1978) and Gray, Mallinson et al. (1981) are among those who have used LEFM successfully to explain and predict fracture phenomena in polymers.

In polymers, it is found that a crack could grow at stress intensity values which are less than the fracture toughness K_{Ic}, a phenomenon not covered by standard time-independent fracture mechanics theory. The slow crack growth stress intensity will be denoted by K_c. In slow crack growth, three principal stages have been identified:

i) An initial incubation period where no crack growth occurs. However, crazing occurs whereby crazes start to form in the vicinity of the crack tip,

ii) Crazes start to break resulting in the slow growth of a crack at a rate which could be characterised by a $K_c/\dot{a}$ graph.

iii) Fracture in an unstable manner (i.e. $K_c=K_{Ic}$) or ductile failure by net section yielding when the net section stress is high enough.

Many authors (e.g. Marshall (1982)) have shown that the crack growth rate, $\dot{a}$, is uniquely dependent on the current value of the stress intensity factor, K_c, under certain conditions. These conditions are:

i) Plain strain conditions exist at the crack tip,

ii) The plastic zone is small compared to the specimen dimensions to ensure that LEFM assumptions are satisfied,

Results from experiments all show that for crack propagation, the stress intensity factor K_c increases with crack speed $\dot{a}$.

Several researchers (e.g. Qian, Lu et al. (1989), Brown and Bhattacharya (1985)) investigated the existence of a threshold K below which no crack can propagate. Results showed that these K values were extremely low ($0.08MNm^{-3/2}$ by Qian, Lu et

al. (1989)) and therefore unrealistic for practical purposes. For example, if Y=1 and σ =5MPa, the defect size would have to be less than 81μm for zero crack growth. Moreover, the results were based on tests carried out for a finite period of time (10,000hrs) which is not conclusive evidence that a crack will not grow after 10,000hrs.

Analysing the incubation time has proved to be somewhat difficult. Gray, Mallinson et al. (1981) on studies of polyethylene resin observed that the incubation time was negligible whereas Chan and Williams (1983) put forward evidence that the period may be quite long. Taylor (1983) showed that the incubation period was about half the total failure time.

For the analysis of slow crack growth, Gray, Mallinson et al. (1981) and Barker, Bowman et al. (1983) made use of $K_c/\dot{a}$ data. They found that for HDPE and some MDPE, the curves tended to obey the relationship:

$$\dot{a} = \beta(K_c)^b \tag{2.8}$$

Plotting this on log-log axes would subsequently yield a straight line, from which the parameters b and β could be extracted. Experiments showed that b and β were material constants provided plane strain conditions were met by the specimens (Chung (1991)). Once these constants are known, the equation can then be integrated to determine the failure time of a crack growing from an initial crack length a_i to a final crack length a_f. Note that this analysis takes no account of the incubation period and therefore the failure time calculated will be a conservative one.

Gray, Mallinson et al. (1981) looked at the slow crack growth characteristics at 80°C of a Rigidex 002-40 and found that the crack growth could not be characterised by the simple power law of equation (2.8) whereas Marshall, Taylor et al. (1982) found that the equation could be used when the tests are conducted at 20°C.

The role of flaw size in the brittle fracture of polyethylenes was studied by Sandilands and Bowman (1986). Their studies showed that the flaw size was very influential in determining the stress rupture lifetime. In one grade of polyethylene, it was found that failure was possible from flaws as small as 45μm, that is, inherent flaws in the polymer.

The initiation site of flaws has been examined by several authors (Barker, Bowman et al. (1983), Sandilands and Bowman (1986)). It was observed that fractures tended to initiate towards the pipe bore. This is due to the higher local hoop stresses at the bore arising from the pipe being thick walled. For an SDR 11 pipe (SDR (standard dimension ratio) is the ratio of the minimum mean outside diameter to the minimum wall thickness), a Lamé analysis predicts that the stress at the bore is 25% higher than that on the outer surface. Furthermore, the extrusion process for pipes give rise to residual stresses in the pipe wall. For pipes cooled from the outer surface, tensile residual stresses are created at the bore and compressive residual stresses on the outer surface. Tensile residual stresses are added to any other applied stresses whereas compressive residual stresses act in a negative manner. It is the combined effect of the two stresses at the bore that leads to the considerably higher hoop stresses at the pipe bore and hence the preferred site of crack initiation.

The failure mechanism for stress cracking has been a topic of extensive research. There is a general agreement that the primary mechanism is craze growth and breakdown. Lustiger and Corneliussen (1987) suggested that failure was interlamellar. They put forward the idea that the tie molecules (chains which start and end in adjacent lamellae) disentangled and relaxed due to long term stress and eventually separated. Brown and Bhattacharya (1985) proposed that the underlying microscopic process for fracture was the development of fibrillation. Fibrils elongate and thin due to creep and eventually break when they reach a critical cross sectional area. The fibrils consist of chains of molecules and thinning is the process of sliding. The eventual fracture of the fibrils is the result of chains separating from each others influence. For crack nucleation, Qian, Lu et al. (1989) said that the nucleating process consisted of converting virgin material into a craze. Crack growth was then the result of disentanglement of the fibrils and further nucleation of a craze at the crack tip during growth. Therefore, crack growth involves the continuous nucleation and fracture of fibrils.

2.4. Determination of Critical Defect Sizes in Polyethylene Pipe

2.4.1 Introduction

At the time of writing, the author is not aware of any experimental slow crack growth data for the TUB 124 HPPE polyethylene grade. Data for other grades were available, among these being BP Rigidex 002-40 (MDPE). It has been reported by Chan and Williams (1983) that for the Rigidex 002-40 MDPE, crack growth from their

experiments was recorded as 10^{-11}m/s. For one of their specimens, it had taken two years for a crack to extend a mere 5mm. We can therefore see that this particular grade is very tough and hence extremely resistant to slow crack growth. Although no slow crack growth data exists for the TUB 124 HPPE, stress rupture curves are available. Fig.2.5 show the stress rupture curves for TUB 124 HPPE and Rigidex 002-40 at 20°C and 80°C. If we compare the stress rupture curves of the TUB 124 HPPE and the Rigidex 002-40 for the 80°C case, we can see that the time for a knee to occur in the TUB 124 HPPE will be longer than that in the Rigidex 002-40 given that a knee has already started to appear for the Rigidex 002-40. Also, for each temperature, the stresses required to cause failure within a given lifetime are higher for the TUB 124 HPPE. We can therefore deduce that the slow crack growth resistance of the TUB 124 HPPE will be greater than that of the Rigidex. On this assumption and the fact that no crack growth data for TUB 124 HPPE exists, the ensuing analysis will concentrate on the Rigidex 002-40. The results obtained for this material will then will taken as a worst case because we know that the results for the TUB 124 HPPE would have been comparable if not better.

The method adopted for determining critical defect sizes in the pipes is to examine the crack growth characteristics of the Rigidex 002-40 grade used in this project.

2.4.2 Theory

2.4.2.1 Effects of Cracks on Net Section Yielding

In section 2.3.2.4, we identified that two modes of failure can exist: net section yielding and stress cracking. Even though long-term failures have been reported as being brittle, it has also been reported that final rupture takes place by a ductile process (Sandilands and Bowman (1986)). This occurs when the brittle crack has grown to such an extent that the remaining net uncracked section is no longer able to support the load applied to the specimen. This is explained in more detail below.

In net section yielding, the nature of the failure stress versus crack depth relationship will be of the following form (the analysis is for through thickness cracks in which the cracked area is proportional to the crack length).

i) For a perfect uncracked specimen, the failure stress (nominally applied stress) would simply be the yield stress, σ_y,

ii) For a crack which has propagated through the entire section, the failure stress would be zero,

iii) For intermediate crack lengths, the failure stress would be inversely proportional to the crack length. This relationship is to be expected because if we have half the section left, we would expect the failure stress to be half of that at full cross section, i.e. $0.5\sigma_y$ (this is shown in Fig.2.6).

In cases where net section yielding takes place, the effect of stress concentration due to the crack is limited and the only real effect of the crack is to reduce the area of the material and hence the ability for the material to sustain loads. For cracks which are not through-thickness, the net section yielding curve will not be linear; it may be parabolic, cubic, ...etc. depending on the geometry of the crack.

2.4.2.2 Slow Crack Growth Model

Williams and Marshall (1975) modelled the slow crack growth behaviour of polymers using a crack opening displacement approach together with the Dugdale line zone model (Dugdale (1960)). They postulated that in a loaded cracked specimen, a craze zone of size c existed ahead of the crack tip. This craze zone would grow and the crack opening displacement (COD) would increase due to creep deformation until fracture occurred. Initially, the yield stress and modulus of the material in the craze are very high and the COD will be small. However, the yield stress and modulus will fall with time due to stress relaxation and the COD will increase due to creep deformation. Fracture would occur when the crack opening displacement reached a certain critical value called the critical COD, denoted δ_c. Macroscopically, this is equivalent to the attainment of a critical strain at the crack tip. The assumption was made that the stress in the craze zone σ_c (=yield stress) was constant along the zone and that the δ_c would remain constant as the crack propagated.

Given that polymers are viscoelastic, power laws were used to represent the time dependence of the modulus E and the craze stress σ_c:

$$\sigma_c(t) = \sigma_0 t^{-m} \qquad (2.9)$$

$$E(t) = E_0 t^{-n} \qquad (2.10)$$

where m and n are constants, σ_0 and E_0 are unit time values, and t is time.

Using Dugdale's line zone model and the above expressions, the following expressions for the line zone size and K_c can be derived:

$$c(t) = \frac{\pi}{8}\frac{K_c^2}{\sigma_c^2(t)} \tag{2.11}$$

$$K_c^2 = \delta_c \sigma_c(t) E(t) \tag{2.12}$$

For relaxation controlled fracture, the time can be assumed to be:

$$t = \frac{c}{\dot{a}} \tag{2.13}$$

By combining all the above equations, the following expression results:

$$K_c = D\dot{a}^{\frac{(m+n)}{2}(1-m+n)} \tag{2.14}$$

This is of the form:

$$\dot{a} = \beta(K_c)^b \tag{2.15}$$

The logarithmic form of this equation is

$$\log \dot{a} = b \log K_c + \log \beta \tag{2.16}$$

Consequently, a log-log plot of $\dot{a}$ against K_c should yield a straight line of slope b and intercept β.

The propagation time τ for a brittle flaw to grow from an initial size to the outside of the pipe can then be derived by combining equations (2.14) and (2.15) to yield:

$$\tau = \frac{1}{\beta \sigma^b \pi^{b/2}} \int_{a_i}^{a_f} \frac{da}{Ya^{b/2}} \tag{2.17}$$

where a_i and a_f are initial and final flaw sizes respectively. In order to perform the above integration, a computer program was written, the integration being performed using a Simpson's Rule algorithm.

2.4.3 Application of Theoretical Model

2.4.3.1 Initial Assumptions

Using $K_c/\dot{a}$ data measured by Marshall, Taylor et al. (1982) for Rigidex 002-40, values for β and b were obtained and are shown in Table 2.1.

Grade	Author(s)	Conditions of Expt.	β	b
Rigidex 002-40	Marshall et al (1982)	SENB, air, 20C	3.61×10^{-10}	10.70

Table 2.1 Slow crack growth data for Rigidex 002-40. SENB=single edge notch bending

During service, the temperature of the pipes underground can fluctuate. However, given that water is being transported by the pipes, it is fair to assume that the average temperature of the pipe will be close to the temperature of the water and less than room temperature. In general, especially at lower temperatures, the value of b appears to remain relatively constant whereas the value of β decreases (see e.g. Gray, Mallinson et al. (1981), Williams (1984)). This means that we can use the values of b and β obtained above (i.e. from 20°C tests) with the assurance that any subsequent results obtained will be underestimating the life of the pipe.

Given that we now have the slow crack growth constants, we can proceed to determine the critical crack sizes for a 50 year failure time. The specification for polyethylene pipes for use in the water industry classifies pipes according to their SDR, these being 11 and 17.6. For each SDR, a maximum operating pressure is quoted (10 bar for SDR 11, 6 bar for SDR 17.6). These pressure values are equivalent to a hoop stress of about 5.5MPa for each SDR. For any given SDR, the stress in the pipe is independent of the thickness (or diameter) because the stress is a direct function of the SDR. Therefore, the stress will be constant if the SDR is constant. This means that we only need to calculate the critical crack sizes for the smallest thickness pipe within any given SDR because we know that for thicker pipes, the critical crack size will be larger. We will therefore look at the following two cases shown in Table 2.2.

	SDR 11 pipe	SDR 17.6 pipe
thickness (mm)	8.2	7.1
outer diameter (mm)	90	125
max. operating pressure (bar)	10	6

Table 2.2 Parameters from limiting pipe cases used for slow crack growth analysis.

Assumptions

To simplify the stress analysis of the pipes, the following assumptions were made:

- A thin wall analysis has been used. This results in the following stresses in the pipe: σ_θ = 5.5MPa, σ_a = 2.75MPa. In fact, a thick walled assumption would have led to smaller values of σ_θ and σ_a so the assumption of thin wall is a conservative one.

- Residual stresses are tensile on the inner surface and compressive on the outer surface. Compressive stresses tend to close cracks and hence are not considered detrimental. However, tensile residual stresses will aid crack propagation and hence need to be taken into account in the stress analysis of the pipe. As residual stresses are very dependent on the extrusion characteristics, it is very difficult to quote a single figure which would be applicable for all pipe grades and pipe sizes. Additional stresses can also be set up by ground pressure and bending which are very difficult to measure and are very dependent on the location of the pipe. A safety factor approach is probably the best way to take into account such stresses. Vancrombrugge (1982) suggests that the effect of addition stresses could double the stress due to internal pressure alone. We have likewise chosen this figure (i.e. a safety factor of 2). This means that the maximum stresses in the pipe are now:

$$\sigma_\theta = 11\text{MPa}, \sigma_a = 5.5\text{MPa}$$

- The parameters obtained so far were for mode I fractures. As defects are most likely to lie in the radial plane for butt fusion welds (i.e. in the plane of the weld), this can be considered a mode I type crack if the stress of interest is taken to be the axial stress, σ_a = 5.5MPa.

- An edge crack, centre crack and semi-circular edge crack are analysed (Fig.2.7). There are several reasons for choosing these crack types. Firstly, the edge crack and centre cracks represent two extreme positions in which a crack can be situated, i.e. at

the edge of the pipe or in the centre of the pipe, so by studying these two particular crack types, we have in effect covered the two extremes and we can therefore say with confidence that the maximum tolerable crack size for any real crack should lie somewhere between the values calculated for these two extremes. Secondly, the analysis assumes that these types of crack run along the entire circumference of the pipe (this is simply because the Y factors are derived with this assumption). In practice, such cracks are very unlikely and therefore the results obtained for the maximum defect sizes will be underestimates. The inclusion of the semi-circular edge crack serves to represent a more realistic type of crack found in practice.

The Y factors for a through-thickness edge crack, a through-thickness centre crack and a semi-circular edge crack are given as (Ewalds (1986)):

$$Y_{edge} = 1.12 - 0.231\left(\frac{a}{w}\right) + 10.55\left(\frac{a}{w}\right)^2 - 21.72\left(\frac{a}{w}\right)^3 + 30.39\left(\frac{a}{w}\right)^4 \qquad (2.18)$$

$$Y_{centre} = 1 + 0.256\left(\frac{a}{w}\right) - 1.152\left(\frac{a}{w}\right)^2 + 12.2\left(\frac{a}{w}\right)^3 \qquad (2.19)$$

$$Y_{semi\text{-}circ} = \frac{2}{\pi}\left(1.04 + 0.202\left(\frac{a}{w}\right)^2 - 0.106\left(\frac{a}{w}\right)^4\right)\left(1.1 + 0.35\left(\frac{a}{w}\right)^2\right) \qquad (2.20)$$

These Y factors correspond to an edge crack of length a in a strip of finite width w, a centre crack of length 2a in a strip of finite width w and a semi-circular edge crack of length 2a in a strip of finite width w. Even though these Y factors are for strips, we can apply them to pipes because a pipe is essentially a strip when we cut along its longitudinal axis and roll the pipe out. Y factors for pipe geometry have been reported by Rajab and Zahoor (1990) and Poette and Albaladejo (1991).

2.4.3.2 Determination of Final Crack Size, a_f

The slow crack growth model is based on brittle crack growth from an initial flaw size a_i to a final flaw size a_f. At first sight, we might take the final flaw size for a circumferential crack in a pipe to be the wall thickness. However, this would be incorrect because the pipe can fail prior to the crack reaching full wall thickness. The two ways it can do so are via unstable fracture or net-section yielding. Therefore, the value of the final flaw size has to be determined by looking at these two failure events and seeing which one is most likely to occur first.

1) Net Section Yielding

For the Rigidex 002-40 polyethylene grade, Chan (1982) found that the yield stress was in the range 20-30MPa at room temperature. Also, at this temperature, the variation of yield stress with strain rate was small at fairly long strain rates. For TUB 124 HPPE, the yield stress at room temperature is 25MPa. Given that the yield stress increases with decreasing temperature, the yield stress of the pipes when buried underneath the ground will be higher than those quoted at room temperature. We can therefore take the values at room temperature as a worst case value (i.e. 20MPa). Since we now know the yield stress, this enables the net section failure diagram to be drawn and this is shown in Fig.2.8. There is no distinction between the SDR 11 and the SDR 17.6 cases if the cracks are assumed to be edge or centre cracks. This is not true for the semi-circular crack.

For a maximum operating stress of 5.5MPa, the critical defect size for edge and centre cracks to cause failure can be determined from the following equation:

$$CD = 1 - 1/Fs \tag{2.21}$$

where CD = critical defect size/wall thickness, Fs = yield stress/maximum rated operating stress).

Hence, taking the yield stress to be 20MPa, Fs = 20/5.5 = 3.64 and hence CD = 1-1/3.64=0.73. This corresponds to a_f=6.0mm for the SDR 11 pipe and a_f=5.2mm for the SDR 17.6 pipe.

For a maximum operating stress of 5.5MPa, the critical defect size for semi-circular edge cracks to cause failure can be determined from the following equation:

$$CD = \sqrt{2\left(\frac{R_o + R_i}{t}\right)\left(1 - \frac{1}{Fs}\right)} \tag{2.22}$$

Hence, taking the yield strength to be 20MPa, Fs = 20/5.5 = 3.64. For the SDR 11 pipe, the critical defect size is 31.2mm and for the SDR 17.6 pipe the value is 35.9mm. The values for the semi-circular crack are much greater than the wall thickness of the pipe and hence net section yielding would never occur. Instead, the pipe would start to leak as soon as the crack penetrates the wall of the pipe. The results are summarised in Table 2.3.

	Critical crack size for net section yield failure in SDR 11 pipe (mm)	Critical crack size for net section yield failure in SDR 17.6 pipe (mm)
edge crack	6.0	5.2
centre crack	6.0	5.2
semi-circular edge crack	> thickness of pipe	> thickness of pipe

Table 2.3 Critical crack sizes for net section yielding.

2) Unstable Fracture

A search for K_{Ic} values for polyethylene reveals values starting from about $1MPam^{1/2}$ for a wide range of testing conditions (different strain rates, temperatures, etc.) (see e.g. Williams (1984)). Chan (1982) performed fracture toughness tests on Rigidex 002-40 and found that, at 20°C, $K_{Ic}=5MPam^{1/2}$. It has been observed for various polyethylenes (e.g. Williams (1984), Mandell, Roberts et al. (1983)) that fracture toughness increases with decreasing temperature and therefore, in a similar way to the yield stress, we will assume that the 20°C value for the fracture toughness represents the fracture toughness of the pipe when it is underground.

Using the value of K_{Ic} obtained above, the critical crack sizes for fast fracture can be evaluated from the equation:

$$K_{Ic} = Y\sigma\sqrt{\pi a} \qquad (2.23)$$

The results for the various crack types are shown in Table 2.4.

Crack Type	Critical crack size for unstable fracture in SDR 11 pipe (mm)	Critical crack size for unstable fracture in SDR 17.6 pipe (mm)
edge crack	5.95	5.25
centre crack	> thickness of pipe	> thickness of pipe
semi-circular edge crack	> thickness of pipe	> thickness of pipe

Table 2.4 Critical crack sizes for unstable fracture.

Now by combining the results of the net section yielding and the fast fracture, we can determine the likely mode of failure for each type of crack modelled. These are shown in Table 2.5.

	Critical crack size for SDR 11 pipe (mm)	Critical crack size for SDR 17.6 pipe (mm)
edge crack	5.95 (fast fracture)	5.2 (net section yielding)
centre crack	6.0 (net section yielding)	5.2 (net section yielding)
semi-circular edge crack	8.2 (leakage)	7.1 (leakage)

Table 2.5 Critical crack sizes and nature of failure.

2.4.3.3 Determination of Critical (initial) Crack Size to Cause Failure in 50 years

Fig.2.9 shows the generated stress rupture life vs. initial crack size curves for Rigidex 002-40 (SDR 11 and SDR 17.6), obtained by solving equation (2.17). It can be seen from the graph that centre cracks and semi-circular edge cracks are much more tolerable as far as rupture life is concerned. From the curves, the critical initial crack sizes for a 50 year lifetime can be obtained and are shown in Table 2.6.

Crack Type	Critical initial crack size for SDR 11 pipe (mm)	Critical initial crack size for SDR 17.6 pipe (mm)
edge crack	1.19	1.11
centre crack	3.11	2.86
semi-circular edge crack	4.25	4.00

Table 2.6 Critical crack sizes for failure in 50 years.

The results between the two pipe sizes show that the SDR 11 pipe can tolerate slightly larger defects than the SDR 17.6 pipe. This is to be expected given the larger wall thickness associated with the SDR 11 pipe.

As stated earlier in this chapter, it is anticipated that the crack growth characteristics of TUB 124 HPPE will be similar to Rigidex 002-40. Therefore, the critical crack sizes calculated above for the Rigidex 002-40 will be valid for the TUB 124 HPPE material.

2.5 Conclusions

This chapter has covered mode I crack growth, the mode encountered predominantly in butt fusion welds. It was found that for the polyethylenes used in this project the critical crack sizes for a 50 year life were calculated to be 1.11mm for a through-thickness edge crack, 2.86mm for a through-thickness centre crack and 4.00mm for a semi-circular edge crack, based on the results for the SDR 17.6 (7.1mm wall thickness) case which produced the smallest tolerable crack sizes. If we now consider the case of a real crack, it is improbable that it will be an edge crack running along the entire circumference (i.e. a through-thickness edge crack) nor is it likely to be a centre crack running along the entire circumference. It is therefore justifiable to say that the critical crack size for a real defect will be greater than 2.86mm. The case of a semi-circular crack is more realistic and this is reflected in the critical crack size value of 4.00mm.

In NDT inspection, the ability for a flaw to be detected is to large extent dependent on the flaw area. In fracture mechanics analysis, it has been assumed that for the edge and centre crack cases the dimension normal to the crack size is infinite and for the semi circular edge crack it is twice the crack size. We have said that the critical crack size for a real defect will be more than 2.86mm. The nearest case that fulfils this criterion is a semi-circular edge crack of size 4.00mm which has an area of about $2.51 \times 10^{-5} m^2$; this will be equivalent in area terms to a circular crack of diameter 5.65mm. Therefore, for NDT purposes, provided the area of a defect is less than that of a 5.65mm diameter circular planar defect, the crack will be subcritical and the weld will be deemed acceptable for use for at least 50 years.

For electrofusion coupler welds, the principal mode of loading is believed to mode II. Not much work has been done on this mode of loading for polymers in slow crack growth owing to the fact that mode I is by far the most common mode of loading. It has been stated by Williams (1984) that it is possible to postulate a condition for fracture in mode II. As far as unstable fracture is concerned, experience shows that the K_{IIc} value is very high (much larger than the K_{Ic} value). For instance, wood has K_{IIc} approximately equal to $5K_{Ic}$ (Barrett and Foschi (1977)). It is therefore not unrealistic to assume that the critical crack sizes for mode II failure will be considerably larger than those calculated for mode I failure. There is also the fact that the effective thickness for crack propagation in an electrofusion joint is much greater than the wall thicknesses of the pipes used in this project because the crack travels in a direction

parallel to the axis of the pipe. It therefore seems reasonable to use the same critical defect size obtained for the butt-fusion weld for the electrofusion weld.

The analysis was conducted assuming the smallest wall thickness pipe. Haagensen et al (1988) state that for larger specimens, the fatigue strength may be lower than that of smaller, geometrically similar ones. Therefore, the critical defect size cannot simply be scaled up with the thickness of the pipe. However, given that the analysis so far has been a conservative one, we can assume that the critical defect size for larger pipes will be no smaller than the value calculated for the smallest wall thickness pipe. Therefore, any nondestructive testing technique which is capable of detecting defects of the sizes calculated for the smallest thickness pipe would in principle be able to be used for thicker pipes.

To summarise, the critical crack sizes based on area for both butt-fusion and electrofusion welds will be taken as 5.7mm. This value serves as an absolute minimum which a nondestructive testing technique must be able to detect comfortably.

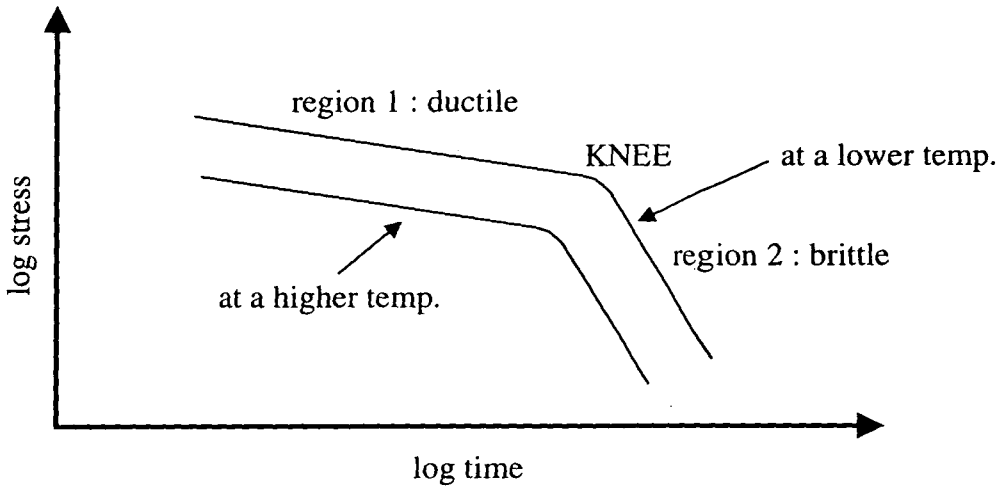


Fig.2.1 Example of a typical stress rupture plot

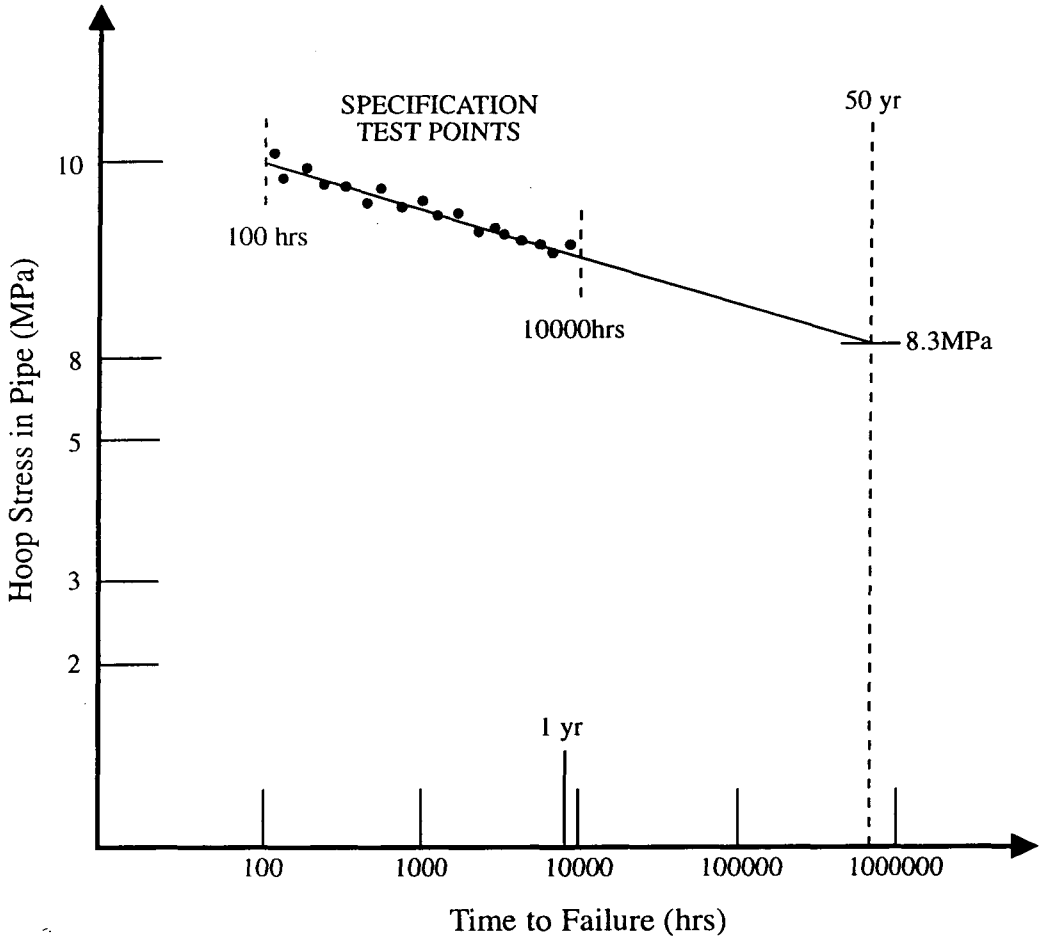


Fig.2.2 Example of a regression line for predicting 50 year failure stress

BIBL. LONDIN. UNIV.

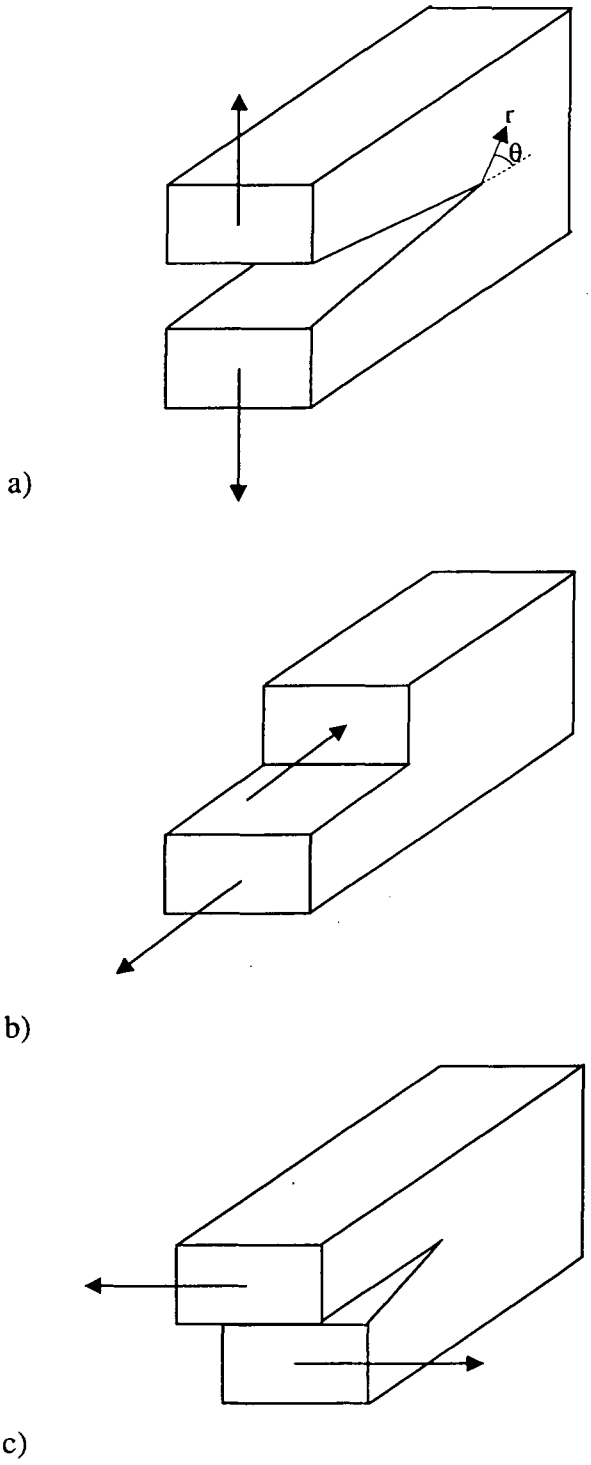


Fig.2.3 Fracture modes encountered in fracture mechanics analysis: a) Mode I (opening mode); b) Mode II (edge sliding mode); c) Mode III (tearing mode)

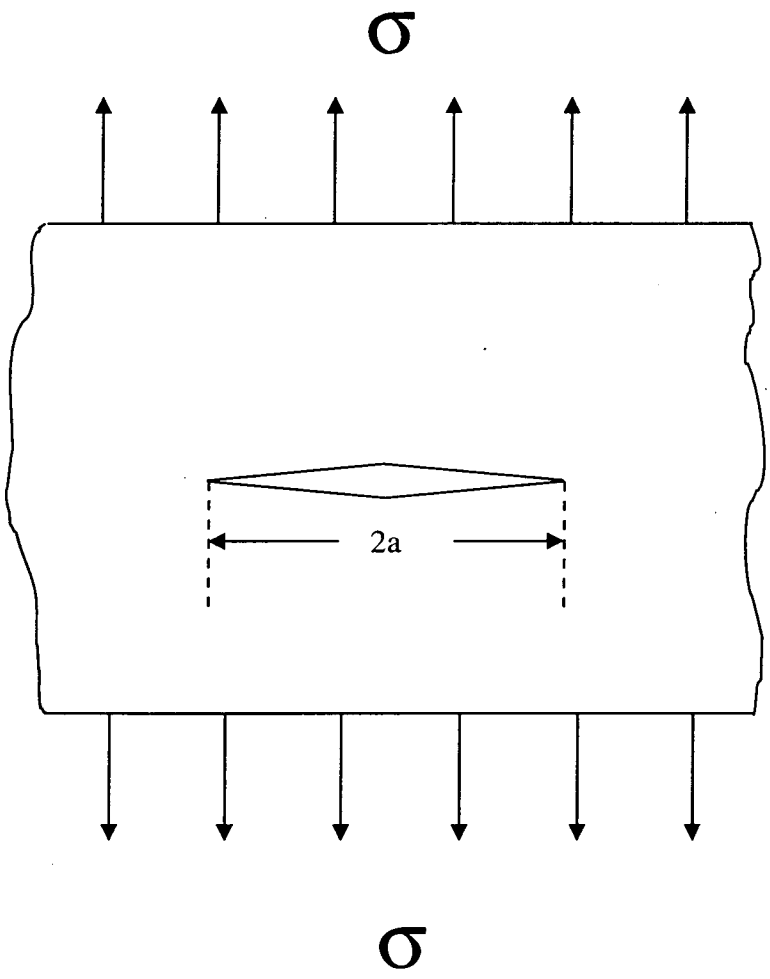


Fig.2.4 Crack in an infinite plate

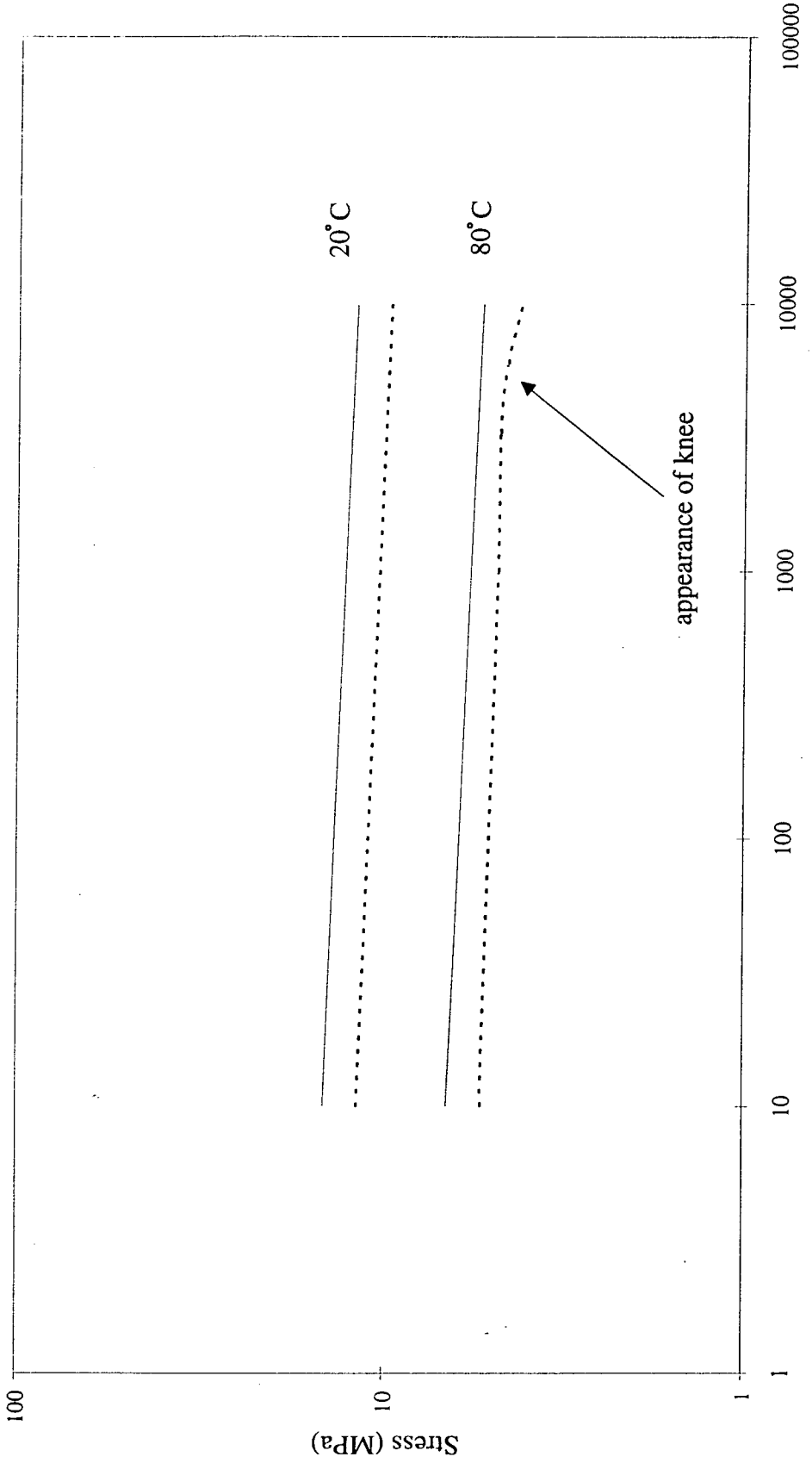


Fig.2.5 Comparison of stress rupture performance between TUB 124 HPPE and Rigidex 002-40

——— TUB 124 HPPE

- - - - - - - - - Rigidex 002-40

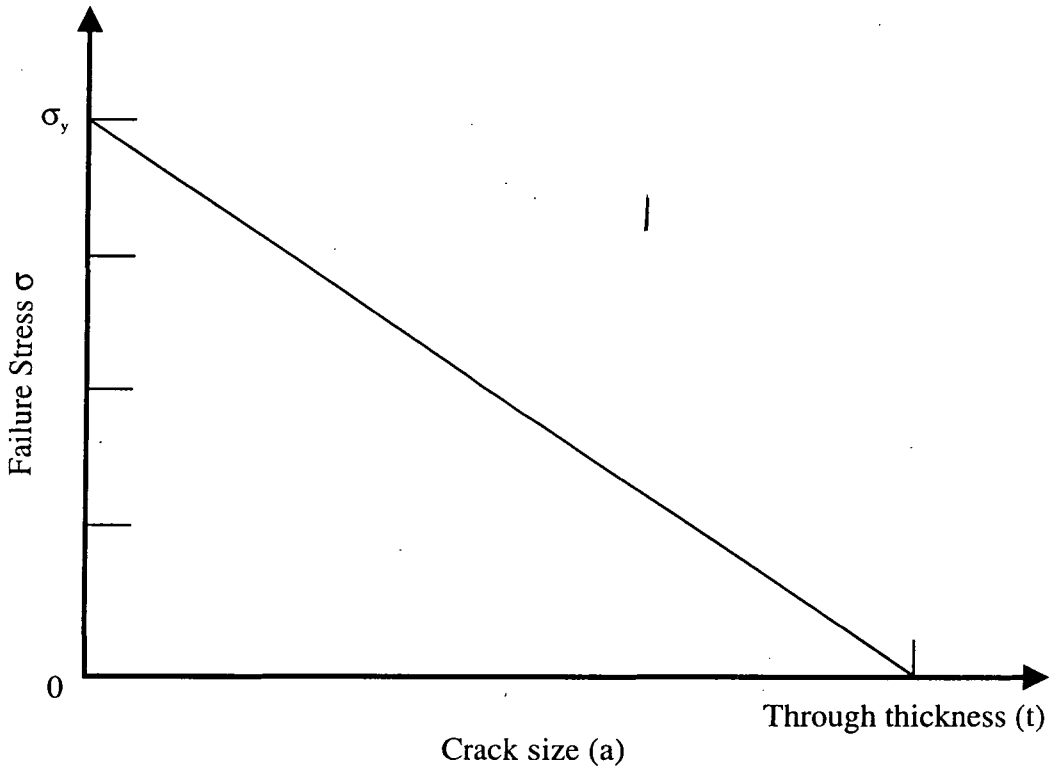


Fig.2.6 An example of a net section yield curve

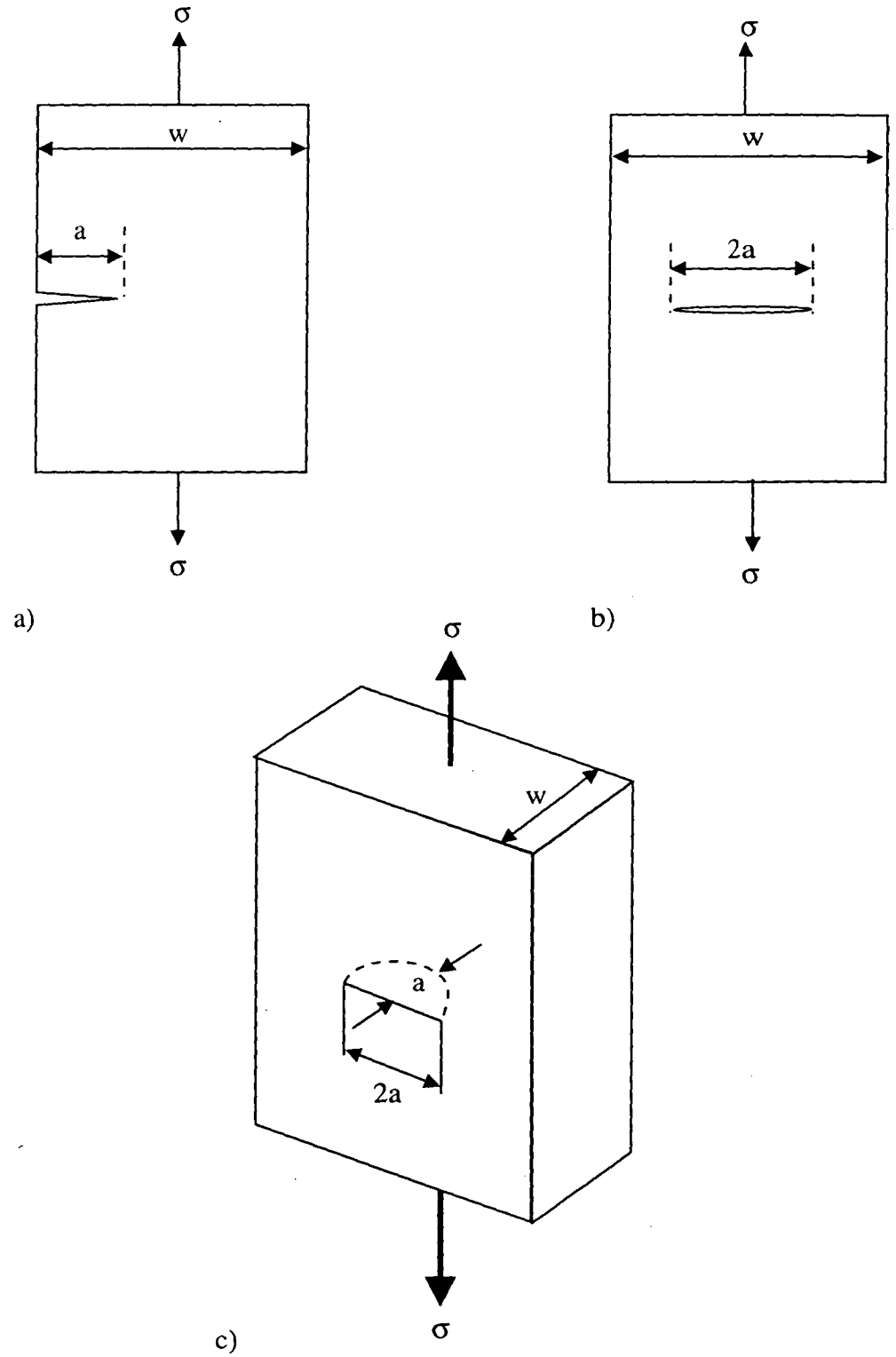


Fig.2.7 Crack types used for slow crack growth analysis. a) edge crack; b) centre crack; c) semi-circular edge crack

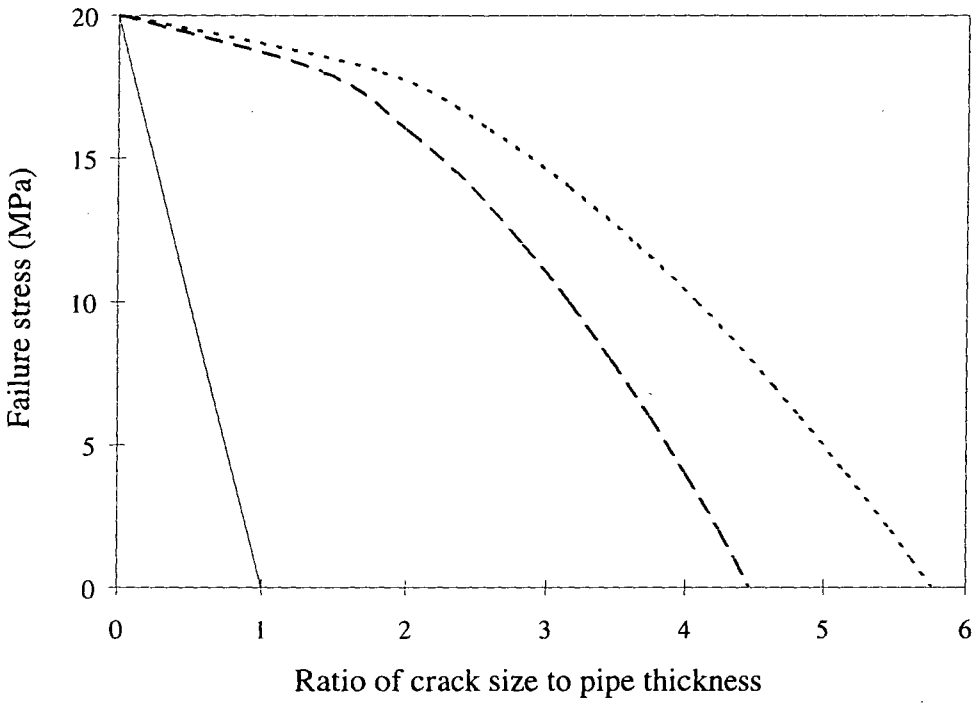


Fig.2.8 Net section yield curves for edge, centre and semi circular cracks.

———————— edge and centre crack (SDR 11 and SDR 17.6)

- - - - - - - - - - - semi-circular edge crack (SDR 11)

- - - - - - - - - - - - semi-circular edge crack (SDR 17.6)

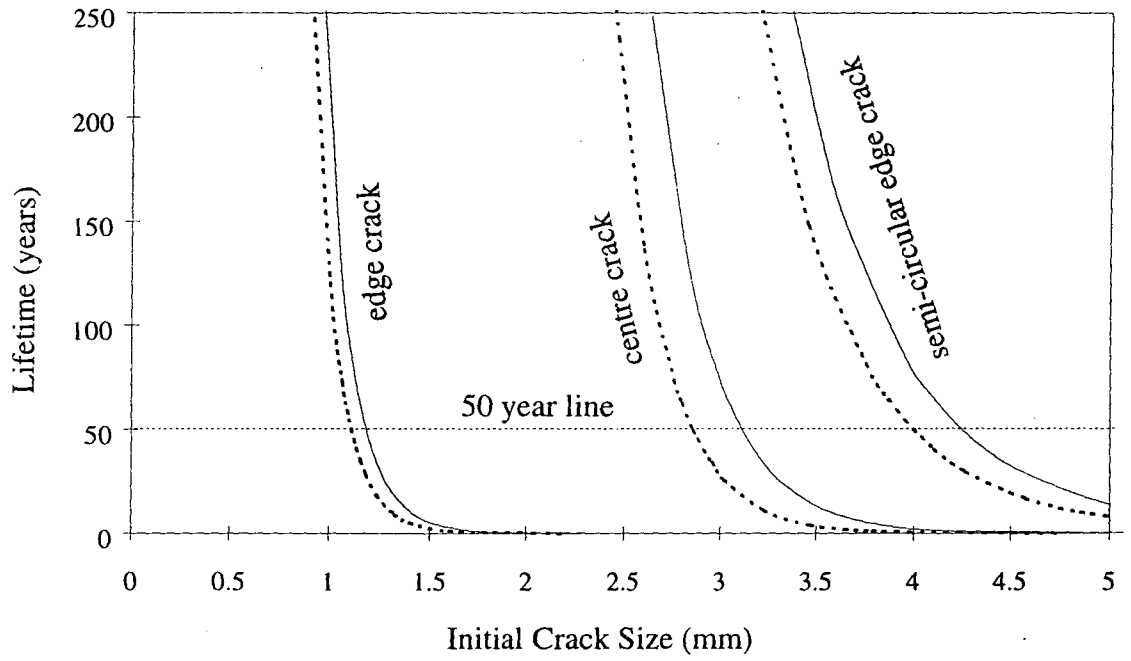


Fig.2.9 Stress rupture life vs. initial crack size for Rigidex 002-40.

——————— SDR 11

..... SDR 17.6

CHAPTER 3

Acoustic Properties of Polyethylene

3.1 Introduction

In order to conduct any analysis of the feasibility of using ultrasonics to detect defects in polyethylenes, it is imperative that we know the acoustic properties of the materials we are inspecting. The properties that have been measured are the bulk wave velocities and the bulk wave attenuations. Knowledge of the bulk wave velocities is important because without these, the modelling of ultrasonic waves would be impossible. In addition, experiments such as those which involve waves incident at non-normal angles to a plane surface would be difficult to perform. The attenuation is of particular importance in materials such as polyethylene because it dictates how far a bulk wave can propagate through a material and still be measurable. This chapter therefore describes the results obtained from experiments performed to determine these acoustic properties.

3.2 Longitudinal Bulk Wave Properties

3.2.1 Longitudinal Bulk Wave Velocity

Thin square specimens (2mmx40mmx40mm) were obtained from a TUB 124 HPPE pipe and a Rigidex 002-50 pipe. For each grade, three specimens were obtained, each one being cut from one of the three orthogonal planes associated with a pipe (i.e. axial, hoop and radial planes) (see Fig.3.1). For each specimen, a 10MHz centre frequency longitudinal plane transducer was used to obtain a front face and back face reflections, the specimen being immersed in water (schematic shown in Fig.3.2). Fig.3.3a shows a typical time domain response (this particular one from a TUB 124 HPPE specimen). Three signals are observed; the first corresponds to the front face reflection; the second is the first back face reflection; the third is the second back face reflection. In order to measure the phase velocity of the polyethylenes, the 'Amplitude Spectrum Method' was adopted (Pialucha; Guyott et al. (1989)). In this method the time domain response comprising the front face reflection, together with at least one of the back face reflections is captured in digital form and the whole time history is subsequently Fourier transformed. The frequencies of the various minima are then located. These minima correspond to through thickness acoustic resonances of the

specimen set up by the reverberations within the specimen destructively interfering with the front face echo and are related to the phase velocity, c_{ph} by:

$$c_{ph} = \frac{2tf_n}{n} \tag{3.1}$$

where t is the specimen thickness, n is the mode number of a resonance and f_n is the frequency of the mode n resonance. If one of the semi-infinite layers has a higher acoustic impedance than the specimen and the other semi-infinite layer has a lower acoustic impedance than the specimen, then the back face reflections have to be phase inverted before a Fourier transform is taken. Alternatively, we can take the position of the maxima rather than the minima. Fig 3.3b shows the spectrum of Fig.3.3a. Using the amplitude spectrum method, the phase velocities were obtained and are shown in Figs.3.4a and 3.4b for TUB 124 HPPE and Rigidex 002-50 respectively. The error is expected to be less than 1%. It can be seen that the variation in velocity with frequency for both TUB 124 HPPE and Rigidex 002-50 is small, with a variation of less than 5% over the frequency range 2-14MHz. Longitudinal bulk waves can therefore be assumed to be non dispersive. For the TUB grade, the phase velocity in the radial direction is slightly higher than those for the other two directions with the difference being less than 5%. For the Rigidex grade, there is no noticeable difference in phase velocity for the three directions. If we compare velocities between the two grades, we can see that the TUB grade has values up to 10% higher.

3.2.2 Longitudinal Bulk Wave Attenuation.

The longitudinal bulk wave attenuation can be calculated by using the time domain results from the experiments of the previous section. By referring to Fig.3.5, if the pressure of the incident plane wave is I, then the pressure P_{FI} of the wave reflected from the front face is I R_{wp}, where R_{wp} is the reflection coefficient from the water/polyethylene interface and is given by

$$R_{wp} = \frac{Z_p - Z_w}{Z_p + Z_w} \tag{3.2}$$

where Z_p is the acoustic impedance of the polyethylene and Z_w the acoustic impedance of the water.

Therefore, $P_{FI} = I\, R_{wp}$ (3.3)

At interface 1, the pressure P_{T1} of the transmitted wave is given by

$$P_{T1}=I\,T_{wp} \tag{3.4}$$

where T_{wp} is the transmission coefficient from the water to the polyethylene. By following the progress of this wave to the back face of the specimen and back to the transducer, we arrive at the following expression for the longitudinal bulk wave attenuation in the polyethylene:

$$\alpha_L = \frac{1}{2t}\ln\left(\left|\frac{P_{F1}}{P_{T2}}\right|\left(1-R_{wp}^2\right)\right) \tag{3.5}$$

where P_{T2} is the pressure of the first back face echo received by the transducer.

Therefore, by measuring the reflection from the front face and the first back face reflection, we can calculate the attenuation. The division was carried out in the frequency domain so that any frequency dependence will be measured. The results are shown in Figs.3.6a and 3.6b for the TUB grade and the Rigidex grade respectively. Given that the measured amplitudes are relatively sensitive to misalignment of the transducer with respect to the face of the specimen, the error in the calculated attenuation is expected to be relatively large (about 20%). We can see that for both grades, there is little direction dependence of attenuation. The attenuation of the Rigidex grade is higher than the attenuation of the TUB grade by about 30%.

3.3 Shear Bulk Wave Properties

3.3.1 Shear Bulk Wave Velocity

The experimental set-up used for shear bulk wave properties measurement is shown in Fig.3.7. Here we have a 10MHz centre frequency shear wave probe with a perspex delay line. The delay line is then coupled to the specimen by a suitable coupling medium (molasses). Given that the coupling medium has a finite thickness, it will have an effect on the transmission of ultrasound into the specimen. However, if the ratio of the coupling layer thickness to the smallest wavelength within the bandwidth of the input signal is small (less than 0.05), then the layer can be considered invisible and hence it can be assumed that the perspex and polythylene are in contact (i.e. perfect coupling)

In order to try and achieve as near perfect coupling conditions as possible, the pressure on the coupling medium was increased until a stable front face echo was achieved. The time domain trace of the front face and back face echoes was then obtained. The amplitude spectrum was once again used for calculating the phase velocities. Figs.3.8a and 3.8b show the variation of phase velocity with frequency for the TUB grade and the Rigidex grade respectively. As with the longitudinal bulk velocity, there is very little variation in the phase velocity with frequency for either grade.

3.3.2 Shear Bulk Wave Attenuation.

The shear bulk wave attenuation can be calculated using the time domain results from the experiments of the previous section. In a similar way to that used for calculating the attenuation of longitudinal bulk waves, it can be shown that the attenuation α_t in shear waves is given by

$$\alpha_t = \frac{1}{2t} \ln\left(\left|\frac{P_{F1}}{P_{T2}}\right|\left(\frac{1-R_{dp}^2}{R_{dp}}\right)\right) \qquad (3.6)$$

where R_{dp} is the reflection coefficient at the perspex (delay line)/polyethylene interface. Note that if we compare this equation to equation (3.5) we can see that in the present equation there is an extra denominator term inside the natural log expression. This is simply because the polyethylene specimens used for shear wave measurements were air backed as opposed to water backed for the longitudinal wave measurements.

Therefore, by measuring the reflection from the front face and the first back face reflection, we can calculate the attenuation. It was noticed that the back face echoes obtained from the 2mm thick Rigidex specimens were extremely small and as a result thinner samples 1mm thick had to be used. The frequency domain results are shown in Figs.3.9a and 3.9b for the TUB and Rigidex grades respectively. We can see that for the TUB grade, the attenuation is very similar in all directions. For the case of the Rigidex grade, the attenuation in the hoop direction (i.e. normal to the hoop plane) is noticeably larger than that in the other two directions. The attenuation of the Rigidex grade is significantly larger than the attenuation of the TUB grade which accounted for the very small back face echoes from the 2mm thick Rigidex specimens. If we compare the bulk shear wave attenuation to the bulk longitudinal wave attenuation, we can see that there is a significant difference, the bulk shear wave attenuation being over 5 times higher. The implication of this from a practical point of view is that the

use of shear waves for ultrasonic testing will be very difficult over any appreciable propagation distance. For instance, at 2MHz, the attenuation in the TUB grade is about 350Np/m. If we tried to propagate a shear wave through a 10mm thick piece of TUB polyethylene at 2MHz, the amplitude of the wave would drop by 30dB. For longitudinal waves, the corresponding drop would only be 4dB. One possible advantage is that for techniques where unwanted shear waves are generated, these will die away very quickly due to the high attenuation.

3.4 Ultrasonic Examination of Weld Region

Welding frequently leads to a change in the structural properties of a material such as the fracture toughness. From an ultrasonics point of view, the interest is to determine whether the bulk waves change their propagation characteristics as they travel through the welded region. In order to do this, two Rigidex specimens were used. One was cut from a section of a pipe away from the welded region (parent material); the other was cut from a region containing the weld itself (Fig.3.10). A pulse-echo test was performed on both specimens using water to couple a 10MHz plane transducer to the specimen. The results showed that there was no difference in the amplitude of the back face signal and probably more importantly, there was no observable reflection from the weld. There is therefore no significant difference between the weld and parent material acoustic properties.

3.5 Conclusions

Acoustic properties measurements have been conducted on the two grades of polyethylene used in this project: TUB 124 HPPE and Rigidex 002-50. The measurements were carried out on specimens obtained from a pipe, with each specimen being cut in one of the three principal planes of the pipe. The phase velocity measurements showed that dispersion was not significant for either longitudinal or shear bulk waves. The results from the different planes showed that the polyethylenes were generally isotropic with slight variations in phase velocity, these variations being less than 5% for bulk longitudinal waves and less than 10% for bulk shear waves. Attenuation measurements showed that the attenuation of longitudinal waves was essentially the same for the three principal planes, with the attenuation in the Rigidex grade being higher than that in the TUB grade. For shear waves, the attenuation in general is much larger than for longitudinal waves, with the shear wave attenuation being more than five times higher than that of longitudinal waves. Between different principal planes, there is little variation in shear wave attenuation for the TUB grade

but some evidence of anisotropy can be seen in the results for the Rigidex grade, although the anisotropy is not very large (less than 25%).

Measurements have also been conducted on a sample containing a real butt fusion weld. The results showed that the existence of the weld would not affect ultrasound propagating through it (i.e. it has similar acoustic properties to the parent material) and therefore the weld region can be assumed to be a homogeneous material with the properties of the parent pipe.

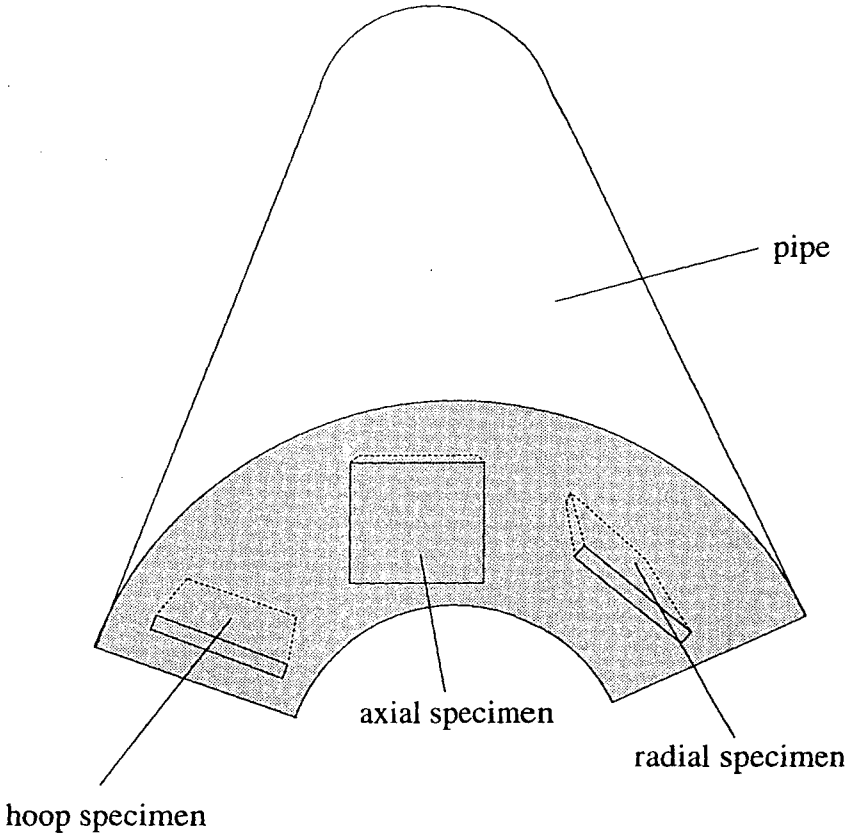


Fig.3.1 Schematic of specimens cut from orthogonal planes in polyethylene pipe

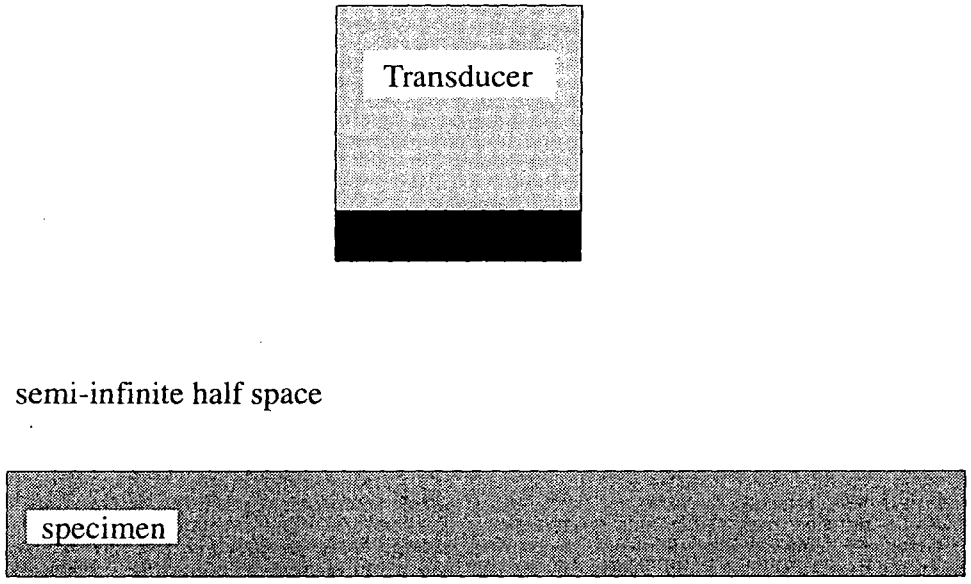
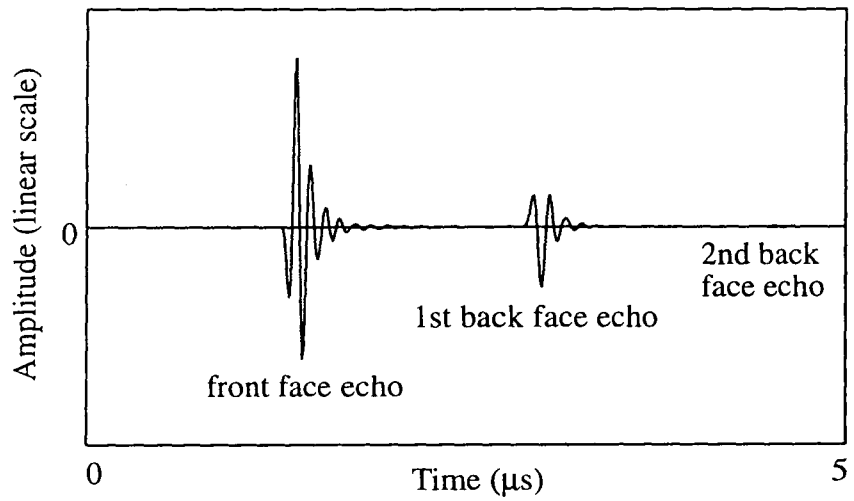
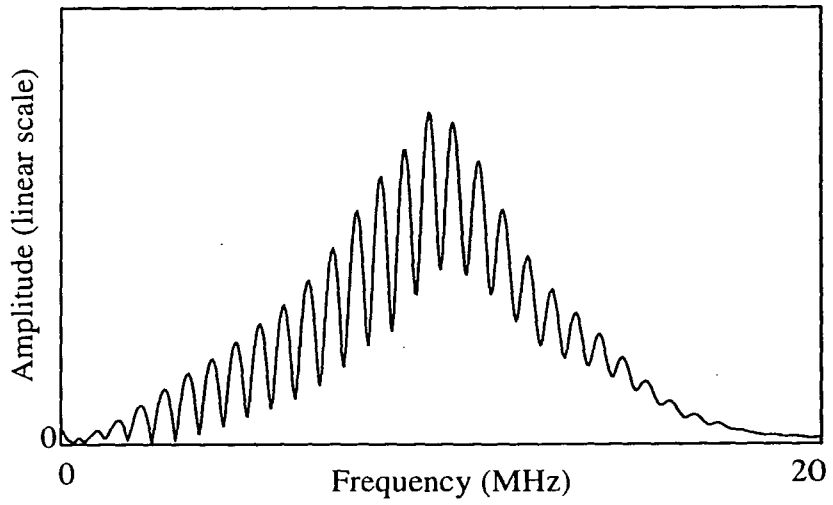


Fig.3.2 Schematic of a typical set-up used for velocity and attenuation measurement

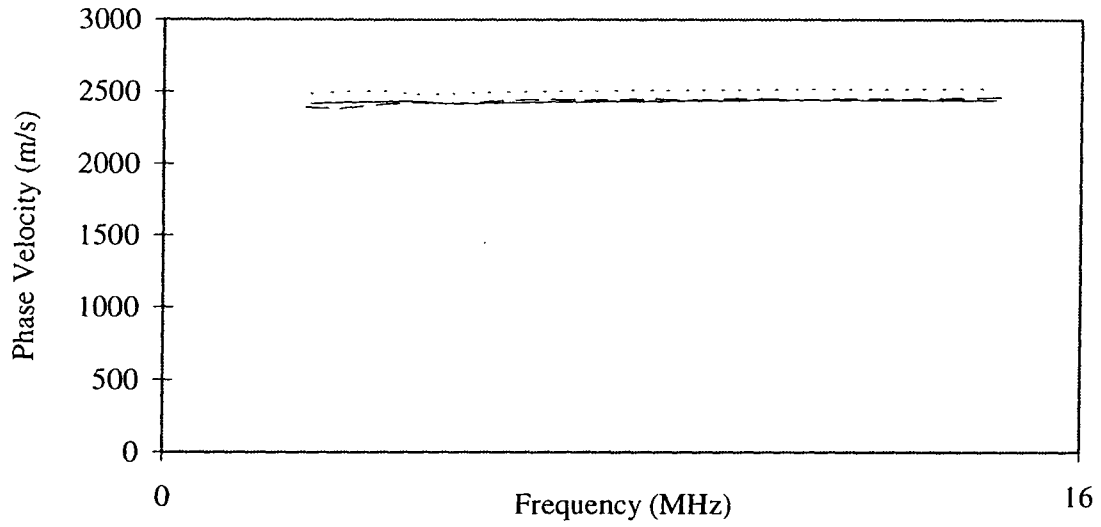


a)

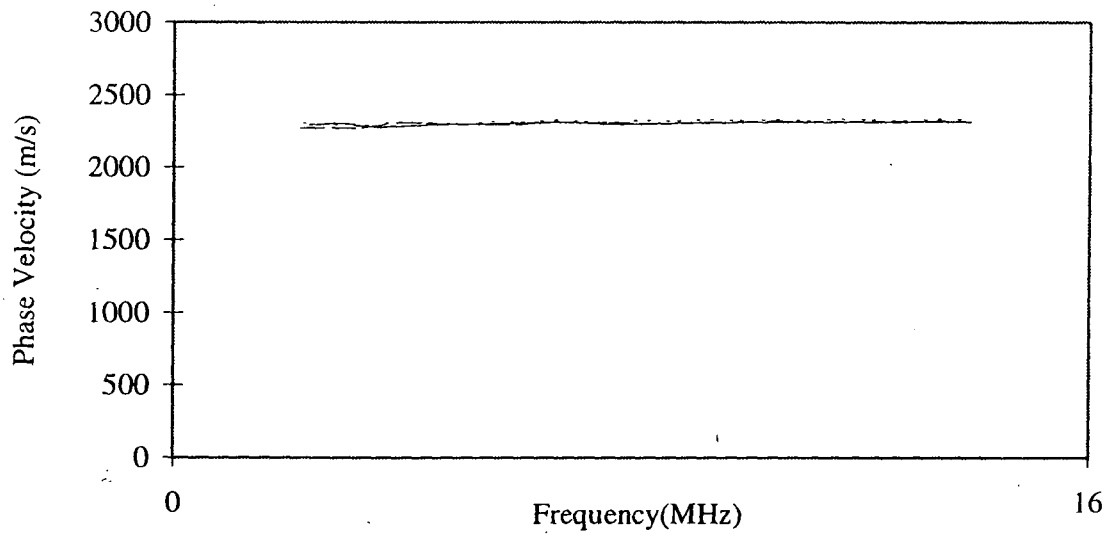


b)

Fig.3.3 Typical response of a polyethylene plate. a) Time domain response of a polyethylene specimen (TUB grade); b) spectrum of a)



a)



b)

Fig.3.4 Bulk longitudinal wave phase velocity variation with frequency. a) Bulk longitudinal wave phase velocity for TUB 124 HPPE; b) Bulk longitudinal wave phase velocity for Rigidex 002-50

———— normal to axial plane
..... normal to radial plane
— — — — — normal to hoop plane

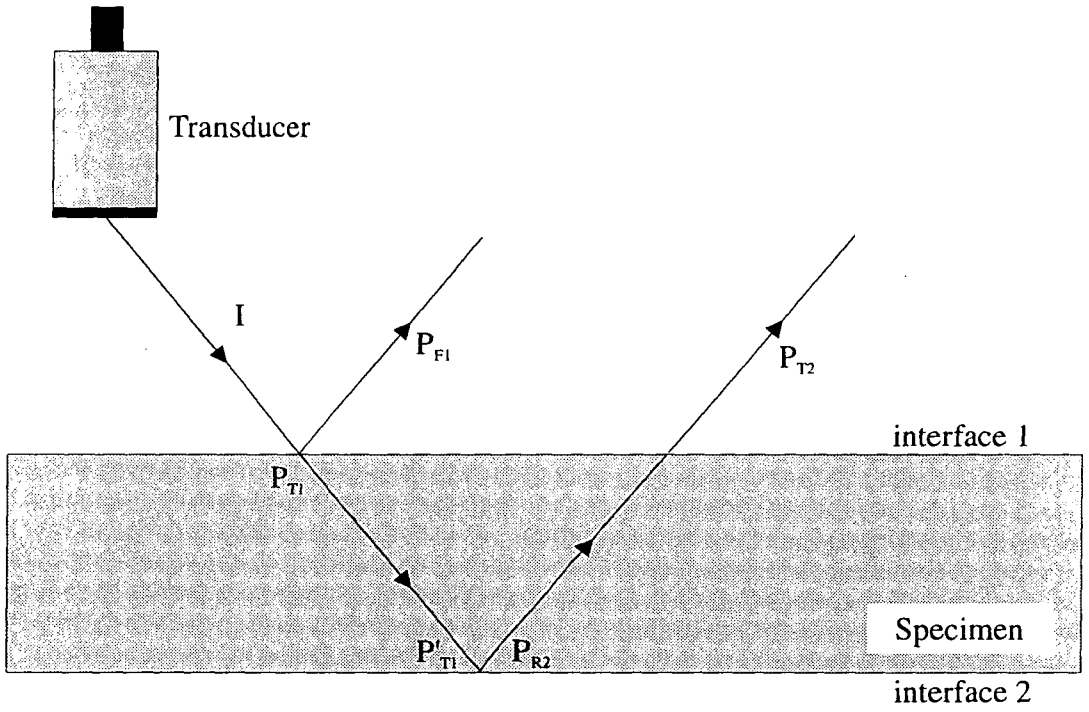
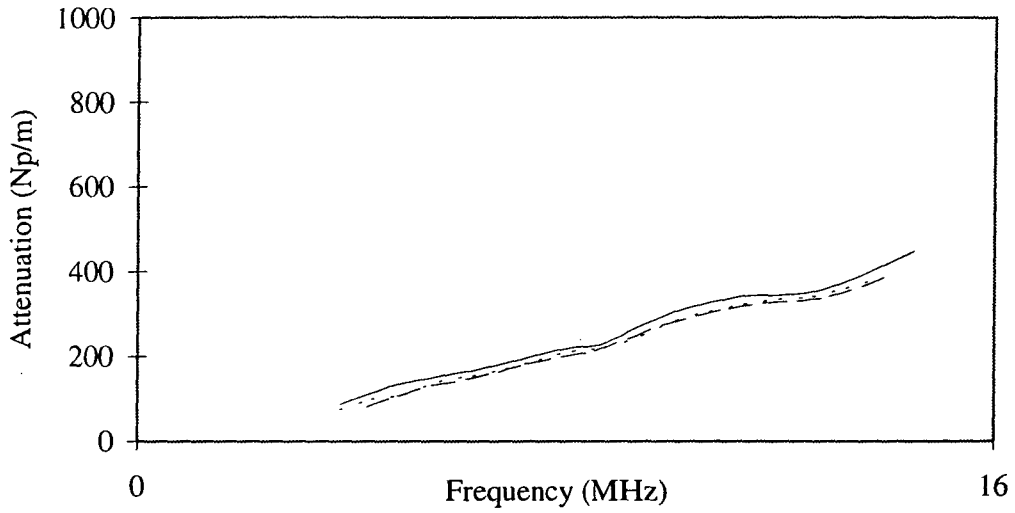
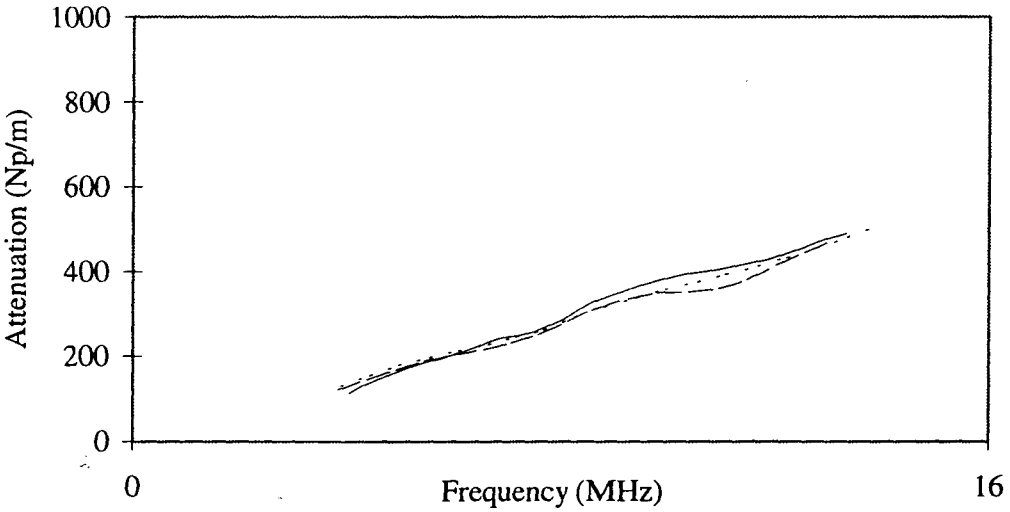


Fig.3.5 Schematic of reflection and transmission of waves used for attenuation calculation (rays shown non-normal for clarity)



a)



b)

Fig.3.6 Bulk longitudinal wave attenuation variation with frequency. a) Bulk longitudinal wave attenuation for TUB 124 HPPE; b) Bulk longitudinal wave attenuation for Rigidex 002-50

———— normal to axial plane
..... normal to radial plane
— — — — — normal to hoop plane

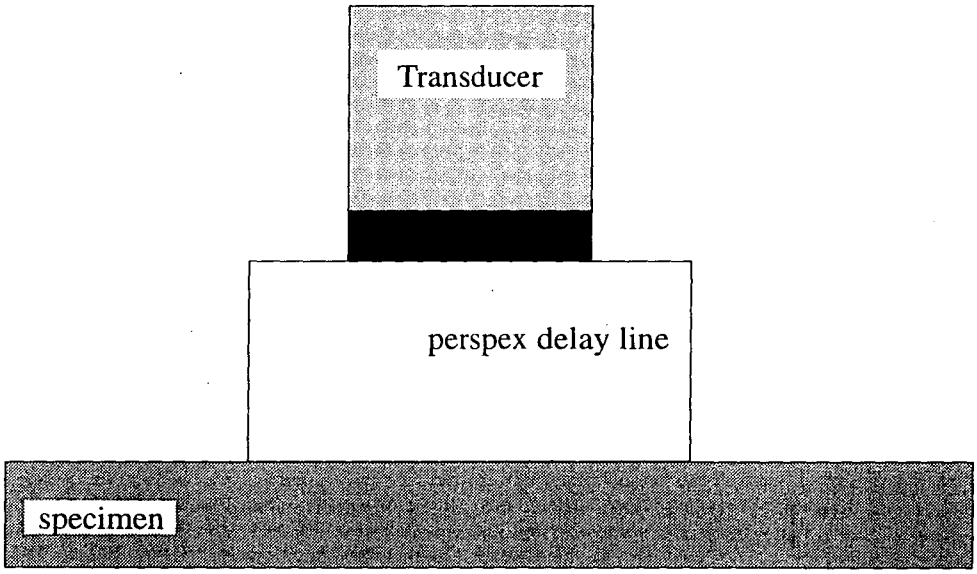
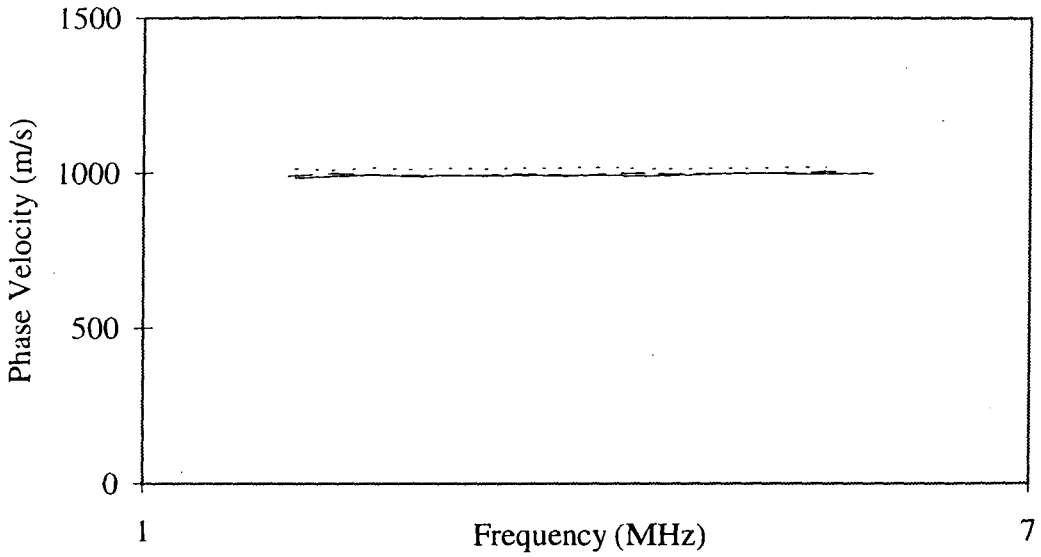
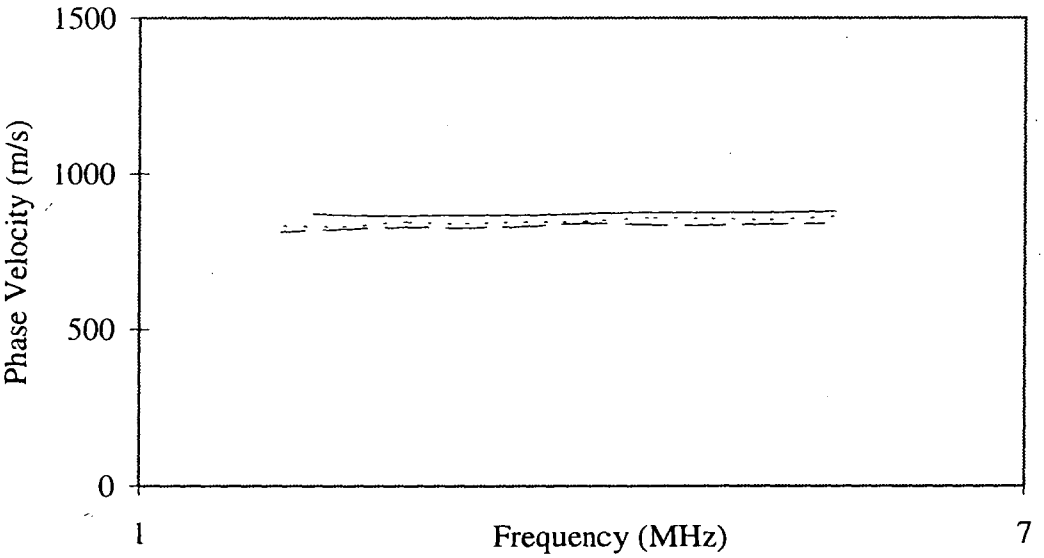


Fig.3.7 Schematic of experimental set-up used for measurements involving shear waves



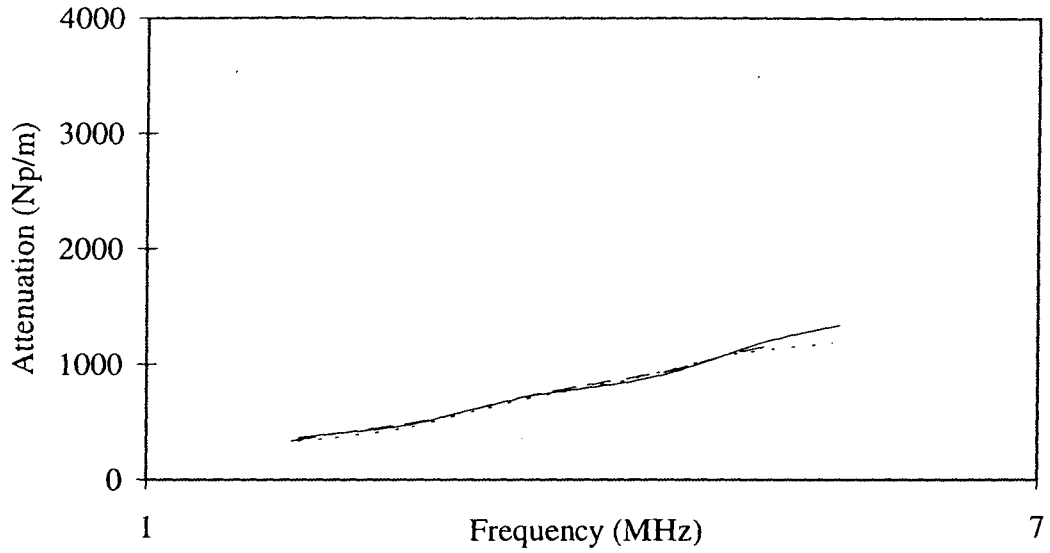
a)



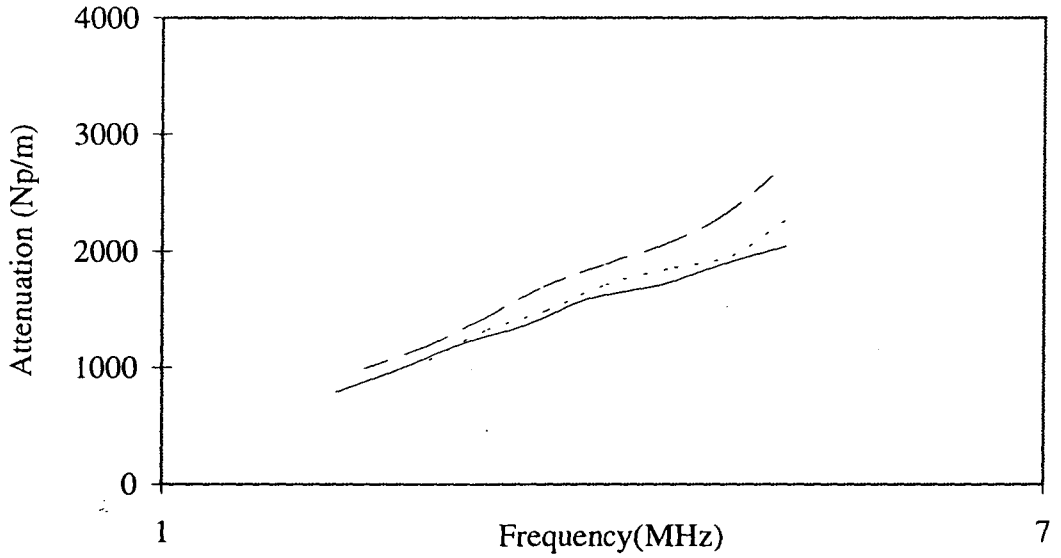
b)

Fig.3.8 Bulk shear wave phase velocity variation with frequency. a) Bulk shear wave phase velocity for TUB 124 HPPE; b) Bulk shear wave phase velocity for Rigidex 002-50

——— normal to axial plane
..... normal to radial plane
– – – – – normal to hoop plane



a)



b)

Fig.3.9 Bulk shear wave attenuation variation with frequency. a) Bulk shear wave attenuation for TUB 124 HPPE; b) Bulk shear wave attenuation for Rigidex 002-50

———— normal to axial plane
..... normal to radial plane
– – – – – normal to hoop plane

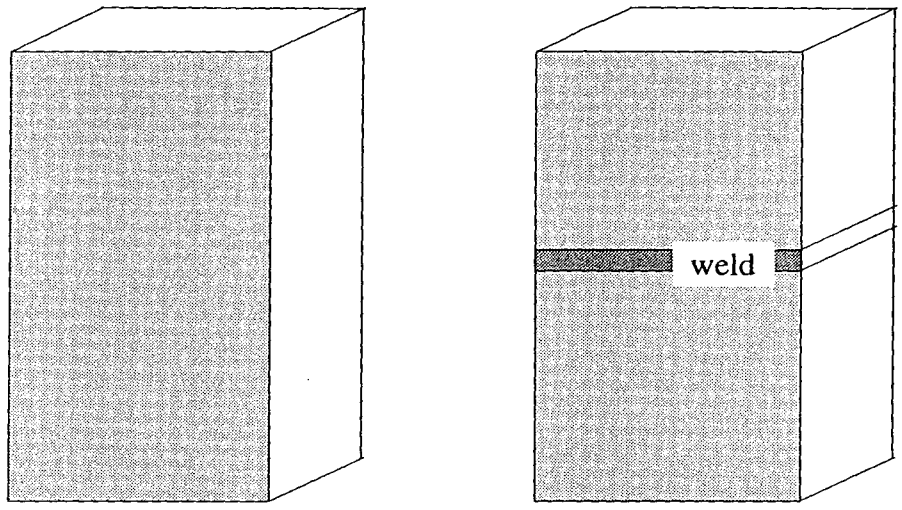


Fig.3.10 Specimens used for examining the effect of the weld material on ultrasound

CHAPTER 4

Normal Incidence Inspection of Electrofusion Welds

4.1 Introduction

In a technique using normal incidence inspection, an ultrasonic transducer is placed normal to the specimen to be inspected and ultrasonic energy is transmitted via a suitable coupling medium into the testpiece (Fig.4.1a). In a defect-free testpiece we would expect to see a reflection from the front face and then a reflection from the back face, followed by reflections due to the reverberations within the specimen. Fig.4.1b shows a typical time domain trace obtained using a defect-free polyethylene sample. Note that due to high attenuation, only one reverberation can be seen. A defect will manifest itself as a reflection located in the time domain trace between the front and back face reflections. By measuring the time of flight and amplitude of this reflection, it is possible to ascertain the position and to some extent the size of the defect under scrutiny. The normal incidence technique can be implemented in a variety of ways. One such implementation requires the use of a scanning rig which consists of a transducer fixed to a scanning head which moves within a scanning frame. The result is to produce a scan (known as a C-scan) in which the amplitudes of the monitored signals are represented by a graduated colour or black and white scale.

Normal incidence inspection systems are almost all based on C-scanning. This approach is fairly well understood and although it is recognised to be slow, it is known to be able to produce good results in the field of defect detection. In general two types of transducers, plane and focused, can be used for normal incidence inspection. Several approaches exist for plane transducers. The simplest of these is probably the '6dB down' approach (see e.g. (Szelazek (1989))). Here, the assumption is made that the echo obtained when the probe is aligned for maximum response will halve (-6dB) when the axis of the probe is aligned with the edge of the defect. An inherent assumption is that the defect size is similar to, or larger than the beam diameter which in reality may not be the case. Therefore, for small defects, this approach will prove unsatisfactory. Another approach is the Distance-Gain-Size (DGS) approach (Krautkramer (1959)). Here, the measured echo amplitude is compared with the echo amplitude from known regular shaped reflectors in order to

determine the size of the defect. This approach is intended for flaws which are smaller than the beam diameter.

In general, systems employing plane transducers tend to be less accurate at sizing small defects because the width of the acoustic beam is large in comparison with the defect. This limitation can be largely overcome by using focused transducers where the beam widths can be very small. It will be shown that for an electrofusion weld, the beam width required is relatively small and therefore the use of plane transducers can be ruled out. Also, given that the scan times using plane and focused probes are comparable and that small defects are being sought, there is little advantage in resorting to plane transducers and therefore the normal incidence inspection will concentrate on the use of focused transducers.

4.2 Focused Transducer C-Scanning

4.2.1 Introduction

For the detection of small defects, scanning arrangements are usually based around the use of focused transducers. Plane transducers can be used to reduce the scan pitch needed to detect a given size of defect provided the defects are relatively large. As a result of a focused acoustic beam, focused transducers have small beam widths at the focal plane (Kino (1987)). The resolution is very dependent on two key parameters, the focal spot size and the focal length. The focal spot size (diameter) is related to the wavelength λ in the medium in which the transducer is immersed, the radius of curvature R and the radial width a, by the formula (Kino (1987)),

$$\text{spot size} = 1.2\frac{\lambda R}{a} \qquad (4.1)$$

From this equation, we can see that the theoretical limit for the spot size is just over a wavelength, occurring when the transducer is a full hemisphere. Because of diffraction, the real focal length does not lie at the geometric focus defined by the radius of curvature of the transducer but is actually nearer to the lens (Silk (1984)). In comparison with plane transducers, focused transducers do not suffer significantly from near field effects (Silk (1984)) or misalignment problems (Drinkwater (1995)).

In order to investigate the use of focused transducers for electrofusion joints, a C-scan system was used, a schematic of which is shown in Fig.4.2. The samples were of two

types. One type consisted of sections cut from electrofusion joints which then had flat bottomed holes drilled into them from the pipe side to simulate defects (Fig.4.3). For ease of scanning, the top and bottom surfaces were machined to be flat and parallel. The other type consisted of sections cut from electrofusion joints which had foreign material (aluminium inserts, mud) placed at the joint region prior to fusion taking place, in order to simulate defects (Fig.4.4).

Before any scanning can take place, it is necessary to establish the variables which are likely to be influential on the efficiency of the normal incidence technique. Two variables were identified as being important. The first variable is the spot size of the transducer. This defines the resolution of the scanned image; the smaller the spot size, the higher the scan resolution. In addition, if we inspect the weld from outside the coupler, the wires in front of the joint interface will affect how well we can inspect the joint interface. The wire spacing will determine how much ultrasonic energy can propagate between the wires through to the joint interface where it can then interact with defects. Physically, a beam with a small spot size should be able to penetrate through small gaps between the wires.

The second variable of interest is the frequency of the excitation signal. We know from the results of Chapter 3 that the attenuation in the polyethylenes is relatively high and increases with frequency. Therefore, employing a high frequency may be problematic. The frequency also affects how well we can resolve signals reflected back from different interfaces. This will be important because if we wish to scan from the outside of the pipe, then we could imagine the top of the wires in the electrofusion weld as being one interface and the actual joint being another. The higher the frequency, the easier it will be to resolve the signal returning back from the joint interface from the signal reflected off the wires. This is likely to influence our decision of whether we should scan from the inside or the outside of the pipe.

4.2.2 Initial Scans

The initial set of scans were conducted on sections cut from an electrofusion joint (Fig.4.3). Given that the average vertical distance between the top of the wires and the weld interface was small (<0.5mm), the transducer was focused on the wires. Focusing on the interface rather than the wires resulted in changes in the reflected amplitudes from the wires and the defects but the changes were not significant. A 5MHz focused transducer with the specifications shown in Table 4.1 was used. Note that the spot size calculations were based on taking the wavelength in polyethylene

Frequency (MHz)	Diameter (mm)	Focal Length (mm)	Spot Size (mm)
5	14	30	2.6
1	22	38	11.3

Table 4.1 Details of the focused transducers used for C-scanning

even though the transducers were immersed in water. The calculated spot sizes will therefore be different from reality but given that the velocities of water and polyethylene are not too dissimilar, the differences will be relatively small.

Fig.4.5a shows a typical time domain trace when the transducer is situated above a defect. The first signal is the reflection off the front face of the specimen. The second signal comprises of two main pulses; one due to the reflection off the wires and the other due to the reflection off the flat bottom hole defect. An electronic gate was placed over the reflection from the wires (Fig.4.5a) and a scan was produced as shown in Fig.4.5b. The scan shows quite well the existence of the wires and their relative positions. The lack of wires showing at the top edge of the scan stems from the fact that the bondline was not completely flat with respect to the transducer face. Therefore, as the transducer moves away from the centre of the scanning region (Fig.4.6) the wires are no longer normal to the transducer and hence the amplitude of the received signal will be reduced. When a gate was placed over the second reflection (Fig.4.7a), a second scan was produced (Fig.4.7b). The three flat bottom holes can be seen fairly easily.

To complement the C-scan work, X-radiographs were taken of the joints. Fig.4.8 shows a radiograph of the joint from which the presence of the wires as well as the flat bottomed holes can be identified with ease. This is to be expected for this particular sample, since the amount of mass removed from the parent material is relatively large. It is doubtful whether X-rays would be able to detect the defect if it was a disbond where the amount of mass removed is minimal. If we take a close look at the scan in Fig.4.7b and in particular at the defects, the amplitude seems to fluctuate across them. We can gain an insight to why this occurs by looking at Figs.4.9a and 4.9b. Fig.4.9a shows the time domain trace when the amplitude of the reflected wave from the defect is a maximum. Fig.4.9b is similar except that the amplitude is now a minimum. The difference in the appearances of these two time domain traces can be attributed to the fact that in Fig.4.9a, the insonifying beam lies directly between two wires (Fig.4.9c) and hence maximum energy can get through to the defect. In Fig.4.9b, the beam is directly above a wire (Fig.4.9d) so that minimal energy gets through to the defect.

A scan was performed on a similar specimen but the holes now being 2mm in diameter (Fig.4.10a). In this particular case the scan reveals that one of the holes seems somewhat smaller than the others even though all the holes were supposed to be the same size. To confirm that one of the holes was actually smaller, a radiograph was obtained (as shown in Fig.4.10b). The radiograph supports the information obtained from the scan and therefore it appears as if one of the holes was not fabricated correctly.

4.2.3 Effect of Spot Size and Frequency

In order to determine the effect of spot size on scans, two scans were carried out on a section from a pipe joint containing two 4mm flat bottom holes. The average wire spacing was 0.5mm and the wire diameter was 0.5mm. The first scan (Fig.4.11a) was produced using a 1MHz focused transducer with a 9mm spot size (see Table 4.1). The second scan (Fig.4.12a) was obtained using a 5MHz focused transducer with a 2.6mm spot size (see Table 4.1). In the first scan, because the frequency used was relatively low, the reflections from the wires and those from the defect could not be resolved (Fig.4.11b). Therefore a gate had to be placed over both reflections. The scan shows that slight fluctuations can be seen, these being due to the wires. However, no defects have been detected because the amplitude of the reflection from the wires was considerably larger than those due to the defect. In the second scan the situation is different. The spot size is now smaller, so more energy can be directed towards the defect and hence relatively large reflections from the defect are obtained. The reflections are now more resolvable (Fig.4.12b) and therefore a gate could be placed over the reflection from the defect. In addition, the higher frequency helps to increase the resolvability of the reflection from the defect in the time domain. This is evident in the scan which clearly shows the presence of the defects.

If we now look at the results of scanning a specimen with a larger wire spacing of 1.5mm and a wire diameter of 0.5mm using the same 1MHz probe used previously, the scan shown in Fig.4.13 is produced. We can see that in this case, the defect is clearly visible (the defect being a 8mm diameter aluminium circular disk reflector). This is because even though the reflections are not separable, the fact that the spacing is larger (3 times larger than in the previous joint) means that more energy can propagate through to the defect. The result of this is that the amplitude of the reflection from the defect (Fig.4.14a) is much larger than that from the wires (Fig.4.14b) and therefore putting a gate over the combined signal is essentially the same as putting a gate over the reflection from the defect alone.

4.2.4 Comparison of Scanning from Inside and Outside of Pipe

The next step is to determine the merits of scanning from the inner surface of the pipe rather than from the coupler surface which may not be flat as a result of markings moulded on by the manufacturers. The obvious advantage is that the surface on the inside is smooth. In addition, the fact that the defects will be located beneath the wires means that in the presence of a defect, the first reflection will be due to the defect. The joints used had a wire spacing of 1.3mm, a wire diameter of 1.5mm and the distance between the top of the wires and the joint interface was about 1mm. The same 5MHz focused transducer as used previously was employed for the scanning.

Firstly scans were taken from the coupler side, one from a good bond (Fig.4.15a) and the other from a defective bond (Fig.4.15b) which is simulated by the presence of a thin rectangular layer of aluminium at the interface. The samples shown in Fig.4.4 were used. The previous samples (i.e. Fig.4.3) were not used because we wanted to scan from both sides of the specimen and this was not possible when the defects (i.e. the flat bottom holes) were not embedded. The width of the aluminium was 27mm. Note that both scans are to the same amplitude scale. As expected, the scan from the good bond shows no sign of defects. Note also that there is very little indication of the wires. This is because the distance between the top of the wires and the joint interface was relatively large and as a result the reflection from the wires did not fall significantly within the gate. The scan from the defective joint shows the presence of a defective layer indicated by the large amplitudes. We know the large amplitude regions represent the defect rather than the wires because the reflections from the wires were outside the monitoring gate. The contrast between the two scans is good.

Scans were then carried out for a good and defective joint from the inside of the pipe (Fig.4.15c and Fig.4.15d), both to the same amplitude scale. In a defective joint, scanning from the inside of the pipe results in a fairly uniform large amplitude scan (Fig.4.15d) with no significant influence from the wires. This is in contrast to the corresponding scan in Fig.4.15b where low amplitude streaks were present. These were caused by the fact that the beam was directly above a wire and was hence unable to inspect the weld region directly below the wire.

Further scans were produced, this time on joints that were covered with mud paste prior to welding in order to simulate real defects (this sort of defect is conceivable if welding is performed in a muddy trench under wet conditions). Scans were taken from the outside for a good and bad joint (Figs.4.16a & 4.16b). The scan of the defective

joint clearly shows defective areas (dark patches). The influence of the wires on the scan can be seen from the fact that the dark patches are cut off by light patches at fairly regular intervals.

If a scan from the outside is necessary then from a frequency point of view, it is desirable to be able to resolve the reflection from the wire and the reflection from the interface. In order to achieve this, a high frequency is required. Frequencies of the order of 5-10MHz were found to be suitable although in the 10MHz region, noise started to become a problem. Given that the typical distance between the top of a wire and the probable location of a defect is greater than 0.5mm, the minimum frequency required for complete separation would be (based on a 3 cycle signal) 6MHz.

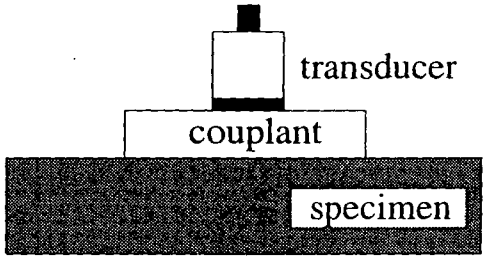
In the scans conducted using a 1MHz frequency probe, it should be noted that the gate was placed over the entire wave train of reflections from the wire and the interface as it was difficult to resolve the echoes. In situations where the impedance mismatch between the plastic and the defect is high, e.g. air voids, and the wire spacing is relatively large, the reflection from the defect will be large, and usually somewhat greater than that from the wires so putting a gate over the both reflections is not a problem. The problem arises when the plastic/defect impedance mismatch is small, e.g. if a disbond is filled with water, and/or the wire spacing is small. In this case the signal coming from the wires may be larger than that coming from the defect and hence the scan may not pick up the presence of the defect. Going for a higher frequency will resolve the problem although this is offset by the fact that the attenuation increases.

4.3 Discussion & Conclusions

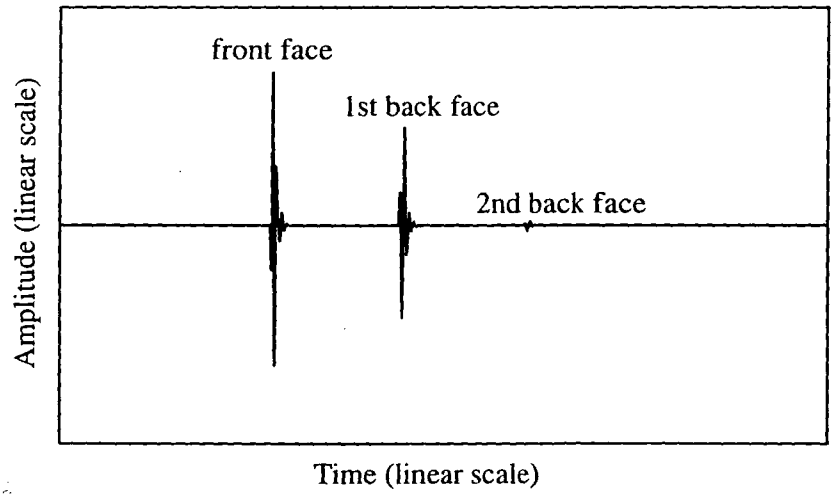
Various normal incidence techniques have been discussed with respect to the detection of defects in electrofusion welds.

Studies performed using focused probe C-scanning have proved successful in inspecting artificial defective joints. The recommended set-up would be to scan from the inside surface of the pipe where the surface is consistently smooth and does not undulate. The accuracy of the scan will be dependent among other things on the spot size of the transducer. It is for this reason that scanning using plane transducers is limited to the detection of gross delaminations. If scanning from the inside is not practically feasible, then scanning can be performed from the outside of the coupler. Fortunately, it has been shown that scanning from this side is possible. The only real

limitation is that the area directly below a wire cannot be inspected. However, given that wire diameters are relatively small in comparison to the sizes of defect that are of interest (see Chapter 2), the presence of the wires is not problematic. Frequencies in the range 5-10MHz should be used in order to be able to resolve reflections from the wires and the defects as well as providing small spot sizes to penetrate between the wires in the coupler. Scanning from the coupler side will not be successful if the wire spacing becomes too small so that not enough energy can reach the defect. However, to date, all scans performed on joints in the frequency range 5-10MHz have been successful and therefore scanning from the outside of the pipe would be feasible. Given that portable C-scanning systems are readily available for inspection inside or outside the pipe, such systems could easily be purchased and the appropriate focused transducer(s) used.



a)



b)

Fig.4.1 Conventional normal incidence inspection. a) Typical arrangement of a normal incidence technique; b) Normal incidence time domain response of a polyethylene

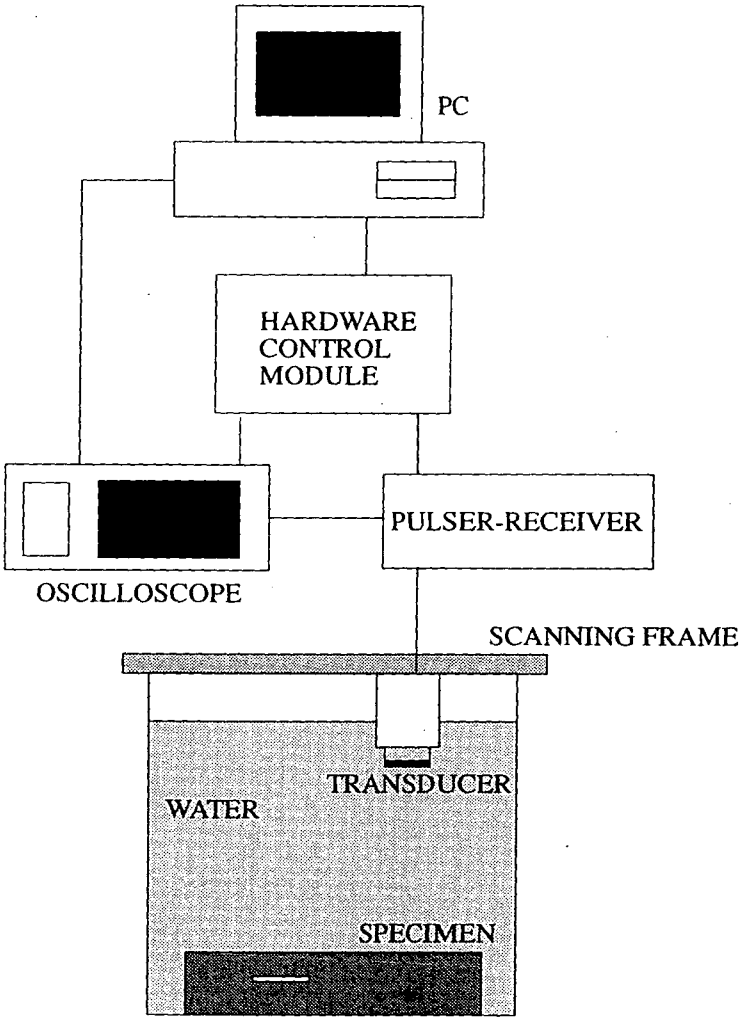
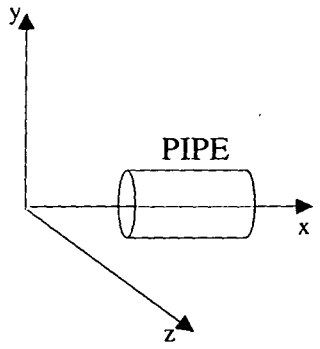
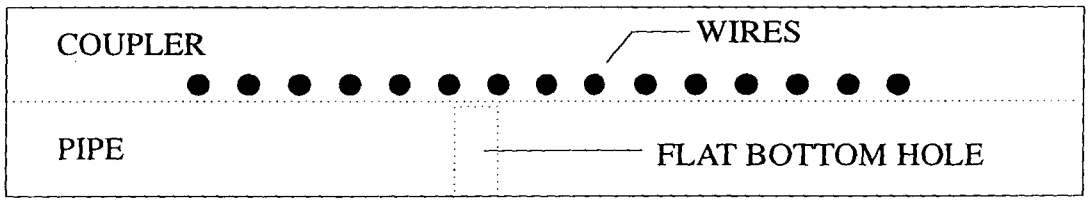


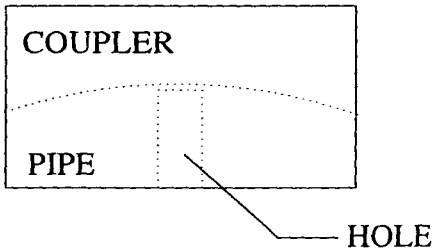
Fig.4.2 Schematic of C-scan system



Coordinate system used with respect to pipe

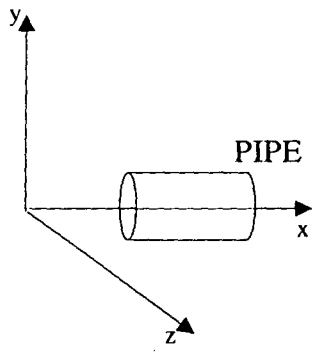


a)

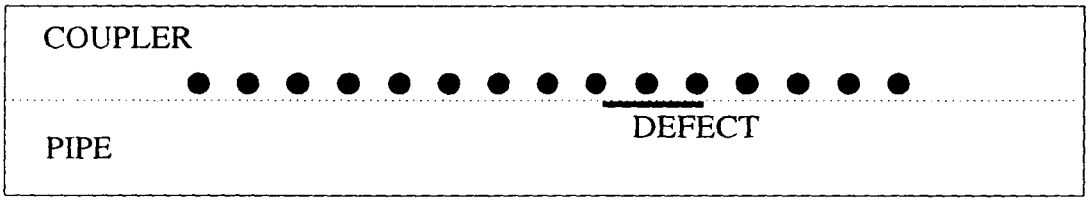


b)

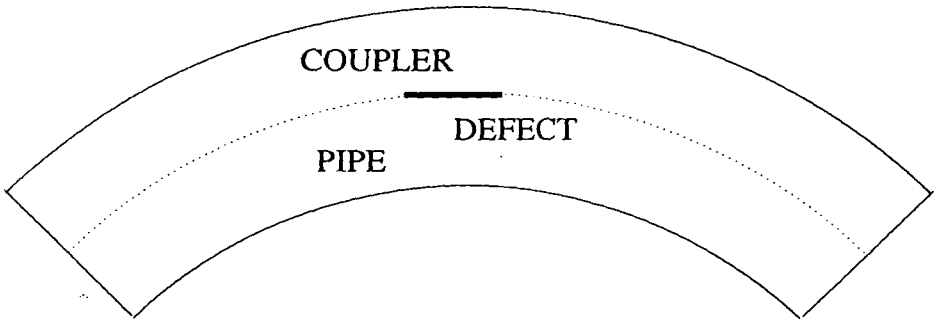
Fig.4.3 Cross sectional views of flat bottom hole samples along a) xy plane; b) yz plane



Coordinate system used with respect to pipe

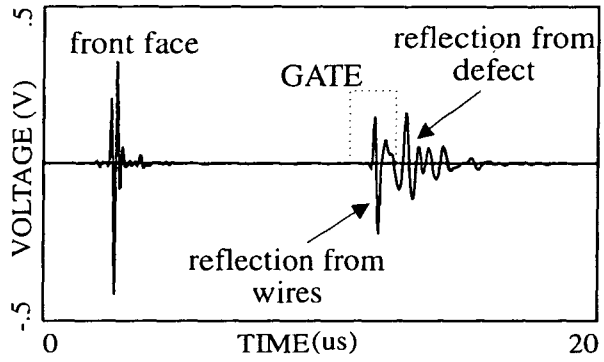


a)

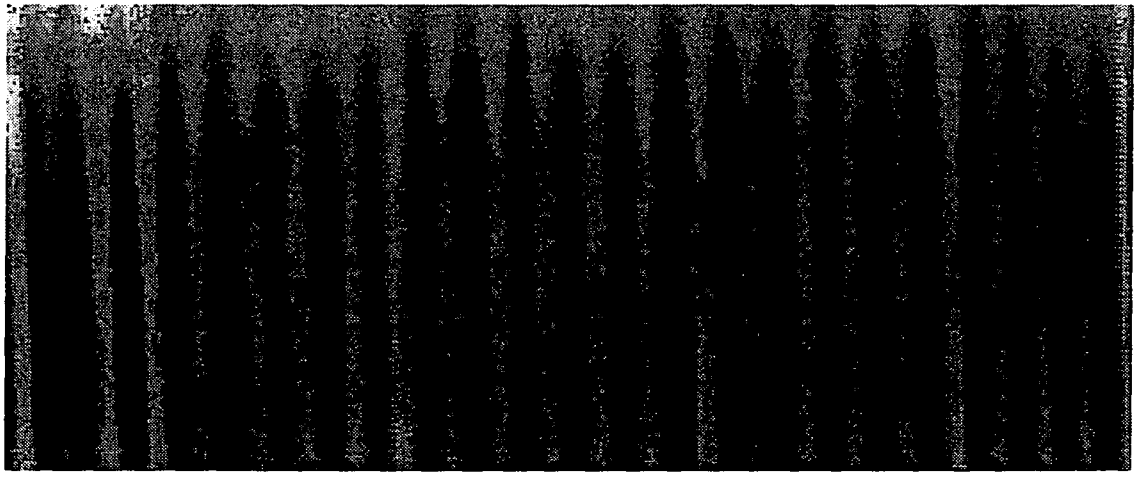


b)

Fig.4.4 Cross sectional views of samples used for inserting defects along the weld interface. View taken along a) xy plane; b) yz plane

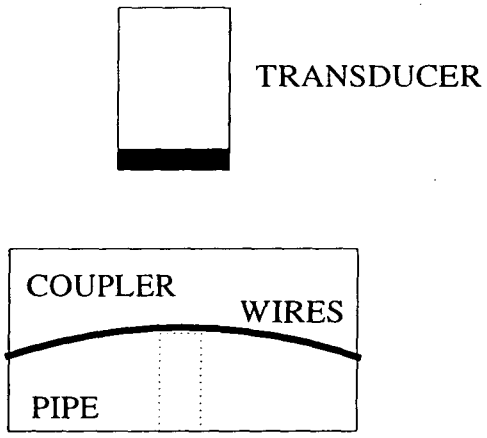


a)

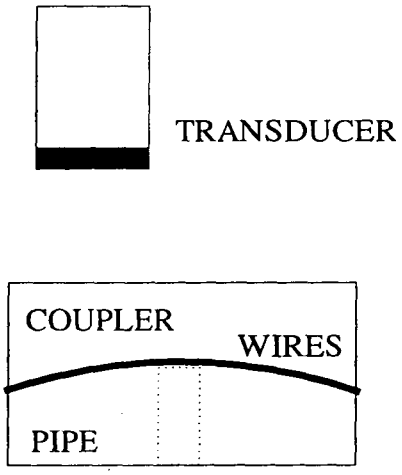


b)

Fig.4.5 Scanning of electrofusion flat bottom hole joint with gate placed over reflection from the wires. a) Time domain trac with gate placed over reflection from the wires; b) C-scan showing existence of wires when gate is placed over the reflection from the wire. Specimen is 42x18mm. Scale: 70-150mV

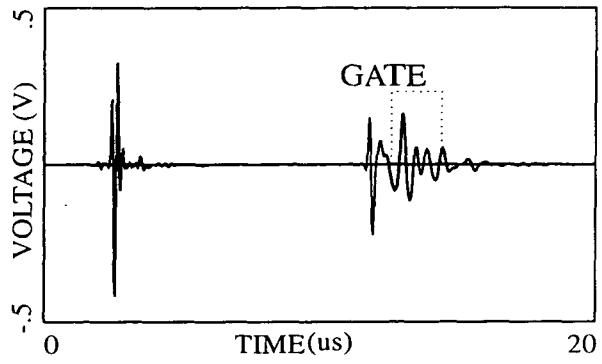


a)

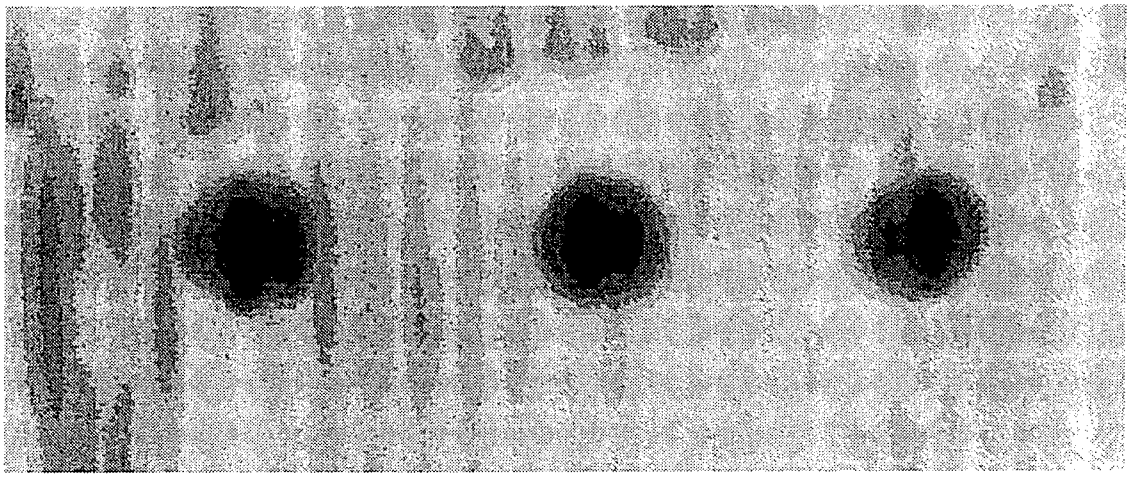


b)

Fig.4.6 Diagram showing the position of the transducer face relative to the wires when a) wires are virtually normal to transducer; b) wires are oblique to transducer



a)



b)

Fig.4.7 Scanning of electrofusion flat bottom hole joint when gate placed over reflection from the defect. a) Time domain trace with gate placed over reflection from the defect; b) C-scan showing existence of 4mm holes when gate is placed over the reflection from the defect. Specimen is 42x18mm. Scale: 20-300mV (white-black)

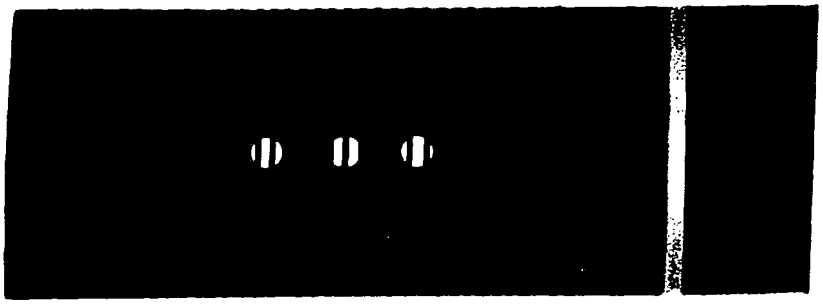


Fig.4.8 Radiograph showing electrofusion joint with three 4mm flat bottomed holes

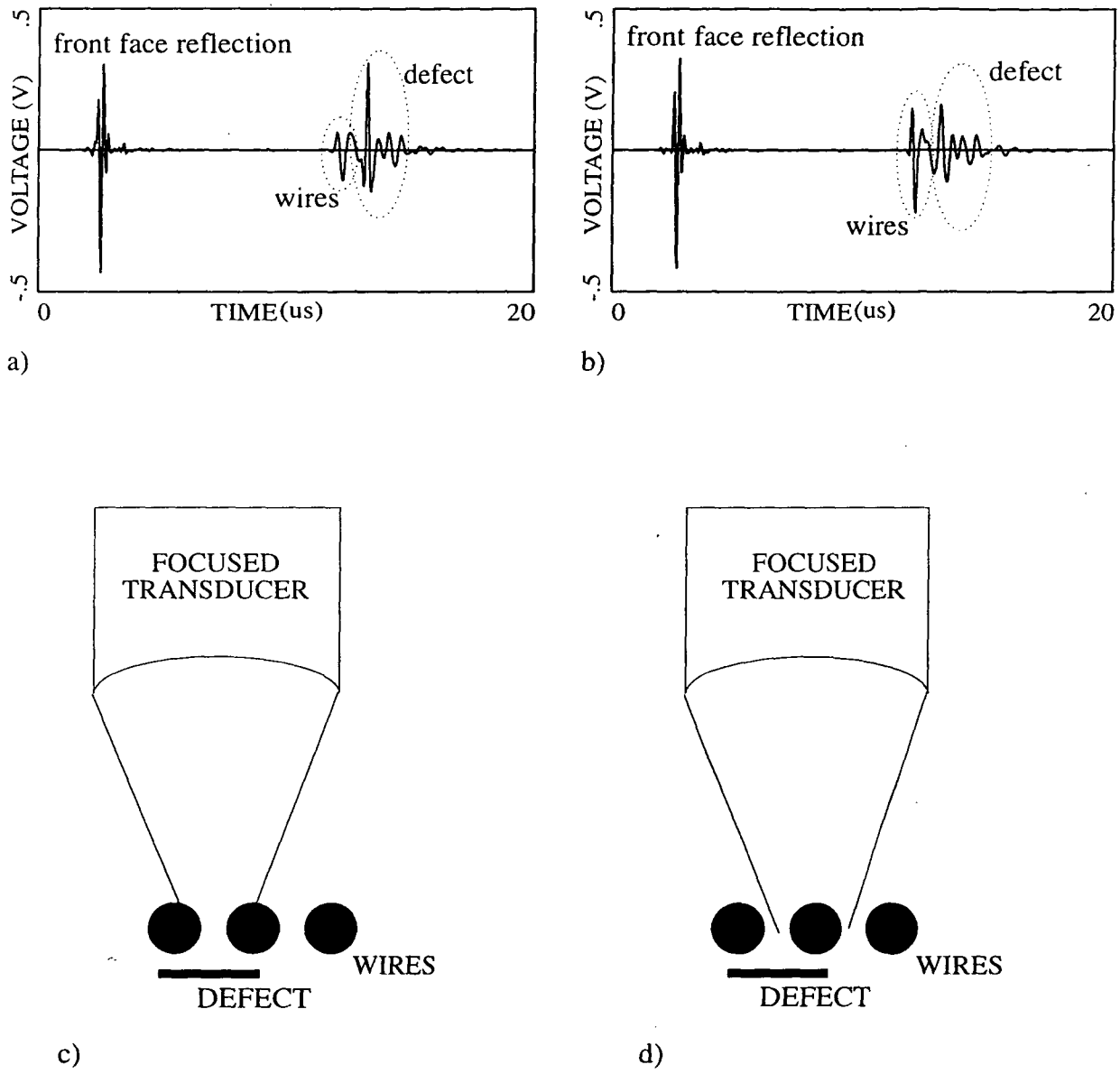
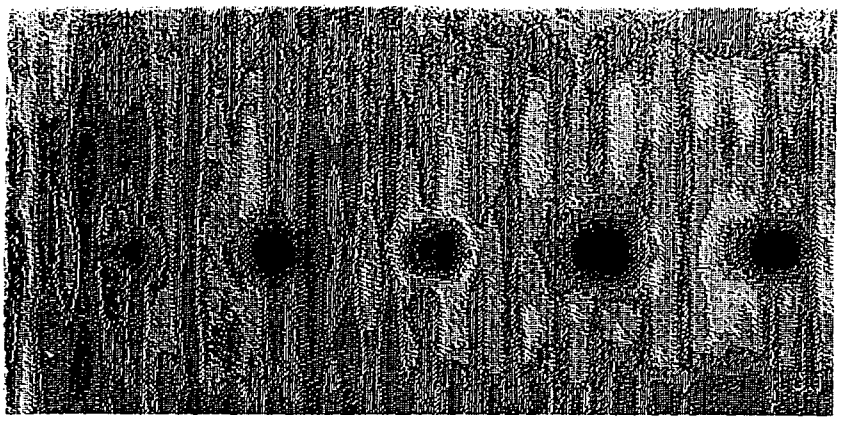
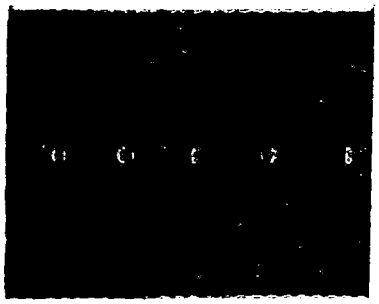


Fig.4.9 Effect of wires on received signal from the joint. a) Time domain trace of a defective joint with signal from the defect maximised; b) Time domain trace of a defective joint with signal from the defect minimised; c) Diagram showing position of transducer for maximum energy propagation to defect; d) Diagram showing position of transducer for minimum energy propagation to defect

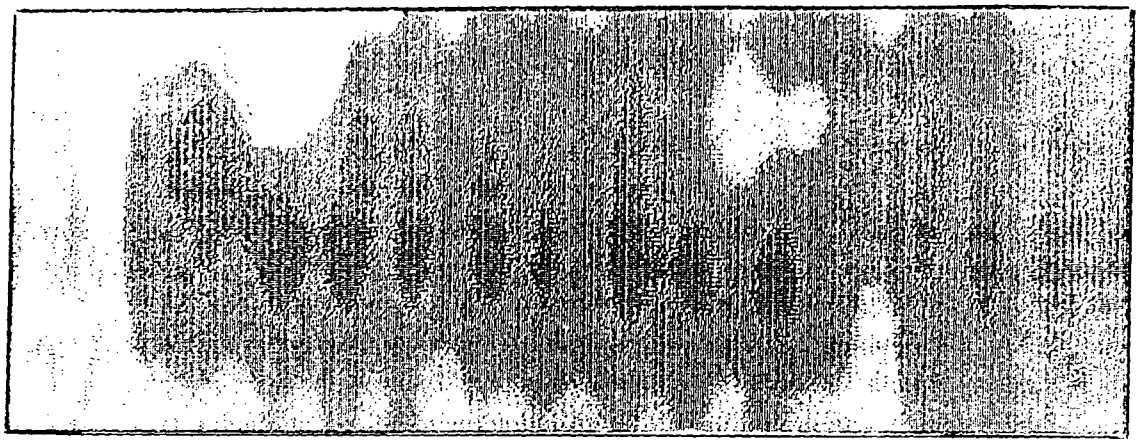


a)

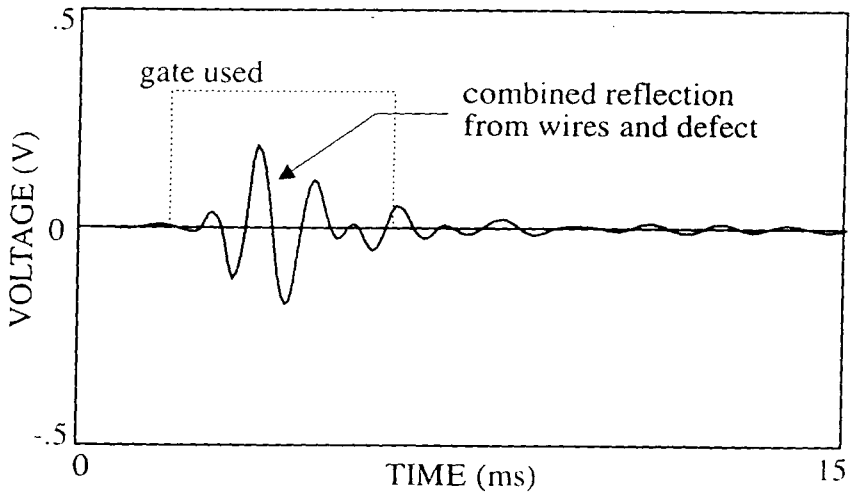


b)

Fig.4.10 Scanning of electrofusion joint containing five 2mm flat bottom holes. a) C-scan of joint. Scan area 50x20mm. SCALE: 70-500mV (white-black); b) Radiograph showing electrofusion joint with five 2mm flat bottomed holes. The scan shows that one of the holes (extreme left) is smaller than the others

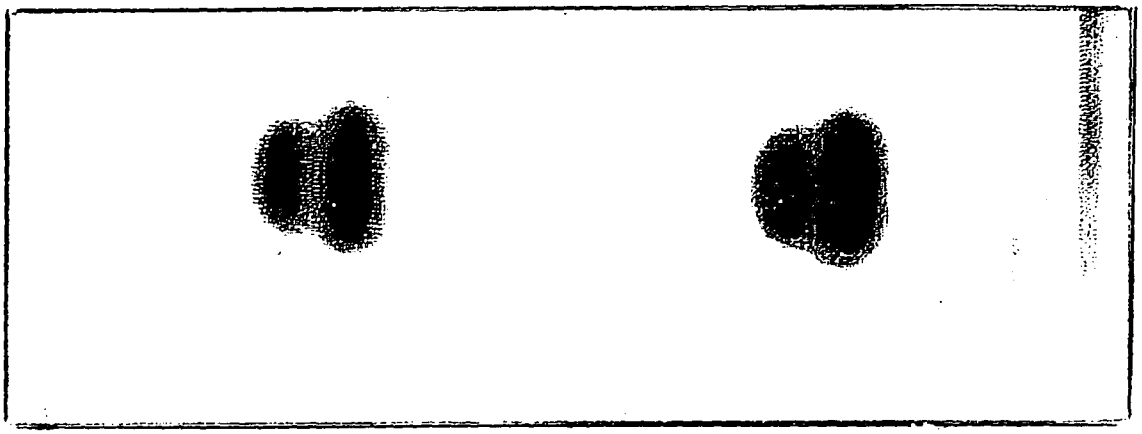


a)

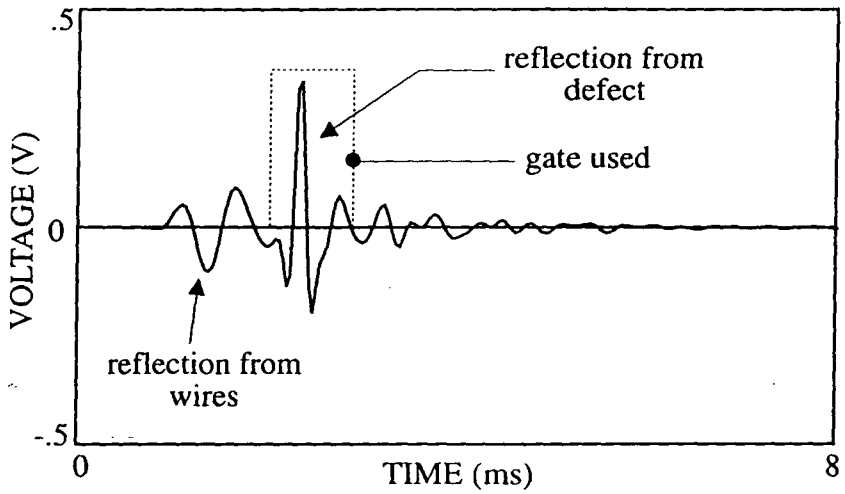


b)

Fig.4.11 Scanning of electrofusion joint containing two 4mm flat bottom holes using 1MHz transducer; a) C-scan of joint. Gate placed over reflection from wires and defect. Scan area 30x12mm. SCALE: 0-150mV (white-black); b) Typical time domain history of reflections from the wires and the defect (note that earlier signals have been chopped out)



a)



b)

Fig.4.12 Scanning of electrofusion joint containing two 4mm flat bottom holes using 5MHz transducer; a) C-scan of joint. Gate placed over reflection from defect. Scan area 30x12mm. SCALE: 0-350mV (white-black); b) Typical time domain history of reflections from the wires and the defect (note that earlier signals have been chopped out)

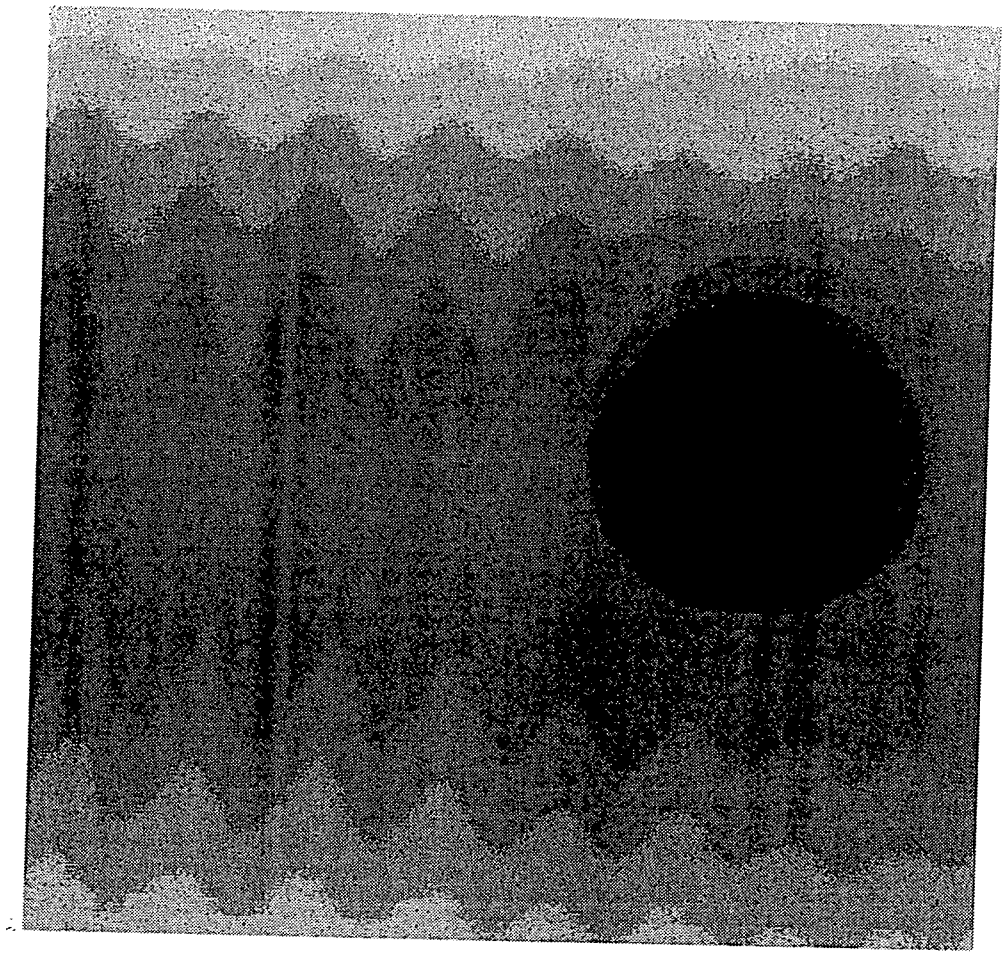
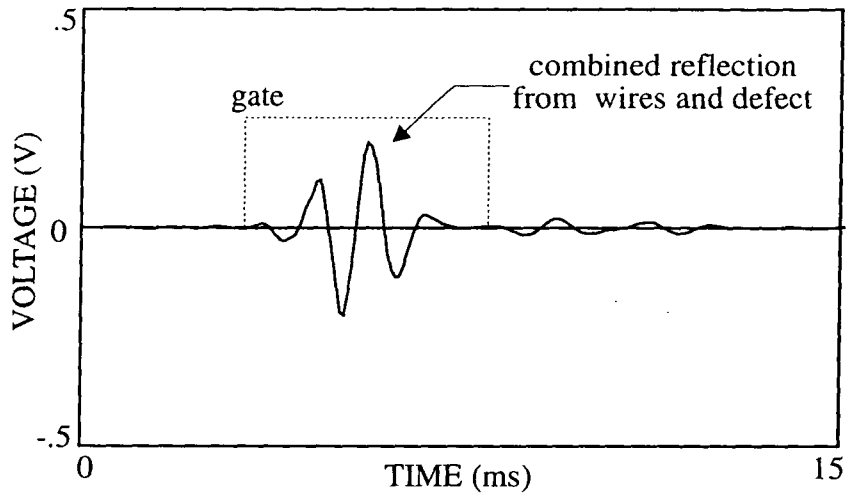
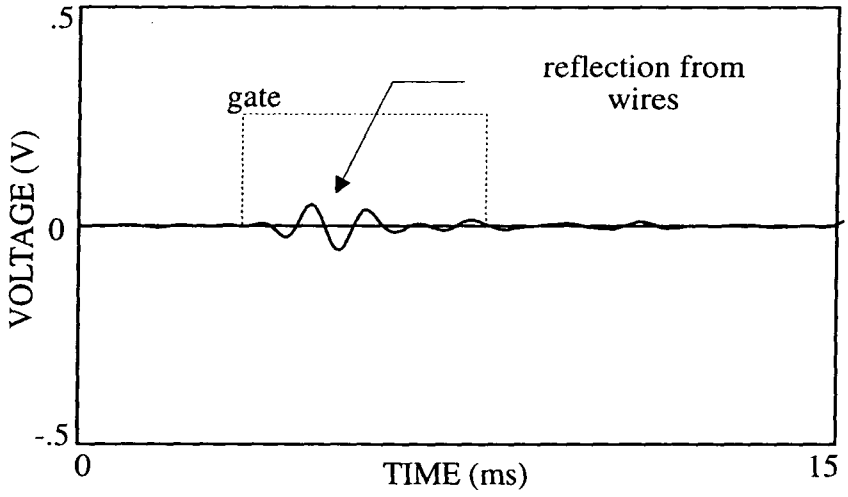


Fig.4.13 C-scan of joint containing an 8mm diameter aluminium circular reflector using a 1MHz transducer. Gate placed over reflection from wires and defect. Scan area 20x20mm. SCALE: 30-350mV (white-black)



a)



b)

Fig.4.14 Effect of large spacing between wires and weld interface on the signal received by the transducer. Time domain history when transducer is over a) a defective region; b) a good region

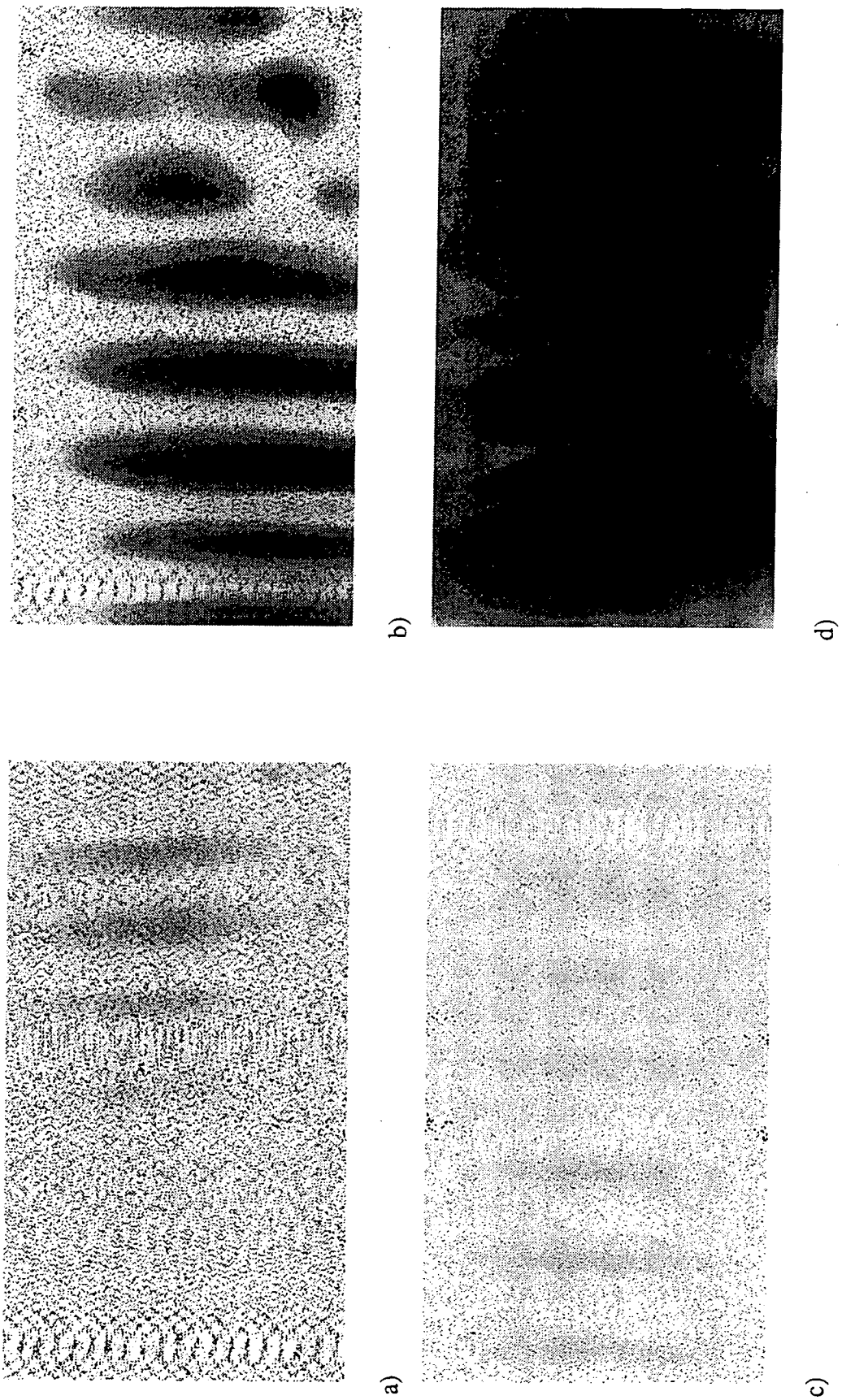
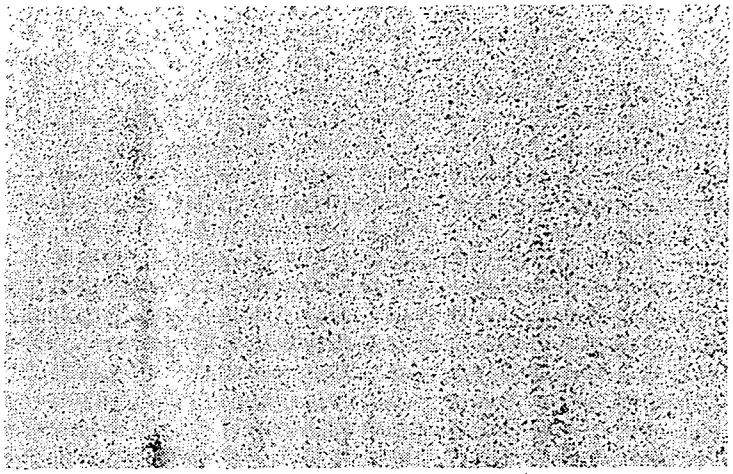
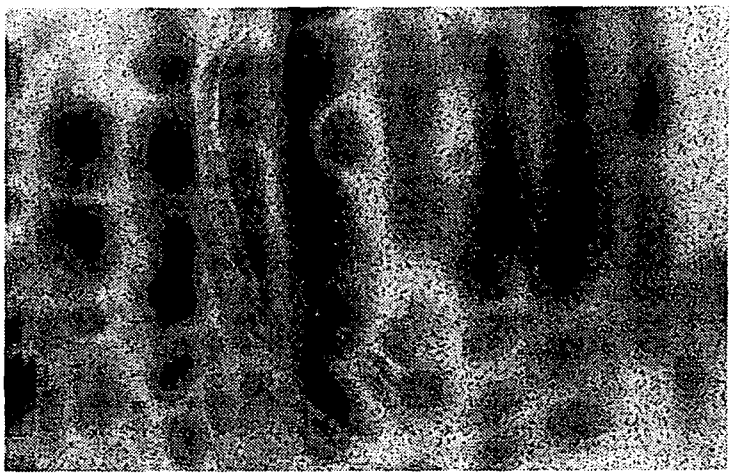


Fig.4.15 Effect of scanning from inside and outside of pipe. a) C-scan of undefective joint from coupler side; b) C-scan of defective joint (aluminium layer) from coupler side; c) C-scan of undefective joint from inside pipe; d) C-scan of defective joint from inside pipe. Extent of defect is larger than scanned area. Scan area 21x11mm. SCALE: 10-150mV (white-black)



a)



b)

Fig.4.16 Comparison of scans between a good joint and a joint containing mud paste. a) C-scan of an undefective joint; b) C-scan of a defective joint (mud and water). Both scans taken from coupler side. Extent of defective area is larger than scanned area. Scan area 30x20mm. SCALE: 10-150mV (white-black)

CHAPTER 5

Plate Wave Inspection of Electrofusion Welds

5.1 Introduction

The plate wave technique is similar to the normal incidence technique in the sense that reflections are monitored and time of flight and amplitude measurements can be made to determine the position and size of a defect. The main difference between the two techniques lies in the direction of propagation of the waves, with plate waves propagating along the length of the testpiece rather than normal to it. In addition, a large number of modes can exist at any given frequency and, depending on the geometry of the testpiece and the frequency employed, the waves are capable of propagating over large distances (several metres). The main attraction of plate waves is that inspection times can be considerably lower than those required for normal incidence inspection and consequently the use of such waves for the inspection of electrofusion welds will be investigated.

The plate wave technique works by having a receiving transducer positioned at some remote point on the structure to be inspected. The received signal will contain information concerning the integrity of the line between the transmitting and receiving transducers. Alternatively, echoes returning to the transmitting transducer may be monitored. To illustrate the inspection advantage of plate waves, consider a defect in a plate, as shown in Fig.5.1a. Using a plate wave, the existence of the defect will lead to a reflection of the plate wave. If the defect is positioned further to the left or right, a reflection of the plate wave would still occur, even though the transmitting transducer has not been moved. The entire length of the plate is therefore inspected from a single transducer position. If a normal incidence technique is used to inspect the same specimen, we would have to perform a scan along the plate (Fig.5.1b) and this method would consequently take considerably longer. The plate wave technique therefore monitors a line rather than a point (which is the case in C-scanning) and hence potential saving in inspection times may be obtained.

5.2 Theory of Plate Waves

Lamb (1917) obtained a theoretical solution to the problem of harmonic waves in an elastic solid layer with free boundaries. These waves have since become known as

plate, normal or Lamb waves. Lamb waves consist of a family of waves that propagate independently along plates and whose energy is constrained within the plate. Mathematically, they can be obtained by finding the eigensolution of a characteristic equation. The following solution presented is similar to that used by Viktorov (1970).

Consider a Lamb wave propagating in a plate of thickness 2d. Scalar (ϕ) and vector (ψ) potentials can be defined so that they obey the wave equation and satisfy the boundary conditions,

$$\phi = (A \cosh(qy) + B \sinh(qy))e^{i(kx-\omega t)} \quad (5.1)$$

$$\psi = (C \cosh(sy) + D \sinh(sy))\, e^{i(kx-\omega t)} \quad (5.2)$$

where A, B, C and D are arbitrary constants,

$q = \sqrt{k^2 - k_1^2}$, $\quad s = \sqrt{k^2 - k_2^2}$,

k is the Lamb wave wavenumber, k_1, k_2 are the longitudinal and shear bulk wave wavenumbers respectively

The field potentials are related to the stresses by,

$$\sigma_{xx} = \lambda\left(\frac{\partial^2\phi}{\partial x^2} - \frac{\partial^2\phi}{\partial y^2}\right) + 2\mu\left(\frac{\partial^2\phi}{\partial x^2} - \frac{\partial^2\psi}{\partial x\partial y}\right) \quad (5.3)$$

$$\sigma_{yy} = \lambda\left(\frac{\partial^2\phi}{\partial x^2} - \frac{\partial^2\phi}{\partial y^2}\right) + 2\mu\left(\frac{\partial^2\phi}{\partial y^2} - \frac{\partial^2\psi}{\partial x\partial y}\right) \quad (5.4)$$

$$\sigma_{xy} = \mu\left(\frac{2\partial^2\phi}{\partial x\partial y} + \frac{\partial^2\psi}{\partial x^2} - \frac{\partial^2\psi}{\partial y^2}\right) \quad (5.5)$$

By substituting eqns.(5.1) and (5.2) into eqns.(5.3), (5.4) and (5.5) and applying zero stress boundary conditions at the top and bottom surfaces, it can be shown (Viktorov (1970)) that,

$$(k^2+s^2)^2 \cosh(qd) \sinh(sd) - 4k^2qs \sinh(qd) \cosh(sd) = 0 \quad (5.6)$$

$$(k^2+s^2)^2 \sinh(qd) \cosh(sd) - 4k^2qs \cosh(qd) \sinh(sd) = 0 \quad (5.7)$$

The above equations can be rewritten in the form,

$$\left(\frac{\tan k_2 d\left(1-\left(\frac{c_2}{c}\right)^2\right)^{1/2}}{\tan k_2 d\left(\left(\frac{c_2}{c_1}\right)^2 - \left(\frac{c_2}{c}\right)^2\right)^{1/2}} + \left(\frac{4\left(\frac{c_2}{c}\right)^2 \left(1-\left(\frac{c_2}{c}\right)^2\right)^{1/2} \left(\left(\frac{c_2}{c_1}\right)^2 - \left(\frac{c_2}{c}\right)^2\right)^{1/2}}{\left(2\left(\frac{c_2}{c}\right)^2 - 1\right)^2} \right)^{\pm 1} \right) = 0 \qquad (5.8)$$

where c is the Lamb wave velocity, and c_1 and c_2 are the longitudinal and shear bulk wave velocities respectively.

Note that the equation is now given in terms of the parameter c, the phase velocity of the Lamb wave. In fact, if the phase velocity is known, it is possible to calculate parameters such as stress, displacement and group velocity. It can be seen that two sets of solutions exist, depending on the +ve and -ve signs. A +ve sign refers to symmetric modes whereas a -ve sign refers to asymmetric modes. It can also be seen that the equation is dependent on the wavenumber which can be related to the frequency. Therefore, at any given frequency, the number of real roots of eqn.(5.8) will give the number of propagating modes possible at this frequency.

Once the phase velocity has been determined, the group velocity can be calculated. The group velocity is defined as the velocity at which energy is propagated along the plate and is generally given by,

$$c_g = \frac{\delta\omega}{\delta k} \qquad (5.9)$$

where k is the wavenumber of the Lamb wave.

As mentioned earlier, Lamb waves can be divided into two distinct groups known as symmetric and asymmetric modes. Symmetric modes share the characteristic that the motion of the mode is symmetric about the centreline of the plate whereas in asymmetric modes the motion is antisymmetric. The two simplest symmetric and

asymmetric modes are the s_0 and a_0 modes, which are shown in Fig.5.2a and 5.2b at a low frequency-thickness. The existence of Lamb waves is governed by the frequency, the plate thickness and the wave speed of the particular Lamb mode. The usual way in which the Lamb wave data is shown is in the form of dispersion curves which relate the Lamb wave velocity to the frequency-thickness product. Dispersion curves may be obtained by solving Lamb's equation. A typical dispersion curve for aluminium is shown in Fig.5.2c. By knowing the frequency and thickness of the plate, it is possible to determine which modes can be excited in the plate and at what speed they will travel. Whether they are excited or not will depend on the form of the input supplied to the plate. For example, if a symmetric input is supplied, asymmetric modes cannot be excited even though an asymmetric mode can exist at the given frequency-thickness according to the dispersion curves. The usual way in which Lamb waves are excited is to use transducers angled to the specimen surface, the idea being that the horizontal wavenumber in the coupling medium matches the horizontal wavenumber in the plate required for a certain Lamb wave to exist. The angle required to excite a particular mode can be obtained from the coincidence principle (e.g. Firestone and Ling (1951)),

$$c / c_L = \sin \theta \qquad (5.10)$$

where c is the velocity in the coupling medium, c_L is the Lamb wave velocity and θ is the angle of incidence. In real, finite transducers, a range of angles is excited due to the phenomenon of beam spreading and hence from the coincidence principle a range of velocities will exist at which Lamb waves may be excited. Therefore a zone of excitation can be constructed to determine the modes which can be made to propagate by a given transducer. In most circumstances, the excitation of several modes means that signals may become extremely complicated. This is further complicated by the fact that these modes may be dispersive which means that in the time domain their waveforms may change as a result of certain frequencies propagating quicker than others. It is therefore desirable to excite the smallest number of modes possible, preferably in a non-dispersive region (Alleyne and Cawley (1992)).

Once excitation has taken place, the Lamb waves propagate along the plate until they are impeded by an inhomogeinity such as a void, change in section or simply the end of the plate. By measuring the time of flight and amplitude of reflected Lamb waves it is possible to determine the location and extent of a defect. This basic technique has been used by numerous researchers (e.g. Alleyne (1991), Worlton (1957)).

In practice, two configurations are used for the excitation and detection of Lamb waves. Pulse echo involves having either a single transducer used both as a transmitter and a receiver, or two transducers on the same side of the probing area, one for transmitting and the other for receiving. In pitch-catch, two transducers are placed at opposite ends of the inspection region. The pulse-echo configuration is the more widely used of the two because of its sensitivity to the presence of defects: in a defect-free specimen, no unexpected reflections will occur, whereas the presence of a reflection would automatically imply a defect of some sort. This is not the case for the pitch-catch method where the difference between the received signal in a defect-free specimen and that in a defective specimen may not be large.

Lamb wave theory was originally developed for plates (Lamb (1917)) but the theory has been extended to cover cylindrical geometry (pipes, rods) (e.g. Gazis (1959)). The principal difference in the dispersion curves is that there is a 'double infinity' of modes (Zemanek (1972)) and as a result the dispersion curves become more complicated. Experimental work has been carried out on tubular structures. Silk and Bainton (1979) looked at the generation of the L(0,1) and L(0,2) modes, which are comparable to a_0 and s_0 modes respectively in a flat plate. Lockett (1973) gives a good discussion on the use of Lamb waves for flaw detection in tubes. Meeker and Meitzler (1964) present a comprehensive review of Lamb wave propagation in plates and pipes.

5.3 Overview of Problem

The use of Lamb waves for the inspection of pipes is very attractive given that there is the potential to conduct tests very quickly. It is necessary to determine which modes are most suited for defect detection along the weld line and therefore a feasibility study will be conducted.

In order to investigate the possibilities of using Lamb waves for the detection of defects in electrofusion joints in plastic pipes, a numerical approach based on finite elements has been adopted. The finite element approach has been used successfully by various researchers (Alleyne and Cawley (1992), Guo and Cawley (1994)). In the first instance, the geometry of the joint has been modelled as a stepped plate, essentially consisting of two different thickness plates joined end to end. The thinner plate represents the parent pipe (i.e. unwelded part) and the thicker plate the actual joint. A feasibility study using finite element analysis has been carried out to determine whether Lamb waves can be successfully used in such a geometry for defect detection. The use of finite element analysis to model Lamb wave propagation has been

demonstrated by Al-Nassar et al (1991), Sabbagh and Krile (1973) and Koshiba et al (1984). The present work concentrates on exciting two particular Lamb modes, s_0 and a_0 in the parent pipe, and then looking for reflections off defects located in the welded region. These two particular modes were chosen because at low frequency-thickness products only these two modes exist and therefore there is no complication from other modes. The properties of aluminium have been chosen for the analysis. This was done for two reasons. Firstly, aluminium plates were readily available for experimental verification of the finite element results. Secondly, an elastic finite element analysis can be performed which simplifies the computation. In the polymers used in this project, the a_0 and s_0 modes have very similar mode shapes to those for the same modes in aluminium and therefore the results obtained using aluminium will be valid for the polymers (see Chapter 6). The finite element analysis is conducted in two parts. The first deals with the reflection and transmission of Lamb waves across the step (Fig.5.3a), and the second deals with the reflection off a planar defect (modelled as being semi-infinite) situated in the welded region (Fig.5.3b). The defect has to chosen to be planar because planar defects are believed to be the most likely type of defect found in electrofusion welds. These two cases are then combined to produce overall reflection ratios for Lamb wave propagation and detection at the parent plate end (Fig.5.3c). The author is not aware of any work published to date on the interaction of Lamb waves with a stepped plate. However, research on the subject of Lamb wave interaction with delaminations in an elastic isotropic plate has been reported by Rokhlin (1979, 1980, 1981) and Lehfeldt and Holler (1967). The work in this chapter brings the two simple structures together to form a new, more complicated structure which has not been looked at previously. The effects of attenuation are also included in the final results.

5.4 Analysis

5.4.1 Dispersion Curves

In order to investigate Lamb waves, it is necessary to decide on the excitation zone on the dispersion curves. Such curves were obtained using software written by Lowe (1993) who formulated the problem in terms of stresses and displacements and solved it using matrix methods. Fig.5.3 shows the phase velocity dispersion curves for aluminium. From a practical point of view, we have said that we want to have the smallest number of modes possible at any given frequency. If we use a frequency thickness lower than 1.55MHzmm (the cut-off frequency for the a_1 mode) then only two possible modes can exist, s_0 and a_0. Given that the s_0 mode is fairly nondispersive

in this range, the investigations will primarily focus on this mode. Note that results were obtained for the a_0 mode incident but are not presented in any detail given their similarity to those obtained using the s_0 mode.

5.4.2 Numerical Simulations of Stepped Plate

The geometry and co-ordinate system of the stepped plate used in the finite element model are shown in Fig.5.4, the thickness of the parent plate (L-end) being fixed at 2mm and that of the joint plate (R-end) being variable (2.5, 3.0, 3.5, 4mm). These small thicknesses were chosen because it meant less elements could be used to model the stepped plate and hence the computations were less demanding. To model the interaction of Lamb waves with the stepped plate, a finite element package, FE77 (Hitchings (1987)) was used. The model was two dimensional, plane-strain, stress free boundaries being assumed. To propagate s_0, a uniform displacement in the x-direction was applied across the thickness of the parent plate (in real life excitation would be via the surface). The symmetry of the input ensures that no other modes are excited. The excitation signal was a 3 cycle, 0.3MHz sinusoidal tone burst enveloped in a Hanning window. This particular frequency was chosen to ensure that the frequency-thickness product corresponded to the s_0 mode being excited in a fairly non-dispersive region on the dispersion curves. In real life, the thicknesses of the pipes are larger than the values used for these studies. However, provided we excite the Lamb wave at the same frequency-thickness product, a larger thickness simply means that the frequency of the excitation signal will be less. The bandwidth of the signal is such that no higher order modes are excited. Fig.5.5 shows the temporal response in the y direction at a surface node 150mm from the L-end of the plate for t_2=2.5, 3, 3.5 and 4mm. Referring to the first of these figures, several signals are present. The initial pulse is the input s_0 pulse. The next pulse is the s_0 mode after it has been reflected from the step. Following this we have a slower a_0 mode arriving, this being the result of mode conversion at the step. Finally, within the time window captured, we have the reflection of the second pulse off the L-end of the plate. If we compare the different traces, we can see that the same pulses exist, the only real difference being in their amplitudes. Several features can be identified from the traces. Firstly, dispersion is evident for the a_0 mode as can be deduced from the broadening of the reflected a_0 pulse when compared to the incident s_0 pulse. Secondly, it can be seen that as the step height increases, the amplitudes of the reflected waves increase, the rate at which the a_0 mode increases being greater than that of s_0.

Fig.5.6 shows the case for Lamb waves transmitted across the step, the monitoring position being 250mm from the R-end of the plate. Two modes are present; the first is the transmitted s_0 mode and the next is the mode converted a_0 mode. Given that the plate now becomes thicker, the frequency-thickness bandwidth increases and the result is that dispersion becomes much more pronounced. What can also be seen is that the amplitude of s_0 remains essentially the same whereas the amplitude of a_0 increases dramatically as the thickness is increased up to twice the thickness of the parent plate. In addition, as the thickness increases, we can also see the appearance of other modes (Fig.5.6d). These are modes which are being excited near their cut-off frequency thickness values which accounts for their dispersive nature. From the dispersion curves of Fig.5.3 these modes are most probably the a_1 and s_1 modes.

To analyse the results from the FE model, a number of surface nodes were monitored in both parts of the stepped plate and two-dimensional Fourier analysis (2D FFT) was performed to decompose the signals (which are in time and space) into both the frequency and wavenumber domains. The advantage of doing this is that modes with the same frequency can be differentiated owing to the fact that the modes have different velocities and hence wavenumbers. Fourier analysis in the frequency domain alone cannot achieve this. It is necessary to use this analysis when signals due to different modes start to overlap and hence are impossible to separate out in the time domain. The two-dimensional Fourier transform is given by (Alleyne and Cawley (1991)),

$$F(k,\omega) = \int_{-\infty}^{+\infty}\int_{-\infty}^{+\infty} u(x,t)e^{-i(kx+\omega t)}\,dx\,dt \qquad (5.11)$$

To evaluate the integral on numerical results obtained using FE analysis, a discrete Fourier transform is performed. This is achieved by carrying out a Fourier transform of the time domain history of the response of each monitored point in order to obtain a frequency spectrum for each point. Subsequently an array is formed by fixing the frequency and obtaining at this frequency the amplitudes of each point. A spatial transform is then performed on this array to give information relating the amplitude, wavenumber and frequency. This procedure is then repeated at all relevant frequencies.

In addition to being able to distinguish between different Lamb modes, if a complex 2D FFT is performed then it is possible to separate out waves which have the same wavenumber but travel in opposite directions. Consider the spatial Fourier transform at a fixed frequency,

$$F(k) = \int_{-\infty}^{+\infty} g(x)\, e^{-ikx}\, dx \qquad (5.12)$$

Let us assume that a signal is composed of a forward propagating wave as well as a backward propagating wave, both with wavenumber of amplitude $|k_n|$ and omitting the time dependence term, i.e.

$$g(x) = Ae^{ik_n x} + Be^{-ik_n x} \qquad (5.13)$$

then assuming that k_n is positive the spatial Fourier transform at $k = k_n$ is given by,

$$F(k_n) = \int_{-\infty}^{+\infty} g(x)\, e^{-ik_n x}\, dx \qquad (5.14)$$

$$= \int_{-\infty}^{+\infty} (Ae^{ik_n x} + Be^{-ik_n x})\, e^{-ik_n x}\, dx$$

$$= \int_{-\infty}^{+\infty} (A + Be^{-2ik_n x})\, dx$$

$$= \int_{-\infty}^{+\infty} A\, dx \qquad (5.15)$$

In a similar way, $$F(-k_n) = \int_{-\infty}^{+\infty} B\, dx \qquad (5.16)$$

Therefore, $F(k_n) \neq F(-k_n)$ so by carrying out a spatial transform, waves in opposite directions will automatically be separated from each other, even though they have the same wavenumber amplitude $|k_n|$.

Fig.5.7a shows the frequency spectrum for the case of t_2=2.5mm (Fig.5.5a); the whole time record of Fig.5.5a was used. It is difficult if not impossible to tell which modes are propagating. Fig.5.7b shows the wavenumber spectrum of the incident wave at 0.3MHz obtained by performing a 2D FFT on an array of points located on the left half of the stepped plate (points with time domains similar to that of Fig.5.5a). On the same vertical scale, Fig.5.7c shows the wavenumber spectrum for the reflected waves and Fig.5.7d the wavenumber spectrum for the transmitted waves (by performing a 2D FFT on an array of time domain responses on the right half of the stepped plate). From these figures, we can determine exactly how many modes are propagating, in which

5.4.3 Numerical Simulations of Lamb Wave-Defect Interaction

We now look at the interaction of Lamb waves with defects. For computational efficiency, we will consider the case of a uniform plate with a delamination and then combine the results with those obtained earlier for interaction with a step. The delamination in question extended to the right hand end of the plate as shown in Fig.5.11a. This model is satisfactory if we consider only the reflections from the start of a real, finite length delamination. The delamination was modelled by the separation of nodes (Guo and Cawley (1993)). Given that couplers can have varying thicknesses depending on the manufacturer, we investigated the detectability of the crack as we varied its planar position through the wall thickness. Four positions were chosen, each being a multiple of 1/8 the thickness of the plate as shown in Fig.5.11b. A wall thickness of 2mm was considered, which ensured that only two modes could exist in the excitation bandwidth. Given that as a result of mode conversion at the step, two modes can be transmitted across the step, we considered separately the case of inputting s_0 and a_0 for each crack position.

Time domain responses were obtained by monitoring the normal displacements on the plate surface (Fig.5.12a). Fig.5.12b shows the time domain response for an input s_0 mode with the crack being situated at a quarter thickness through the plate (position 2 in Fig.5.11b). The first pulse $s_{0,I}$ represents the input mode. The second pulse $S_{0,TRT}$ represents the incident s_0 mode after it has been transmitted past the crack, reflected off the far end of the plate and transmitted past the crack once more. Any signals reflected from the defect should lie between these two pulses. However no intermediate signals can be seen.

It is interesting to compare these results to those obtained by Guo and Cawley (1993) who studied the interaction of Lamb waves with delaminations in composite plates. Their studies showed that the s_0 mode could be used to detect delaminations in cross-ply composites provided the delaminations were not located at positions of zero shear stress; a maximum shear stress correlated with a maximum reflection. Unfortunately, the shear stresses in the s_0 mode in an isotropic plate are very small, as shown in the stress mode shape of Fig.5.12c and so the reflection from a delamination anywhere through the thickness is negligible. In contrast, large shear stresses are seen in the s_0 mode with a cross-plied composite plate (Guo and Cawley (1993)).

Fig.5.12d shows the corresponding time domain plot for an incident a_0 mode. The first pulse $a_{0,I}$ is the input pulse and the second pulse $a_{0,R}$ is the reflected a_0 mode from the

delamination. Note that no s_0 mode from the delamination can be seen; it does exist but its amplitude is very small. The third pulse $s_{0,TRT}$ corresponds to the incident mode being transmitted into the cracked region as s_0, propagating to the far side of the plate where it is reflected and then being transmitted back to the uncracked region as s_0. A reflected a_0 mode from the far side of the plate also exists but as it is slower than the s_0 mode it appears after the $s_{0,TRT}$ pulse and has not been included in the figure. Therefore, a larger reflection from the delamination occurs when the a_0 mode is used as the input, the reflected mode being a_0 rather than a mode converted s_0 and this can again be attributed to the shear stresses in the plate which are now higher (Fig.5.12e). From a practical point of view, it seems that the reflected a_0 mode would be the most promising mode for defect detection. Fig.5.13 shows a plot of the reflection ratio and shear stress versus depth through the thickness of the plate. It can be seen that both profiles are parabolic in nature with maximum reflection ratio correlating with maximum shear stress at the mid-plane of the plate. Fig.5.14 shows a plot of the reflection ratio versus frequency for the a_0 mode when the delamination is situated at the four positions in the plate shown in Fig.5.11. The general trend is that the reflection ratio drops off with frequency although the decay is gradual. What is probably more important is that the values of the reflection ratios are fairly small (i.e. less than 8% for the best position).

5.4.4 Discussion of Results

Inputting an a_0 mode into the parent plate will lead to larger reflections off the delamination. The expense of using this mode is that it is fairly dispersive and may lead to the signal being spatially long and resolution problems may become prevalent. It is possible to decrease the frequency bandwidth of excitation by increasing the number of cycles. However, although this may reduce dispersion, the end result is that the signal will be temporally longer and once again resolution problems may become significant.

Using the case of t_2=3mm, an overall reflection ratio (i.e. the reflection ratio for the whole structure as shown in Fig.5c) has been calculated at a frequency of 0.3 MHz and is shown in Table 5.1 below.

INCIDENT MODE IN PARENT PLATE	RECEIVED MODE IN PARENT PLATE (Refl. Ratio) no attenuation		RECEIVED MODE IN PARENT PLATE (Refl. Ratio) with attenuation	
a_0	a_0	3.50%	a_0	0.0174%
	s_0	1.05%	s_0	0.0029%
s_0	a_0	0.51%	a_0	0.0014%
	s_0	0.15%	s_0	0.0001%

Table 5.1. Overall reflection ratio of reflected Lamb wave from a delamination for different configurations of input and reception Lamb modes (attenuation s_0=0.038Np/mm and a_0=0.0265Np/mm).

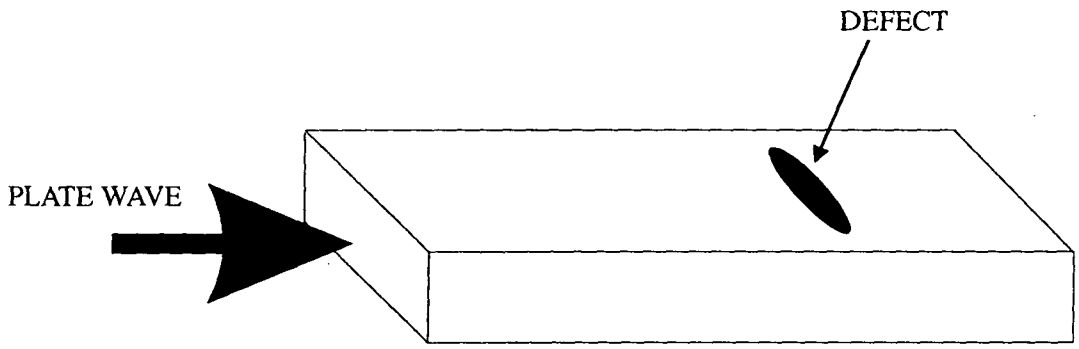
In order to do this, the parent plate is excited with either s_0 or a_0. The amplitude of the transmitted a_0 mode across the step is then taken. Note that studies have been carried out using an incident a_0 mode in the parent plate; the results were very similar to those for the incident s_0 mode and as such have not been shown in this thesis. The a_0 mode is then reflected from the delamination as a_0 and on reaching the step again can be transmitted across it as either a_0 or s_0 to the parent plate. The overall reflection ratio is then defined as the ratio of the amplitude of the received signal to the amplitude of the input signal. From Table 5.1, we can see that using an input a_0 mode rather than an s_0 would be very beneficial, with an increase in the reflection ratio of over 500% if we compare the best input a_0 case with the best input s_0 case. In both cases, the optimum reception mode is a_0.

We now consider how these results would be affected in plastics. The principal effect of a viscoelastic medium is to introduce attenuation. In plastics, this can be very high as is the case in polyethylene. The attenuation of Lamb waves for the zero order modes in a high density polyethylene have been calculated in the same way as that used in Chapter 6 and used to re-evaluate the reflection ratios. The attenuation calculations were carried out assuming a 10mm thick polyethylene plate and a frequency of 90kHz; this gave a frequency-thickness of 0.9MHzmm, the same frequency-thickness as for the aluminium plate. The polyethylene grade chosen for the attenuation calculations was TUB 124 HPPE. The results in Table 5.1 are shown for a propagation path length between the point of excitation of the incident Lamb wave to the delamination position of 100mm. This value is composed of 50mm in the parent plate and 50mm in the joint plate, these values being chosen so that in practice the reflections from the step would be over by the time the reflection from the delamination arrives. We can see that the inclusion of attenuation has reduced the signal to a level much too small to measure.

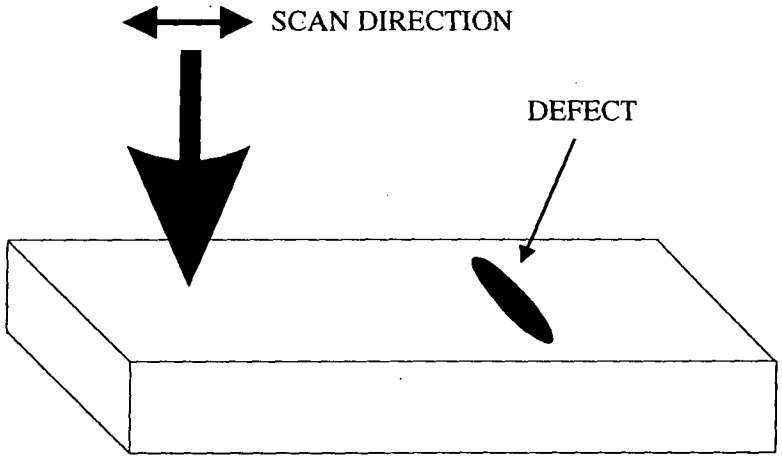
5.5 Conclusions

Finite element analysis has been used to model the propagation of Lamb waves in a step geometry and the interaction of Lamb waves with delaminations. It has been shown that as the step height increases, the ratio of the energy of the transmitted non-mode converted mode to the energy of the transmitted mode-converted mode falls. If the frequency thickness of the plate is such that any higher order modes can exist, maxima and minima are seen in the reflection ratio curves.

Studies on the reflectivity off delaminations have shown that an incident s_0 mode does not produce adequate reflections, the reason being the very low shear stresses generated in this mode in isotropic materials. The situation is much improved when inputting a_0, the reflectivity being a maximum when the defect is located at the mid-plane, where the shear stress is maximum. Given that for most situations the joint thickness is twice the thickness of the parent pipe, defects are most likely to lie at the mid-plane of the joint section. Tests using an incident a_0 mode in the joint region should then produce the maximum reflection possible for the given thickness. In order to achieve as large a reflection as possible off a delamination, it is necessary to maximise the amount of a_0 transmitted across the step. This can be achieved by having an incident a_0 at the parent plate end. If an attenuative medium is considered, the effect of attenuation has been shown to dramatically reduce the reflected signals to levels which would be very difficult to detect. Therefore, the detection of defects using this Lamb wave method is limited to low attenuating materials such as metals and some composites. A further difficulty with the use of Lamb waves in the electrofusion couplers would be the existence of reflections from the heater wires which would exist even in the absence of a delamination. The technique has therefore been demonstrated to be impractical and consequently was not pursued experimentally.



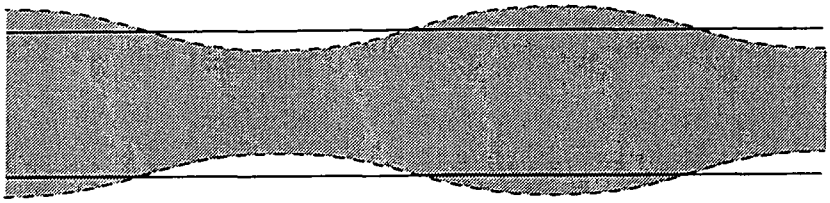
a)



b)

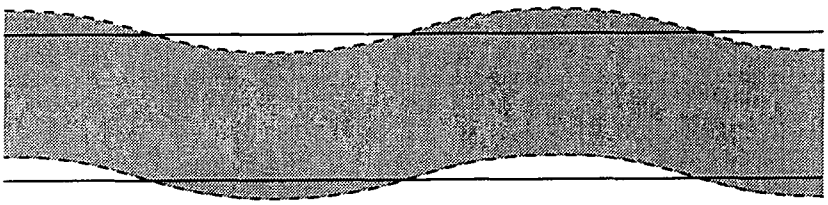
Fig.5.1 Lamb wave inspection in a plate containing a defect. a) Diagram showing direction of plate wave with respect to a defect; b) Diagram showing direction of normal incidence scanning with respect to a defect

symmetric wave

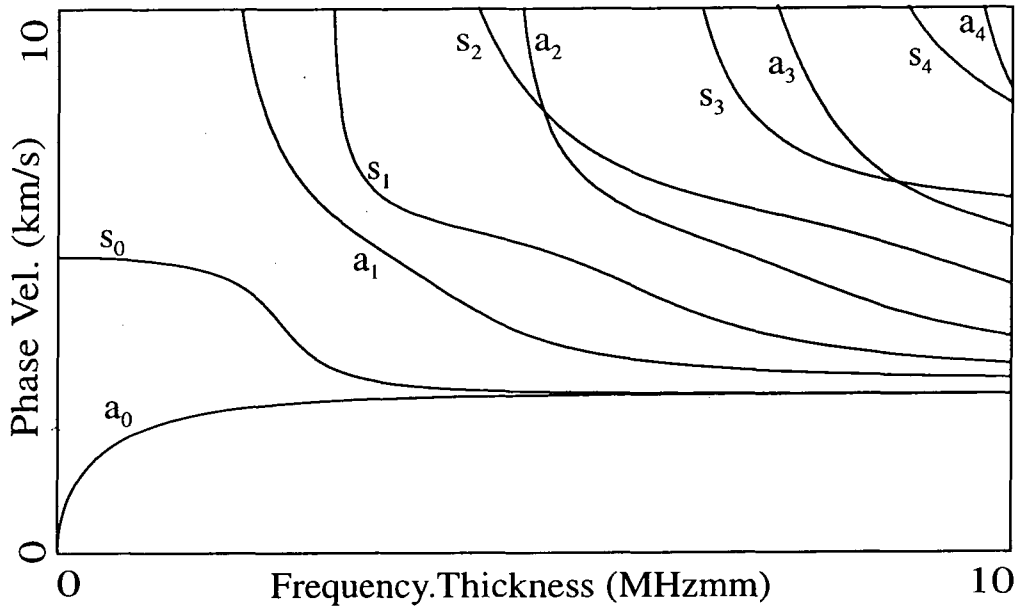


a)

antisymmetric wave



b)



c)

Fig.5.2 Mode shapes of zero order modes at low frequency-thickness. a) s_0 mode; b) a_0 mode; c) Phase velocity dispersion curves for aluminium

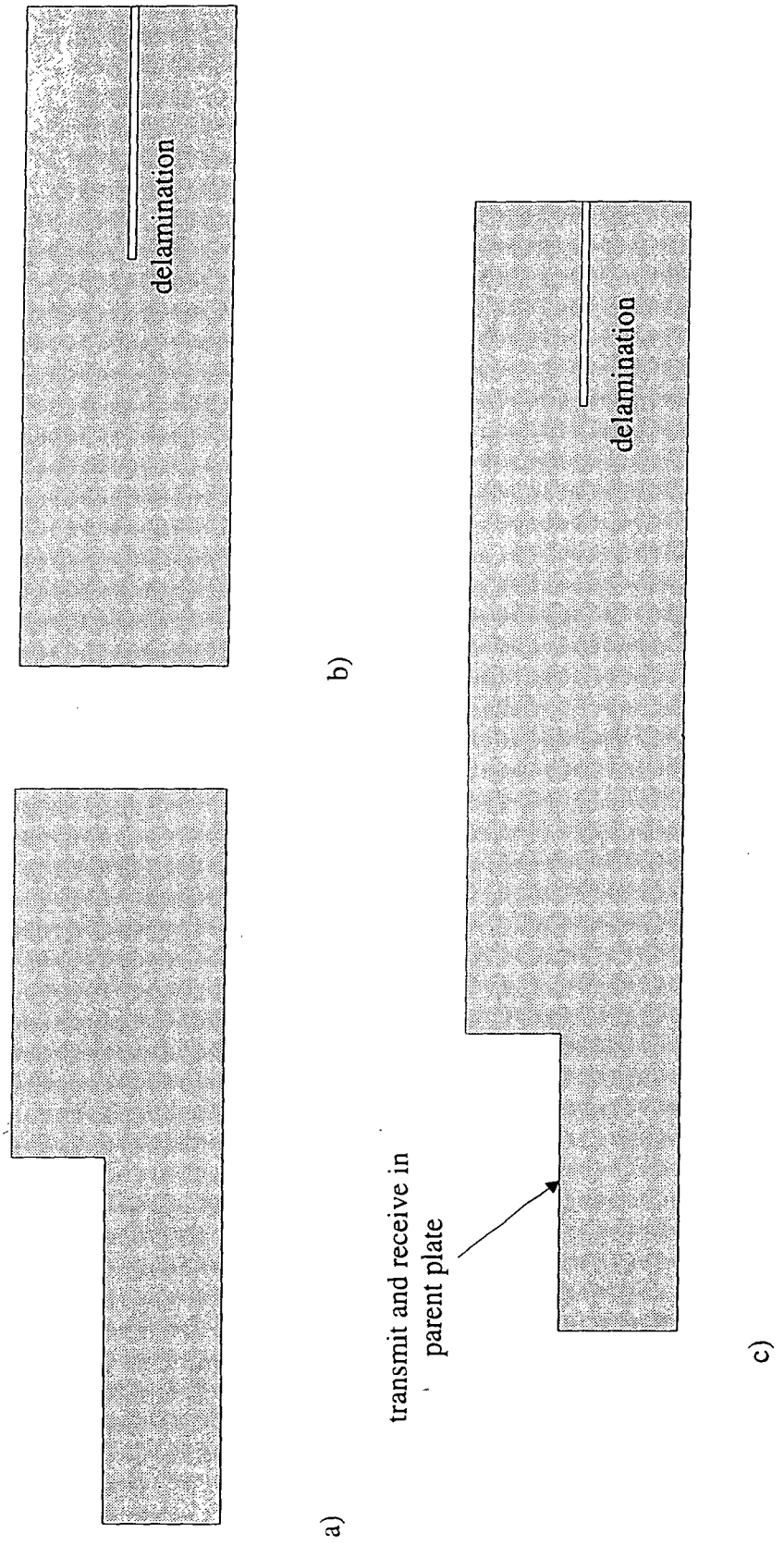


Fig.5.3 Geometries used in FE analysis. a) Geometry of a stepped plate; b) Geometry of a plate with delamination; c) Geometry of joint representing delamination in an electrofusion weld obtained by combining a) and b)

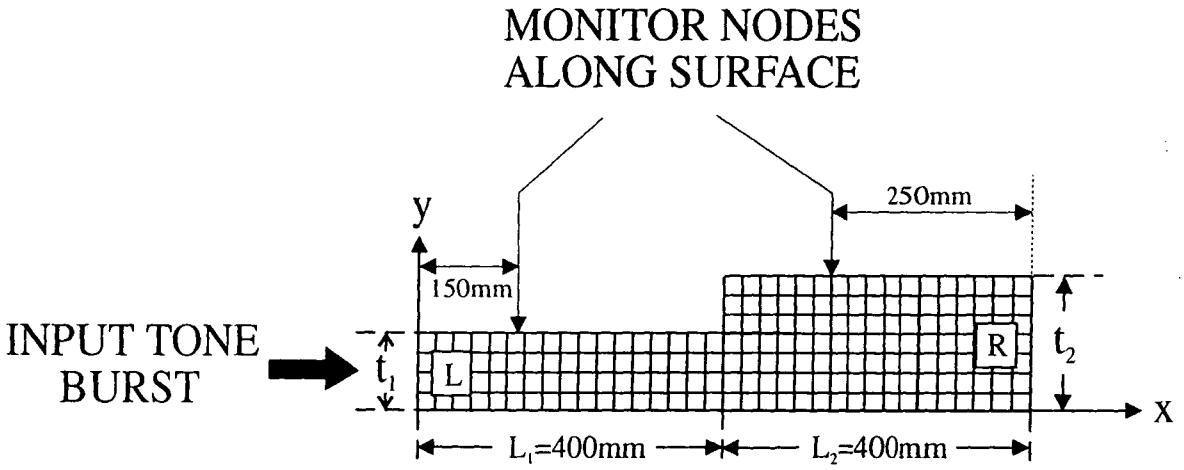


Fig.5.4 Geometry and co-ordinate system for stepped plate (mesh not to scale)

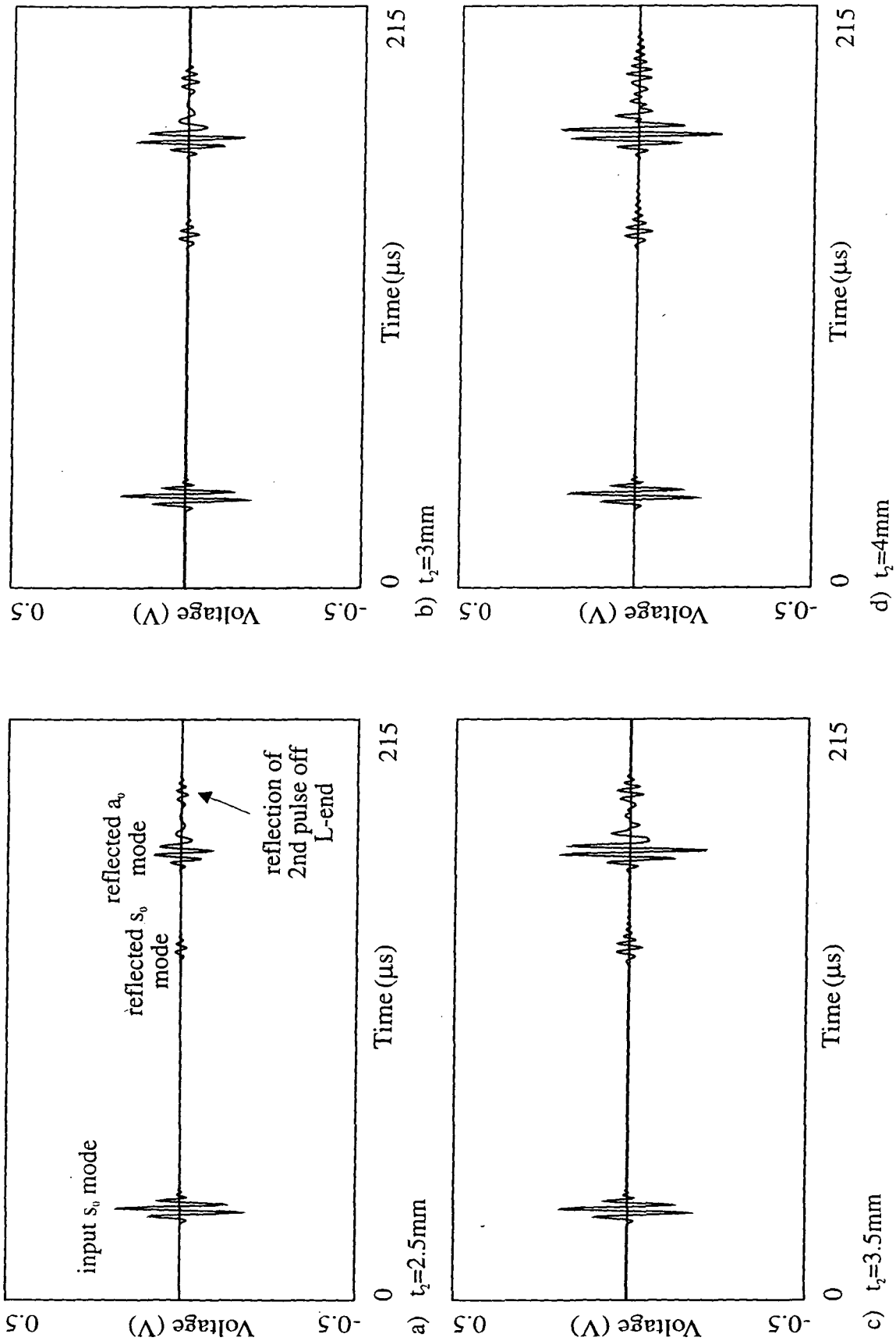


Fig.5.5 Time domain responses (y-direction) of monitored point at 150mm from L-end of plate

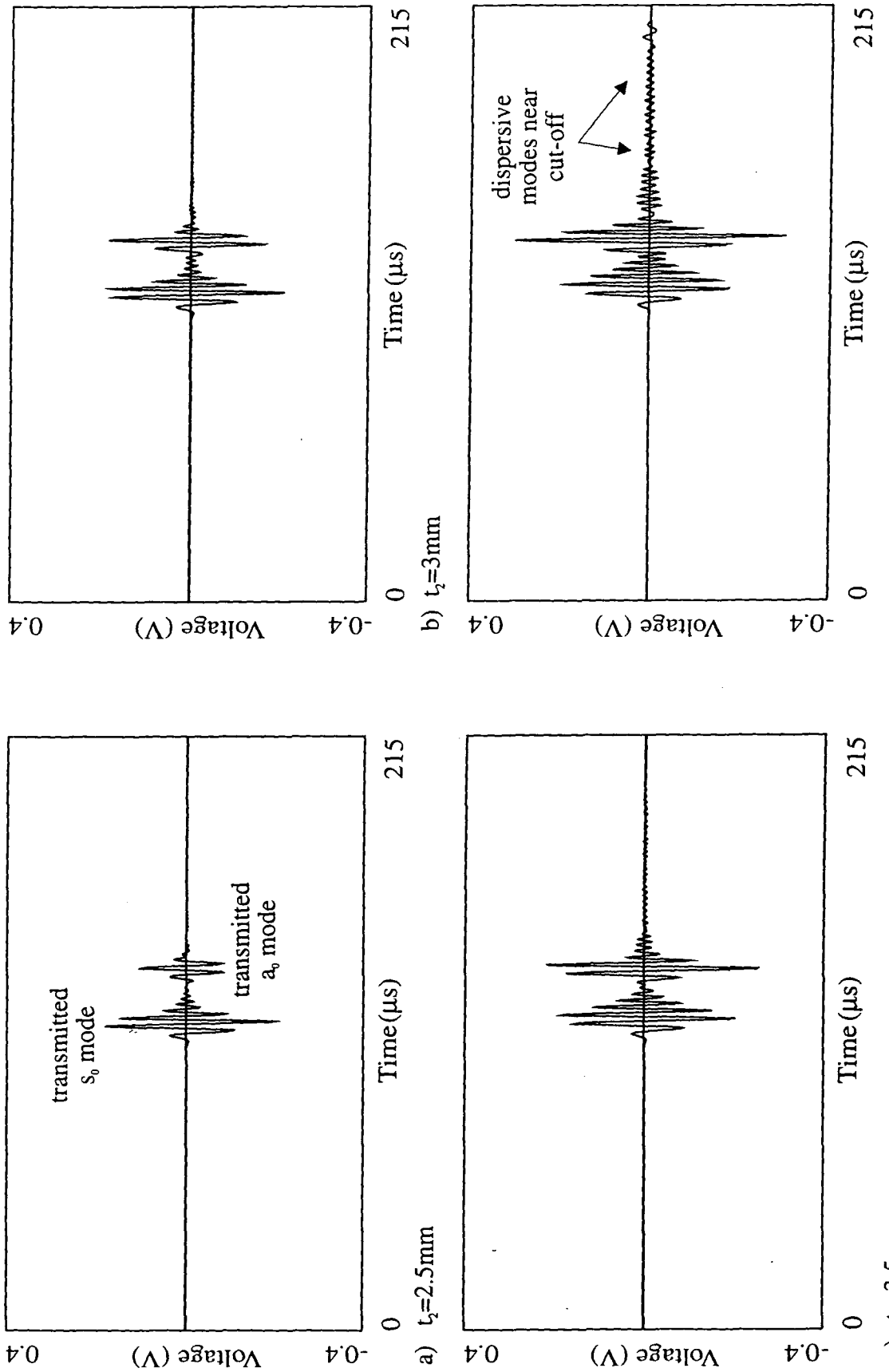
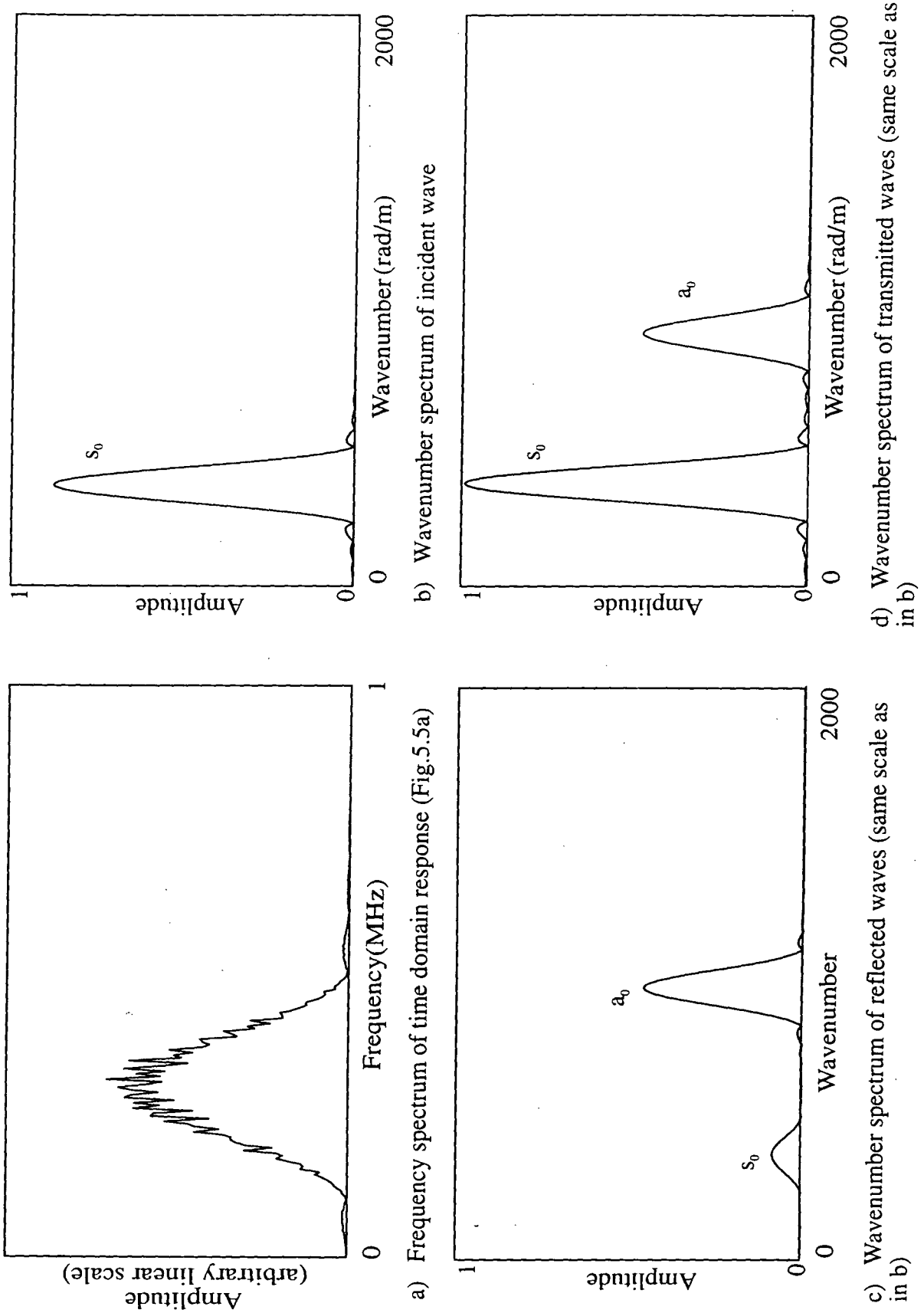


Fig.5.6 Time domain responses (y-direction) of monitored point at 250mm from R-end of plate



a) Frequency spectrum of time domain response (Fig.5.5a)

b) Wavenumber spectrum of incident wave

c) Wavenumber spectrum of reflected waves (same scale as in b)

d) Wavenumber spectrum of transmitted waves (same scale as in b)

Fig.5.7 Frequency and wavenumber spectra for t_2=2.5mm

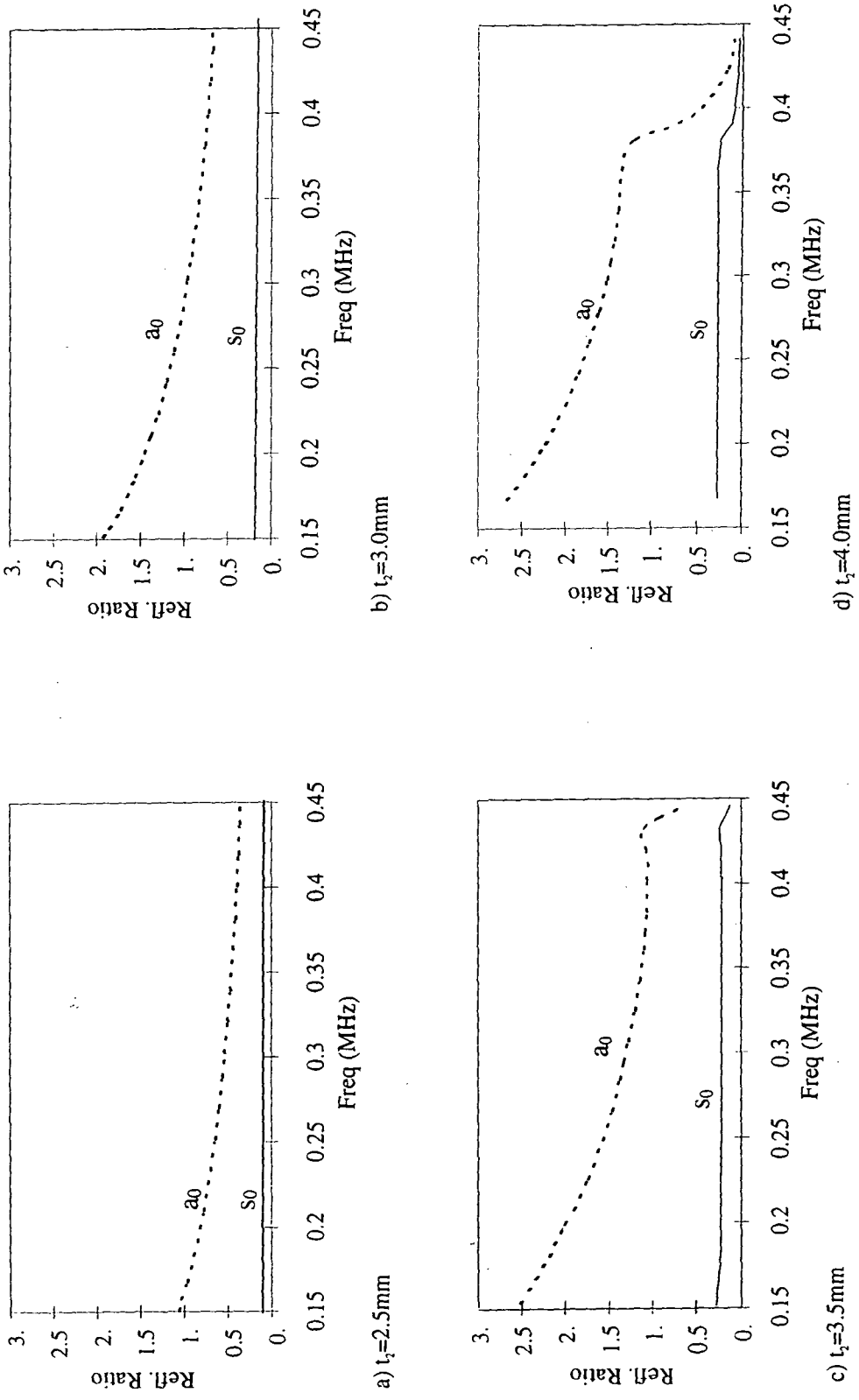


Fig.5.8 Reflection ratios (y direction) vs. frequency

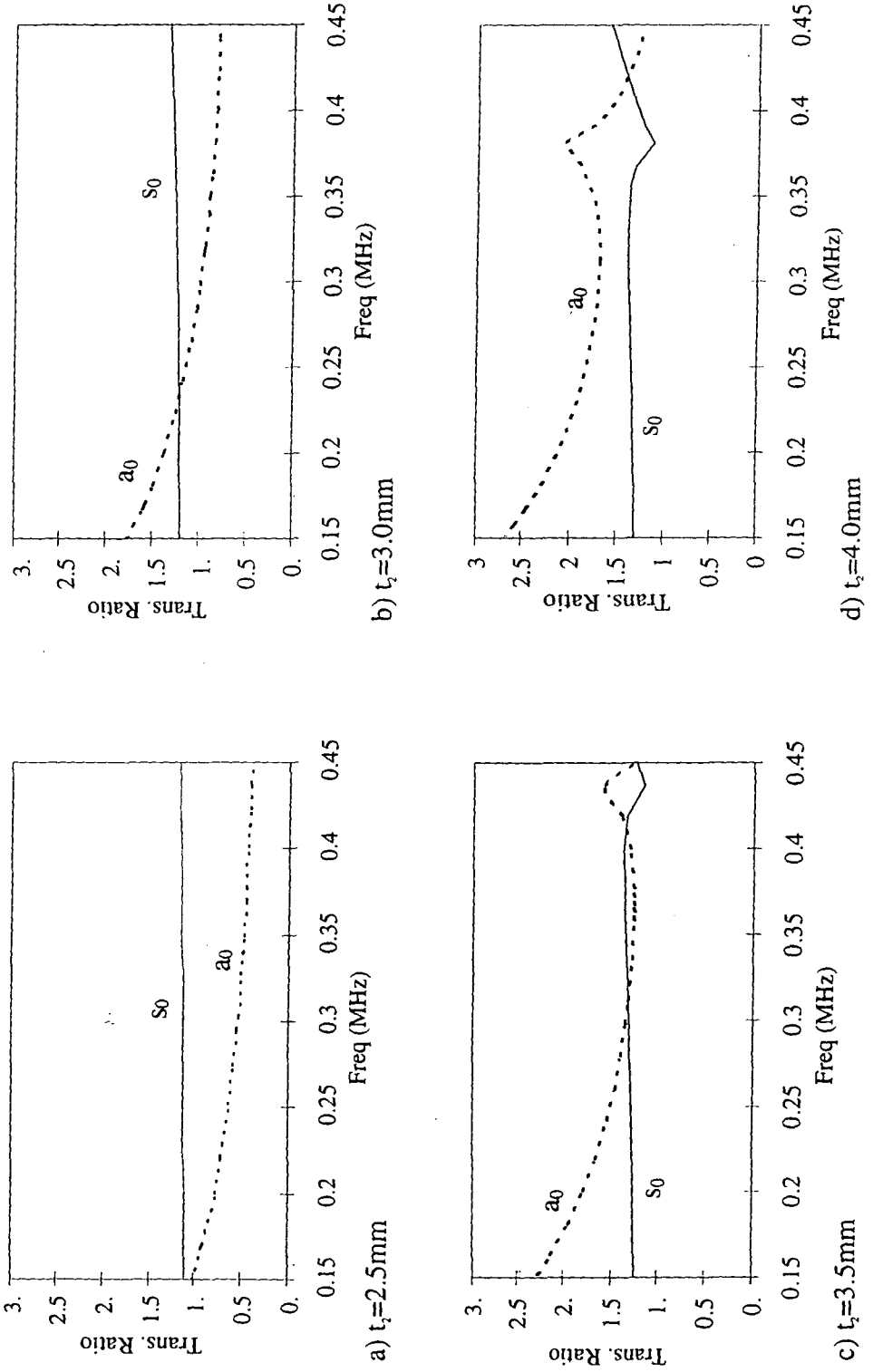


Fig.5.9 Transmission ratio (y direction) vs. frequency

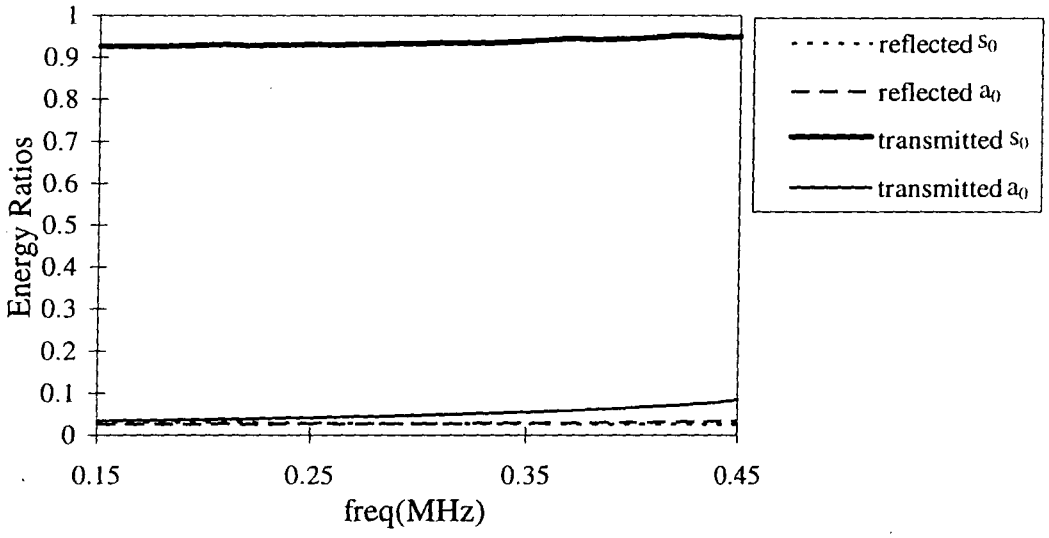
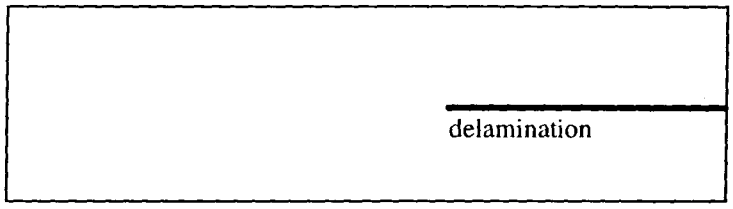
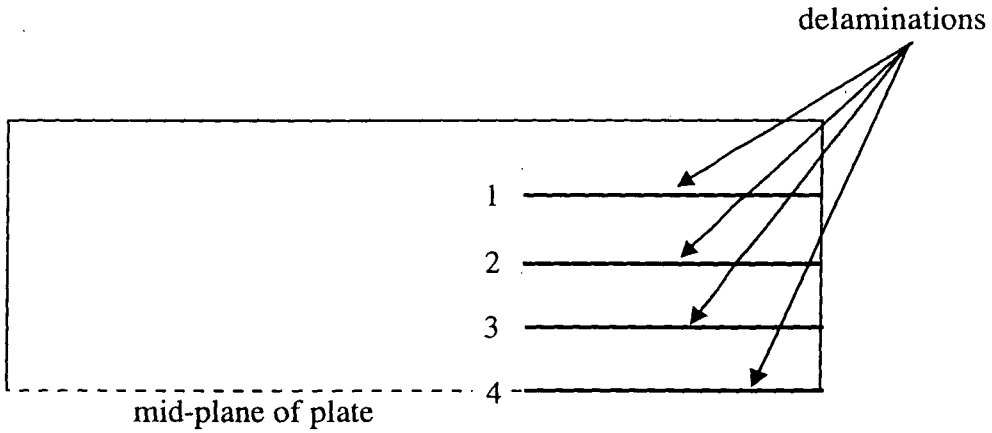


Fig.5.10 Strain energy ratios of the various Lamb waves for t_2=3mm



a)



b)

Fig.5.11 Diagram showing a) extent and b) positions of the delamination used in FE modelling

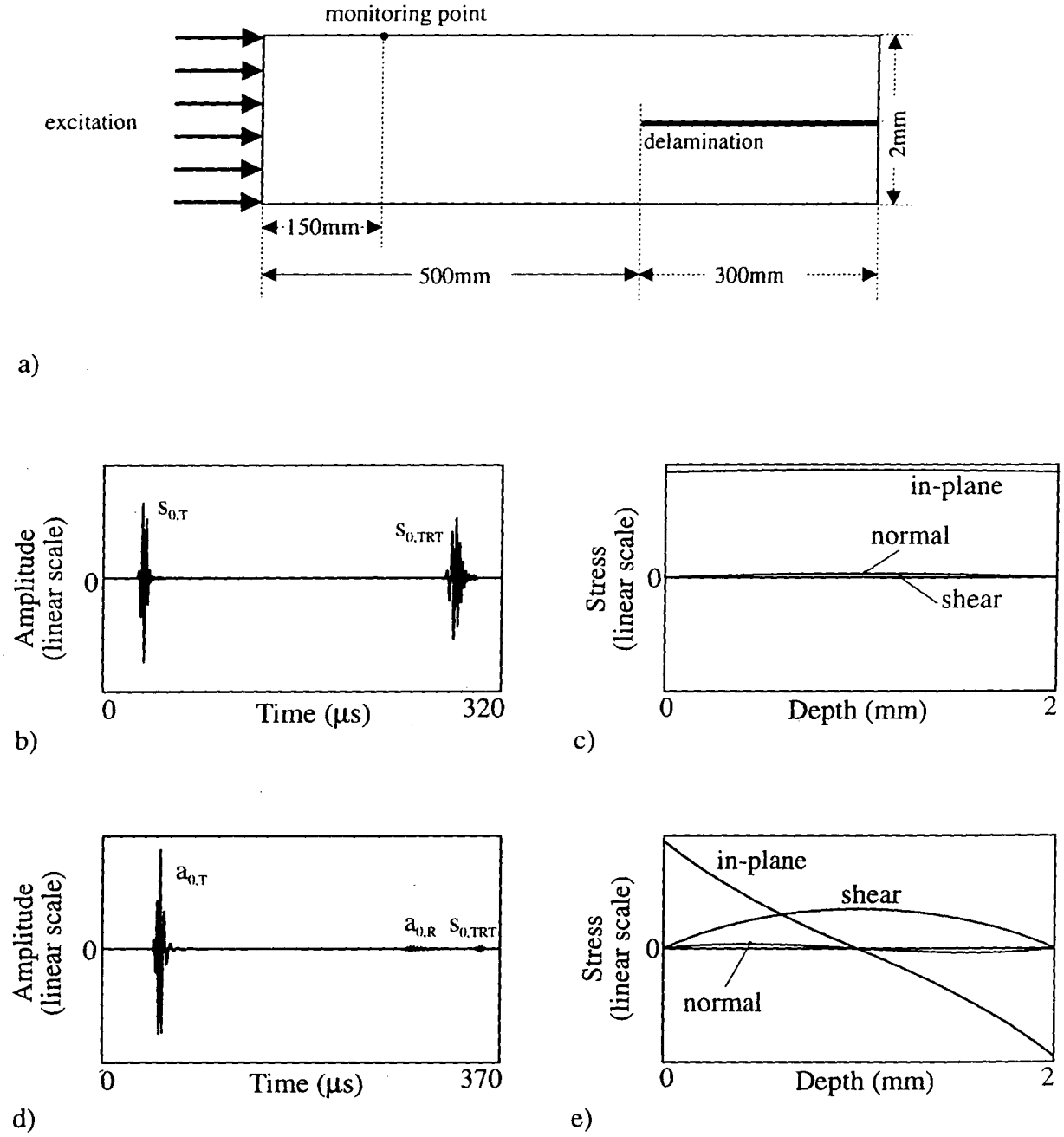


Fig.5.12 FE analysis of delamination in a 2mm plate. a) Schematic showing excitation and monitoring positions on a plate containing a delamination; b) Time domain response of reflected Lamb waves from a semi-infinite delamination (incident s_0); c) Normalised stress distribution (shear and in-plane) for s_0 mode; d) Time domain response of reflected Lamb waves from a semi-infinite delamination (incident a_0); e) Normalised stress distribution (shear and in-plane) for a_0 mode

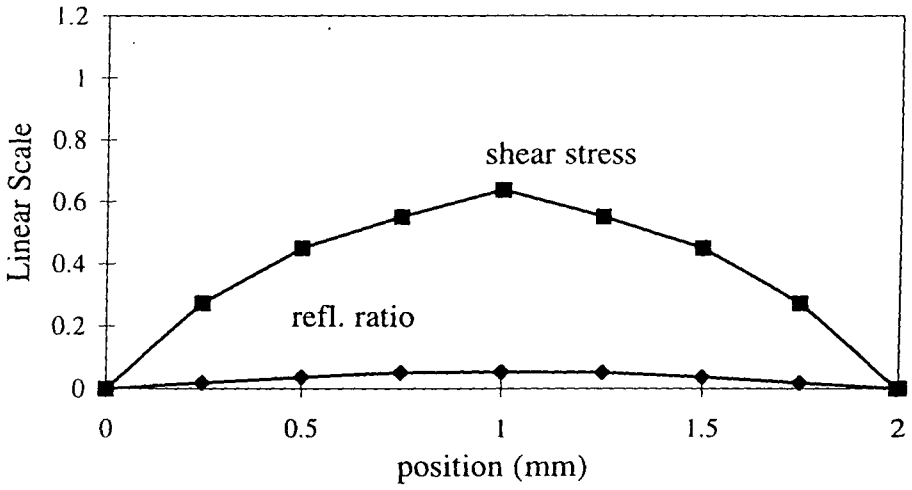


Fig.5.13 Reflection ratio and shear stress vs. position of delamination through plate thickness for a_0 mode

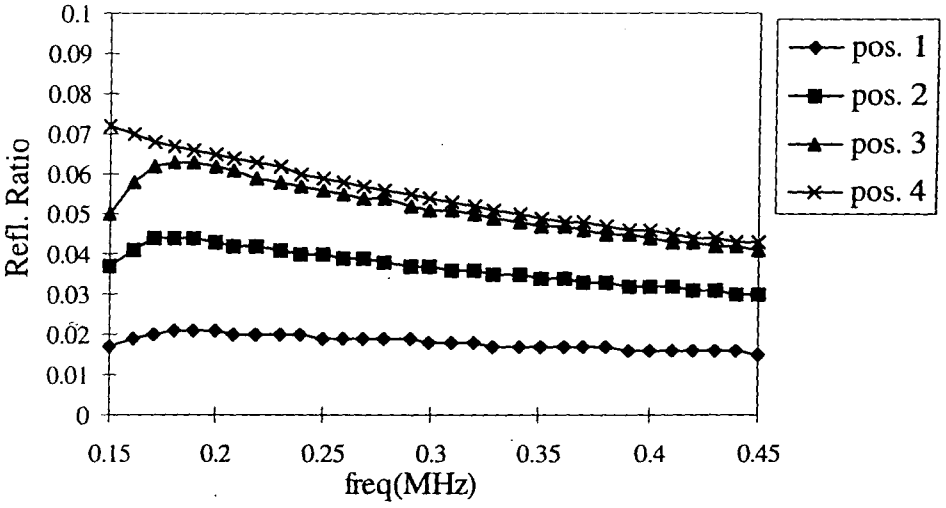


Fig.5.14 Reflection ratio vs. frequency of a_0 mode for four positions of delamination through plate thickness

CHAPTER 6

Lamb Wave Propagation in Attenuative Media

6.1 Introduction

Much of the work undertaken in the field of Lamb waves has to date concentrated on their application to materials which are generally elastic with very little or no internal (material) damping. However in more recent times, the subject of attenuation in Lamb waves has been considered. Attenuation in Lamb waves can be broadly divided into two categories: attenuation caused as the result of energy transfer (commonly known as 'leakage') from the material of interest into the surroundings, and internal (material) attenuation, for example that which is found in a viscoelastic medium. The majority of work published to date has been targeted towards the former category ((Lowe (1993), Alsop (1970), Xu and Mal (1987), Watson (1972), Chimenti and Nayfeh (1985)). In the present project, the problem of 'leakage' is of little importance given that the medium surrounding the material of interest is assumed to be air and hence there is a large acoustic impedance mismatch. However, the same cannot be said about the inherent damping in the material. Therefore, in order for Lamb waves to be used in the plastic materials considered in this project, the attenuation of the material has to be taken into account.

We have already seen in Chapter 3 that the attenuation of bulk longitudinal and bulk shear waves is not insignificant, more so for the latter as the shear wave attenuation is about five times that of the longitudinal bulk wave. From an attenuation point of view, the ideal conditions for a Lamb wave inspection technique would be to have a mode which is predominantly a longitudinal type mode, that is, a mode with minimal shear motion, the reason behind this being that the attenuation will then be governed by the attenuation of longitudinal waves. Therefore one of the interests in this chapter is to investigate the existence of such modes. Alternatively we could go to a lower frequency of operation so that the attenuation would be lower for both longitudinal and shear dominated modes, but by doing so the duration of waves becomes larger and larger and the identification of reflections close to the excitation source may become problematic.

In this chapter we look at the effect of gradually increasing the attenuation in a material from zero up to and beyond that of the TUB 124 HPPE used in this project.

The work is divided into several parts. Firstly we will look at how to incorporate attenuation into the Lamb wave model used previously for calculating Lamb wave dispersion curves. A simple viscoelastic behaviour is assumed and the solution of the wave equation requires the wavenumber to be complex, the imaginary part representing the attenuation of the wave. Dispersion curves can then be predicted by specifying the attenuation values for bulk longitudinal and bulk shear waves. The studies are carried out assuming plate geometry. This is a valid approximation for pipes provided we excite a Lamb wave close to the inspection region so that there is insufficient time for the circumferential field around the pipe to build up and form a pipe mode.

Next we will examine the dispersion curves for a plate in the presence of attenuation. Work of a similar nature has been carried out by Nkemzi (1993). However, little insight into the physical phenomena governing these curves was given. Four levels of attenuation will be considered: when the material has four times the amount of attenuation as given by the measured bulk longitudinal and bulk shear attenuation values, the full amount of attenuation, half the amount of attenuation and zero attenuation. This study will allow us to determine how influential attenuation is on certain modes. From the dispersion curves, it will be shown that four distinct sets of modes exist which have vastly different properties. Explanations will be given as to the nature of these sets.

Following on from this, experimental studies were carried out and will be described. These were conducted to verify the predicted dispersion curves. The chapter finally concludes with a discussion on the implications of attenuation on the feasibility of Lamb wave testing.

6.2 Attenuation Model

So far, the Lamb wave model used for predicting dispersion curves has employed a matrix technique approach based on satisfying the traction free boundary conditions at the surfaces of the plate, the wave field being made up of the superposition of partial waves (Lowe (1993)). The amplitudes of the partial waves are assumed to be constant and hence only elastic behaviour can be investigated using this model. Such a model needs to be modified so that attenuation behaviour can be studied. In order to achieve this, an expression for the attenuation in the partial waves has to be included.

The first step is to decide on an appropriate attenuation model to describe the material behaviour. Many models exist for this purpose (e.g. Malvern (1969), Lazan (1968)). One of the most popular models is the Voigt viscoelastic model (Lowe (1993), Castaings and Hosten (1994)) due to the fact that this model is simple to use and has been shown to be fairly representative of the behaviour of real, attenuative materials. In this model, the damping is modelled by the inclusion of a velocity dependent damping force in the equation of motion for the material. It is commonly known as the 'spring and dashpot in parallel' model in which the spring represents the elastic behaviour of the material and the dashpot the damping.

The brief derivation which follows is similar to that given by Lowe (1993). The effect of damping is to modify the Lamé constants λ and μ into the following operators (Pialucha (1992)):

$$\lambda \text{ becomes } \lambda + \frac{\lambda'}{\omega}\frac{\partial}{\partial t}, \quad \mu \text{ becomes } \mu + \frac{\mu'}{\omega}\frac{\partial}{\partial t} \tag{6.1}$$

where λ' and μ' represent the viscoelastic constants of the material and ω the frequency.

If we substitute these operators into the displacement equation of motion, we get the following equation:

$$\rho\frac{\partial^2 \mathbf{u}}{\partial t^2} = (\lambda+\mu)\nabla(\nabla\bullet\mathbf{u}) + \mu\nabla^2\mathbf{u} + \left(\frac{\lambda'+\mu'}{\omega}\right)\nabla\left(\nabla\bullet\frac{\partial \mathbf{u}}{\partial t}\right) + \left(\frac{\mu'}{\omega}\right)\nabla^2\frac{\partial \mathbf{u}}{\partial t} \tag{6.2}$$

where **u** is the displacement vector.

By using the Helmholtz method (see e.g. Malvern (1969)) to decouple the motion into dilatational and rotational fields, ϕ and ψ, we obtain:

$$\rho\frac{\partial^2\phi}{\partial t^2} = \left(\lambda + 2\mu + \frac{\lambda'+2\mu'}{\omega}\frac{\partial}{\partial t}\right)\nabla^2\phi \tag{6.3}$$

$$\rho\frac{\partial^2\psi}{\partial t^2} = \left(\mu + \frac{\mu'}{\omega}\frac{\partial}{\partial t}\right)\nabla^2\psi \tag{6.4}$$

The aim now is to seek solutions of these equations. It can be shown that functions of the form :

$$\phi, \psi = C_{1,2} e^{i(\mathbf{k} \bullet x - \omega t)} \tag{6.5}$$

where $C_{1,2}$ are arbitrary constants, satisfy the equations, provided that the wavenumber $\mathbf{k}$ is complex, i.e. $\mathbf{k}=\mathbf{k}_r + i\mathbf{k}_i$

Rewriting the above equation yields:

$$\phi, \psi = C_{1,2} e^{i(\mathbf{k}_r \bullet x - \omega t)} e^{-\mathbf{k}_i \bullet x} \tag{6.6}$$

In these equations, the first exponential term describes the propagation of the wave and the second exponential term the exponential decay of the wave. By substituting these equations into eqns. (6.3) and (6.4), we obtain expressions for the longitudinal and shear wave speeds C_L and C_S as follows:

$$C_L = \left(\frac{\lambda + 2\mu - i(\lambda' + 2\mu')}{\rho} \right)^{1/2} \tag{6.7}$$

$$C_S = \left(\frac{\mu - i\mu'}{\rho} \right)^{1/2} \tag{6.8}$$

The velocities can be expressed in terms of wavenumber and frequency by the expression:

$$C_{L,S} = \frac{\omega}{\mathbf{k}} \tag{6.9}$$

Rearranging this equation gives:

$$\mathbf{k} = \mathbf{k}_r + i\mathbf{k}_i = \frac{\omega}{C_{L,S}} \tag{6.10}$$

Given that $C_{L,S}$ are constant for a given material, we can see that the imaginary part (as well as the real part) of the wavenumber (i.e. the attenuation) is linearly proportional to frequency. This model is therefore in good agreement with the experiments conducted in Chapter 3 where the measured attenuation for bulk waves was also found to be reasonably linearly dependent on frequency.

Given that we now have expressions for the propagation of bulk longitudinal and bulk shear waves, we can now solve the modal (Lamb wave) problem in the same way as before, by the superposition of the bulk partial waves and by satisfying the boundary conditions at the surfaces of the plate. The method used for solving this is the same as that used before for solving the elastic Lamb wave case, the only real difference being the addition of the imaginary part of the plate wavenumber (Lowe (1993)).

6.3 The Effect of Material Attenuation on Dispersion Curves

One of the main interests in investigating the effect of attenuation on Lamb waves is to see the influence of different attenuation levels on the dispersion curves. For this study, four particular attenuation cases were selected. The first case corresponds to the material having zero attenuation. The second case is when the bulk longitudinal and bulk shear attenuation values are half the true values. The third case is when the attenuation values are the true values and the final case is when the attenuation values are four times the true values. The way in which the attenuation is varied is by multiplying the longitudinal and shear bulk attenuation coefficients by the same factor. Therefore, if the initial values for the bulk longitudinal wave and bulk shear wave attenuations are α_L and α_S respectively then each time we vary the attenuation input into the dispersion model, the new attenuations are given by $k\alpha_L$ and $k\alpha_S$ where k is a real number. As a result, the longitudinal to shear attenuation coefficient ratio which is given by $k\alpha_L/k\alpha_S$ remains constant for any k. Even though the ratio is a constant, the absolute attenuation suffered by shear waves when the attenuation is increased is actually getting larger relative to the longitudinal waves because the attenuation ratio (not the attenuation coefficient ratio which is simply the ratio of the attenuation coefficients) is given by $e^{k(\alpha_S-\alpha_L)}$. Therefore by increasing k, we increase the attenuation ratio and are essentially increasing the shear attenuation with respect to the longitudinal attenuation.

In all the cases that we will look at, the real part of the bulk velocities (longitudinal and shear) are kept the same. The values for the bulk longitudinal and bulk shear velocities and attenuation are taken as those of a HPPE plate and are shown in Fig.6.1. The thickness of the plate used was 12.7mm. The plate was formed by machining it from a section cut out of a large diameter pipe. It can be seen that the material is slightly anisotropic with the properties in the through thickness direction being different from the properties in the other two orthogonal directions. This is most likely to be the result of differential cooling between the inside and outside of the pipe after the pipe has been extruded. The largest difference is in the shear attenuation values

which differ by about 25%. At present, the Lamb wave model has not been implemented for *anisotropic*, attenuative materials. Therefore an assumption has to be made as to which properties will be used for the Lamb wave model. The bulk properties corresponding to the Lamb wave propagation direction in the experiments (i.e. 0-3) have been chosen.

6.3.1 Zero Attenuation Case

Fig.6.2a shows the phase velocity dispersion curves for the case of zero attenuation and Fig.6.3a shows the corresponding group velocity dispersion curves. The dispersion curves were predicted specifically for a 12.7mm plate so that they could be used later on for comparison with experiments. As a result, the horizontal axis is the frequency axis (rather than the more familiar frequency-thickness axis). The modes shown in bold correspond to those which are longitudinal through thickness modes at cut-off. From the phase velocity dispersion curves it can be seen that the first few non-zero order modes have fairly simple forms and that as the frequency increases their phase velocities tend towards the bulk shear velocity. As the mode order increases, modes start to appear that seem to travel towards the bulk longitudinal velocity but only do so temporarily before continuing down and heading towards the bulk shear velocity. The situation in this asymptotic region corresponds to the longitudinal partial wave becoming parallel to the plate and subsequently becoming inhomogeneous. Similar asymptotic behaviour has been observed by Uberall et al. (1994) and Mindlin (1960).

Uberall et al. (1994) found that the appearance of the longitudinal asymptotic regions became more pronounced as the bulk shear velocity was reduced while keeping the longitudinal bulk velocity fixed. It is noted that the physical character of the Lamb modes in these regions is similar to those observed in a fluid-plate (i.e. in a material which is unable to support shear motion (Redwood (1963)). This case is equivalent to the shear bulk velocity being set to zero in which case all modes tend towards the longitudinal bulk velocity with increasing frequency.

According to Uberall et al. (1994), the existence of longitudinal asymptotic regions tends to suggest that in the longitudinal bulk velocity region, the nature of the mode is essentially longitudinal whereas below the longitudinal bulk velocity region shear behaviour dominates and above the longitudinal bulk velocity the mode can be dominated by shear or longitudinal motion. This is demonstrated in Fig.6.4 where Fig.6.4b shows the dispersion curves for a shear cut-off mode and a longitudinal cut-

off mode. Figs.6.4a and 6.4c show the corresponding longitudinal to shear partial wave amplitude ratios for these modes. For the shear cut-off mode, the amplitude ratio is initially very small as expected. The amplitude ratio then rises when coupling with the partial longitudinal wave occurs. In the region near the bulk longitudinal velocity the amplitude ratio rises to a maximum indicating the longitudinal nature in this region. Below the longitudinal bulk velocity, the amplitude ratio is small, indicating the dominant shear nature of the mode at high frequency. For the longitudinal cut-off mode the amplitude ratio is initially high at cut-off but descends to a minimum. At this point the mode has now become shear dominant. As the frequency is increased the ratio then rises to a maximum in the longitudinal asymptotic region before dropping down as the mode tends towards the shear bulk velocity. Note that above the longitudinal bulk velocity, the longitudinal cut-off mode is not confined to being a longitudinal dominant mode, as can be seen by the clear minimum in the amplitude ratio.

From an academic point of view, it is interesting to note in Fig.6.2a that the longitudinal asymptotic behaviour becomes more pronounced as we increase the frequency. In addition, as the mode order increases, there is an increase in the number of plateauing regions for each mode. By joining these regions together, it is possible to visualize a new set of curves as shown in Fig.6.5. In this figure, each new curve is a single mode, either symmetric or antisymmetric in nature. These curves all start off at cut-off as longitudinal through-thickness modes and tend towards the longitudinal bulk velocity at high frequency. Different line thicknesses have been used to denote plateauing regions belonging to different mode types (symmetric and asymmetric). The case of Lamb modes which are longitudinal at cut-off and tend towards the longitudinal bulk velocity at high frequency are observed in a fluid-plate (Redwood (1960)) where the bulk shear wave cannot exist. As soon as shear waves can propagate, coupling with the longitudinal waves occurs. Uberall et al. (1994) suggest that the coupling between longitudinal and shear bulk waves creates a repulsion effect (mode repulsion) whereby neighbouring dispersion curves of the same type (symmetric or asymmetric) repel each other and therefore like modes never cross. Similar observations have been made by Mindlin (1960). A simple two-degree of freedom spring-mass model for describing the coupling behaviour when two Lamb modes approach each other on the dispersion curves has been given by Yapura and Kinra (1995), although this was not for a single layered plate but for a fluid-solid bilayer.

Turning our attention to the group velocity dispersion curves of Fig.6.3a, we can see that for any given mode, if the phase velocity is above the longitudinal bulk velocity, the group velocities fluctuate through a series of maxima and minima (this can also be deduced from the points of inflexion on the phase velocity curve) and that after this region, the group velocities settle down towards the shear bulk velocity.

6.3.2 Half Attenuation Case

Next, we look at the effect of including half the attenuation value for the HPPE. Figs.6.2b, 6.3b and 6.6a show the phase velocity, group velocity and attenuation dispersion curves respectively. From the phase velocity dispersion curves, there are localised regions in which the velocity seems to go through a sharp change. This change involves a sudden increase in velocity with frequency after which the velocity decreases with frequency as normal. These regions can be identified very easily on the group dispersion curves as they are the regions where the group velocity also undergoes a sharp change. This is simply because the group velocity is the derivative of the phase velocity (i.e. the gradient of the phase velocity versus frequency curve) and the gradient becomes steep very quickly in these regions. This results in very large group velocities which in reality have no physical meaning.

In the regions where the phase velocity undergoes abrupt changes, the tracing of modes was found to be very difficult and as a result, points on these modes had to be found by individual searches. The reason for this difficulty can be explained if we look at a plot of the imaginary part of the wavenumber versus the real part of the wavenumber for the s_4 mode shown in Fig.6.7a. Fig.6.7b shows such a plot for the s_4 mode. The curve tracing routine is based on incrementing (or decrementing) the real part of the wavenumber by a constant amount and then looking for minima in the characteristic equation by iteration of the imaginary part of the wavenumber. This works very well for situations where the gradient is low. One of the situations where it can break down is when the gradient becomes large. When this arises, the trace routine is essentially trying to locate a root vertically above it. In order to locate this root, a very small increment in the real part of the wavenumber is required. This can be very time consuming as it may take a long time to determine what the required increment is. Moreover, if the gradient is infinite, then a solution will never be possible because of the fact that the program assumes a step increase in the real part of the wavenumber. Therefore in order to look for solution points in these steep regions, explicit single point searches have to be made rather than the usual curve tracing. One possible way of improving the curve tracing routine would be to switch the iteration

from the imaginary part of the wavenumber to the real part of the wavenumber in these regions. This amendment was outside the scope and timescale of the project and was therefore not implemented.

Firstly we turn our attention to the phase velocity curve. The convention used for labelling the modes is the same as that used by Victorov (1970) for analysing Lamb modes in elastic plates. We can see that the picture is now somewhat different from that of the zero attenuation case. At the lower frequency end, the dispersion curves appear to be identical to the zero attenuation case with differences starting to occur as the frequency increases. Certain modes (s_4, a_6, s_7, a_8, s_9, a_{11}, s_{13}) now have dispersion curves which are asymptotic to the longitudinal bulk velocity and hence become non-existent below the longitudinal bulk velocity. Three out of the first four such modes stem from modes with shear cut-off (s_4, a_6, s_7); the rest are from longitudinal cut-off modes (a_8, s_9, a_{11}, s_{13}). The other modes asymptote as before to the shear bulk velocity and are either longitudinal or shear at cut-off. Therefore, four distinct group of curves can exist when attenuation is present: shear cut-off modes which are longitudinal asymptotic, longitudinal cut-off modes which are longitudinal asymptotic, longitudinal cut-off modes which are shear asymptotic and shear cut-off modes which are shear asymptotic.

If we now look at the attenuation dispersion curves (Fig.6.6a) (note that the attenuation is measured along the plate), we can see how lossy these groups of modes are. The shear cut-off modes start off at very high attenuation (infinite) at cut-off . This is when the shear partial wave is perpendicular to the direction of propagation and hence no propagation occurs. The modes then start to descend sharply as a result of shear and longitudinal wave propagation occurring at non-normal incidence and hence a Lamb wave can propagate along the plate. A minimum is very rapidly reached because of this sudden change of state (i.e. no propagation at cut-off to propagation immediately below cut-off). As the frequency increases, the bulk shear and longitudinal attenuations also increase (they are linearly frequency dependent) and the overall result is that the attenuation of the Lamb wave increases. For the majority of these modes shear motion is dominant at high frequency and hence the attenuation tends towards the shear bulk wave attenuation. However, for the three shear-cut off modes which are asymptotic to the longitudinal bulk velocity (s_4, a_6, s_7), the attenuation tends towards the longitudinal value. The longitudinal cut-off modes start in the same way. Once they reach a minimum, those with shear asymptotes (s_2, a_4, s_6) tend towards the shear attenuation whereas the rest tend towards the longitudinal attenuation.

The inclusion of attenuation has seemingly altered the longitudinal/shear coupling conditions in such a way that certain modes which were previously separate modes now appear to join up to form parts of dispersion curves analogous to those of a fluid-plate (by this we imply the longitudinal cut-off, longitudinal asymptotic nature of the modes). This occurs between modes of the same type (i.e. symmetric or antisymmetric) and as a result the newly formed mode is also of the same type. In addition, the apparent joining between adjacent like modes results in the two newly formed like modes crossing, a phenomenon not seen in the case of zero attenuation (Mindlin (1960)). This can be demonstrated using Figs.6.8 and 6.9 which show the displacement mode shapes in a region where two asymmetric modes exist , one for the case of zero attenuation and the other for the case of half attenuation. In the zero attenuation case of Fig.6.8, it can be seen that points R and U, which belong to the same mode, have fairly similar mode shapes. This is also true for points T and S which belong to a separate mode. Note that the two modes do not cross. If we now look at Fig.6.9, and once again examine the mode shapes within the same region, we see that points P and Q lie on a single mode, and that points M and N lie on another mode. However, points P and Q correspond closely in position to points R and S in Fig.6.8, these points belonging to separate modes. This can also be said about points M and N, and T and U. The curves of Fig.6.9 therefore appear to be formed from the zero attenuation curves joining whereas without attenuation they were unable to do so. When the modes join to form two new modes, these new modes cross each other, something which is not observed in the zero attenuation case. Therefore, by increasing the attenuation, modes of the same symmetry which were separate are now able to combine to form a single mode.

The joining up of curves only occurs after a certain frequency and it could be deduced from this that the phenomenon is due to the fact that the shear attenuation increases with frequency. The higher shear attenuation would mean that the bulk shear wave would be killed off very quickly and hence we would approach a situation where the coupling between shear and longitudinal waves is weak. Towards the lower frequency end, the bulk shear attenuation is relatively low and hence the situation can be considered to be similar to that when no attenuation is present. It should also be noted that we now have a situation where like modes can cross (e.g. s_9 with s_{11}, a_{11} with a_{13}), a phenomenon which was not observed in the elastic plate case.

We know that for the case of a fluid-plate, we only have modes which are longitudinal at cut-off and longitudinal asymptotic at high frequency. Therefore, we would expect that if the attenuation is high enough, then all longitudinal cut-off modes should

eventually become longitudinal asymptotic. For the present case we can see that three longitudinal cut-off modes have yet to become asymptotic to the longitudinal bulk velocity (s_2, a_4, s_6). If we look at the shear cut-off modes, we can see that there are the same number of modes (i.e. three) which are asymptotic to the longitudinal velocity (s_4, a_6, s_7) and it appears that it is these modes which will eventually join up with the longitudinal cut-off modes if we were to increase the attenuation further.

6.3.3 Full Attenuation Case

The case of full attenuation is now considered. Figs.6.2c, 6.3c and 6.6b show the phase velocity, group velocity and attenuation dispersion curves respectively. If we first look at the phase velocity curves, we see that the number of longitudinal asymptotic modes arising from longitudinal cut-off modes has increased by two (a_4 and s_6). Note that the number arising from shear cut-off has decreased by the same number. From an attenuation argument the fact that the number of longitudinal cut-off modes which have become longitudinal asymptotic has increased can be explained by the fact that the higher attenuation is now reducing the influence of shear motion in the longitudinal cut-off modes. It can also be deduced that as the attenuation increases even further, the first longitudinal cut-off mode will eventually become longitudinal asymptotic. When this is achieved, we have the situation where all longitudinal cut-off modes tend towards the longitudinal bulk velocity and all shear cut-off modes tend towards the bulk shear velocity. Even though the bulk shear attenuation would be high at this stage, the fact that it is not infinite means that shear waves do still exist. The result is that shear cut-off modes will still exist and some coupling between longitudinal and shear waves will still occur in all modes. This is the reason why we do not quite reach the situation of a true fluid-plate.

It is important to check if the longitudinal asymptotic modes do become those of a true fluid-plate as the attenuation tends to infinity. The phase velocity dispersion curves for a fluid-plate are shown in Fig.6.10 where the bulk longitudinal properties for the full attenuation case have been used. The mode shapes of a longitudinal asymptotic mode, whose phase velocity dispersion curve is shown in Fig.6.11 for the case of full attenuation, were examined. The mode was inspected at 700kHz. The displacement mode shapes for this mode are shown in Figs.6.12a-h. The first figure shows the mode shape when we have full attenuation. Subsequent figures correspond to keeping the longitudinal attenuation the same and doubling the shear attenuation each time. Fig.6.12i shows the corresponding mode in the fluid-plate case where the bulk longitudinal properties for the full attenuation case have been used. It should be

noted that as the shear attenuation was increased, the phase velocity dispersion curve for the mode we are looking at did not change significantly. By keeping the longitudinal bulk attenuation fixed, we can see the effect of shear attenuation alone on the mode shapes.

The normal displacement mode shape changes very little as we increase the shear attenuation up to 128 times the full amount of shear attenuation, the major change being in the in-plane displacement mode shape. The amplitude with respect to the normal displacement is initially small and increases with attenuation. In Fig.6.12h, where the shear attenuation has been increased to 128 times the full amount, we can see that the mode shape is now very close to that of the corresponding fluid-plate mode of Fig.6.12i, the only noticeable difference being the in-plane displacement at the surface of the plate which is zero for the fluid plate case and is finite for the solid case. We would expect that in the limit as the shear attenuation tends to infinity, the mode shapes of the two modes would match exactly. In addition, all shear asymptotic modes would no longer exist. Hence the modes in the now highly shear attenuative plate become those of a fluid-plate.

6.3.4 Four Times Attenuation Case

Fig.6.2d shows the phase velocity dispersion curve when the attenuation has been increased to four times the full value for HPPE. Note that the shear cut-off modes are incomplete at high phase velocity. This is because the attenuation now is so high at these velocities that a solution could not be found. We can see from the longitudinal cut-off modes that the extra attenuation has now resulted in all of these modes becoming asymptotic to the longitudinal bulk velocity, as we had predicted. No shear cut-off, longitudinal asymptotic modes remain.

6.4 Experimental Verification of Dispersion Curve Predictions

In this section we describe the results of experiments conducted in order to verify the predicted dispersion curves. Given the abundance of modes found on the curves, it is convenient to select modes which can be measured fairly easily, yet reveal details that can be verified easily by examining the dispersion curves. The parameters which can be measured most easily are the group velocity and attenuation, provided we can obtain modes which are not too dispersive.

We have opted to look at two regions on the dispersion curves. The first mode to be verified is the symmetric s_2 mode, whose dispersion curves are those indicated by the thicker lines in Figs.6.13a, 6.13b and 6.13c. This mode is somewhat unique in that it starts off at low frequency as a longitudinal cut-off mode but does not tend towards the longitudinal bulk velocity, unlike all the other longitudinal cut-off modes. If we look at the attenuation dispersion curve (Fig.6.13c) we see that the result of this is that it starts off at high attenuation, drops steeply to a minimum where the mode is dominated by the longitudinal partial wave, but subsequently, instead of remaining at a low attenuation value with increasing frequency (characteristic of the longitudinal asymptotic modes), it rises and joins up with the shear asymptotic group of curves. The minimum in attenuation corresponds closely to the point of maximum group velocity. Moreover, the group velocity is significantly higher than that of the other modes found at the same frequency. Note also that dispersion is minimised by exciting the mode at its point of maximum group velocity. If we now look at the displacement mode shapes of this mode at its maximum group velocity, shown in Fig.6.13d, we can see that from an excitation point of view, such a mode should be well excited using water coupled probes in which the excitation is due to surface perturbations normal to the surface of the plate because there is significant normal motion at the surface of the plate. It should therefore be relatively easy to excite and detect this mode at its group velocity maximum.

Fig.6.14 shows a schematic diagram of the equipment used to excite and detect the s_2 mode. Two angled polyethylene tubular holders were used for holding the transducers. The holders were then sealed onto the HPPE plate and filled with water so that coupling between the transducers and the plate could be achieved.

In order to excite a given mode the angle of incidence of the transducers (and hence the holders) have to be set correctly. Using the coincidence principle, this angle was found to be 30 degrees. The transducers used were 25mm diameter, 0.5MHz centre frequency plane transducers. The HPPE plate was 12.7mm thick and a frequency of 137kHz corresponding the the frequency of the maximum group velocity was used. Although this is a low frequency in comparison with the centre frequency of the transducers used, it was found that the transducers could be used in the frequency range required. Given that the transducer has a finite diameter some degree of beam spreading will take place, especially at low frequencies. The spread angle θ based on 6dB down points for the main lobe in the angular spectrum can be worked out from the formula for a piston source, (Kinsler and Frey (1982))

$$\theta = \sin^{-1}\left(\frac{0.54\lambda}{a}\right) \qquad (6.11)$$

where λ is the wavelength in the coupling medium and a is the transducer radius.

For the frequency we wish to operate at, the angular spread is computed to be ±28°. In order to provide a controlled excitation signal to the plate an arbitrary function generator was used. The input was a 20 cycle tone burst in a Gaussian window and is shown in Fig.6.15a, together with the corresponding frequency spectrum in Fig.6.15b. The aim of using a large number of cycles is to make the excitation bandwidth as small as possible so that dispersion could be minimised. In addition, the smaller the bandwidth, the less chance there is of exciting neighbouring modes on the dispersion curves. The bandwidth (based on 20dB down points) was found to be ±15kHz. The combined effect of the beam spreading and frequency bandwidth of the input signal is to create an excitation zone on the dispersion curves and is shown in Fig.6.13a. Using this information, we can obtain a good idea as to which modes are likely to be excited with the experimental set-up. The excitation zone indicates that a neighbouring shear cut-off and a neighbouring longitudinal cut-off mode could be excited. A close inspection of these modes reveals that they are considerably more attenuative and also slower in group velocity. Therefore, even if these modes are excited, their presence will not interfere with the measurements because their amplitudes will die away very quickly with propagation distance leaving the s_2 mode.

The measurement sequence consisted of capturing the received signal for different separation distances between the transmitter and receiver, the transmitter position being fixed. The group velocity was then calculated by measuring the time of flight between two successive positions of the receiver and noting their separation distance (a schematic of this is shown in Fig.6.16). The time of flight measurement was made by timing the positions of the maximum amplitude of each received signal. Other more elaborate methods such as the amplitude spectrum method (Pialucha, Guyott et al. (1989)) or phase spectrum method (Sachse and Pao (1978)) can be used to measure the phase velocity but given that the mode is assumed to be non-dispersive, the phase and group velocities will be the same and hence the current method should work just as well and is much quicker to use. The attenuation α was calculated by measuring the amplitudes of the received signal at two successive measurement points and then using these amplitudes in the following formula:

$$\alpha = \frac{1}{t}\ln\left(\frac{A_1}{A_2}\right) \qquad (6.12)$$

where t is the receiver separation distance, and A_1 & A_2 are the amplitudes of the received signals.

Figs.6.17a and 6.17b show the time domain responses of the received signal at two different positions, the latter figure corresponding to the receiver being further away from the transmitter. The separation distance between two receiver positions was 90mm. At the nearer receiver position it appears that only one mode exists. If we compare the pulse shape of this signal to that of the input we can see that they are very similar. At the further receiver position, there still only appears to be one mode and the width of the pulse is very similar to that of the nearer receiver position. Hence our assumption of this particular mode being non-dispersive appears to be justified. Table 6.1 shows the measured and predicted group velocities and attenuations. The experimental results are shown in the right hand column and the predicted results are shown in the left hand column. The results show that the correlation is particularly good for the group velocity with the difference being less than 1%. For the attenuation, the difference is bigger (17%); however this value is still reasonable given the difficulties of measuring attenuation.

	Predicted	Measured	Pencentage Difference
Group velocity (m/s)	1370	1364	0.4
Attenuation (Np/mm)	0.0105	0.0090	17

Table 6.1 Comparison of predicted and measured group velocities and attenuations for the s_2 mode.

The second verification is at a higher frequency. Trying to excite a single mode at higher frequencies is more difficult because many low attenuation modes may exist. Moreover, these modes may be grouped fairly closely together in both the phase velocity and group velocity dispersion curves. From a practical point of view, it would be relatively easy for several modes to be excited due to the angular spread of the transducers and the finite frequency bandwidth of the excitation signal.

The point targeted on the dispersion curves is the a_4 mode at a frequency of 300kHz and a phase velocity of 3000m/s. The phase velocity, group velocity and attenuation

dispersion curves are shown in Figs.6.18a, 6.18b and 6.18c respectively. Using the same phase velocity as in the s_2 case meant that the same transducer set-up could be used. A 20 cycle tone burst in a Hanning window was used and is shown in Fig.6.19a with the corresponding spectrum shown in Fig.6.19b. The 20dB frequency bandwidth was measured to be ±25kHz. The 20dB angular spread was computed to be ±12.5°. From the excitation zone in the phase velocity dispersion curves, we would expect to predominantly excite two modes, s_3 and a_4; several other modes may also be excited. Figs.6.18d and 6.18e show the displacement mode shapes of the two modes. The normal displacement components of the two modes are not as large as for the s_2 mode but nevertheless are still significant and hence water coupled transducers should once again be adequate for excitation.

Figs.6.20a and 6.20b show the time domain responses of the received signal at two receiver positions, the latter corresponding to the further receiver position. The separation between the two receiver positions was 56mm. From Fig.6.20a, it appears as if there are two modes which are overlapping in the time domain. By looking at Fig.6.20b, it can be seen that there are two modes and that they have separated out in time implying that they have different group velocities. The group velocities and attenuations of the two modes have been measured in the same way as before and the results are shown in Table 6.2. If we compare the experimental results on the assumption that we have excited the s_3 and a_4 modes with the predicted results for the s_3 and a_4 modes, we can see that the correlation between experiment and theory is fairly good and therefore we have been able to verify the existence of these two modes. The correlation for the a_4 mode is not as good as that for the s_3 mode. This is most probably due to the fact that the a_4 mode has not been adequately resolved from the much larger s_3 mode and therefore the position of the peak in Fig.6.21a used for the time of flight measurement may not be the true peak. In this particular example, we were fortunate that the difference in group velocities was fairly large and hence we were able to resolve the two modes. By referring to Fig.6.18b, it can be seen that as the frequency is further increased, the difference in group velocities for the low attenuation modes becomes smaller and therefore mode resolution becomes much more of a problem. Mode resolution is still possible in these cases but is at the expense of longer propagation distances and hence smaller signal amplitudes.

	GROUP VELOCITY (m/s)			ATTENUATION (Np/mm)		
	Predicted	Measured	% Diff.	Predicted	Measured	% Diff
s_3 mode	2101	2121	1	0.010	0.013	23
a_4 mode	1594	1365	17	0.023	0.020	15

Table 6.2 Comparison of predicted and measured group velocities and attenuations for modes s_3 and a_4

6.5 Practical Considerations

We have seen from the dispersion curves that for the case of the HPPE, there are modes which have relatively low attenuation. From a practical point of view, it is these modes which will be of interest in nondestructive evaluation (NDE) because of their potential for propagating over significant distances. These modes fall into three groups. The first group consists of modes which start off as longitudinal at cut-off and end up as a shear dominated mode at high frequency (e.g. the s_2 mode). Depending on the attenuation of the material, several of these modes could exist. In our particular case, only one such mode exists. In the general case where several such modes can exist, the most useful of these is the first longitudinal cut-off mode as this mode lies in a region where neighbouring modes are always considerably more attenuative. From an NDE viewpoint this situation is ideal because we will effectively get a single mode to propagate. The major drawback of this mode is that it occurs at a low frequency and therefore the spatial width of the pulse is likely to be large.

The second group consist of modes which are shear at cut-off and are longitudinal asymptotic (e.g. the s_3 mode). For these modes it can be difficult exciting a single mode by virtue of the fact that adjacent low attenuation modes are likely to be excited. From an NDE point of view, such a situation has to be avoided because signal identification could be difficult when several modes are present. This can be overcome to a certain degree by making sure that the input signal is narrow band and that the beam spreading is as small as possible (i.e. a large transducer).

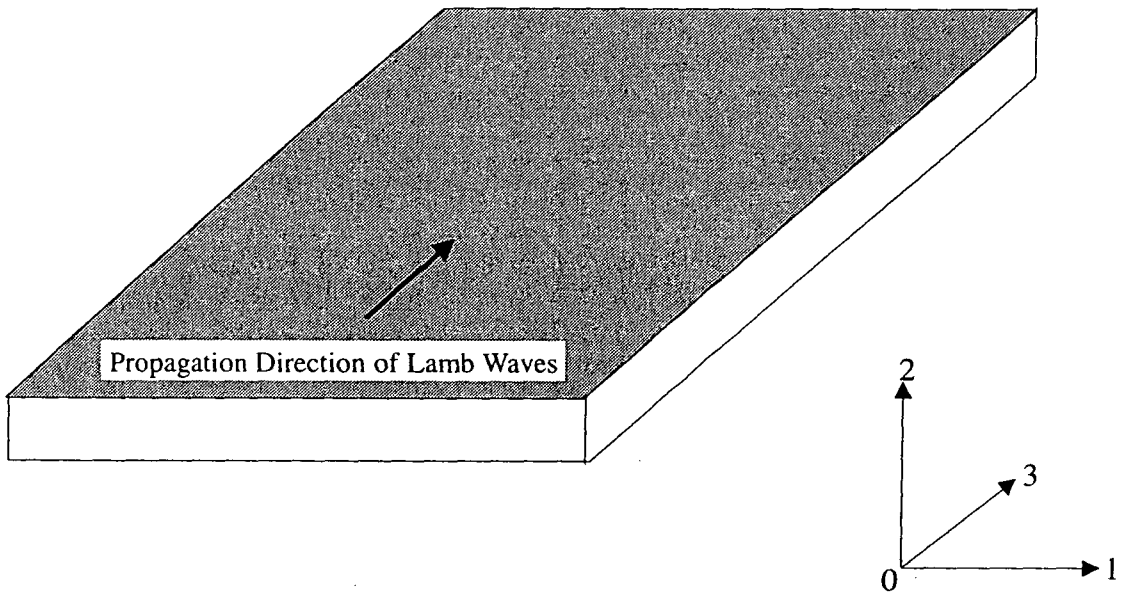
The third group consists of modes which are longitudinal at cut-off and are longitudinal asymptotic (e.g. the a_4 mode). Here, the situation is very similar to that of the previous group. As the frequency is increased the aim of exciting a single mode becomes significantly more difficult.

6.6 Conclusions

In this chapter we have looked at the effects on the dispersion curves of introducing attenuation in a material. When attenuation is not present, the coupling between longitudinal and shear adjacent modes of the same type (symmetric and asymmetric) causes adjacent like modes to deviate from each other. The result is that like modes do not cross each other. Coupling causes the dispersion curves to deviate from those for a fluid-plate where only the longitudinal wave exists. When attenuation is introduced, modes at the higher frequency end start to join up to form curves analogous to those for a fluid plate. This is most probably the result of the coupling conditions approaching those of a fluid-plate due to the fact that if the frequency is high enough, the shear waves are very strongly attenuated. The effect of the large shear attenuation is that certain modes become longitudinal asymptotic. These modes are unique because their attenuation is much lower than the other modes.

The dispersion curves have been experimentally verified using water coupled plane transducers. Two areas on the dispersion curves were selected for verification. These areas contained low attenuation modes; one area had a mode which is longitudinal at cut-off and shear asymptotic (s_2 mode); the other had two modes, one which was longitudinal at cut-off and longitudinal asymptotic and the other which was shear at cut-off and longitudinal asymptotic. Correlation between measurements and predictions (group velocity and attenuation) was found to be good for both cases.

The practical implications of the dispersion curves have been discussed. Of all the low attenuation modes available, the most promising is the s_2 mode as it has the lowest attenuation and is situated in a region on the dispersion curves where other modes are slower and have considerably higher attenuation.



	LONGITUDINAL BULK WAVE		SHEAR BULK WAVE	
DIRECTION	velocity m/s	attenuation Np/wl	velocity m/s	attenuation Np/wl
0-1	2344±2%	0.055±5%	953±5%	0.286±10%
0-2	2480±2%	0.058±5%	1024±5%	0.215±10%
0-3	2344±2%	0.055±5%	953±5%	0.286±10%

Fig.6.1 Bulk wave properties for HPPE plate used in Lamb wave studies

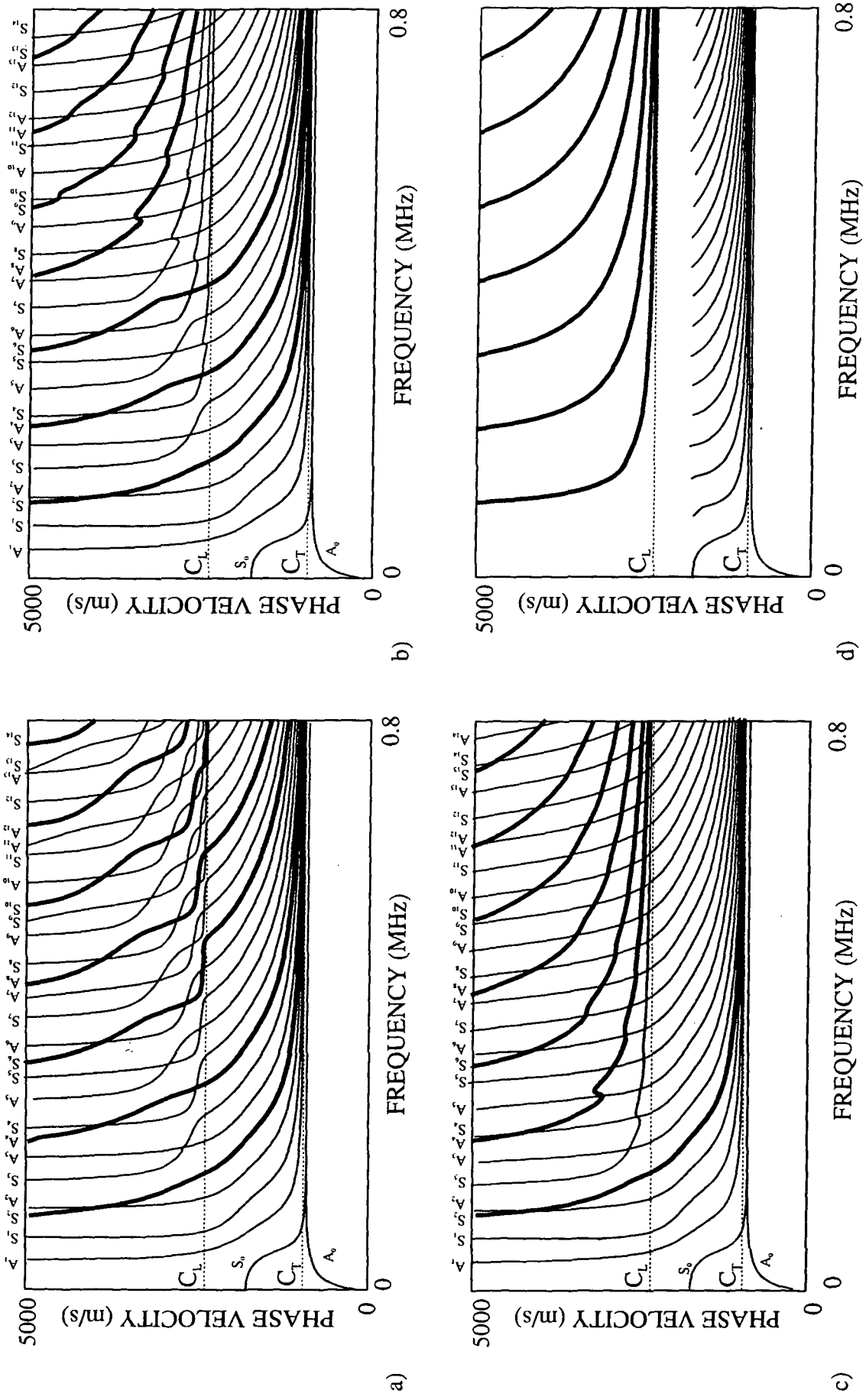


Fig.6.2 Phase velocity dispersion curves for different levels of attenuation. a) zero attenuation, b) half attenuation; c) full attenuation; d) four times attenuation; longitudinal cut-off modes shown in bold

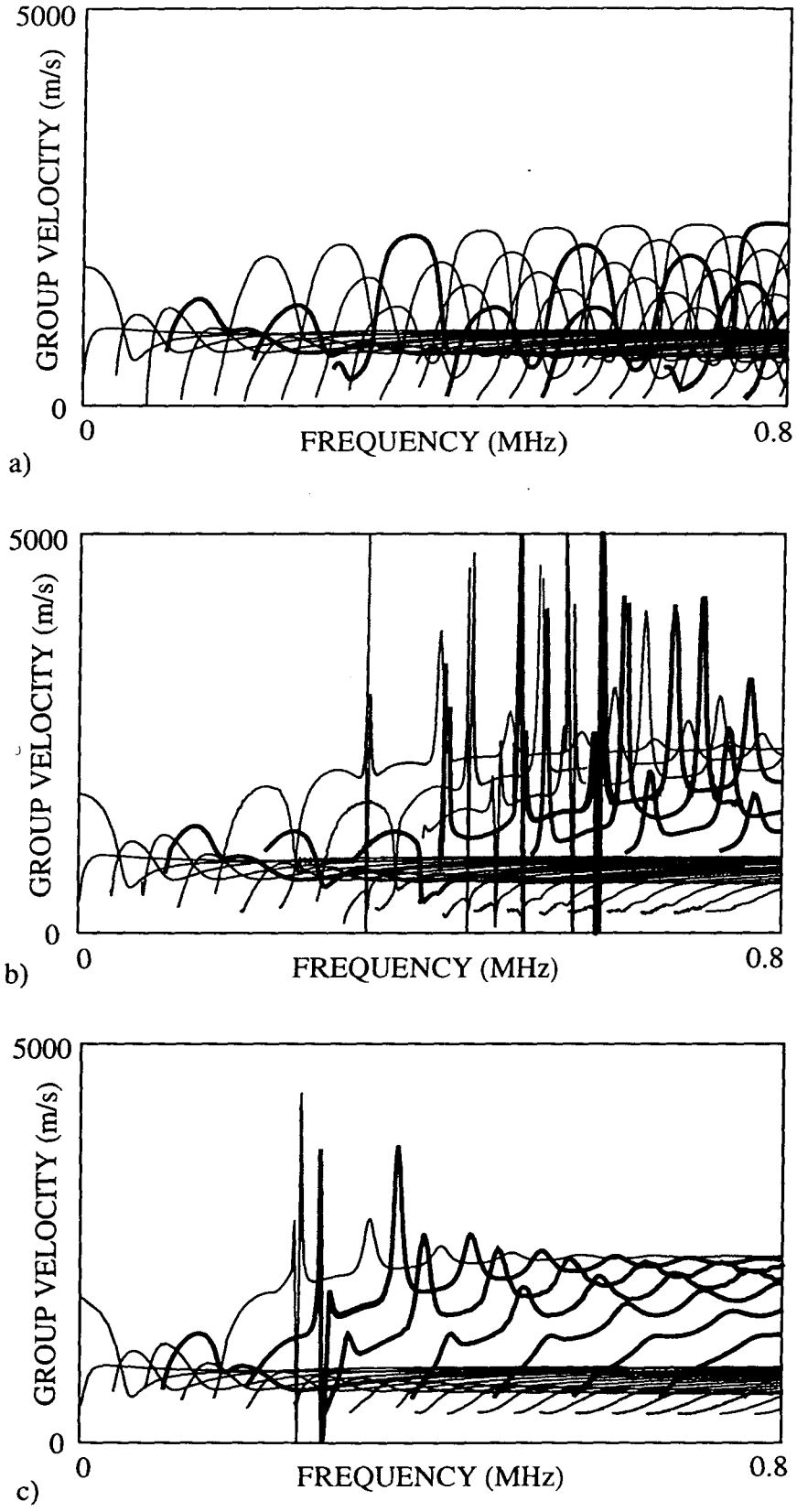
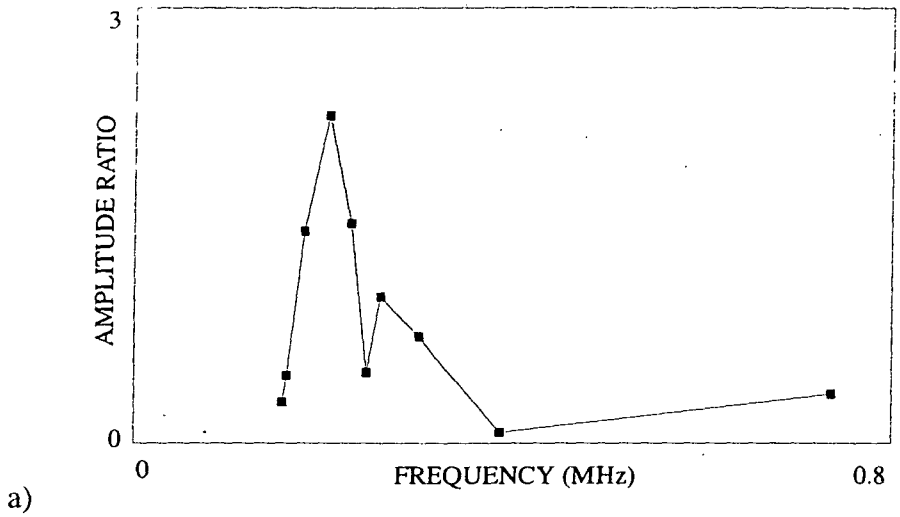
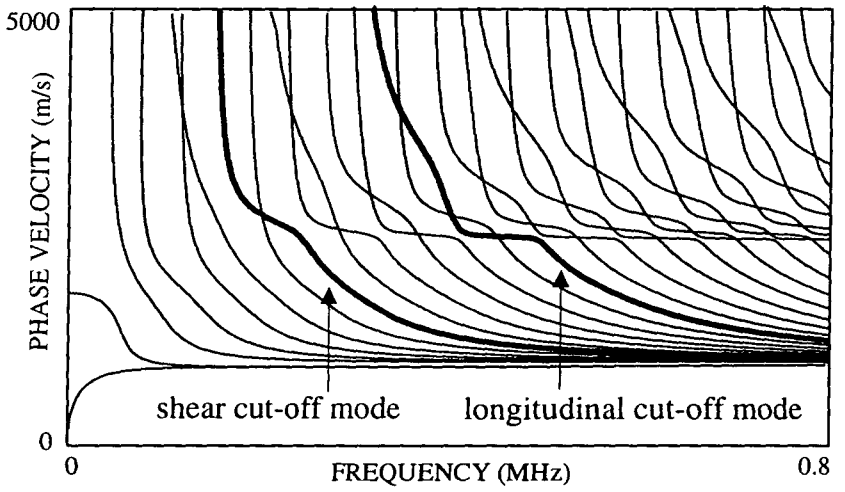


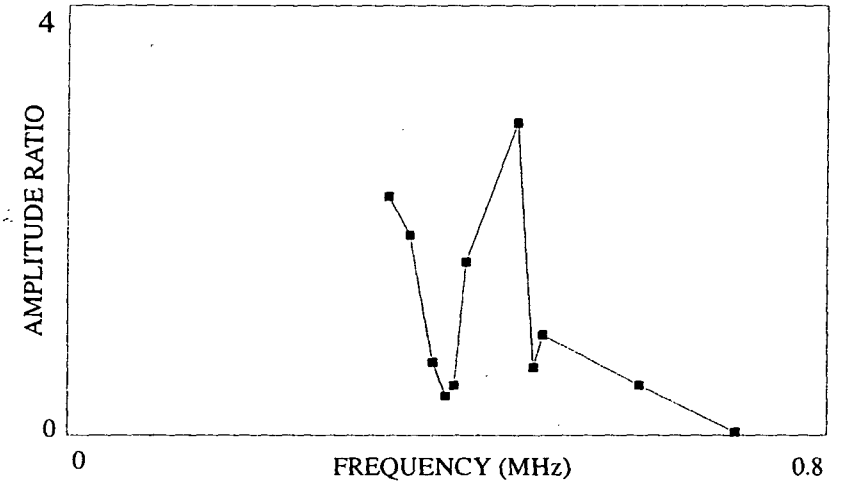
Fig.6.3 Group velocity dispersion curves for different levels of attenuation. a) zero attenuation; b) half attenuation; c) full attenuation; longitudinal cut-off modes shown in bold



a)



b)



c)

Fig.6.4 Investigation of partial wave amplitude ratio for longitudinal and shear cut-off modes. a) Partial wave amplitude ratio (longitudinal/shear) versus frequency for shear cut-off mode indicated in (b); b) Phase velocity dispersion curves indicating longitudinal and shear cut-off modes chosen for partial wave study c) Partial wave amplitude ratio (longitudinal/shear) versus frequency for longitudinal cut-off mode indicated in (b)

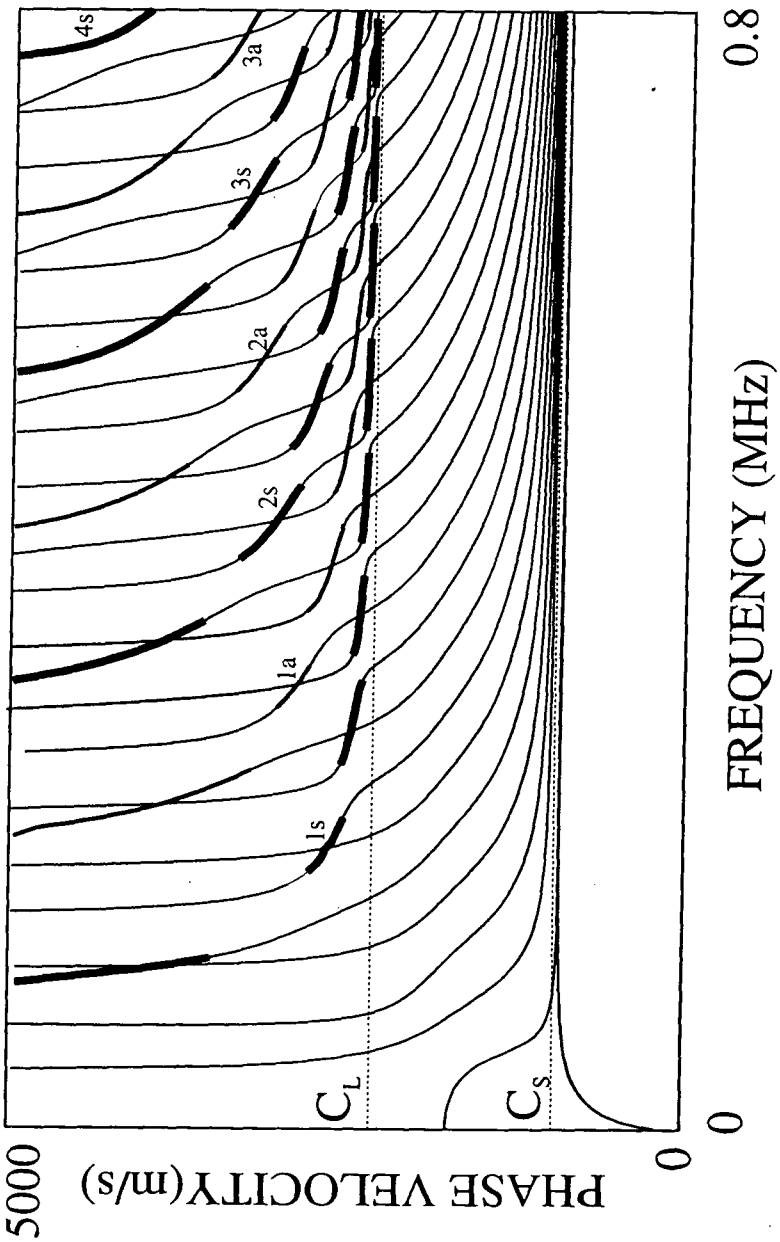
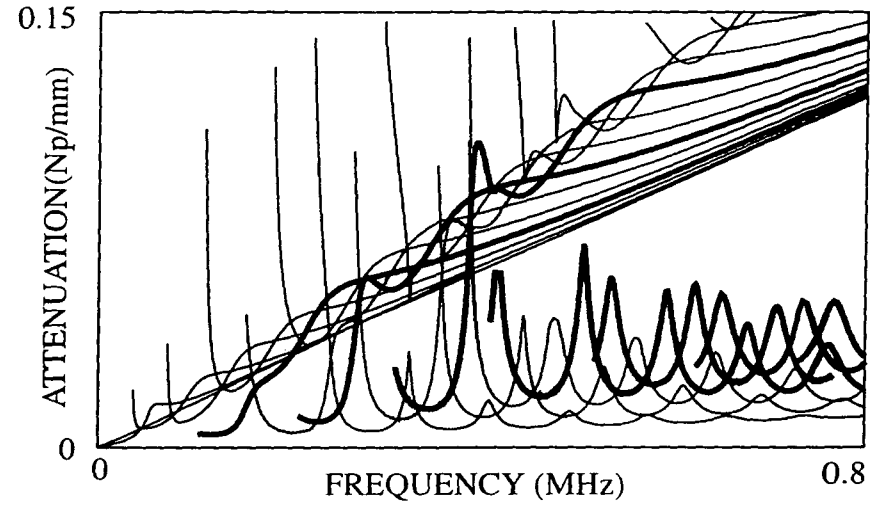
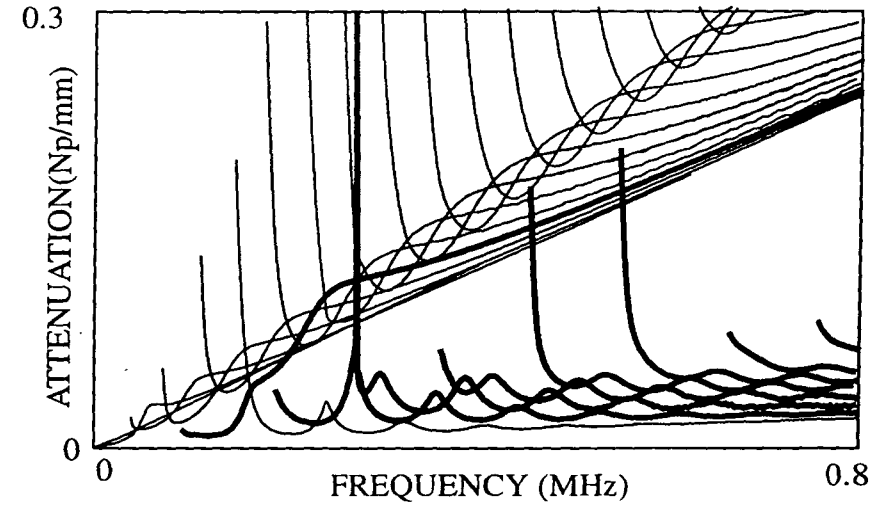


Fig.6.5 Phase velocity dispersion curves highlighting the plateauing regions. Symmetric modes(s) in heavy bold; asymmetric modes(a) in light bold

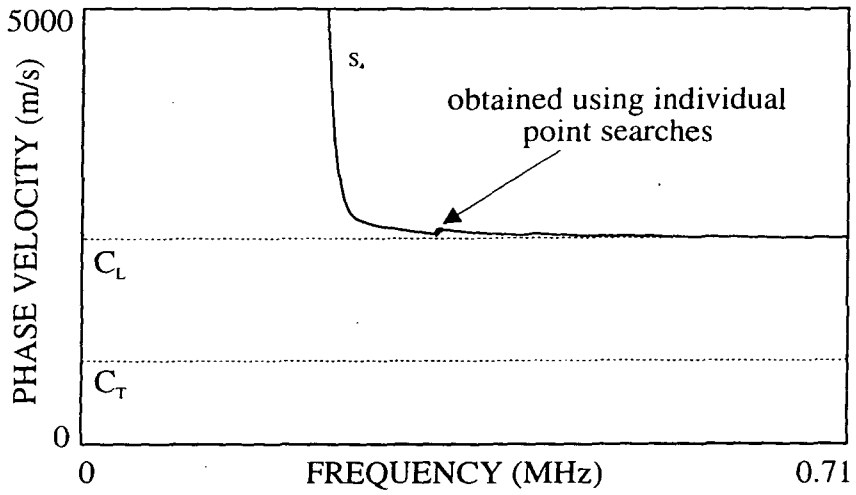


a)

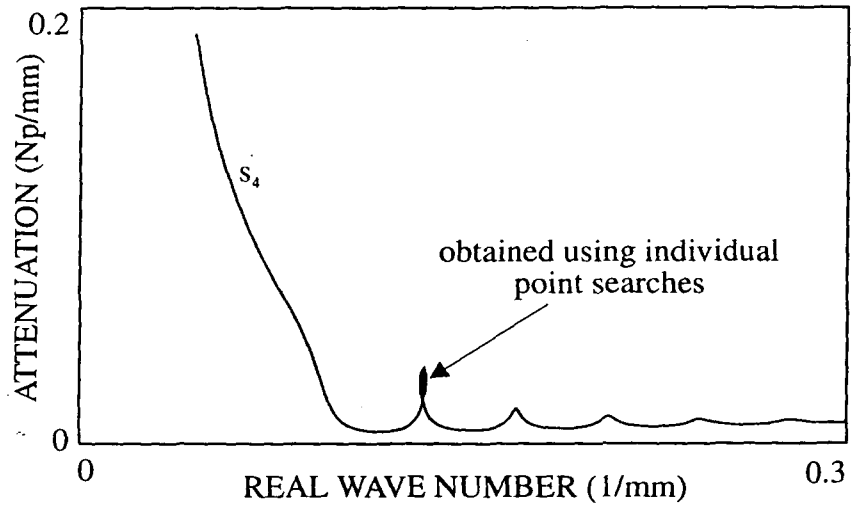


b)

Fig.6.6 Attenuation dispersion curves a) for the case of half attenuation; b) for the case of full attenuation; longitudinal cut-off modes shown in heavy black



a)



b)

Fig.6.7 Dispersion curve tracing in region of abrupt phase velocity change. a) Phase velocity dispersion curve of s_4 mode for half attenuation; b) Plot of imaginary part of wavenumber vs. real part of wavenumber for half attenuation

——————— Obtained using curve tracing

——————— Obtained using individual point search

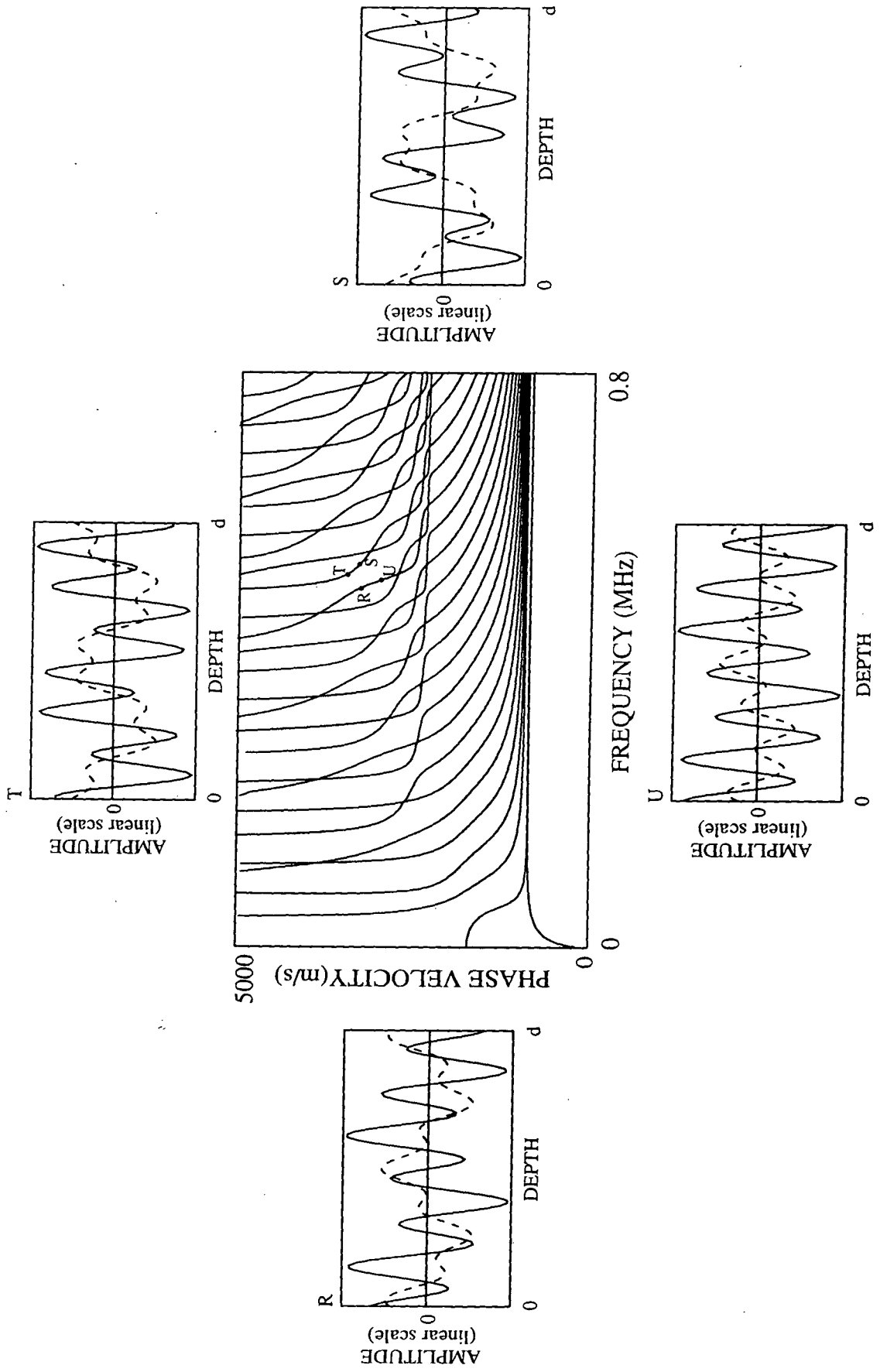


Fig.6.8 Inspection of mode shapes near joining points of two asymmetric modes for zero attenuation case.
Displacement mode shapes: ——— in-plane ---------- normal

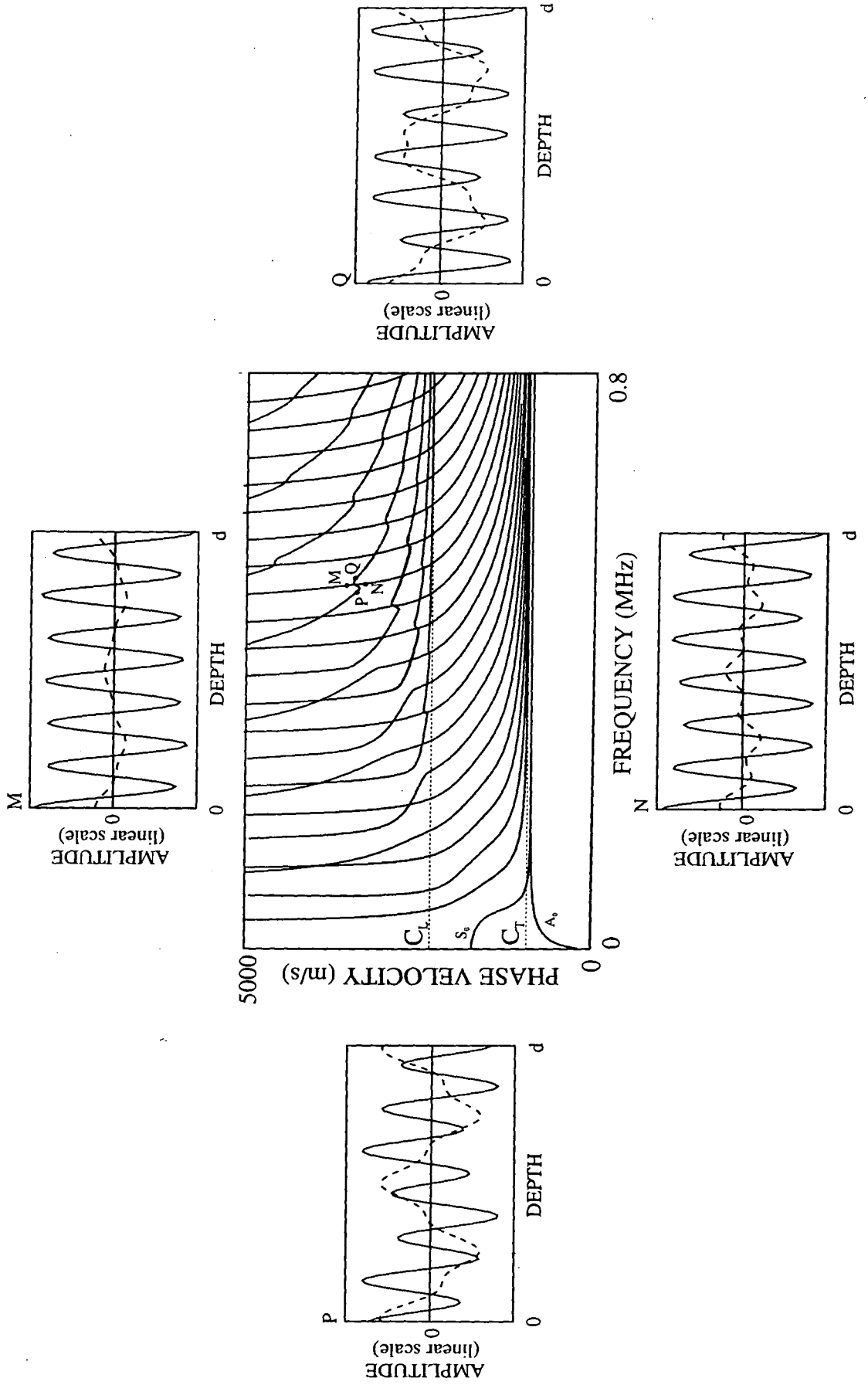


Fig.6.9 Inspection of mode shapes near joining point of two asymmetric modes for the case of half attenuation.
Displacement mode shapes: ——— in-plane ---------- normal

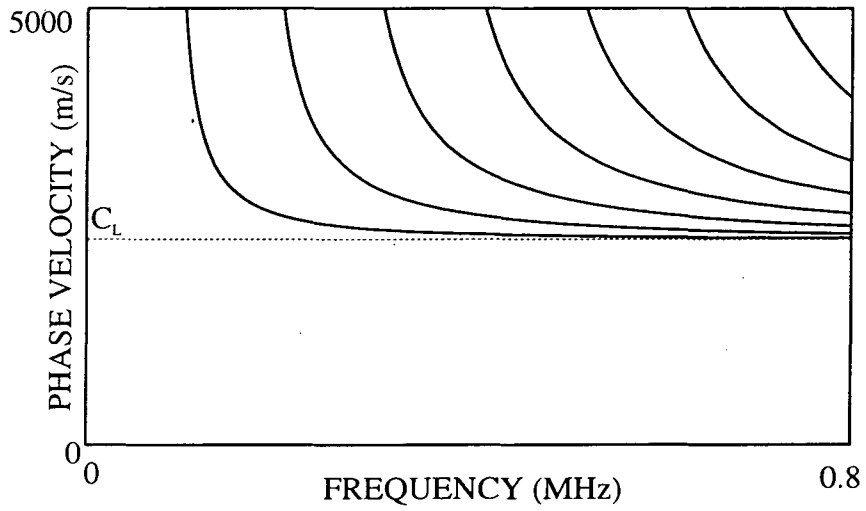


Fig.6.10 Phase velocity dispersion curves for a HPPE fluid-plate

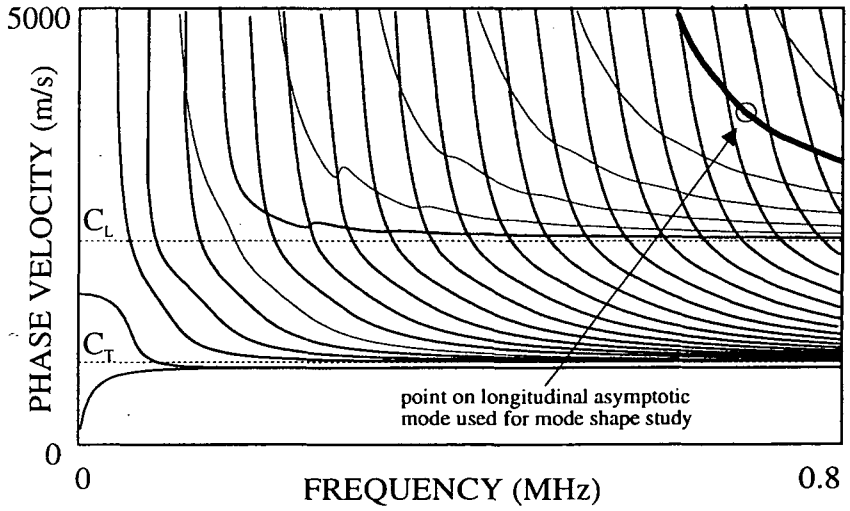


Fig.6.11 Phase velocity dispersion curves showing point chosen for mode shape study

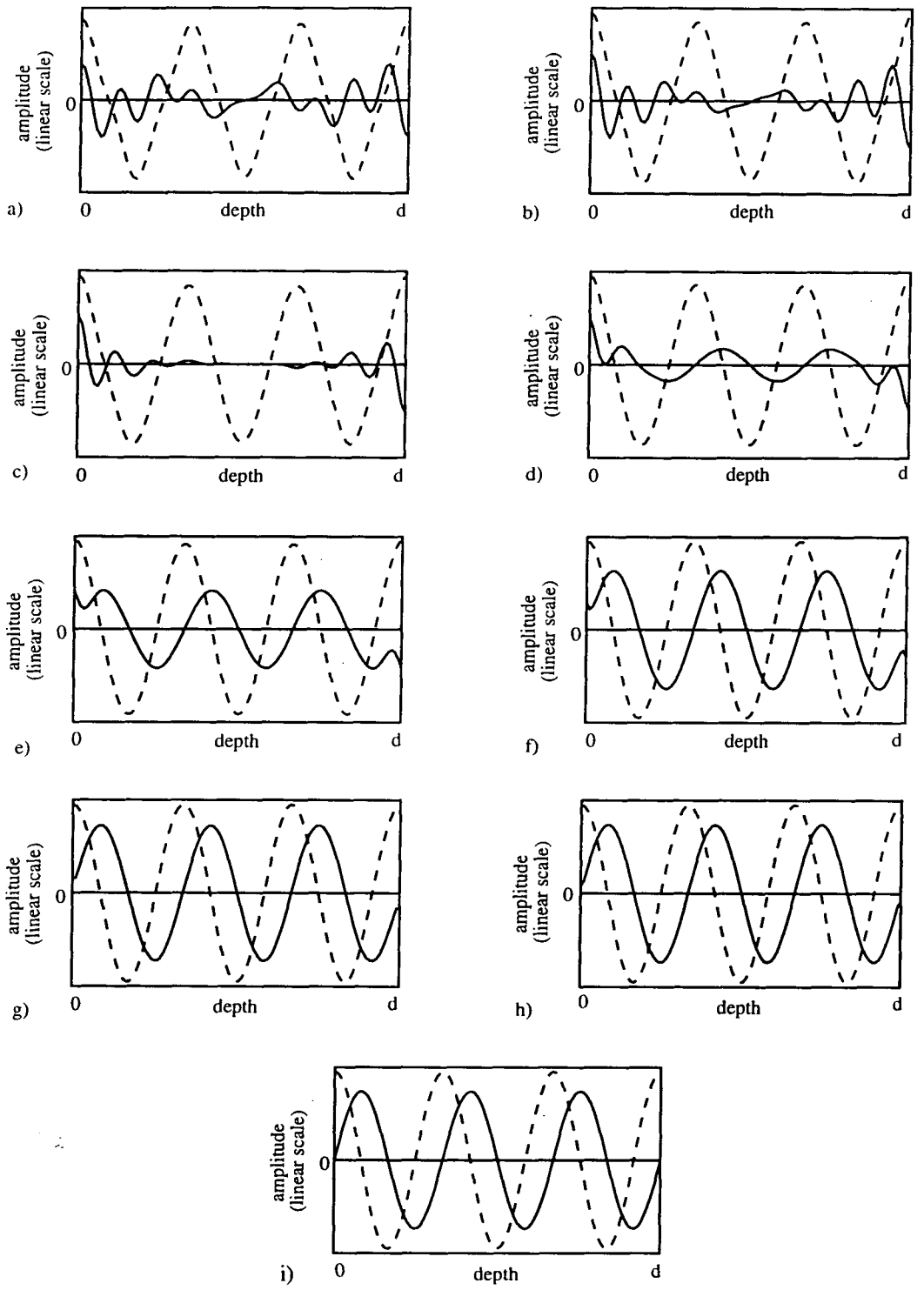
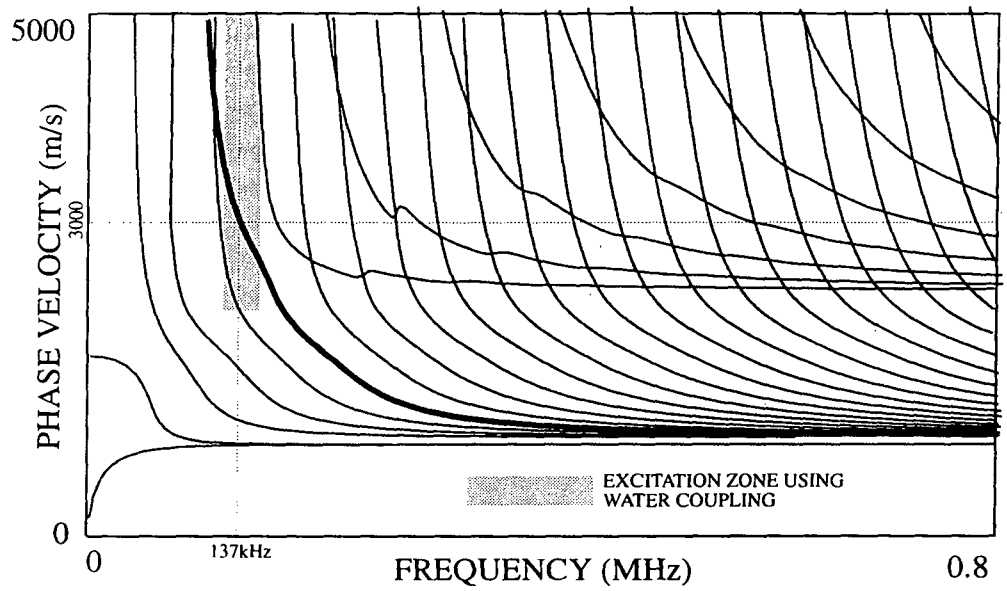
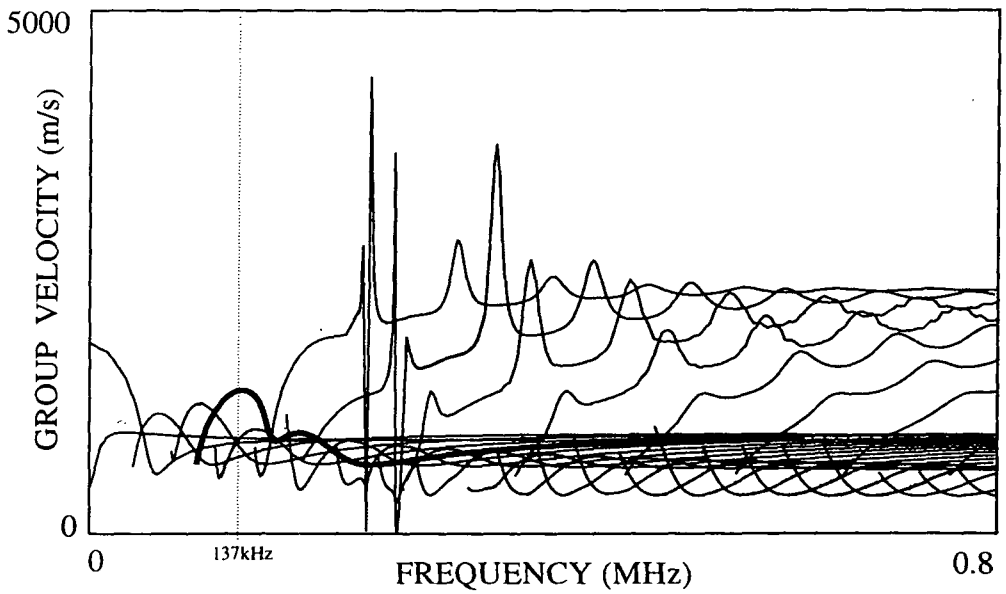


Fig.6.12 Displacement mode shapes of longitudinal asymptotic mode indicated in Fig.6.11 for different attenuation values. a) full att. (long=0.057Np/wl, shear=0.286Np/wl); b) shear att.=2xfull shear att.; c) shear att.=4xfull shear att.; d) shear att.=8xfull shear att.; e) shear att.=16xfull shear att.; f) shear att.=32xfull shear att.; g) shear att.=64xfull shear att.; h) shear att.=128xfull shear att.; i) no shear waves (i.e. fluid plate case)

———— in-plane displacement ---------- normal displacement

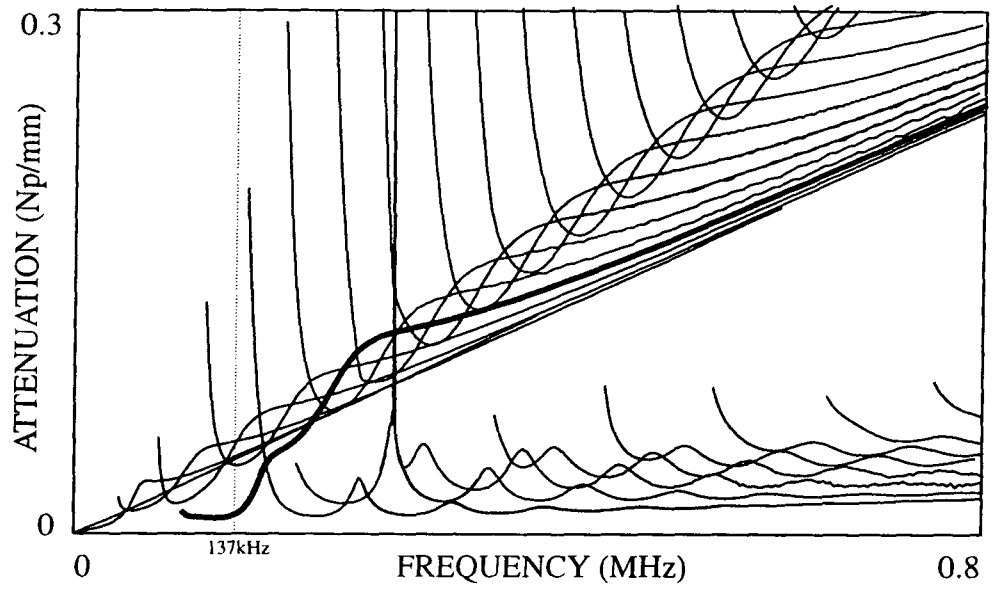


a)

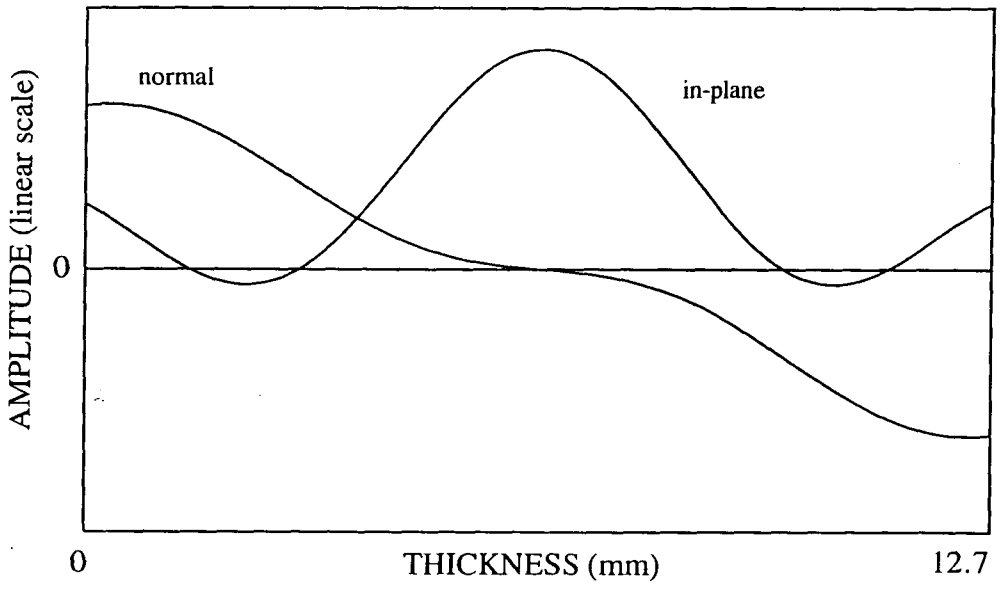


b)

Fig.6.13 Dispersion curves and mode shapes for s_2 mode. a) Phase velocity dispersion curves showing s_2 mode and excitation zone used in experimental phase; b) Group velocity dispersion curves showing s_2 mode used in experimental phase



c)



d)

Fig.6.13 Dispersion curves and mode shapes for s_2 mode. c) Attenuation dispersion curve for s_2 mode d) Displacement mode shapes at point of interest (f=137kHz, C_{ph}=3000m/s)

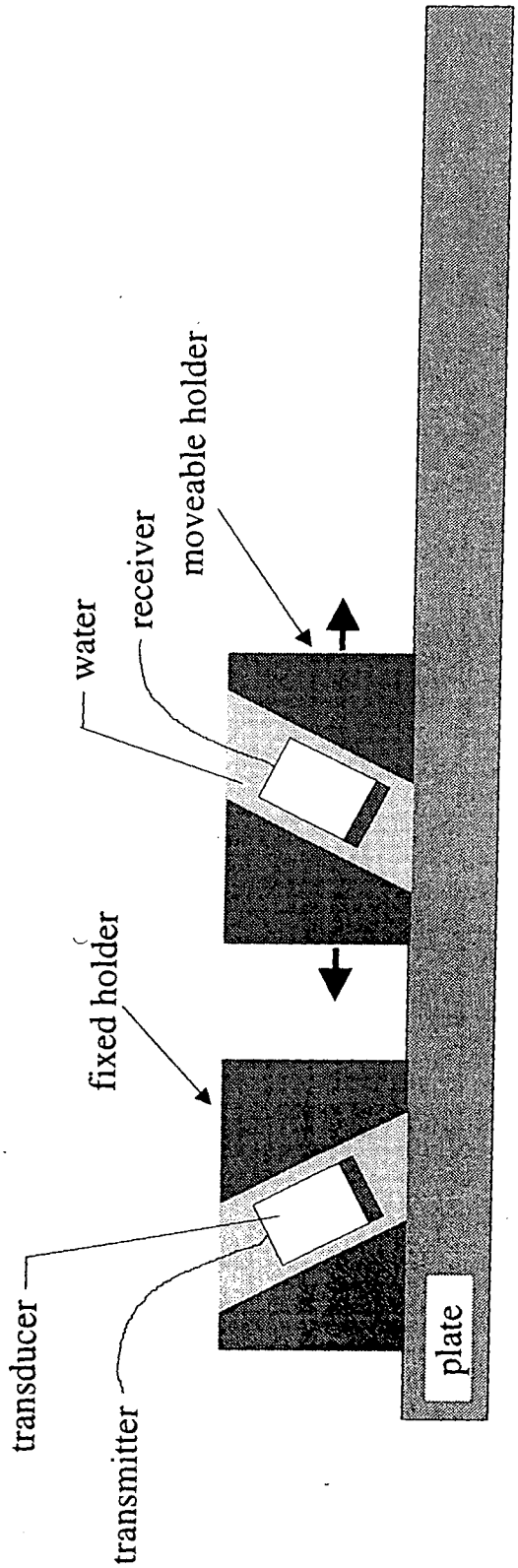


Fig.6.14 Schematic diagram of set-up used for Lamb wave measurements

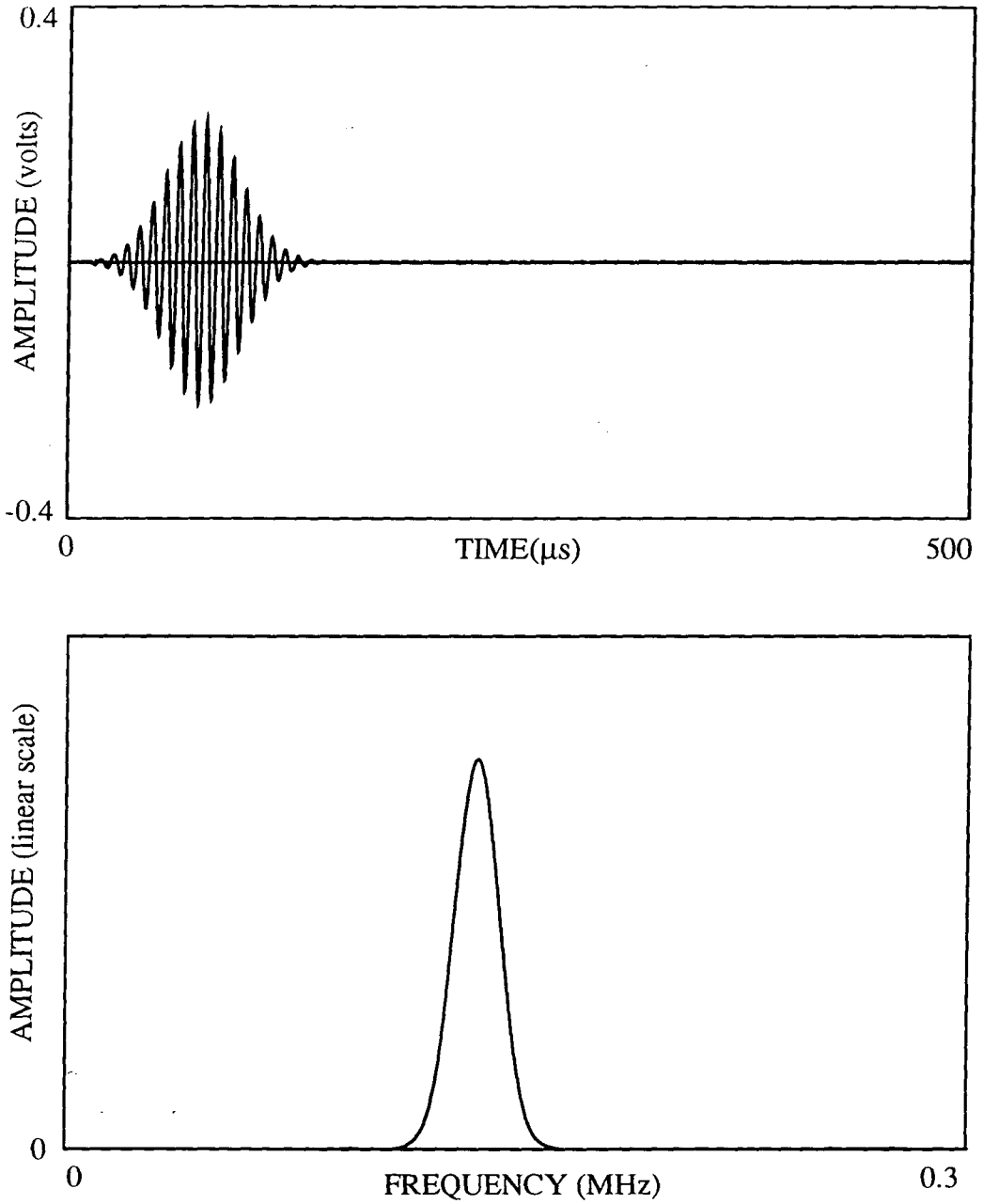


Fig.6.15 Details of input signal for excition of s_2 mode. a) Time history of 137kHz, 20 cycle tone burst input signal; b) Frequency spectrum of above signal

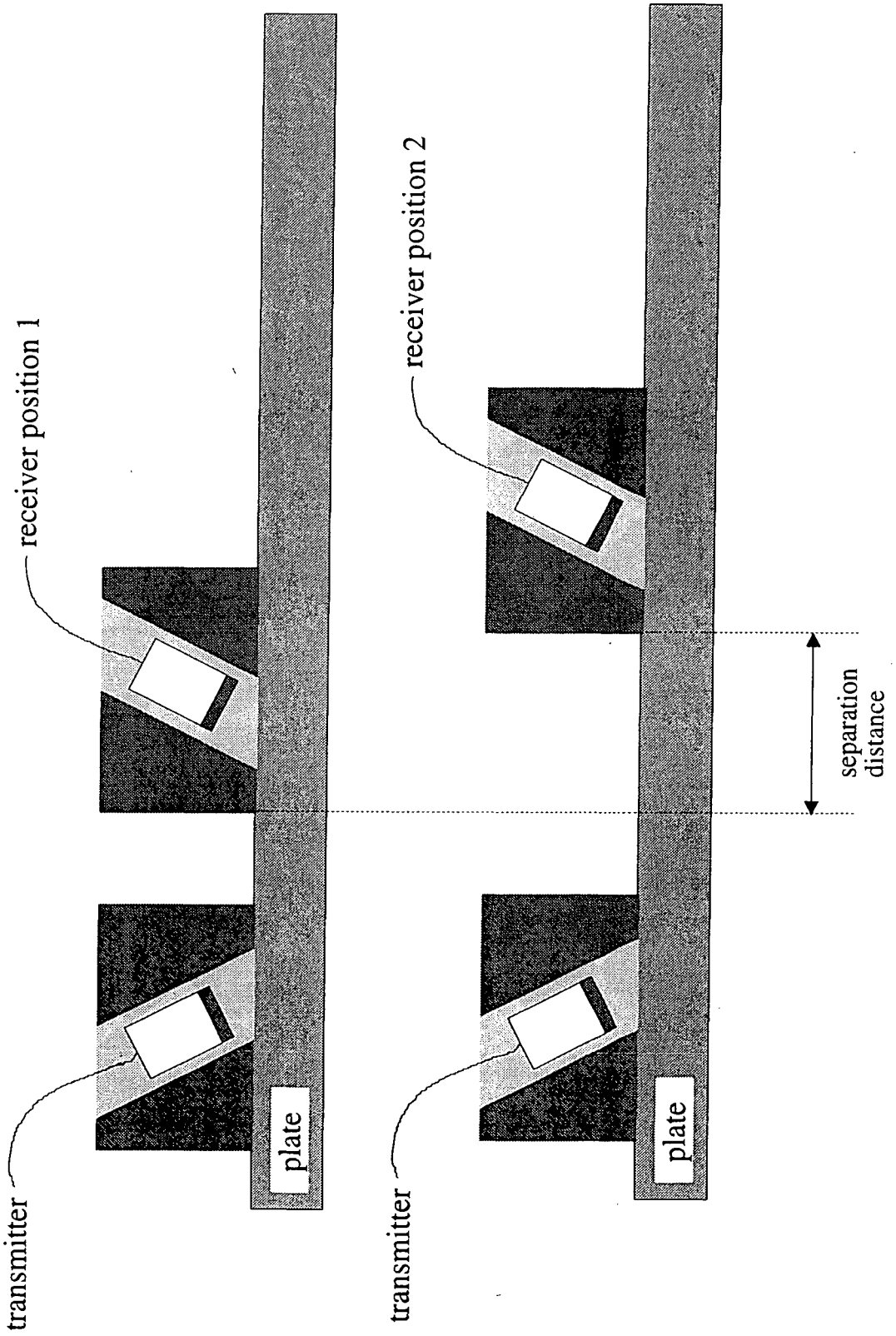
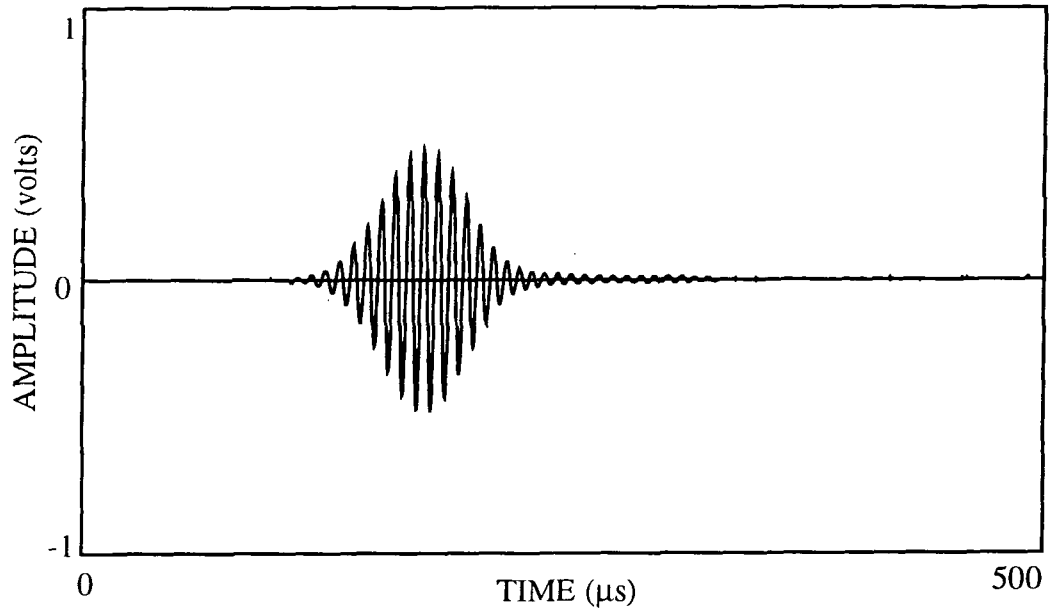
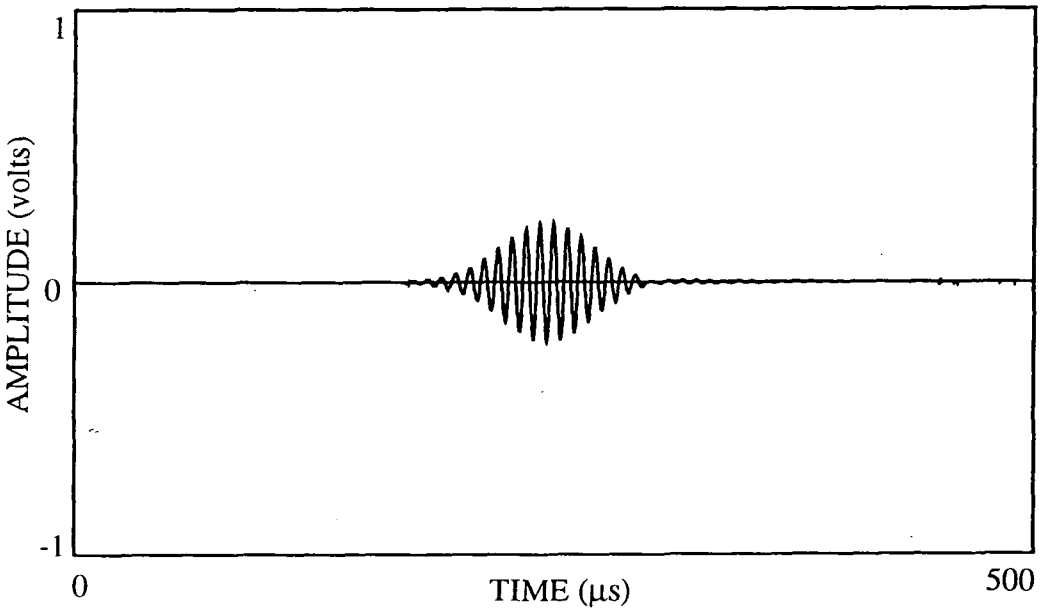


Fig.6.16 Schematic diagram showing the measurement sequence for monitoring Lamb waves along a HPPE plate

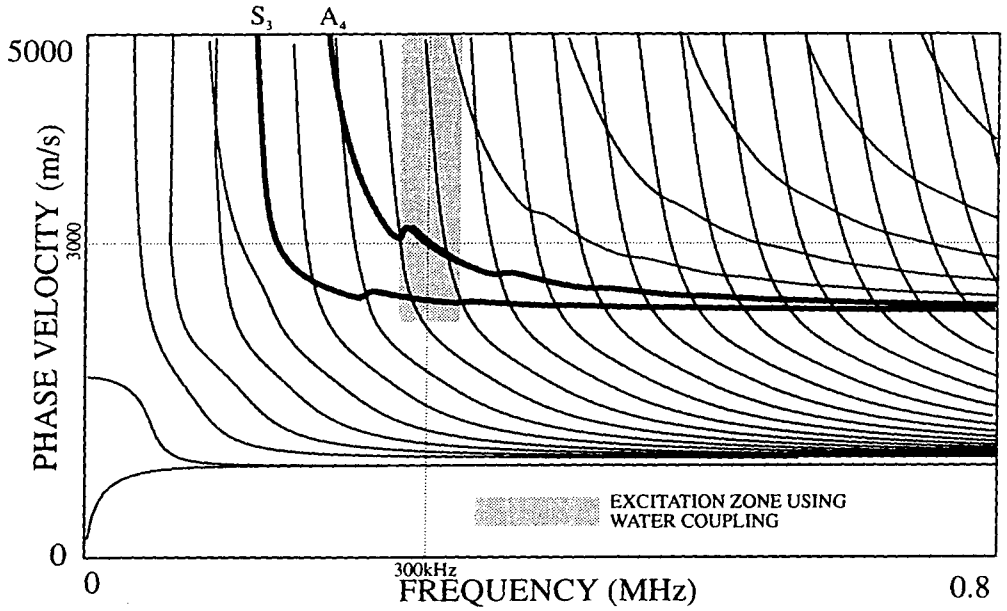


a)

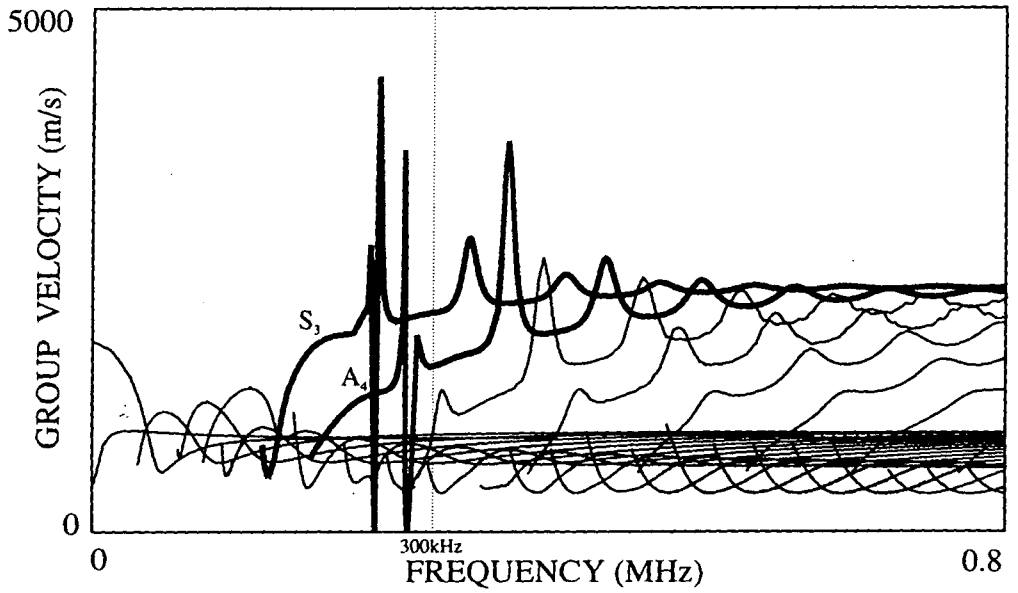


b)

Fig.6.17 Time domain history of received signal. a) Time history of received signal at receiver position 1; b) Time history of received signal at receiver position 2

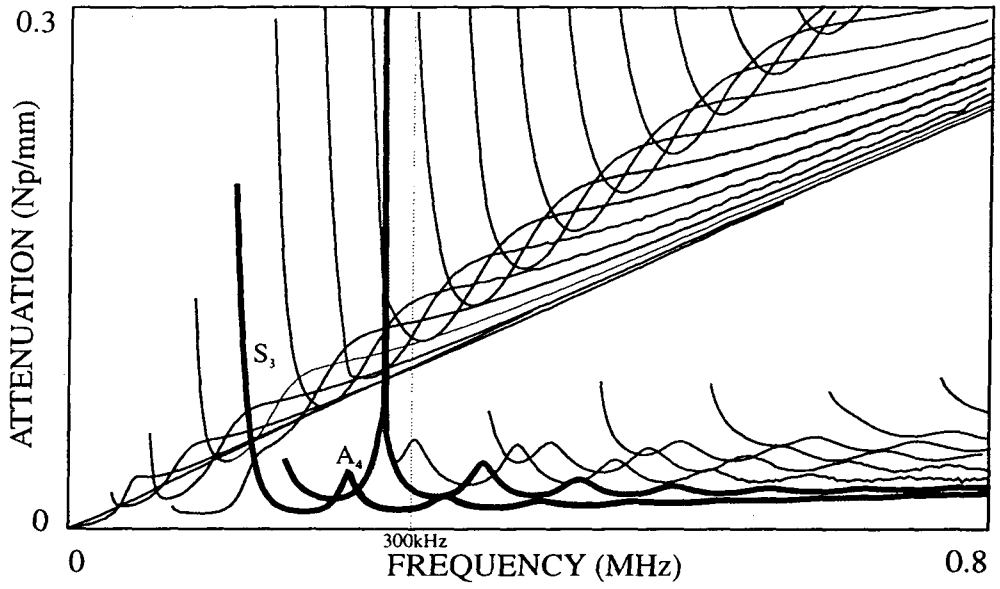


a)

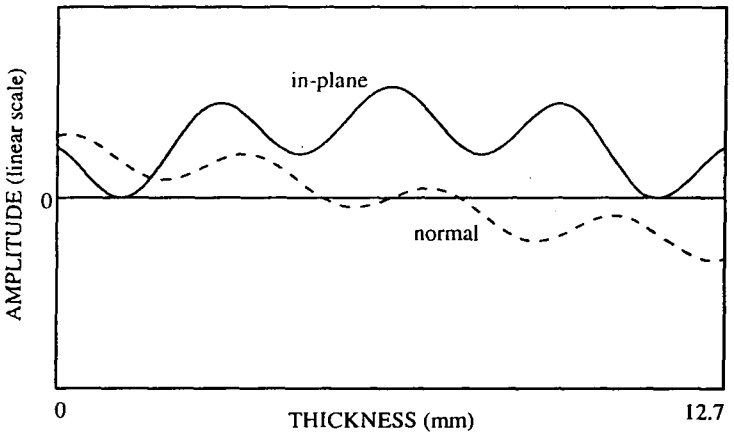


b)

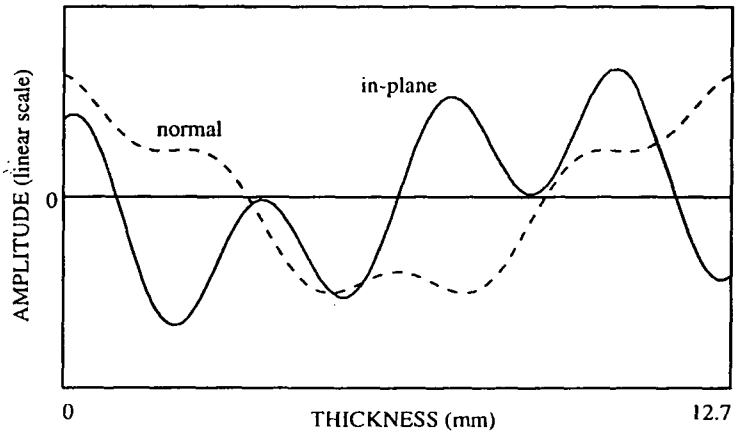
Fig.6.18 Dispersion curves and mode shapes for modes s_3 and a_4. a) Phase velocity dispersion curves showing s_3 and a_4 modes and excitation zone used in experimental phase; b) Group velocity dispersion curves showing s_3 and a_4 modes mode used in experimental phase



c)



d)



e)

Fig.6.18 Dispersion curves and mode shapes for modes s_3 and a_4. c) Attenuation dispersion curve for s_3 and a_4 modes; d) Displacement mode shapes for s_3 mode at f=300kHz and C_{ph}=3000m/s; e) Displacement mode shapes for a_4 mode at f=300kHz and C_{ph}=3000m/s

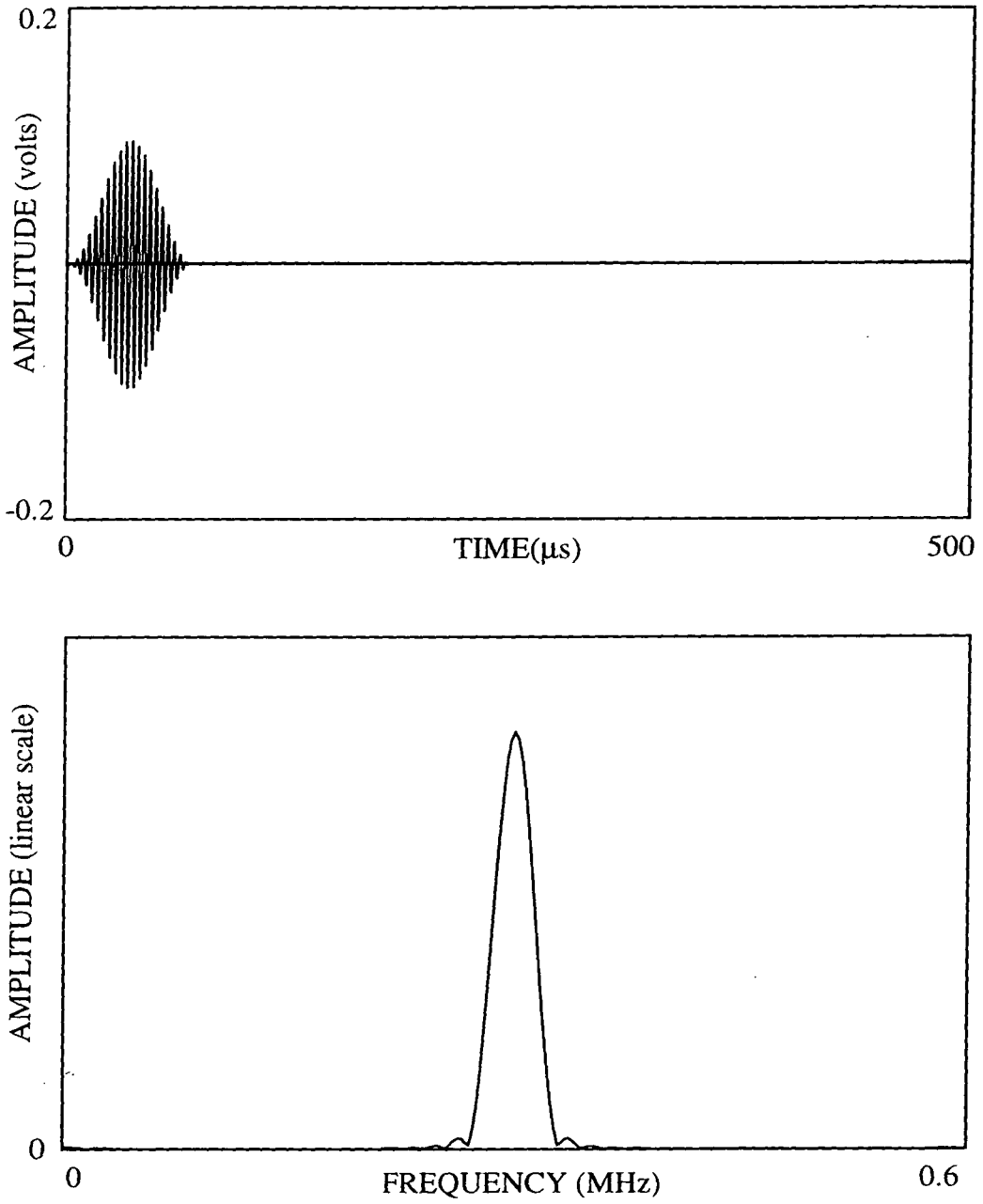
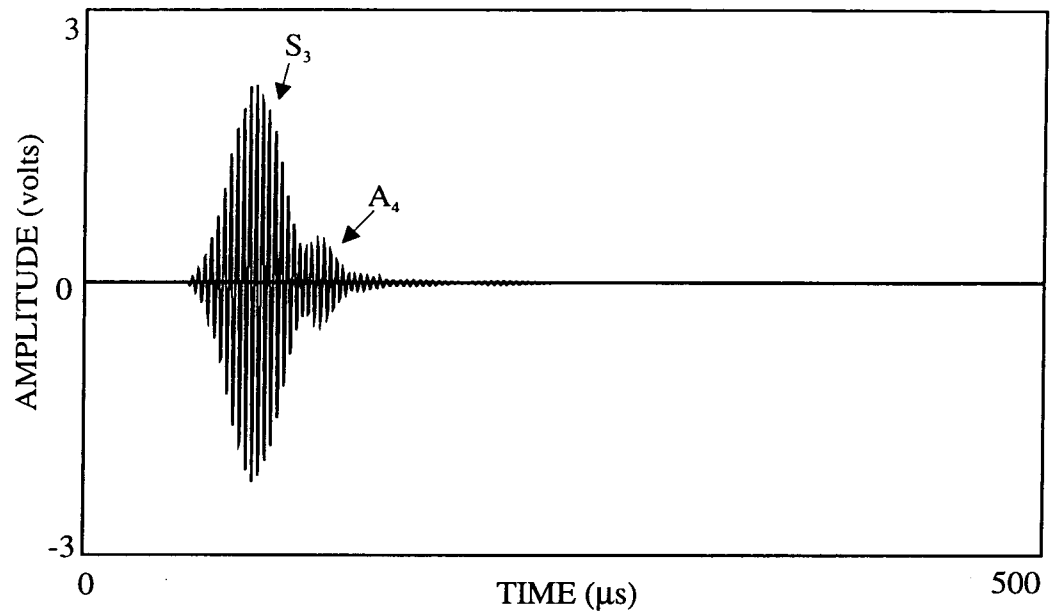
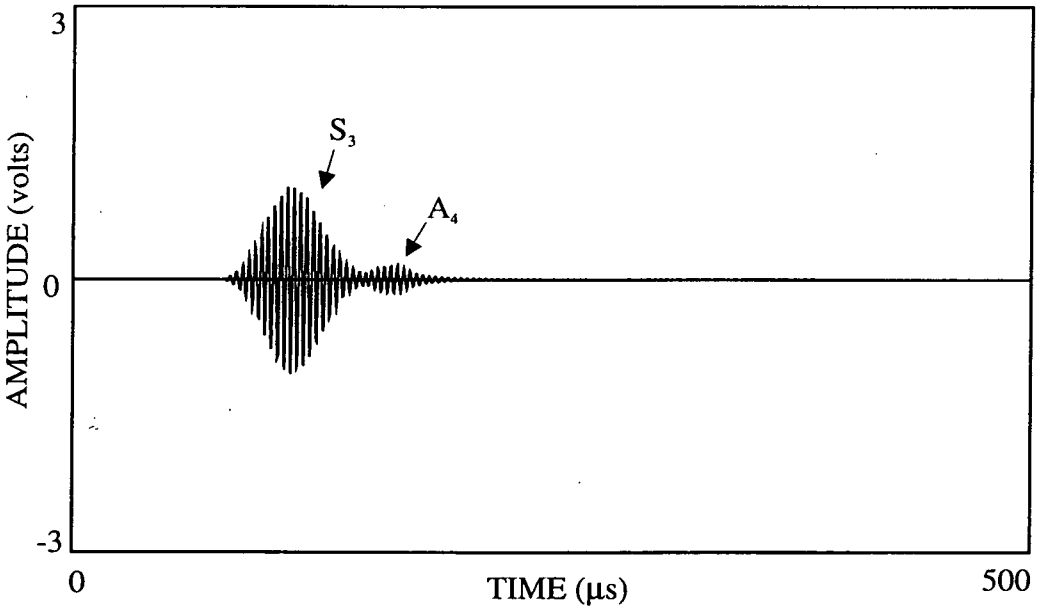


Fig.6.19 Details of input signal for excitation of s_3 and a_4 modes. a) Time history of 300kHz, 20 cycle tone burst input signal; b) Frequency spectrum of above signal



a)



b)

Fig.6.20 Time domain history of received signal. a) Time history of received signal at receiver position 1; b) Time history of received signal at receiver position 2

CHAPTER 7

An Investigation into the Use of Dry Coupled Transducers for the Excitation of Lamb Waves in Pipes

7.1 Introduction

Traditional methods of exciting stress waves in pipes involve the use of piezoelectric transducers which are coupled to the pipe by means of a couplant, usually in the form of a gel. In addition a delay line is commonly used to separate the excitation pulse from subsequent reflections. This technique works well for applications in which the speed of the required wave in the pipe (Lamb wave) is higher than the speed of the bulk wave in the delay line which is being used to couple the transducer onto the pipe. Problems arise when the Lamb wave we are interested in travels slower than the wave in the delay line. This situation is most common when dealing with materials such as plastics where the Lamb wave velocities can be relatively low. By using the coincidence principle (see e.g. Cremer (1942)), the higher wave speed in the delay line would render the excitation of certain wave modes at certain frequency-thickness ranges impossible by this technique. There are two possible solutions to this problem. The first involves using a suitable delay line in which the bulk velocity is lower than that of the Lamb wave we are interested in. Materials such as water or low attenuating rubber are viable candidates. The second solution is to look for an alternative excitation source which no longer relies on the coincidence principle for exciting the mode. For the latter solution a dry coupling system would be desirable as this would make the set up more manageable in the field (i.e. not having to deal with liquid couplants).

Experiments have been performed in a separate project in the NDT section using a specific type of dry coupled-transducer on steel pipes for the generation and reception of Lamb waves (Alleyne and Cawley (1996)). The coupling between the transducers and the pipe was achieved using pressure loading only (i.e. no intermediate coupling medium). The results have been promising. The project in which these experiments were conducted investigates the use of Lamb waves for the detection of corrosion in steel pipelines. In its most basic terms the corrosion can be thought of as being a defect in the pipe from which a reflection would occur if a Lamb wave strikes it.

Given that the aims of the corrosion detection project and those of this project are similar, it was decided that a collaboration be made to investigate these transducers further. The work was essentially divided into two parts. One part deals with the numerical modelling of the transducers. The other part deals with the experimental side of the project. The majority of the numerical modelling was undertaken by myself and is presented in this chapter.

Two types of dry coupled transducers were investigated: expansional and shear. Figs.7.1a and 7.1b show schematics of the two types. Both involve in-plane vibration. These types of exciters were chosen because the Lamb modes which are of interest are predominantly in-plane modes. The advantages of these transducers are that they are relatively inexpensive, and can be made compact so that the size of the inspection system could be kept to a minimum. The main disadvantage is that they do not rely on the coincidence principle and therefore the targeting of a particular mode becomes more difficult because a large number of modes could be excited.

The analysis of the transducers can be separated into two distinct parts. The first part deals with the question of how the transducers should be arranged on the pipe and will involve looking at the effect of varying different layout parameters such as non-uniformity of the transducers around the pipe and the number of transducers. The important issue in this part of the work is to determine how low a baseline level or noise floor can be achieved, the baseline being the result of coherent noise due to the excitation of other modes. This is necessary because typical reflection amplitudes from a defect are likely to be small and therefore a high noise floor level is liable to mask the reflection. The second part concentrates on the individual transducers themselves and the aim is to study the effect of choosing different parameters for the different components which go to make up the transducer (e.g. backing material, shim thickness). The majority of the work conducted is based around the excitation of Lamb waves in *steel* pipes, given that the equipment used was funded specifically for the steel pipe project. Therefore, an elastic analysis is conducted. Given that the investigation is primarily concerned with the efficiency with which Lamb modes can be excited using the transducers, the ensuing propagation is of secondary importance and hence the effect of attenuation (which is relatively high in the polyethylene pipes) will not be a determining factor from an excitation point of view. An elastic analysis is therefore perfectly valid for this work and the results will therefore be of a general nature. The overall aim of this work is to arrive at a suitable dry coupling technique for the excitation of Lamb waves in steel pipes. If the results are promising, then the method could subsequently be used on plastic pipes.

The layout for the rest of this chapter is essentially divided into two parts. In the first part we will look at targeting a particular mode for excitation and subsequently address the issue of transducer layout. In the second part the transducers themselves will be discussed and finally conclusions will be drawn.

Part One: The Effect of Transducer Layout on the Efficiency of Lamb Wave Excitation

7.2 Lamb Mode Selection

Before we can perform any analysis, it is necessary to decide on a suitable mode which could be used for defect detection and hence be the target for excitation. The main requirements for this mode are as follows:

i) it should be non dispersive so that the shape of the pulse does not change and hence the different frequency components do not travel at different speeds. This is important when amplitude measurements are used to relate the amplitude of a reflection to the size of a defect.

ii) it has a relatively large group velocity in relation to other modes so that this mode could then be resolved from the slower modes which may propagate as a result of it being impossible or difficult to eliminate those modes.

iii) the excitation source should be simple to set up to excite the required mode.

In order to investigate this problem, dispersion curves are employed. In the ensuing work, an 89mm outer diameter, 5.5mm wall thickness steel pipe was used. Figs.7.2a and 7.2b show the phase velocity and group velocity dispersion curves for this pipe respectively. Note that torsional modes have not been shown. The terminology used for naming the modes is the same as that used by Silk and Bainton (1979) where L(0,n) modes correspond to axisymmetric modes and F(a,b) modes to flexural modes.

From a dispersion point of view, it can be seen from the group velocity dispersion curves that there are several modes which could be used, e.g. L(0,1) between 0-10kHz, L(0,2) between 40-100kHz, F(1,3) between 50-100kHz. Note that the L(0,2) mode is fairly non-dispersive over a relatively large frequency range.

From a velocity point of view, two modes stand out, these being L(0,1) and L(0,2). These two modes have the highest group velocities of all the modes shown. Having one or two modes is desirable as there is then less chance of different modes overlapping and hence signal identification will be much easier.

Next we consider the question of excitation. The most convenient modes to excite in a controlled manner would be the zero harmonic (L(0,n)) modes as this would involve using a set of transducers equally spaced around the pipe with the inputs all being equal in amplitude and phase in order to try and create a uniform field around the pipe. Exciting the flexural (F(a,b)) modes in a controlled manner is a more difficult task as the transducers need to be excited non-uniformly around the pipe. Therefore, by considering the arguments just put forward it would appear that the most suitable modes would be either L(0,1) or L(0,2).

If we look at the frequencies over which these modes are suitable, L(0,1) would have to be used at fairly low frequencies. The implication of this is that the pulse length would be very long and it would hence be very difficult to resolve the reflection from a defect with that of the outgoing pulse unless the defect is expected to lie a long distance away from the excitation region. For example, if we choose to operate at 5kHz, the pulse length based on 8 cycles would be 7.3m. L(0,2) is a more attractive proposition as an operating frequency of about 70kHz would correspond to a pulse length of 0.6m for 8 cycles. In terms of a pulse-echo system this implies that the first 300mm from the excitation source cannot be inspected.

We have seen in Chapter 5 that modes which have a small shear stress component contribute very little in terms of reflectivity from a defect which is oriented in the pipe axis direction. Fortunately, the situation for butt fusion welds is favourable as the defect orientation is perpendicular to the pipe axis direction. L(0,2) has therefore been chosen as the mode to be excited, the centre frequency of excitation being 70kHz. A check on the mode shapes of this mode (Fig.7.3) shows that the motion is predominantly in-plane and hence transducers which induce an in-plane excitation to the pipe will be beneficial. Note that the depth corresponds to the depth through the wall thickness of the pipe and that the motion is axially symmetric. Although this mode has been targeted for excitation, the fact that L(0,1) is present at this frequency means that this mode will also be excited. At this frequency it is relatively dispersive. Fortunately its group velocity is approximately half that of L(0,2) and therefore reflections caused as a result of this mode impinging on a defect will be of little importance because the first arrival of a reflection will be due to L(0,2).

7.3 The Effect of Transducer Positioning on the Pipe

This section looks at the way transducers are positioned on the pipe. Having identified that the zero harmonic L(0,2) mode is to be excited, the next stage is to determine how we would go about exciting this mode. We will firstly discuss the parameters which are likely to affect the efficiency with which the L(0,2) mode can be excited. Four parameters are of interest. The first concerns the issue of selecting the number of transducers to be used. The second concerns the effect of transducers being misaligned in the axial direction. The third looks at the effects of circumferential misalignment of the transducers and the final parameter is non-uniformity of the input signal on the pipe surface.

7.3.1 Number of Elements

One of the most important issues to be resolved is the question of how many transducers should be used around the pipe. For a zero harmonic mode, the transducers have to be placed at equal angular intervals around the pipe. The more transducers we have the more uniform the field and hence the more chance we have of exciting a pure zero harmonic mode. In addition, as we increase the number of transducers, the input amplitude increases and as a result the L(0,2) mode will be more strongly excited. There will however be an increase in the cost of the system.

The modes which can be excited and the number of transducers around the pipe circumference are linked: if we assume that the transducers are all perfect then if we have n equally spaced transducers around the pipe then only modes of harmonic numbers 0, n, 2n , ... can be excited since only these modes have points around the circumference which are in phase with one another beneath each transducer. This is illustrated in Fig.7.4 for the zero and eighth harmonics. The harmonic number gives the number of wavelengths around the circumference.

Two different numbers of transducers have been chosen for investigation, one being 8 transducers and the other being 16. The advantages of using 8 are that potentially less adjustments need to be made and costs could be kept low. The envisaged disadvantage is that because we are using 8 transducers, modes having a harmonic number of 8 are liable to be strongly excited. From the dispersion curves (Figs.7.2a and 7.2b), it can be seen that the F(8,1) mode exists in the frequency-thickness zone of excitation and may therefore be excited. The actual amplitude of this mode will depend on its excitability. If the excitability is small then using 8 transducers would not be

problematic. If the excitability is large then increasing the number to 16 will overcome the disadvantage because the cut-off frequency of the F(16,1) mode is well above 70kHz.

7.3.2 Axial Misalignment of Transducers

A potential problem when placing the transducers onto the pipe is that one or more transducers could be axially misaligned. The interest here is to determine how much misalignment can be tolerated and this will largely depend on how large the reflection coefficient is from defects we are looking for. Fig.7.5 shows a schematic of an axially misaligned transducer.

In order to analyse misalignment problems, a simple model was created. This model assumed that each transducer would emit a signal identical to a two dimensional Dirac delta function (i.e. a Dirac delta function in the axial and circumferential directions). A computer program was written to decompose the input of the transducers into the harmonic wavenumber and axial wavenumber domains. In this way, it is possible to determine how much of each harmonic is being excited at any given axial wavenumber or harmonic wavenumber when a given parameter such as the alignment of a transducer is altered. Details of the theory and the implementation of this model are given in the Appendix.

Fig.7.6a shows the harmonic wavenumber distribution (or harmonic spectrum) when 8 ideal transducers are used. Note that modes at non-integer harmonics do not exist but for convenience points representing integer harmonics have been joined up. The particular case shown corresponds to zero axial wavenumber. However, when all transducers are ideally placed (i.e. there is no axial misalignment), the axial wavenumber has no influence on the harmonic spectrum because we essentially have a single Dirac delta function along the axial direction (i.e. it is not a function of the circumferential position) and hence all axial wavenumbers will be excited equally. It can be seen that only two harmonics are excited, these being of order 0 and 8 as expected (higher order harmonics, i.e. 16, 24, 32, ... have not been shown). Figs.7.6b, 7.6c and 7.6d show the result of misaligning one transducer by 1, 2 and 3mm respectively when the axial wavenumber (k) is 1000rad/m. The figures show that the general effect of the misalignment is that all harmonic numbers between 0 and 8 are equally excited and that their amplitudes increase with misalignment distance whereas the amplitude of the 0th and 8th harmonics decrease. As the misalignment increases, so too does the amplitude of the non-zero harmonics. However, axial wavenumber

now has an influence on these amplitudes. If we first look at the case of the harmonic number n=0 or 8 for a 1mm axial misalignment (Fig.7.7a), we can see that the excitation amplitude varies periodically in axial wavenumber, going through a series of maxima and minima. The position of the first maximum occurs at k=6284rad/m and corresponds to a complete wavelength given by the axial spacing between the ideal transducers and the misaligned transducer. Further maxima are given by multiple wavelengths occupying the same misalignment distance. If we now look at the case where $0<n<8$ (Fig.7.7b) we see that the distribution is still periodic but the main difference between this case and that of n=0 is that the positions of the minima and maxima have been reversed. So now at k=6284rad/m we have a minimum and therefore cancellation must be occurring at this particular axial wavenumber. It is as if there is an odd number of half wavelengths occupying the distance between the ideal transducers and the misaligned transducer.

At this stage, the harmonic spectra results obtained would not be sufficient to determine how each harmonic will be excited because the assumption would have to be made that all harmonics have the same excitability, that is to say, if a unit force input is applied to any harmonic mode, it will have the same amplitude response whatever the mode. In this case the harmonic spectra would represent directly the response which would be achieved on a pipe. In reality this is not the case and in order to try and establish the excitability of the harmonics, a finite element model using harmonic number analysis was conducted. This involves modelling the response of the pipe to a given excitation for each harmonic number (i.e. 1, 2, 3, etc..) separately.

The finite element package used is the same as that used previously for the work on Lamb waves in electrofusion welds. By carrying out FE predictions for each harmonic number up to 8 we can then apply the weighting factors calculated from the Fourier analysis (i.e. the harmonic spectrum) on each harmonic and then sum up the responses according to the superposition principle. The pipe used in the model was 1.5m long and the forcing was applied near one end of the pipe (Fig.7.8a). The forcing pattern applied to the surface of the pipe is shown in Fig.7.8b. The excitation was applied over a finite length to simulate a real transducer. The input used for the harmonic analysis was the same for all harmonics, the input being an 8 cycle tone burst at 70kHz centre frequency; the frequency spectrum of this input is shown in Fig.7.8c. The harmonic finite element runs were conducted by David Alleyne (researcher on the steel pipe corrosion project at Imperial College).

Figs.7.9a-7.9i show the time domain responses from harmonic number 0 to harmonic number 8 when the response is monitored 40mm downstream of the start of the excitation region. In Fig.7.9a, the first signal is the outgoing signal comprising the L(0,1) and L(0,2) modes and the second is the L(0,2) mode reflected from the right hand end of the pipe. The first signal is smaller than the reflected L(0,2) mode because of destructive interference between the outgoing L(0,1) and L(0,2) modes. A point was monitored further along the pipe and showed that the L(0,1) and L(0,2) modes separated out in the time domain. The results show that the modes which are likely to be most problematic are the fourth and fifth harmonic modes (Fig.7.9e,f) as these modes are very dispersive and hence are liable to interfere with any reflections which may occur in a pipe. Fig.7.10 shows the superposed response for the ideal case of 8 transducers. It can be seen that when we compare this with that of order 0 (Fig.7.9a), the fact that we can excite order 8 means that there is some significant increase in the baseline level immediately after the outgoing signal. The baseline signal is essentially due to the existence of the flexural modes. Therefore, even in the ideal case, 8 transducers would not be suitable for exciting a low baseline level signal.

If we now take the case of 16 transducers then as mentioned previously, in the ideal case 8th order modes would not be excited and this is reflected in the superposed response which is identical to Fig.7.9a. Figs.7.9j-7.9l show the harmonic analysis responses for harmonic numbers 9, 10 and 11 (on the same scale as those of orders 0-8) and it is fairly evident that these modes should not be too problematic. We have only looked at modes up to and including order 11 because higher order modes will not be excited within the frequency bandwidth of the 8 cycle tone burst input (Fig.7.8c). In all subsequent calculations and figures, 16 transducers will be used. Figs.7.11a-7.11c show the superposed response after the weighting factor (i.e. those obtained directly from the harmonic spectrum) for each harmonic has been applied for the 1, 3 and 5mm misalignment cases. Note that the reflected L(0,2) mode is no longer visible due to the time scale chosen. The harmonic spectra were all calculated for k=240rad/m because this wavenumber, which represents the largest wavenumber of all the modes which can be excited (this was calculated from the phase velocity dispersion curves), was found to have the largest amplitudes for the non-zero order modes and the lowest amplitude for the zero order mode. This means that we are assuming a worst case scenario because we are taking the case where the amplitude ratio of the zero harmonic to the non zero harmonics is a minimum.

The baseline ratio is defined as the maximum amplitude of the baseline level following the outgoing signal divided by the amplitude of L(0,2) (see Fig.7.11c). The

baseline ratio has been calculated and plotted against the misalignment distance in Fig.7.12. The figure also shows curves plotted for the cases where 2 and 3 transducers are misaligned, as well as a worst case which corresponds to all transducers being misaligned. In the cases where more than one transducer is misaligned, the harmonic spectrum for the non zero order modes is no longer uniform but will have minima and maxima, the position of these being dependent on the positioning of the misaligned transducers. For a given number of misaligned transducers there exists a large number of possible configurations in which the misaligned transducers can be placed. For instance, they could be arranged adjacent to each other or maybe opposite each other. As a result a lot of time would be required to calculate the baseline ratio because the amplitude for each harmonic would have to be taken into account when computing the overall response. To simplify the analysis, the weighting factors were obtained by going through the different possible configurations and the amplitude of the largest non-zero harmonic was noted down, irrespective of which configuration it came from. It was then assumed that all non zero order modes have this same amplitude. In this way, we have in effect analysed a worst case situation. The results show that the variation in baseline ratio with misalignment distance is linear and as expected increases with the number of misaligned transducers. Therefore, we now have a relatively simple method for assessing the baseline ratio for any number of misaligned transducers and hence by knowing the minimum reflection ratio expected from a defect we can design a transducer system to have a maximum axial tolerance which would allow the reflection from a defect to be resolved.

Experiments performed on the steel pipes with defects simulating corrosion (Alleyne & Cawley (1996)) gave minimum reflection coefficients of about 0.5%. Therefore, to be able to resolve any defects we would require a baseline level i.e. the signals which arise from unwanted flexural modes, to be lower than this level. A value of 0.25% for the baseline level would therefore be appropriate. This implies that the alignment tolerance on a single set of transducers, based on a pulse-echo type system (i.e. using the same transducers to pulse and receive) would have to be about 5% maximum. That is to say, the transducer(s) could be misaligned such that any resulting flexural waves can have a maximum amplitude of 5% the amplitude of the input wave. From the graphs we are able to determine that the maximum allowable misalignment distance for a single misaligned transducer is 6.4mm. A misalignment of such proportions would in reality be relatively easy to spot visually. In fact, with 3 misaligned transducers we can tolerate a misalignment of 2.2mm for each transducer which should not be too difficult to design for. The worst case possible is when we have half

the transducers misaligned in one direction and the other half in the other direction. With this set-up, the tolerable misalignment for each transducer is 0.8mm.

7.3.3 Circumferential Misalignment of Transducers

Now we turn our attention to the circumferential misalignment of the transducers. The question being raised in this section is how much can the transducer be misaligned circumferentially before unwanted modes become significant. Fig.7.13 shows a diagram of a circumferentially misaligned transducer. The model described in the previous section was once again used to explore this issue. Figs.7.14a-7.14c show the spectra for a single transducer being misaligned by 2, 4 and 6 degrees respectively from its ideal position. The trend of the spectra is the same: from harmonic number 1 to harmonic number 11 the amplitude increases. Circumferential misalignment is therefore more influential towards the higher order modes. In a similar fashion to the work carried out on axial misalignment, a graph of circumferential misalignment against baseline ratio is plotted in Fig.7.15 for 1, 2, 3 misaligned transducers and for the worst case situation. The worst case situation is achieved when half the transducers are misaligned in one direction and the other half in the other direction. The trends are similar to those found in the axial misalignment case.

If we now use this data on the steel pipe, a single misaligned transducer can be misaligned by 8.8 degrees which is equivalent to 6.8mm circumferentially. For three transducers this value is 2.6mm (3.3 degrees) and for the worst case it is 1.1mm (1.42 degrees). It is now interesting to compare the tolerance levels for a given baseline level for the two misalignment cases (i.e. circumferential vs. axial). If we take a baseline level of 5% for the worst case scenario, we know that the maximum axial misalignment is 0.8mm whereas the maximum circumferential misalignment is 1.1mm. The difference is not large and it can therefore be deduced that the same amount of effort has to be made in ensuring that the both axial and circumferential misalignment are kept as small as possible.

7.3.4 Non-Uniform Excitation Amplitude of Transducers

Ideally, all transducers would operate with the same input amplitude to the pipe. However, fluctuations in amplitude may occur. We therefore need to determine a bottom limit concerning how large the discrepancy in the amplitudes can be for a given baseline ratio. To achieve this, we looked at varying the input amplitude of a single transducer and computing the response of the pipe using the model. This was

done for the cases where the amplitude of the imperfect transducer differed by 10%, 30% and 50%. Figs.7.16a-7.16c show the harmonic spectra. The analysis was then repeated for 2 and 3 transducers and finally the results for a worst case situation were computed. The worst case corresponded to half the transducers having an amplitude below that of the mean while the other half having amplitudes above the mean, the difference from the mean being the same for both sets of transducers. A graph of the baseline ratio versus % amplitude difference of an ideal transducer is calculated and is shown in Fig.7.17.

Fig.7.17 shows that the complete removal of a single transducer would result in a baseline level of 3.5% (equivalent to 0.1% reflection coefficient) which is within the tolerable limits for corrosion. If we look at the worst case situation, then by applying these results to the steel pipe, we see that provided the amplitudes of the transducers vary by less than 11% each, the detection of defects with 0.25% reflection coefficient will be perfectly viable.

7.4 Summary of Transducer Placement and Consistency Requirements

The first half of this chapter has looked at the effects of varying different parameters on the excitation of flexural modes in a pipe. These flexural modes have been identified as being the cause of the baseline level accompanying the main excitation signal and the aim is to reduce this baseline to a level which is acceptable. The acceptability will be highly dependent on the defect which the Lamb wave technique is expected to detect.

The cases of 8 and 16 transducers around the pipe have been investigated using Fourier analysis and finite element modelling. It was found that because of the presence of eighth order modes, the use of 8 transducers is not recommended as the set-up tends to excite those modes. The major cause of coherent noise with 16 transducers was found to be the 4th and 5th harmonic flexural modes. In a perfect set-up such modes would not be excited. In reality, the excitation may not be completely axisymmetric. Possible causes of asymmetry are axial misalignment and circumferential misalignment of the transducers. A parametric study carried out on a steel pipe reveals that the axial misalignment tolerance is less than that for circumferential misalignment, though the difference is not great.

Studies have also been carried out on the effect of non-uniform excitation amplitudes. For the steel pipe, it was shown that having one transducer inoperative would not be

problematic as the baseline level is within the acceptable limit for corrosion detectability. A maximum amplitude tolerance of ±11% for each transducer was found to be acceptable. Given that we now have graphs relating the baseline ratio to different types of misalignment it is possible to calculate an overall baseline ratio simply by combining the results from the different misalignment cases. For example, if we have, say, a 0.5mm axial misalignment, a 0.5 degree circumferential misalignment and an amplitude variation of 5%, then using the worst case results, we would have a baseline ratio of 7.6%. If this value is too high, then one of the tolerances has to be reduced and the baseline ratio recalculated.

Part 2: The Design of Piezoelectric Transducers for the Excitation of Lamb waves in Pipes

7.5 Introduction

In the first half of this chapter, we looked at the effects of varying the transducer layout on the efficiency of exciting a pure Lamb mode, L(0,2), in a pipe. The second half of the chapter concentrates on the physical aspects of the piezoelectric type transducers chosen for Lamb wave excitation in pipes; in particular, the relationship between the components which make up the transducer and the efficiency with which the L(0,2) mode can be excited will be explored.

Probably the most important part of any transducer is the vibrating element itself. For this project, two particular types of elements have been chosen for investigation, both piezoelectric in nature and made of Lead Zirconate Titanate (PZT). The first type of element is known as an expansional element, so called because one half of the length of the element vibrates in antiphase with the other half, creating an 'expansional' type motion (Fig.7.1a). The second type of element is known as a shear element because the top half of the element vibrates in antiphase to the bottom half, producing a 'shear' type motion (Fig.7.1b). From the mode shapes of L(0,2) in the first half of this chapter (Fig.7.3), we can deduce that both types of elements should favour the excitation of the L(0,2) mode as they should couple well to a mode with predominantly in-plane displacements.

In the rest of this chapter we will look at each type of element in turn in order to determine which of the two types of element is more suited to the excitation of L(0,2). Finite element analysis will be used to model the elements and we will look at the

response of a pipe when these elements are attached to it. The analysis will aim to address three key issues which are likely to affect the efficiency of these elements for exciting the L(0,2) mode. The first issue looks at the response of the transducer when excited. The interest here is to find out whether the transducer rings, the ringing being the result of structural resonances of the transducer. The second issue is to determine how well the elements couple to the required Lamb mode (i.e. we want to maximise input into the L(0,2) mode). The third issue concerns the sensitivity of the excited L(0,2) mode to the point of contact of the transducers on the pipe. Ideally, we would like to have transducers which are not sensitive to the way they are loaded.

7.6 Expansional Piezoelectric Elements

7.6.1 Components of a Transducer

In practice, piezoelectric transducers seldom consist solely of a piezoelectric element. If we consider the components of a conventional piezoelectric transducer, we would find a protective layer (shim) on the front of the piezoelectric element to prevent the element from being scratched. Behind the piezoelectric element we would find a backing layer, usually made of a material with high damping but with an acoustic impedance similar to that of the piezoelectric element so that energy can readily propagate into the backing.

7.6.2 Effect of Backing.

Ringing is a potential problem when we are dealing with a relatively thin and flexible element, the ringing being caused by bending resonances of the element. This ringing could be suppressed if the element is bonded to the pipe but this means that the element would be permanently fixed to the pipe. If the ringing amplitude is relatively large then this will contribute to the unwanted baseline level discussed earlier in this chapter. In order to suppress such resonances, a stiff backing may offer a solution. Furthermore, a stiff backing can also help to prevent bending failure of the brittle piezoelectric element. We therefore we need to look at how the ringing is affected by different backing materials.

To begin with, we shall look at the simple case of a piezoelectric element with a protective shim (an 'unbacked transducer'). The transducer is initially assumed to be free from any support. An outline of the FE model is given in Fig.7.18 showing the dimensions of the components. The dimensions of the piezoelectric element were

chosen on the basis that piezoelectric elements with these dimensions were readily available commercially. The thickness of the shim was chosen on the basis that 0.1mm thick brass plates were readily available. The excitation of the piezoelectric element was modelled by assuming an in-plane sinusoidal force function across the length of the element (see Fig.7.19a) so that the forcing on one half length of the element is in the opposite direction to the forcing in the other half. For each node on the piezoelectric element, a 70kHz centre frequency, 4 cycle tone burst in a Hanning window was applied (Fig.7.19b). The corresponding spectrum is shown in Fig.7.19c. Plane stress conditions were assumed on the basis that the transducers were to be relatively thin in the width direction.

To check the response of the transducers, the time domain history at one of the bottom edges of the shim was monitored in the in-plane direction (we did not monitor at the centre because the displacement there would be zero due to symmetry). Fig.7.20a shows the time domain response of the monitored point. There is a large initial signal. This is the direct response of the piezoelectric element to the excitation signal. Following this, we have a series of slightly lower amplitude signals. The signals appear to 'ring on' and are of a different frequency from the centre frequency of the input signal which can be confirmed by computing the frequency spectrum of the signals, shown in Fig.7.20b. This was achieved by gating out the initial 4 cycle signal. To smooth out the spectrum, a Hanning window was applied to the ringing signals prior to computing the spectra. In fact, the spectrum shows that there are three frequency peaks all at frequencies which are different to the centre frequency of the input signal, these occurring at 12.7kHz, 64.5kHz and 98.6kHz. Given the 'ringing' appearance and the appreciable difference in frequencies between the input signal and the subsequent signals, it can be deduced that the lower amplitude signals are the result of structural resonances of the transducer. Resonances at frequencies which are not too close to the centre frequency of the input signal are possible due to the relatively broad bandwidth of the excitation signal, as can be seen from Fig.7.19c.

In order to try and establish the identity of these resonance modes, a standard eigenvalue analysis was carried out using the same FE model and the natural frequencies were consequently calculated. Given that the input to the piezoelectric element is symmetrical about the vertical mid-plane of the transducer, we would only expect modes symmetric about the vertical mid-plane to be excited in the element. Fig.7.21 shows the displacement mode shapes of the first three symmetric modes. The corresponding natural frequencies of these modes are 12.8kHz, 69.3kHz, 99.0kHz. We can see by comparing these frequencies with those obtained from the time-

marching FE analysis that they are in quite good agreement, hence reinforcing our theory that resonances of the transducer are being excited. They are not identical because different numbers of elements were used. Note that the most strongly excited mode is the third symmetric mode. This mode is dominated by in-plane motion and we would therefore expect such a mode to be fairly well excited given the in-plane nature of the excitation.

Next, we attach the transducer to a large steel block. The block is necessary so that we can model the effects of energy radiation away from the transducer; otherwise the transducer would ring on indefinitely which does not occur in reality. A large block was chosen so that reflections from the sides of the block would only occur after a large interval of time. An outline of the modified FE model is given in Fig.7.22 showing the dimensions of the various components. Due to the difference in size between the block and the transducer, the transducer is shown enlarged and the location of the transducer on the block has been indicated. The same point on the transducer was monitored and the time domain response of that point is shown in Fig.7.23a. The spectrum of the ringing signals is shown in Fig.7.23b (after gating out the initial signal). The frequency of the ringing is now centred at 145kHz (note that there is energy in the input signal at 145kHz although the energy content is low (Fig.7.19c)). The attachment onto the steel block has clearly altered the boundary conditions for the transducer. The deflected shape of the mode at 145kHz is shown in Fig.7.23c and was obtained by monitoring points around the transducer. It can be seen that the mode being excited is very similar to the first symmetric mode for a free transducer (i.e. Fig.7.21a) which was not very strongly excited previously in the free transducer case. The effect of coupling to the steel block has therefore altered the boundary conditions of the transducer and consequently the resonance frequencies have increased. Given that there that are no frequency peaks below 145kHz, it is possible that the resonance mode at 145kHz represents the first symmetric mode.

We have attached the transducer to the block for performing time marching FE analysis. Modelling the transducer using eigenvalue analysis is difficult because of the difficulty in specifying appropriate boundary conditions to model the boundary between the transducer and the block. We could carry out an eigenvalue analysis on the whole system but the results would be dominated by the modes of the block. We have already obtained the first three resonance frequencies assuming free boundary conditions and can see that the frequencies are lower than that obtained from the time-marching FE analysis when the transducer is attached to the block. We can similarly obtain resonance frequencies by analysing the transducer with its base clamped to the

block. The first three symmetric mode resonance frequencies are 708kHz, 759kHz and 854kHz. We can see that these values are much higher than those from the time-marching FE analysis. Given that the steel block is not rigid (i.e. not infinitely stiff) nor is it infinitely compliant, it can be assumed that the true resonance of the coupled transducer will lie somewhere between the values calculated for the two different boundary conditions.

The next stage is to look at the cases where there is a backing on the transducer. We have chosen a range of materials with different acoustic impedances for the backing, the details of which are given in Table 7.1.

MATERIAL	Density (kg/m^3)	Long. Bulk Vel. (m/s)	Shear Bulk Vel. (m/s)
Tungsten epoxy	9000	1194	573
PZT	7500	3225	1549
Brass	8400	4400	2200
Steel	7700	5900	3230

Table 7.1 Properties of various backing materials

Note that damping was not included in the model. The modified outline for the FE model of the transducer is shown in Fig.7.24. Figs.7.25a, 7.25c, 7.25e and 7.25g show the time domain responses of transducers with the various backings when the transducer is attached to the steel block and Figs.7.25b, 7.25d, 7.25f and 7.25h show the corresponding spectrum of the ringing signals. If we look at the case of a tungsten epoxy backing (Fig.7.25a), we can see that the amplitude of the ringing is appreciable compared with the amplitude of the input signal. From the spectrum (Fig.7.25b), we can see that there are two frequency peaks, at 60kHz and 87kHz, indicating that two structural resonances are being excited. The frequencies of these resonances are fairly close to that of the input signal (70kHz). The usual methods of eliminating unwanted signals at frequencies different to the input frequency are to use filtering or to make the bandwidth of the input signal narrower by increasing the number of cycles. In this particular case both methods will be ineffective at frequencies so close to the centre frequency of the input signal. If the backing material is the same as the piezoelectric material (i.e. PZT), the time domain results indicate appreciable ringing (Fig.7.25c). The ringing occurs at a frequency of 83kHz (Fig.7.25d) which is still too close for filtering to be effective. There is also some resonance activity at 137kHz. Opting for brass as the backing material results in quite low levels of ringing (Fig.7.25e). The frequencies of the ringing are at 114kHz and 156kHz (Fig.7.25f) which should be able

to be filtered out quite comfortably. If the backing material is steel, the situation is slightly better than that of brass as the ringing level is even lower (Fig.7.25g) and the frequency higher at 155kHz (Fig.7.25h).

In order to gain some insight into the variation of resonance frequencies with backing material, it is useful once again to look at the eigenvalue solutions for the transducer. Given that it is difficult to model the exact boundary conditions between the transducer and steel block, we will assume that the transducer is free. We have seen that by assuming free boundary conditions, the calculated eigen frequencies do not agree well with those obtained from time-marching FE analysis when the transducer is attached to the block. However, trends obtained from the free case can be used to predict what happens in the coupled case on the assumption that trends obtained from the free transducer case will be similar to those of the coupled case.

If we first look at the case of the tungsten loaded epoxy backing (this backing was chosen because it is commonly used as a backing material in ultrasonic transducers), then from the time marching FE results two modes are present at 60kHz and 87kHz (Fig.7.25b). We neglected damping in the FE model because the interest was in looking at the effect of stiffness of the backings. These frequencies are much lower than that for the unbacked transducer. From the eigenvalue analysis, the first three symmetric modes assuming free boundary conditions are 29.4kHz, 36.0kHz and 49.0kHz. If we change the backing to a stiffer material, PZT, the eigen frequencies of the three lowest order symmetric modes have all increased considerably to 71.9kHz, 87.6kHz and 127.0kHz. Their mode shapes are similar to those of the tungsten epoxy backing case and have not been shown. The effect of the stiffer material is therefore to increase the eigen frequencies. The resonance frequencies obtained from the time-marching FE analysis have likewise increased, to 83kHz and 137kHz (Fig.7.25d). Finally, if we look at the case of a very stiff material, steel, the eigen frequencies for the first two symmetric modes are now 138kHz and 177kHz. The resonance frequency obtained from the time-marching FE analysis was 155kHz. The comparisons are summarised in Table 7.2.

Backing Material	Frequencies of max. response from time-marching FE analysis (kHz) when transducer is attached to block	Natural frequencies from eigenvalue FE analysis (kHz) for free transducer
Tungsten epoxy	60, 87	29, 36, 49
PZT	83, 137	72, 88, 127
Steel	155	138, 177

Table 7.2 Comparison of frequencies of maximum response from time marching FE analysis with natural frequencies from eigenvalue analysis

We can therefore see a general trend; the stiffer the backing, the higher the eigen frequencies and the higher the resonance frequencies obtained from time-marching FE analysis. If we compare all the different backing cases, then from a ringing point of view, we can see that the best cases correspond to the transducer having either no backing or a steel backing. The steel backing gives slightly lower levels of ringing. From a practical point of view, the inclusion of a backing is useful as it allows the transducer to be more rigid and robust.

Up to now, we have only considered symmetric modes. In fact, for all the eigenvalue cases we have run so far, the lowest frequency mode has always been a symmetric mode. If we were to increase the thickness of the backing, we would expect the natural frequency of symmetric longitudinal bending modes to increase (i.e. modes which bend in the xy plane (Fig.7.26a shows the coordinate sytem used for the transducer; Fig.7.26b shows the mode in question). However, by doing so, it may lower the natural frequencies of other modes, for example lateral bending modes (Fig.7.26c) where the modes bend in the yz plane. Although non-symmetric modes were not modelled in the time-marching FE analysis, they may exist in real life, for example, due to asymmetry in the attachment of the transducer to the pipe. Their influence can be minimised by keeping the height of the transducer small. Also, given the fact that the excitation in the element is heavily biased towards the excitation of modes in the xy plane, the lateral bending modes should not be too problematic.

We have said that the effect of changing the backing thickness is to alter the natural frequencies; increasing the backing thickness increases the resonance frequencies of symmetric longitudinal bending mode but decreases the resonance frequencies of lateral bending modes. There is also interest in determining whether the backing thickness affects the amplitude of the excited L(0,2) mode.

So far, all FE runs have been carried out with the transducer connected to a large steel block. Given that we now wish to look at how well the L(0,2) mode is excited in a steel pipe, all subsequent FE runs are carried out with the block being replaced by a pipe. Fig.7.27 shows the outline of the amended model. The pipe was 2m long, 5.5mm thick and had an outer diameter of 89mm. The transducer was positioned on the outer surface of the pipe midway along the length of the pipe. Points along the surface of the pipe were monitored. The positioning of the transducer at the centre of the pipe was to ensure that at the monitoring points the outgoing signals would not be affected by the reflected signals from the ends of the pipe. The model was assumed to be axisymmetric. This meant that i) the transducers were modelled as a ring transducer and ii) only the L(0,n) class of pipe modes can be generated in the pipe. Strictly speaking, the modelling of the transducers as being axisymmetric is not representative of the real transducers which have a finite width. The results will therefore not be directly comparable to those which can be obtained from experiments. However, the trends should be the same and given the enormous computational time difference between an axisymmetric and a three dimensional model, an axisymmetric model is felt to be sufficient provided we accept that only trends are being studied, not absolute results. Steel has been chosen for the backing material since the earlier studies showed that it was the most satisfactory backing material.

Figs.7.28a, 7.28b and 7.28c show the time domain responses for backing thicknesses of 10mm, 8mm and 6mm for a monitored point which was 518mm away from the front edge of the transducer. The particular monitoring point was chosen because at this point, the L(0,2) and L(0,1) modes had separated enough for them to be completely resolvable in the time domain. In all subsequent time domain plots, the same point is monitored. The first signal corresponds to the directly transmitted L(0,2) mode. The second pulse is the slower L(0,1) pulse and we can see from the width and number of cycles that some dispersion has taken place in this mode. The results show that the effect of backing thickness (and hence mass) seems to have negligible influence on the amplitude of L(0,2).

7.6.3 Effect of Shim Thickness

The next parameter to be studied is the influence of the thickness of the shim on the excitation amplitude of L(0,2). Three thicknesses of shim were investigated: 0.1mm, 1mm and 2mm. The shim material was brass.

Figs.7.29a, 7.29b and 7.29c show the time domain responses of the monitored point for the three cases. It can be seen that as we increase the shim thickness, the amplitude of the L(0,2) mode drops. This can be attributed to the fact that as the shim thickness gets larger and larger, the shear stiffness of the shim decreases whereas the axial stiffness increases. Therefore, in order to maximise the amplitude of the L(0,2) mode, it is necessary to make the shim as thin as possible.

7.6.4 Effect of Loading Position of the Transducer on the Pipe

Ideally, when we load a transducer onto the pipe, the axial position of contact between each transducer and the pipe will be the same for all transducers. In practice, this may not be the case. For example, the pipe might not be perfectly smooth and therefore the actual position of contact that the transducer makes with the pipe may be more towards one end of the transducer rather than across the whole transducer. Given such potential problems, it is important that we investigate how the loading position affects the excitation of the L(0,2) mode.

To carry out this investigation, we looked at several different loading cases. In each case, we assumed that a certain percentage of the bottom face of the shim was in contact with the pipe and this was modelled using finite elements by joining the shim to the pipe only at those points (or nodes) where contact is made. The backing used is once again steel and a 0.1mm thick brass shim is assumed. Fig.7.30a shows the case when full contact is made. If we now assume that 4/7 of the shim area is in contact (the 7 refers to the number of elements used to model the length of the shim), then the time domain response of Fig.7.30b is obtained. We can see that the amplitude of L(0,2) has increased significantly. If we now look at the case where only 1/7 of the shim area is in contact (Fig.7.30c), the contact occurring at the centre of the shim, we can see that the amplitude of L(0,2) has dropped by over 90% compared to the previous case. There is clearly a large variation in the amplitude of L(0,2) when the contact area between the transducer and pipe is varied.

If we now look at the two cases corresponding to contact occurring at one end of the transducer then by overlaying the respective time domain responses, we can see that there is almost a 180° phase shift between the two signals (Fig.7.31). This phase shift is due to the difference in the direction of the excitation at the contact position; when the transducer is coupled to the pipe at the left hand end, the excitation direction is out of phase with the excitation which occurs when the transducer is coupled at the right hand end. The reason it is not exactly 180° is because there is a small phase shift due

to the fact that the axial positions where the contact takes place were not the same, but were separated by almost the length of the transducer (Note that the monitoring position on the pipe was fixed).

We have therefore seen that depending on where the transducer is loaded onto the pipe, the amplitude of the excited L(0,2) mode can vary by a large percentage. Furthermore, the phase of the excited mode can change. Such a situation is to be avoided because a difference in amplitude or phase between different transducers can give rise to the excitation of flexural (F(m,n)) modes as seen in the first part of this chapter.

7.7 Shear Piezoelectric Elements

7.7.1 Effect of Backing

For the shear piezoelectric elements, the effect of the backing material on structural resonances is expected to be similar to that for expansional piezoelectric elements because the structural properties are the same. There may however be an influence of the backing thickness on the amplitude of L(0,2). To see if this is the case, we used the same FE model used previously for looking at transducer loading position using expansional elements. The forcing was applied to the top face of the piezoelectric element and the forcing function was assumed to be constant along the length of the element. The shim thickness was taken to be 1mm. All other conditions such as the input to the piezoelectric element and the monitored points are the same as for the expansional element cases. Figs.7.32a, 7.32b and 7.32c show the time domain responses for 10mm, 8mm and 6mm thicknesses of backing. The results show that a decrease in thickness leads to a decrease in the amplitude of L(0,2). A possible reason for this is that the shear element needs a seismic mass for it to provide excitation to the pipe (as in an accelerometer).

7.7.2 Effect of Loading Position of the Transducer on the Pipe

The issue of loading position of the shear type transducer is expected to be different from that of the expansional type transducer given that one type of forcing is symmetrical about the vertical mid-plane (expansional elements) whereas the other is not (shear elements). We have seen in the case of expansional elements that there is a change in phase of the excited L(0,2) mode as a result of the difference in forcing direction when the transducer is loaded onto the pipe at the front of the transducer and

at the back. This directionality of forcing is not present for the shear elements and we would therefore expect the phase problem to be eliminated.

Figs.7.33a, 7.33b and 7.33c show the time domain responses for the full contact, 4/7 contact and 1/7 middle contact. The results show that the variation in amplitude between different cases is considerably less than that for expansional elements (Fig.7.30a-7.30c). Furthermore, by referring to Fig.7.34 which shows the time domain responses for the alternately edge loaded cases plotted on the same figure, we can see that apart from a slight phase change (due to the difference in the axial position on the pipe where the transducers were loaded), the two signals are in phase. This can be attributed to the fact that all points along the length of the piezoelectric element vibrate in phase, which was not the case for the expansional elements. It is therefore clear that the response of shear elements is much less sensitive to loading position.

Experimental evidence of this is shown in Fig.7.35b (Alleyne and Cawley (1996)) where the shear element was used as a receiver and made contact with the pipe at alternate edges of the element. A ring of 16 expansional transducers was used to excite the L(0,2) mode. Fig.7.35a shows the corresponding results for the expansional elements. Note that in the experiments, the loading position on the pipe was the same for both ends of the transducer; this is the reason why there is no small phase shift evident in the time domain responses between the two loading cases.

7.8 Summary of the Design of Dry-Coupled Piezoelectric Transducers for Lamb Wave Excitation in Pipes

In the second half of this chapter, we have investigated the parameters which are likely to affect the efficiency with which the L(0,2) Lamb mode can be excited in a steel pipe. Two element types have been looked at: expansional elements and shear elements.

One of the main problems was identified as being ringing in the transducer due to structural resonances being excited. Choosing a low stiffness backing is undesirable as the resonant frequency(ies) may lie close to the centre frequency of the input signal even though there may be damping in the backing. It was found that a stiff backing would increase the resonance frequency and at the same time reduce the amplitude of the ringing due to the lower amplitude of forcing at higher frequencies in the input signal. The ringing could then be removed by simple filtering in the frequency

domain, which could not have been achieved if the ringing frequency was close to the frequency of the input signal.

The amplitude of L(0,2) was found to vary significantly with the loading position of the transducer on the pipe for expansional elements. One of the main problems for these type of elements was that the phase of the excited Lamb mode could change if contact with the pipe was made on different halves of the transducer. This was not the case for shear elements. Given the considerably lower sensitivity of shear elements to loading position, transducers based on shear elements would therefore be more suited towards the excitation of a single L(0,2) mode. At present, real transducers based on shear elements are being investigated experimentally and results to date have been promising.

7.9 Conclusions

A form of dry coupled transducer for exciting Lamb waves in pipe structures has been investigated. The particular system investigated was that of a 5.5mm thick, 89mm outer diameter steel pipe where reflection coefficients of about 0.5% from defects using the L(0,2) mode were required. The aim was to develop these transducers for steel pipes with the possibility of then applying them for use on polyethylene pipes.

The investigation was separated into two parts. The first part looked at the question of how many transducers should be placed around the circumference of the pipe. It was found that the number of transducers used had to be chosen carefully in order not to excite unwanted modes whose harmonic number corresponded to the number of transducers used. The issue of consistency of positioning of the transducers on the pipe was also addressed. The results showed that the failure of a single transducer would not make the detection of defects difficult. Tolerance levels for three key parameters were computed, these being axial misalignment of the transducer, circumferential misalignment of the transducer and excitation amplitude of the transducer. The results showed that the axial misalignment tolerance (0.8mm) was less than that for circumferential misalignment (1.1mm) but the difference was not great. The excitation amplitude tolerance for each transducer was found to be about 11%.

The second part of the investigation looked at the design of the actual transducers. Given that the L(0,2) mode is predominantly an in-plane mode, two types of piezoelectric transducers were studied: expansional and shear. It was found that ringing in the transducers could be reduced by using a stiff backing, e.g. steel. One of

the main differences between expansional and shear transducers was that the expansional transducers were sensitive to how they were loaded onto the pipe. This problem was very much reduced when using shear transducers. Therefore, shear piezoelectric elements with a steel backing were chosen as the ideal transducers for exciting L(0,2) in a steel pipe. To date, such transducers have been manufactured and are being used successfully on steel pipes to detect corrosion (Alleyne and Cawley (1996)).

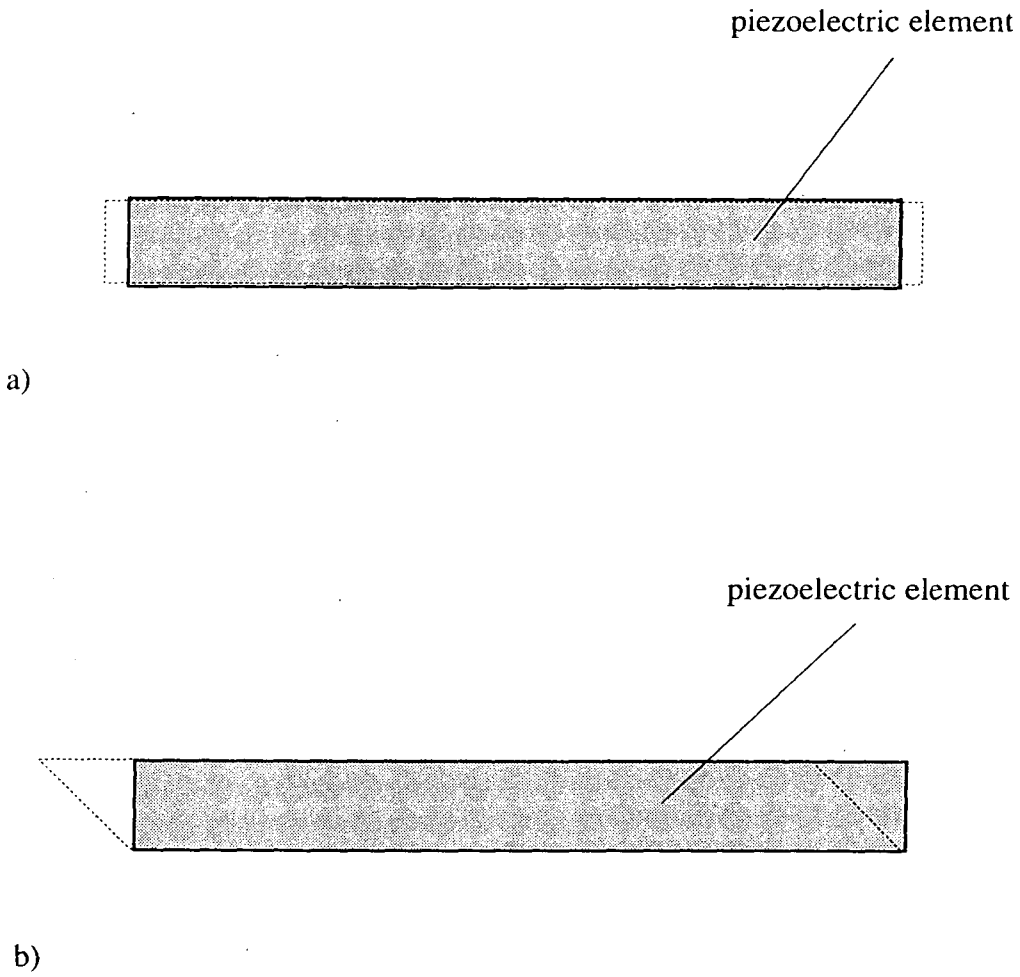
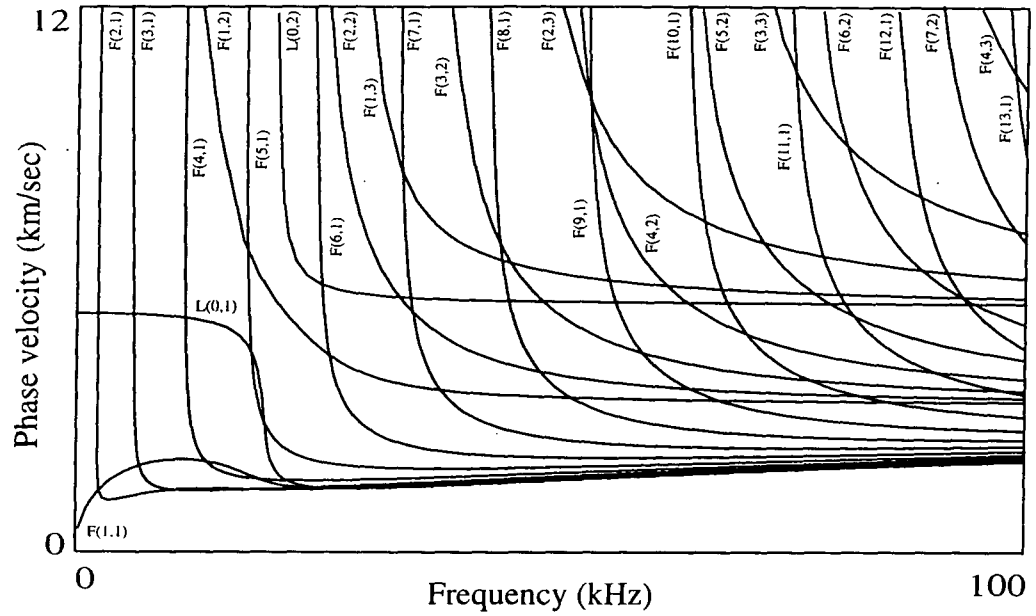
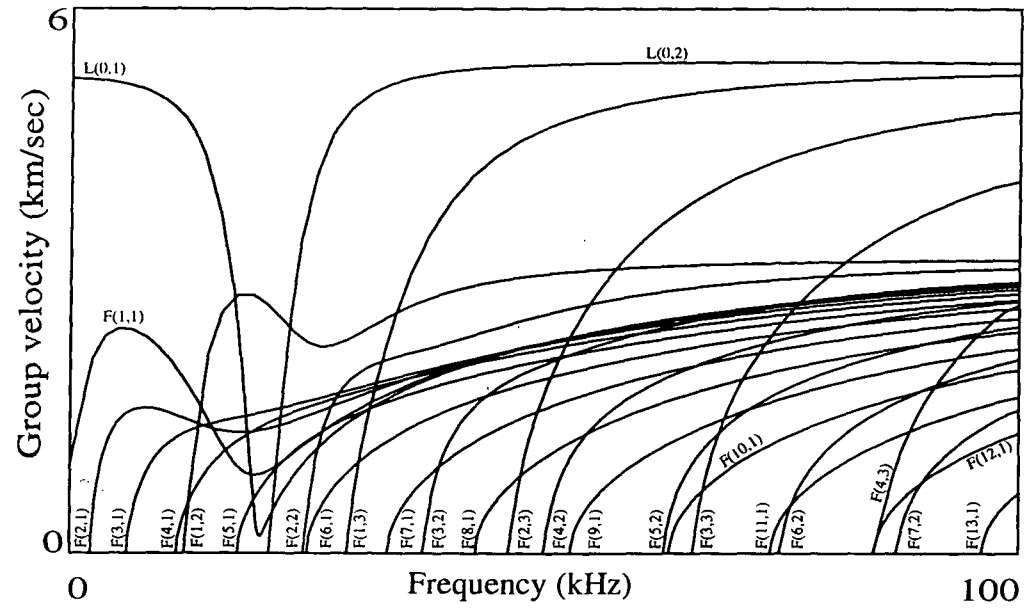


Fig.7.1 Expansional and shear piezoelectric transducers. Schematic of a) expansional piezoelectric element; b) shear piezoelectric element

———— original shape ..... displaced shape

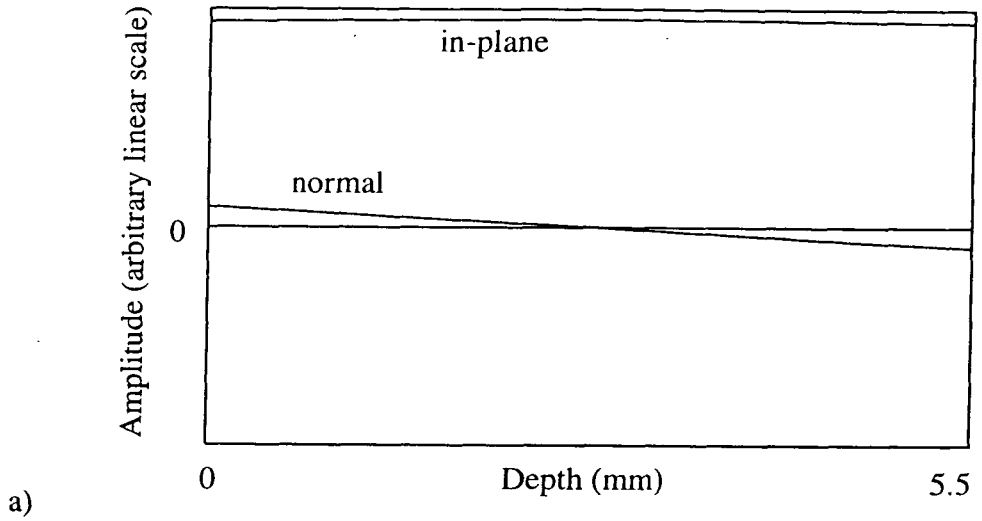


a)

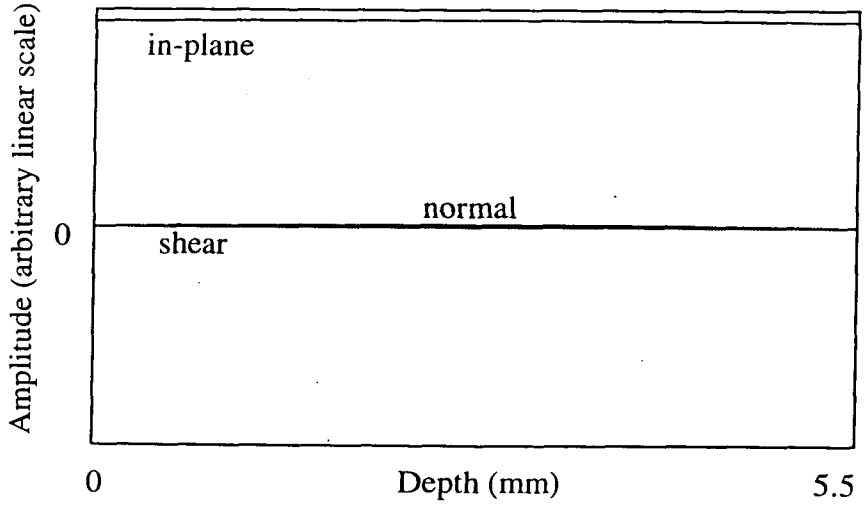


b)

Fig.7.2 Dispersion curves for an 89mm diameter, 5.5mm thick steel pipe. a) Phase velocity; b) Group velocity

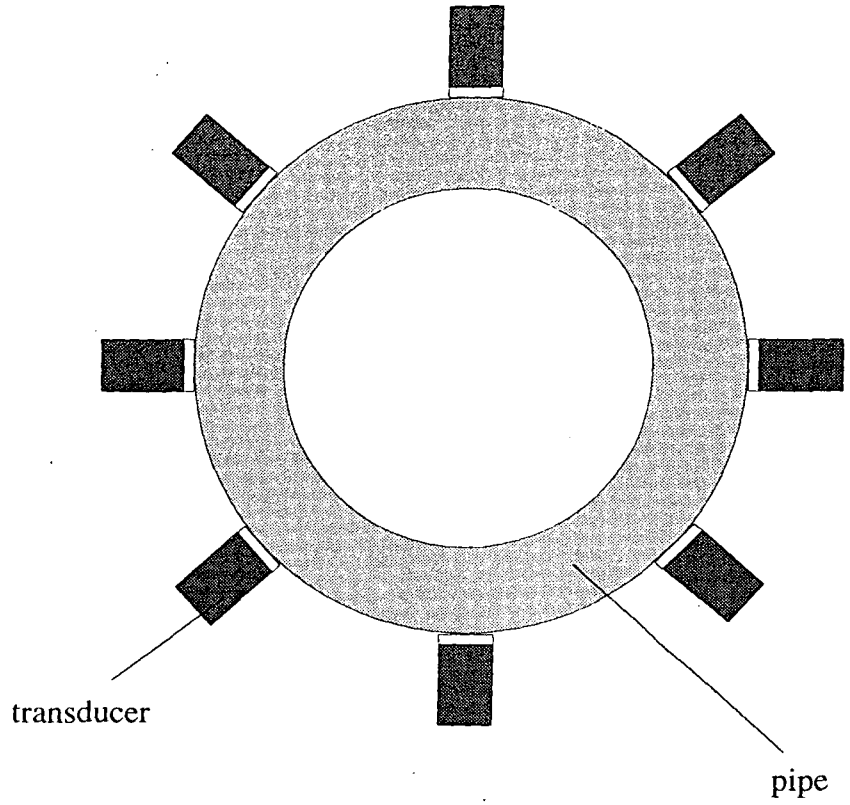


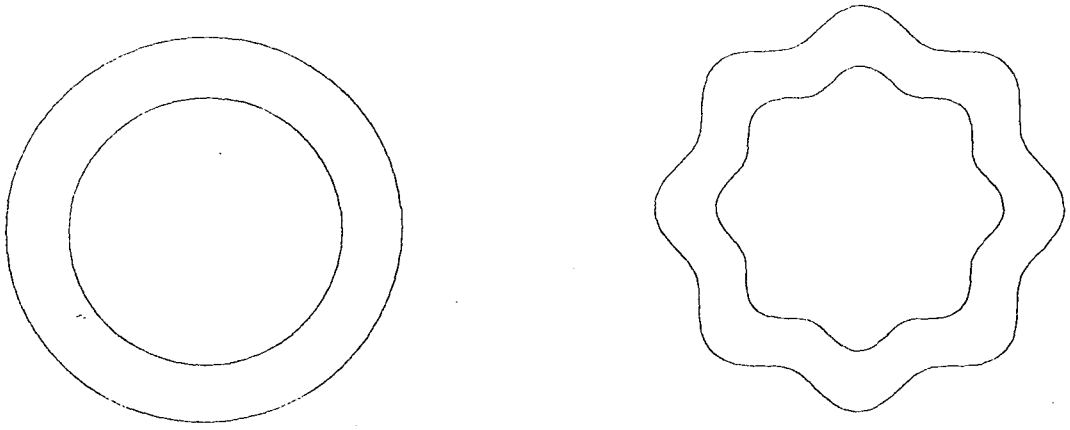
a)



b)

Fig.7.3 Mode shapes for L(0,2) mode at 70kHz. a) Displacement; b) Stress





zero harmonic mode shape

eighth harmonic mode shape

Fig.7.4 Diagram of set-up of transducers on a pipe and possible excited modes for 8 perfect transducers

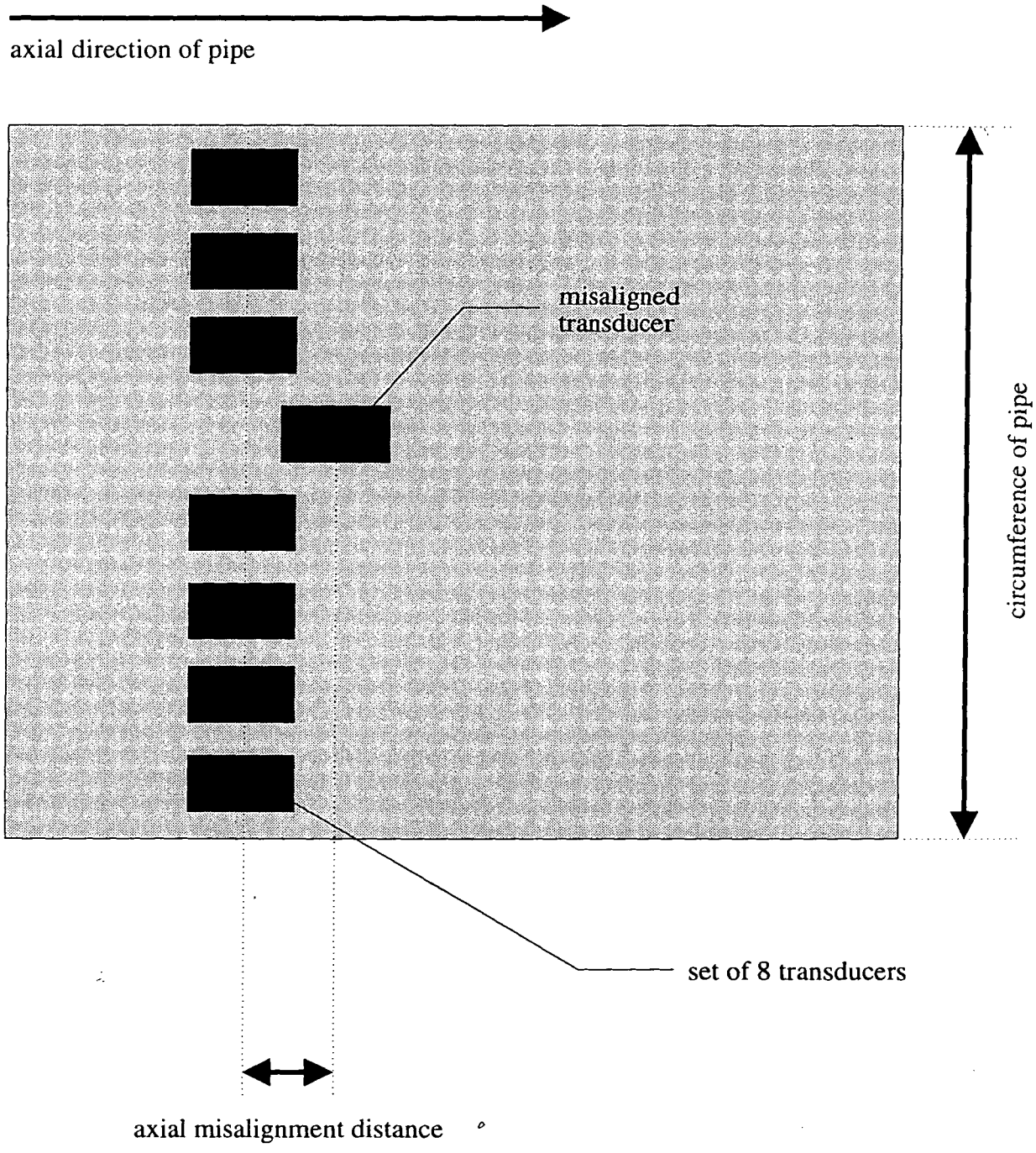


Fig.7.5 Diagram showing axial misalignment of a transducer

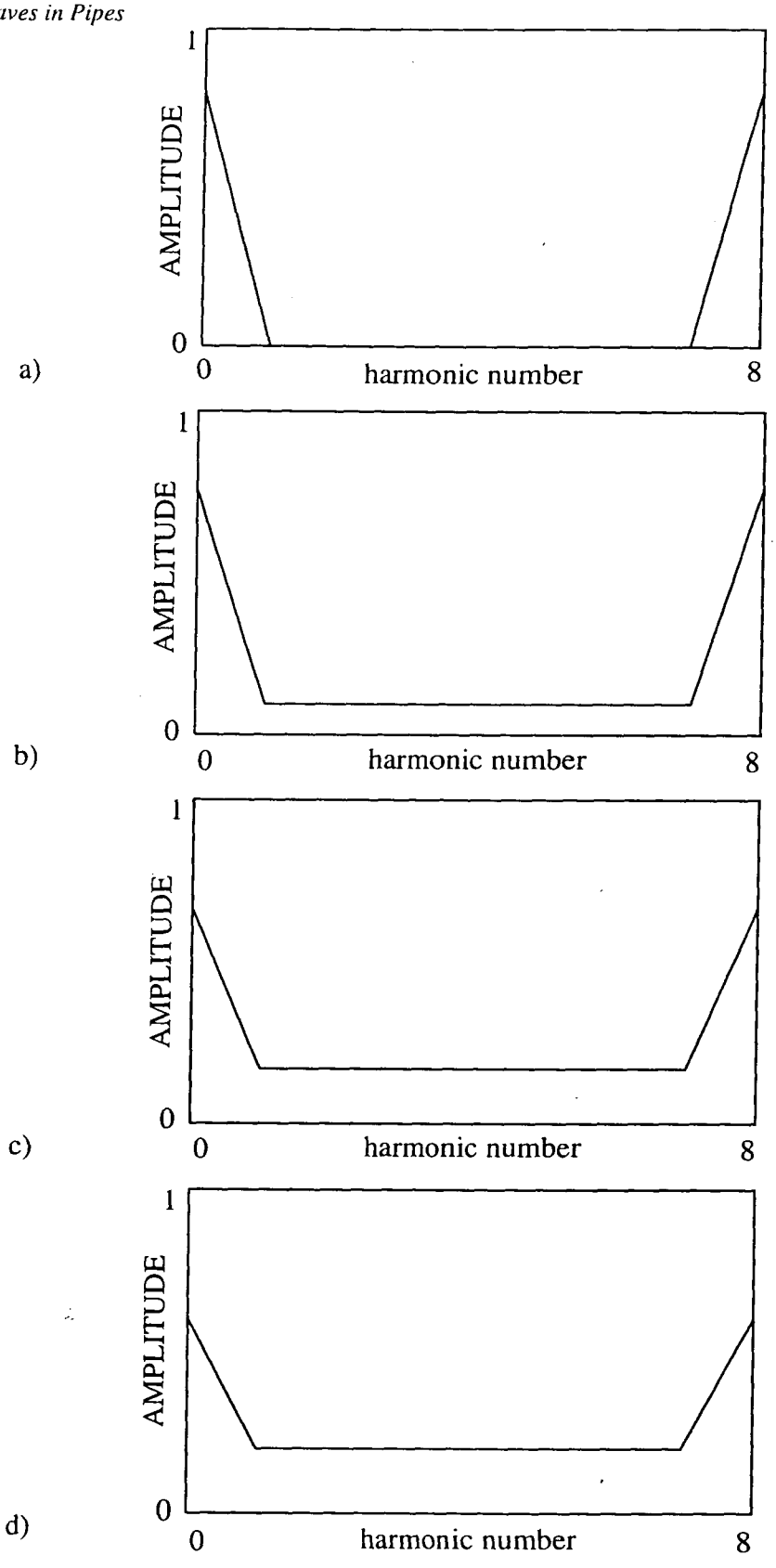
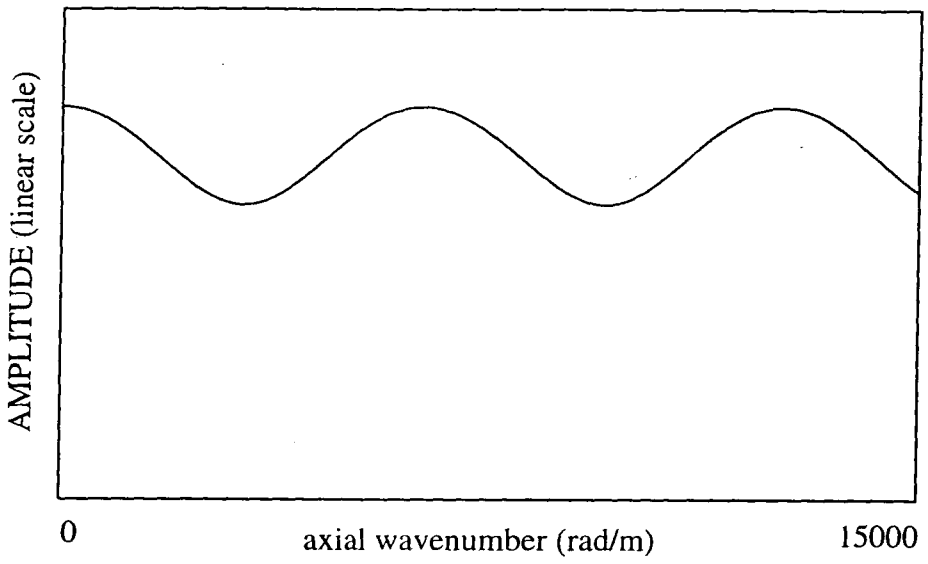
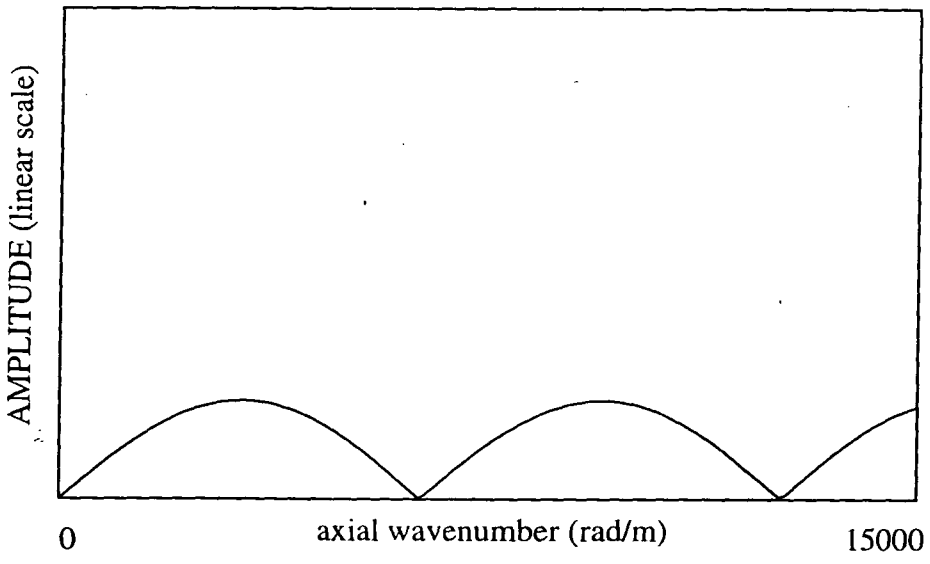


Fig.7.6 Harmonic spectra for 8 transducers around the pipe when a) all transducers are perfect; b) a transducer is misaligned by 1mm (k=1000rad/m); c) a transducer is misaligned by 2mm (k=1000rad/m); d) a transducer is misaligned by 3mm (k=1000rad/m)



a)



b)

Fig.7.7 Axial wavenumber spectrum when a single transducer is misaligned by 1mm. a) n=0 or 8; b) n=1 to 7

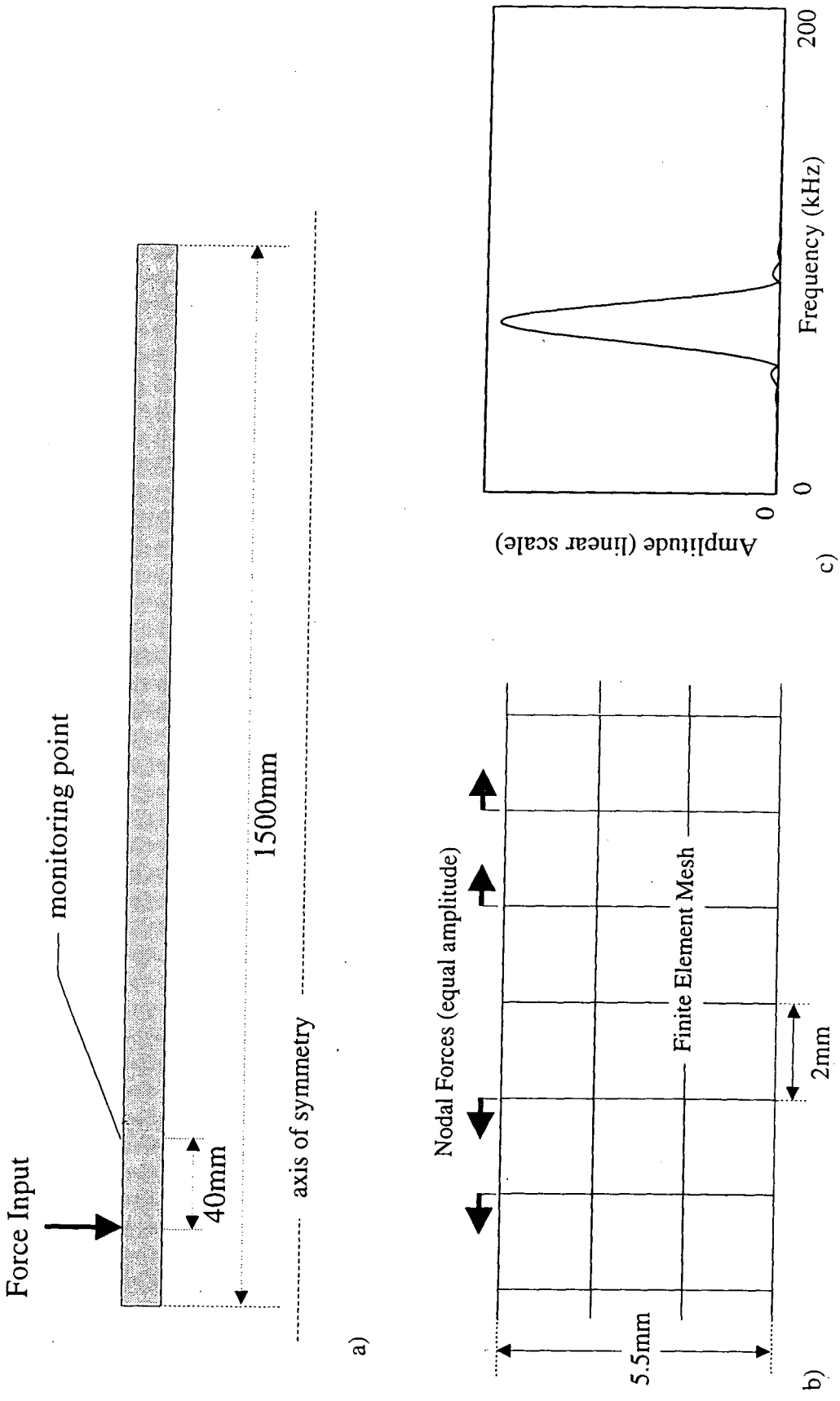


Fig.7.8 Details of FE model used to analyse Lamb wave propagation in steel pipe. a) Schematic of the layout used for FE modelling; b) Forcing pattern used for harmonic number analysis; c) Frequency spectrum of 70kHz centre frequency, 8 cycle tone burst in a Hanning window.

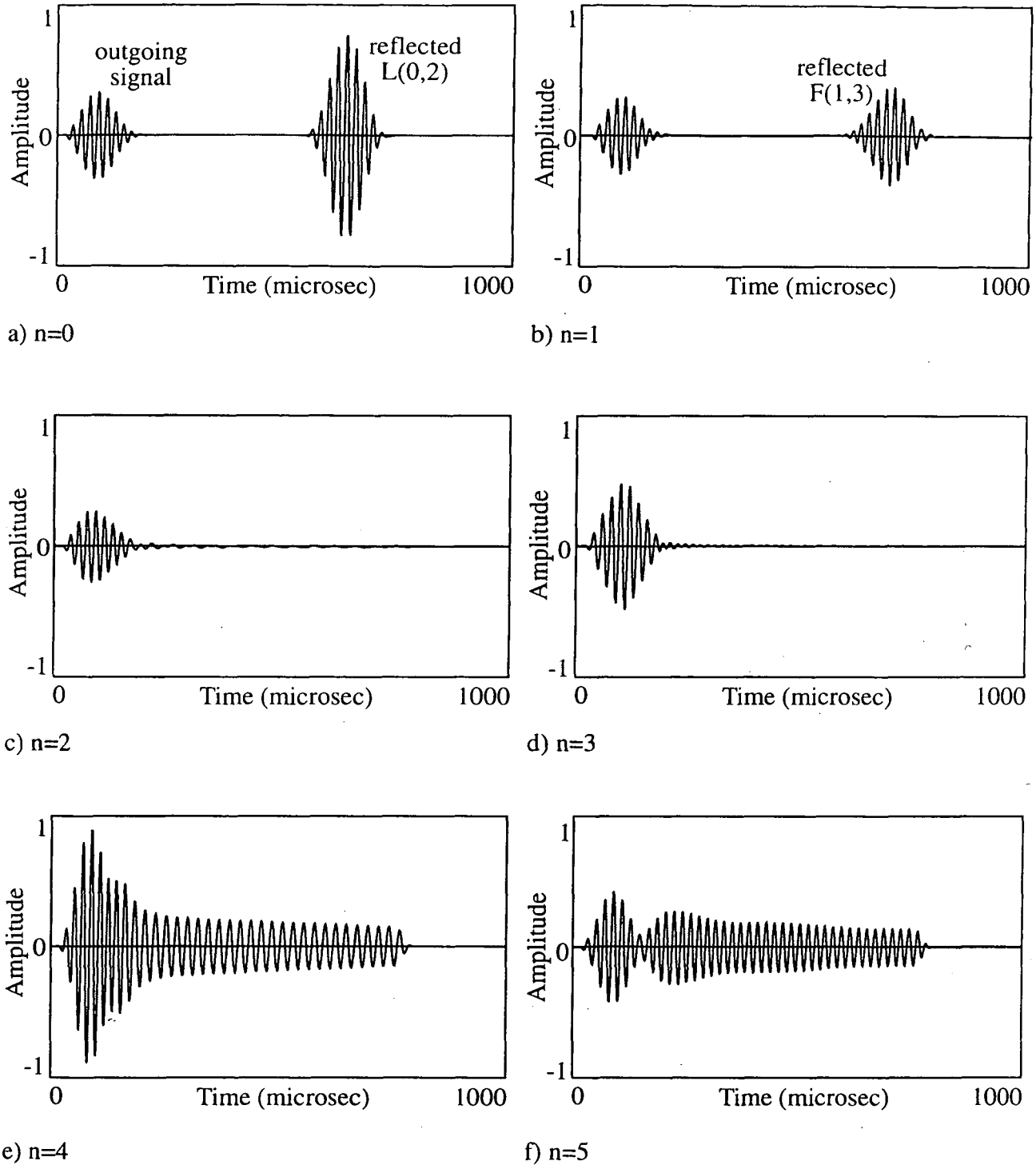


Fig.7.9 Harmonic number FE responses for different harmonic numbers

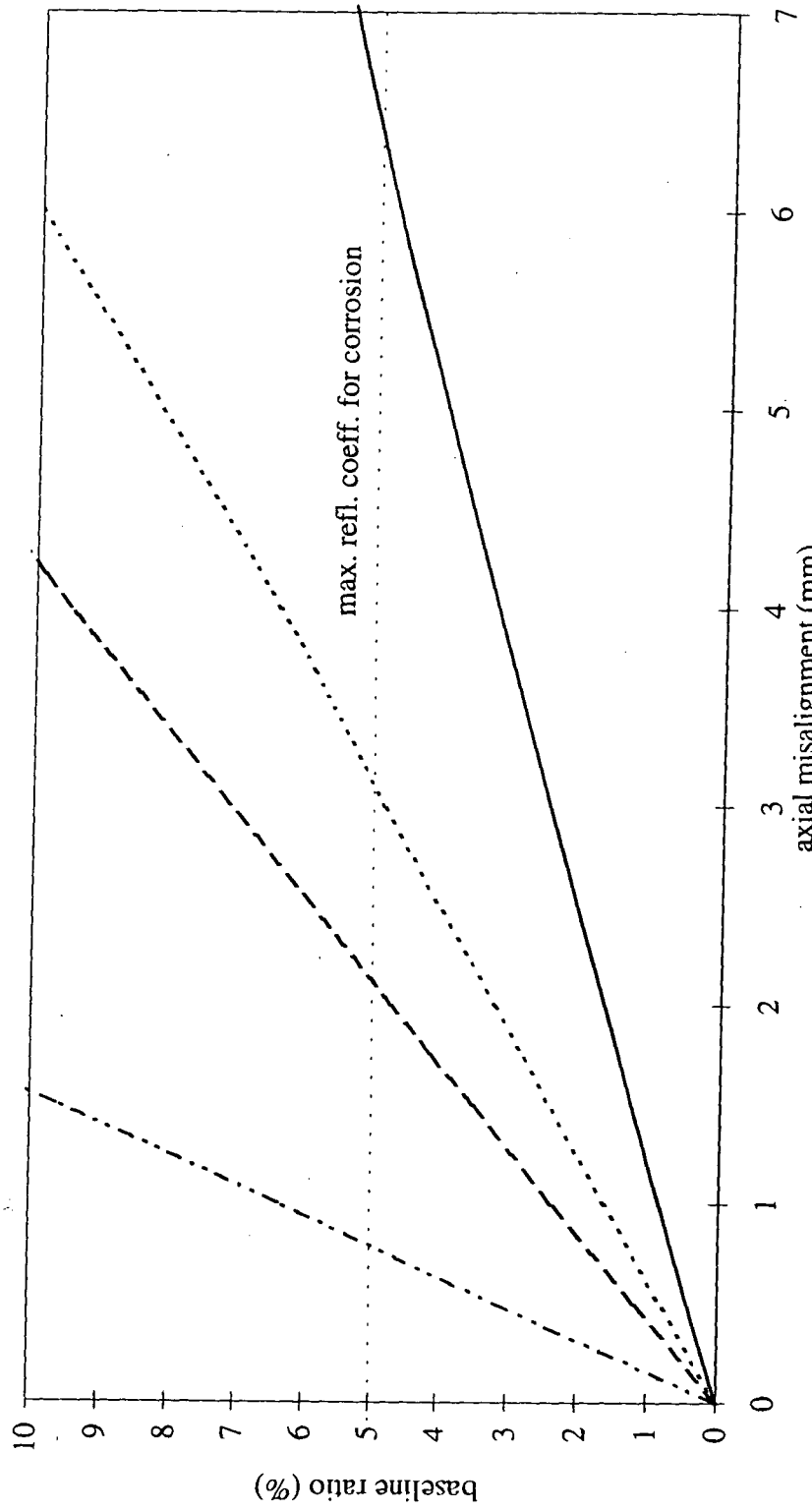


Fig.7.12 Graph of baseline ratio vs. axial misalignment distance

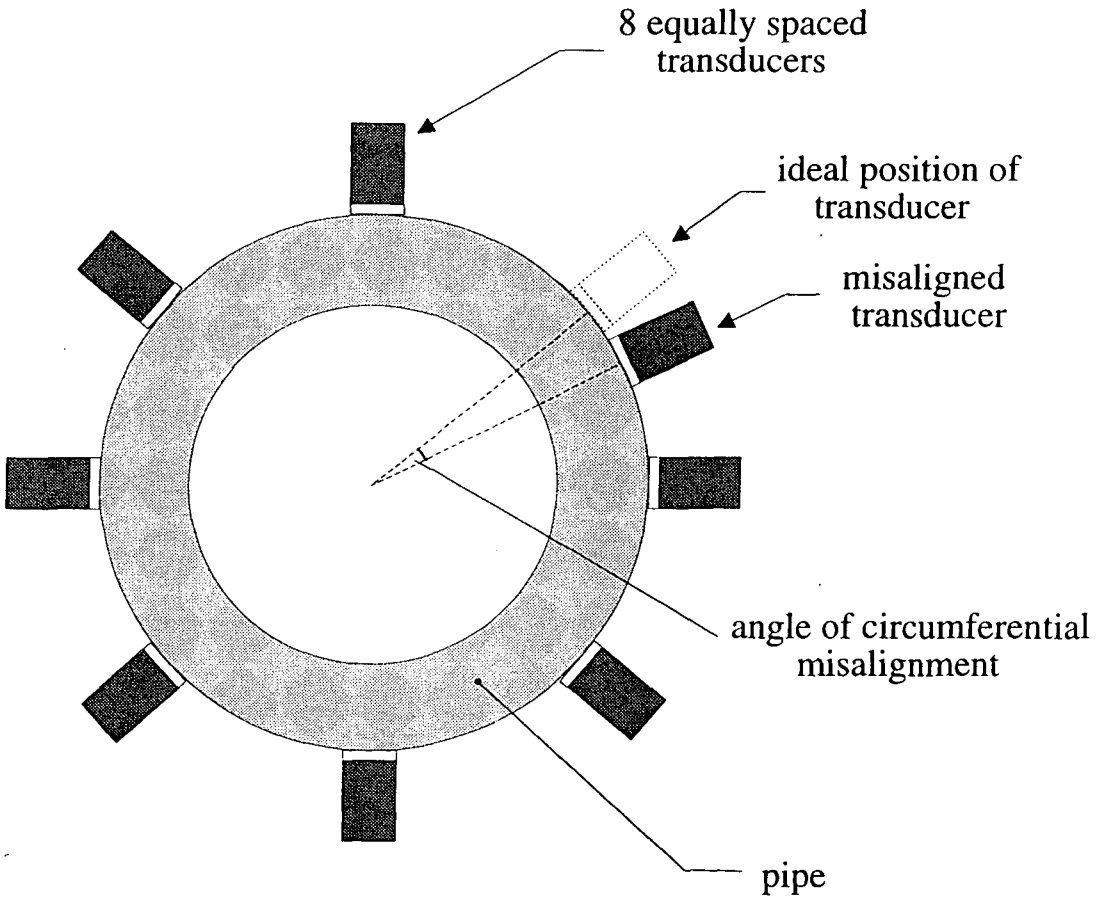


Fig.7.13 Diagram showing a circumferentially misaligned transducer

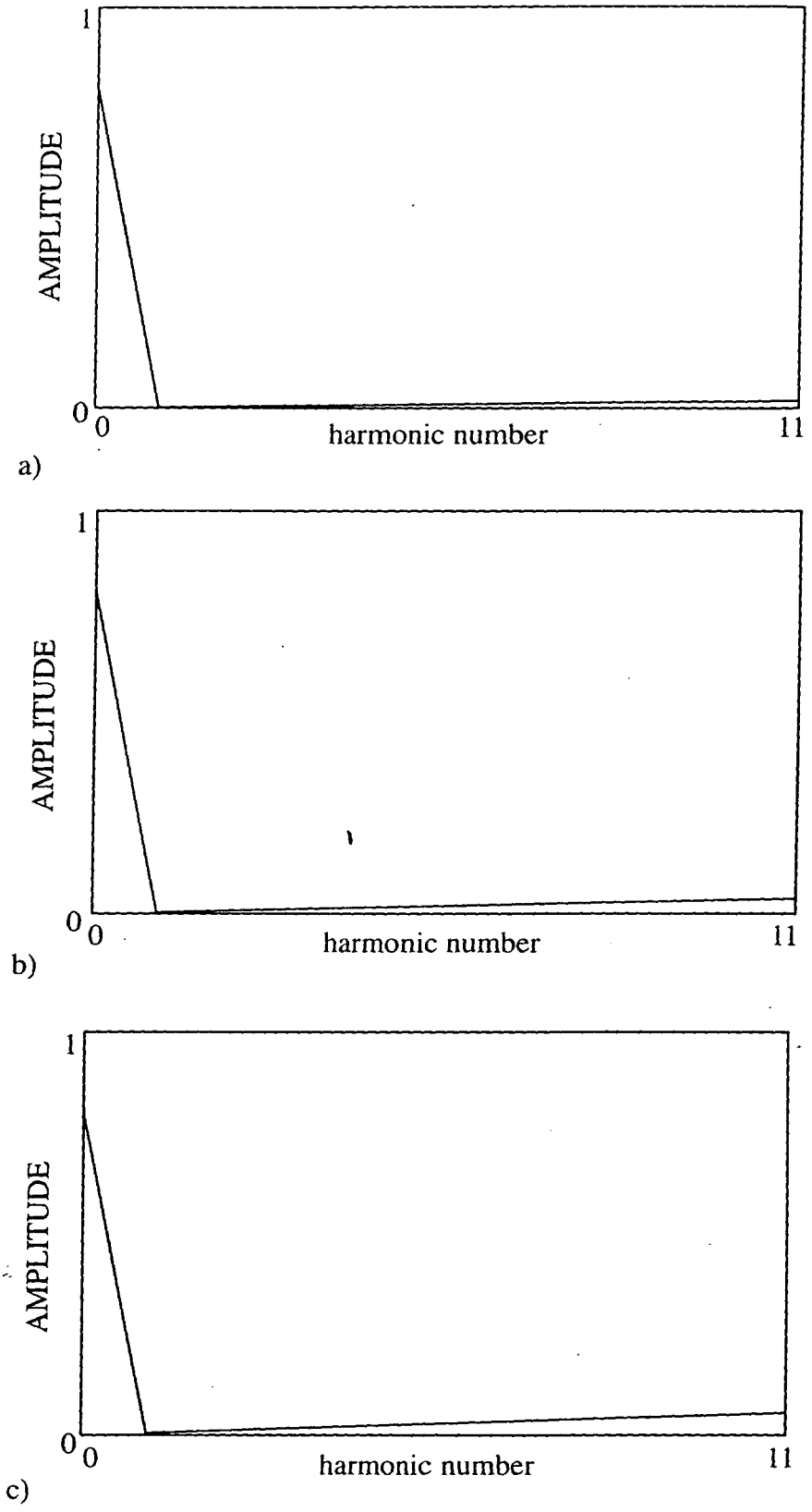


Fig.7.14 Harmonic spectra when 1 transducer is circumferentially misaligned by a) 2 degrees; b) 4 degrees; c) 6 degrees

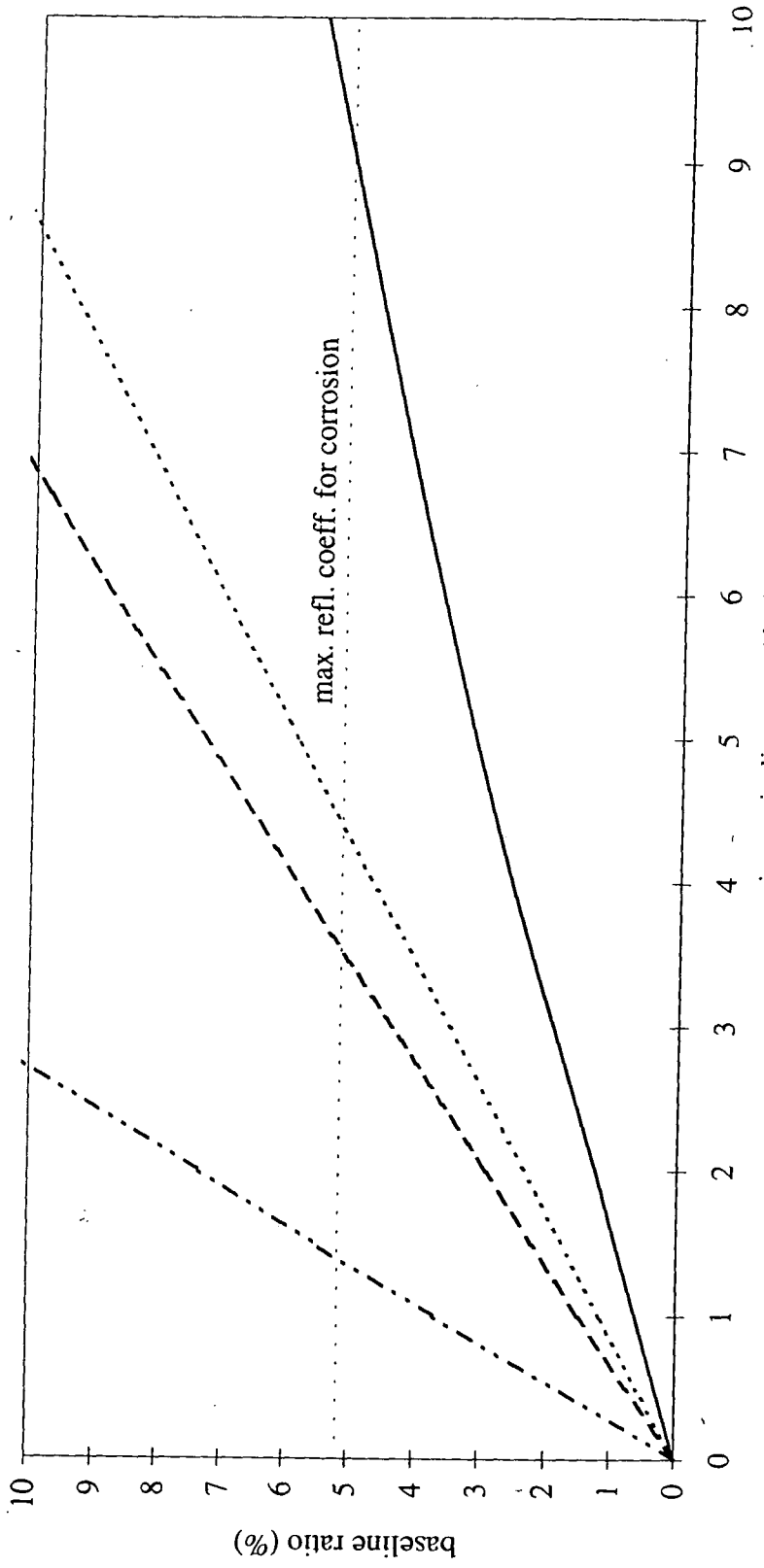


Fig.7.15 Graph of baseline ratio vs. circumferential misalignment distance

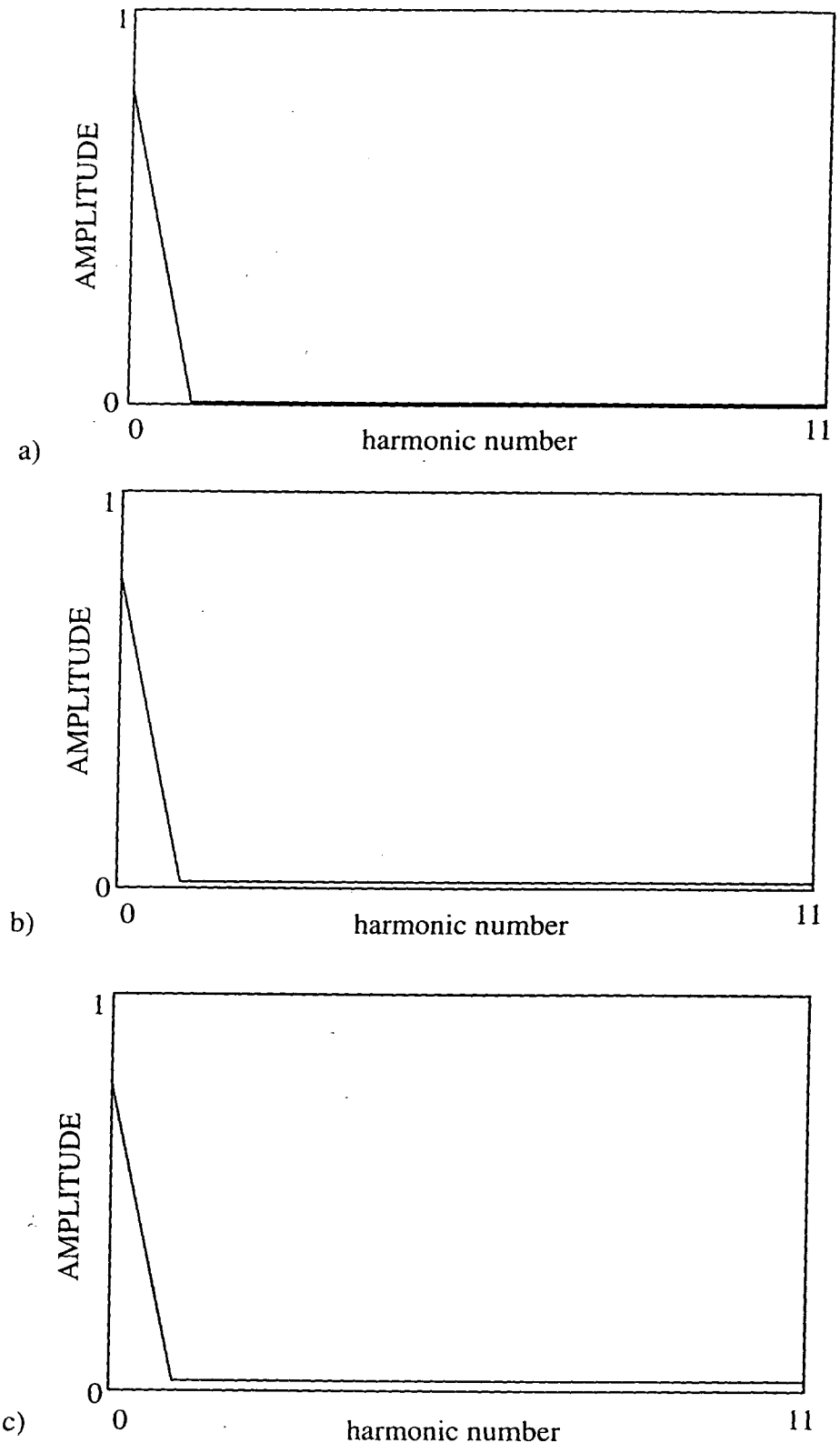


Fig.7.16 Harmonic spectra when the amplitude of one transducer differs from the rest by a) 10%; b) 30%; c) 50%

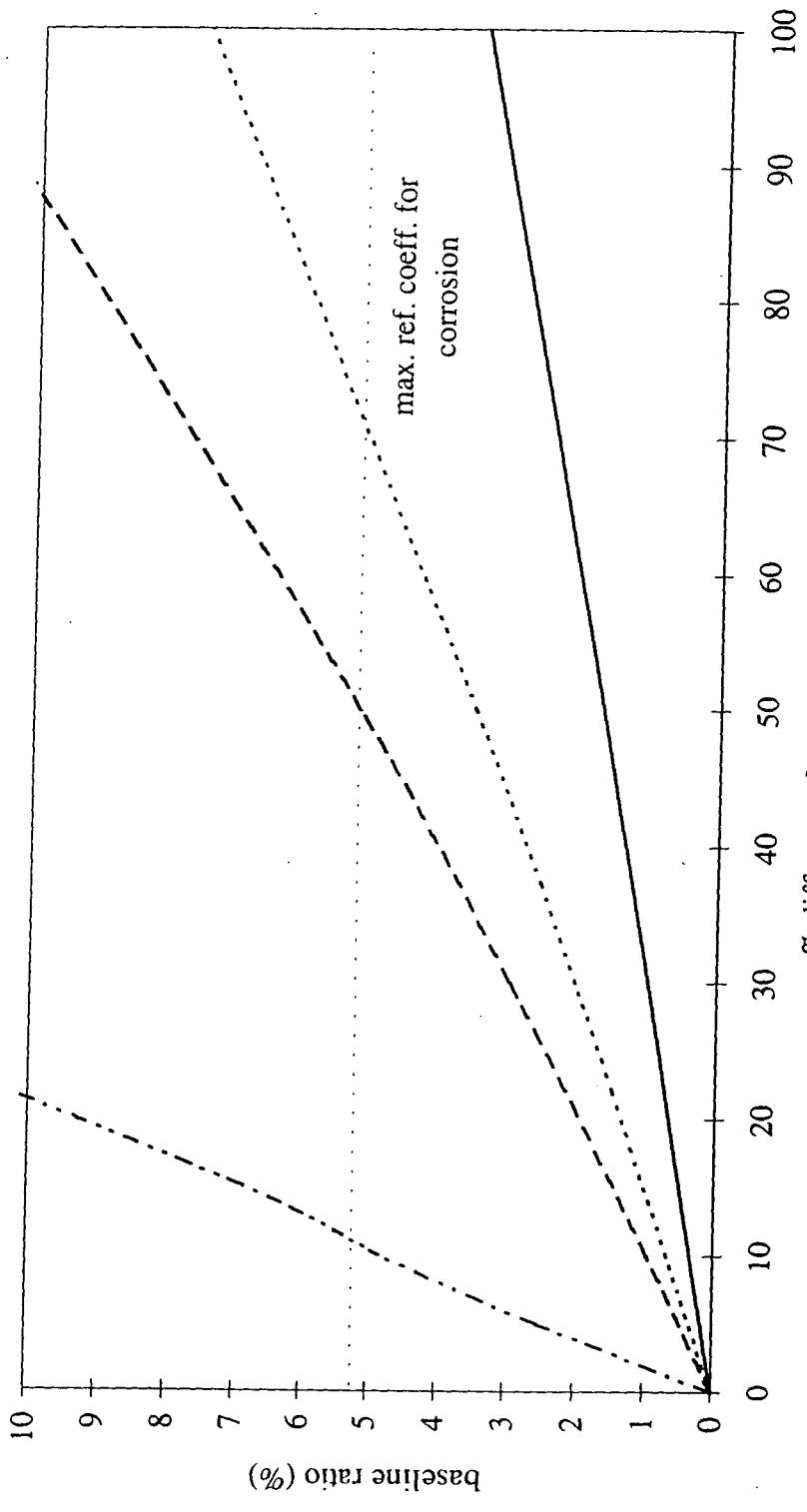


Fig.7.17 Graph of baseline ratio vs. % amplitude difference from an ideal transducer

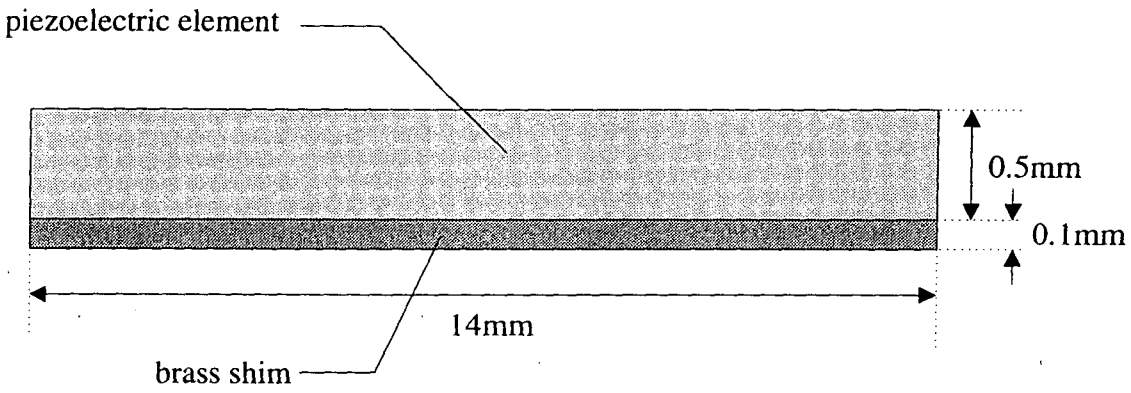


Fig.7.18 Schematic showing the outline and dimensions of the FE model used for looking at the response of a free expansional transducer

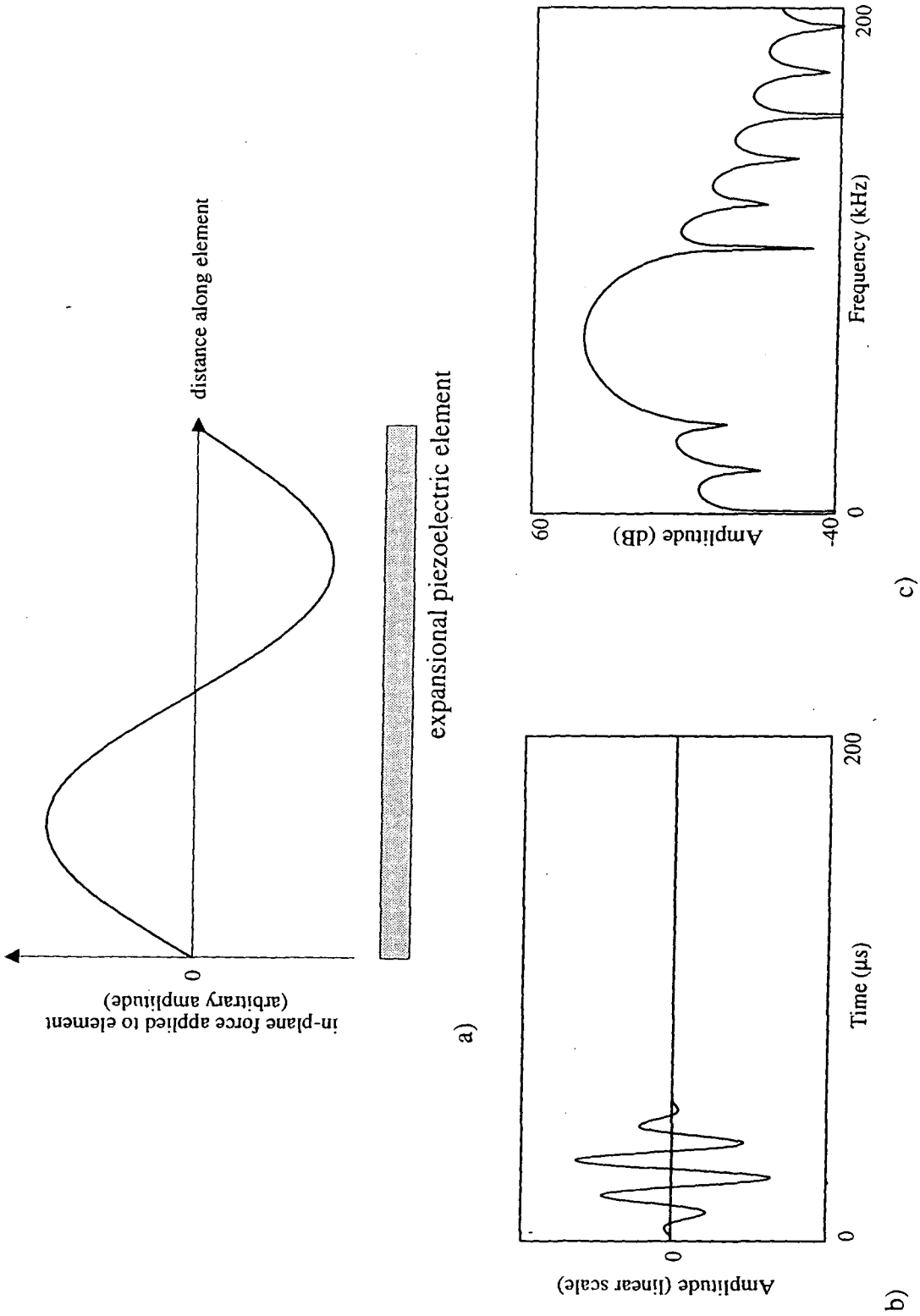
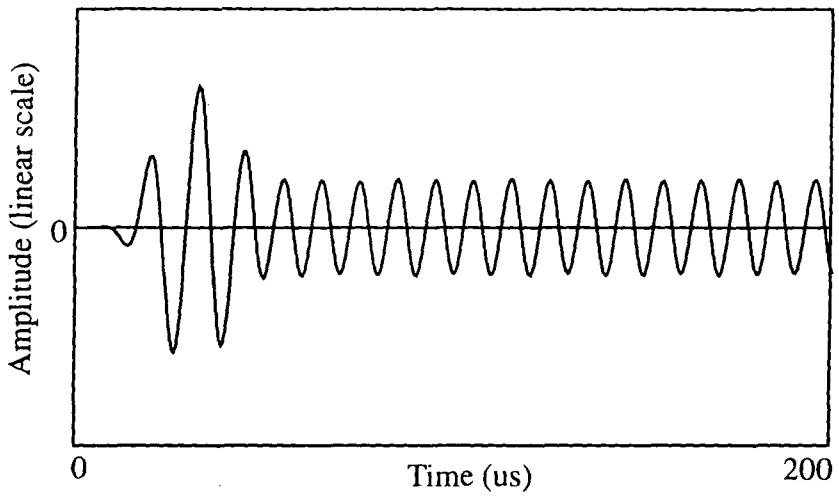
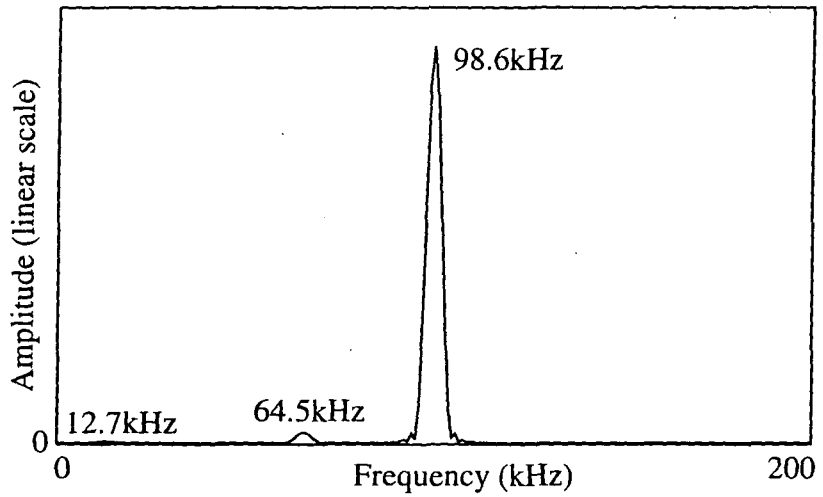


Fig.7.19 Details of excitation input. a) Sinusoidal force function used for excitation of piezoelectric element (70kHz, 4 cycle sinusoidal tone burst in a Hanning window); b) Signal used for excitation of piezoelectric element; c) Spectrum of b)

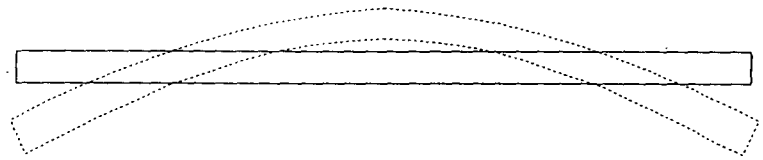


a)

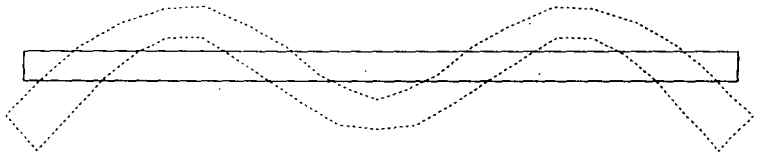


b)

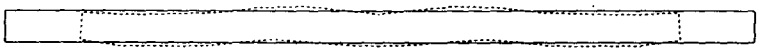
Fig.7.20 Response of an unbacked, freely supported transducer. a) Time domain response; b) Frequency spectrum of ringing signals showing resonance peaks



a)



b)



c)

Fig.7.21 Displacement mode shapes of an unbacked transducer with free boundary conditions. a) first symmetric mode (12.8kHz); b) second symmetric mode (69.3kHz); c) third symmetric mode (99.0kHz)

———— original shape ..... deflected shape

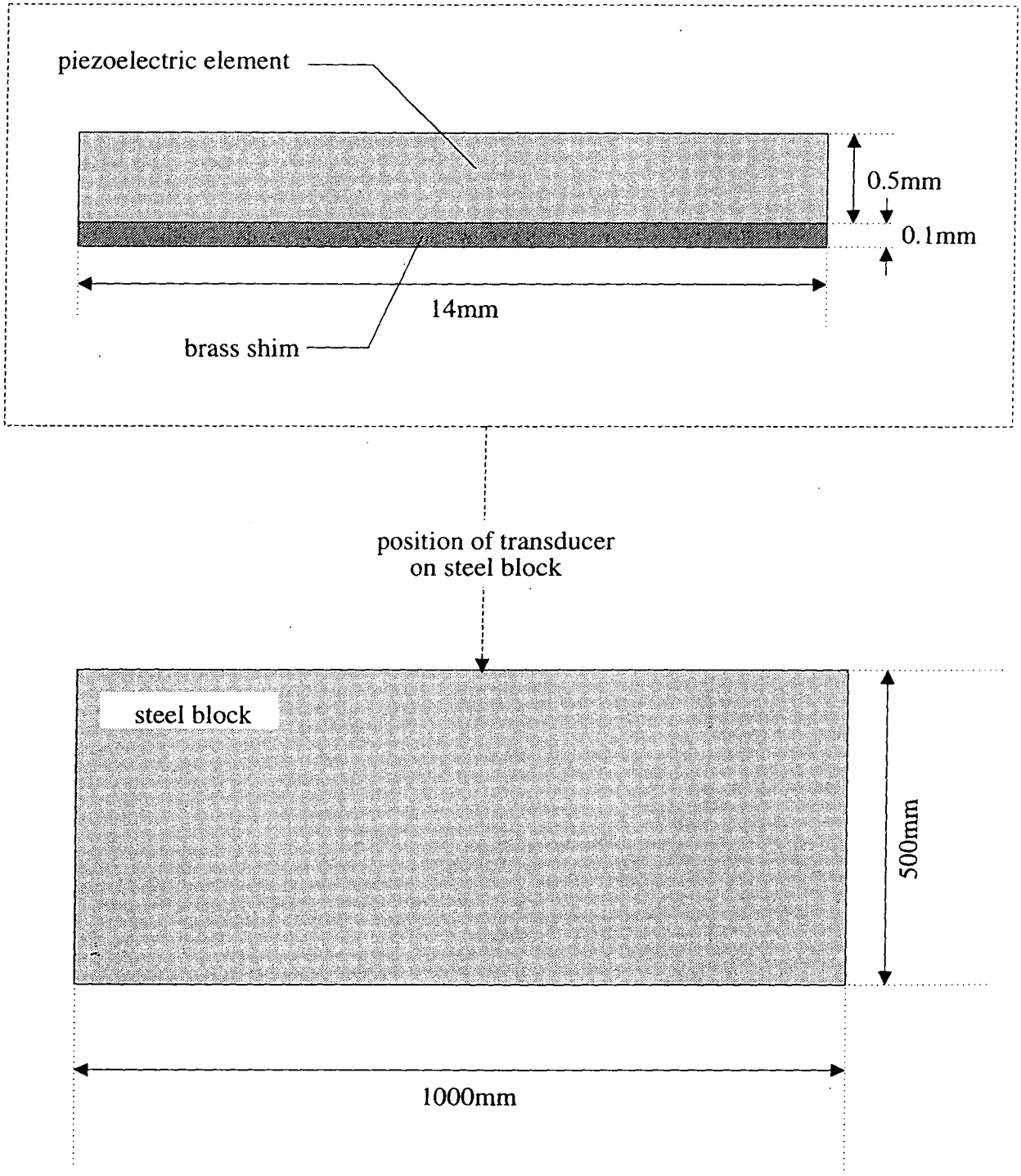
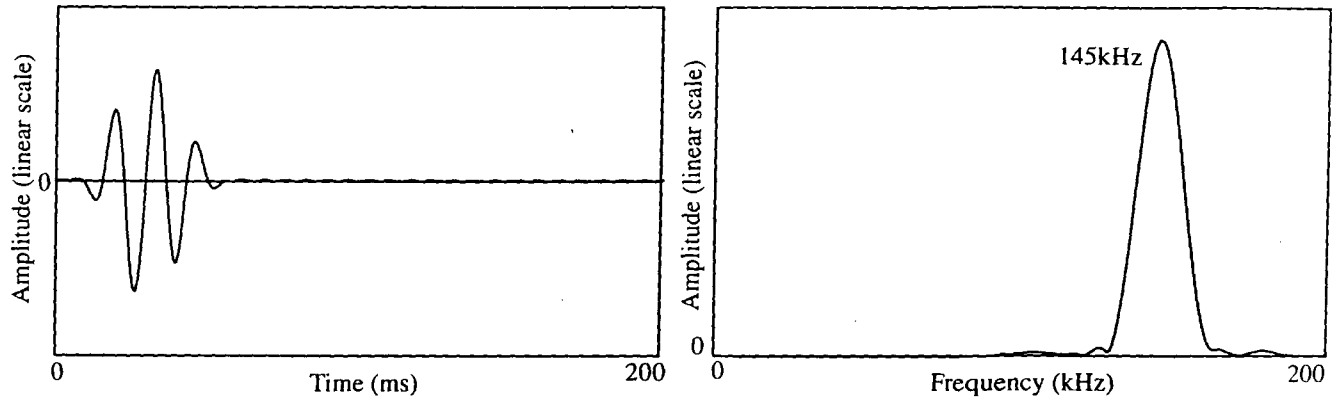
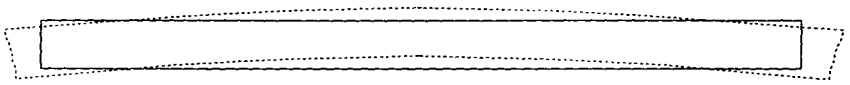


Fig.7.22 Schematic showing the outline and dimensions of the FE model used for looking at the response of an expansional transducer





c)

Fig.7.23 Response of an unbacked transducer coupled to a steel block. a) Time domain response; b) Frequency spectrum of ringing signals; c) deflected shape of resonance mode

——————— original shape ..... deflected shape

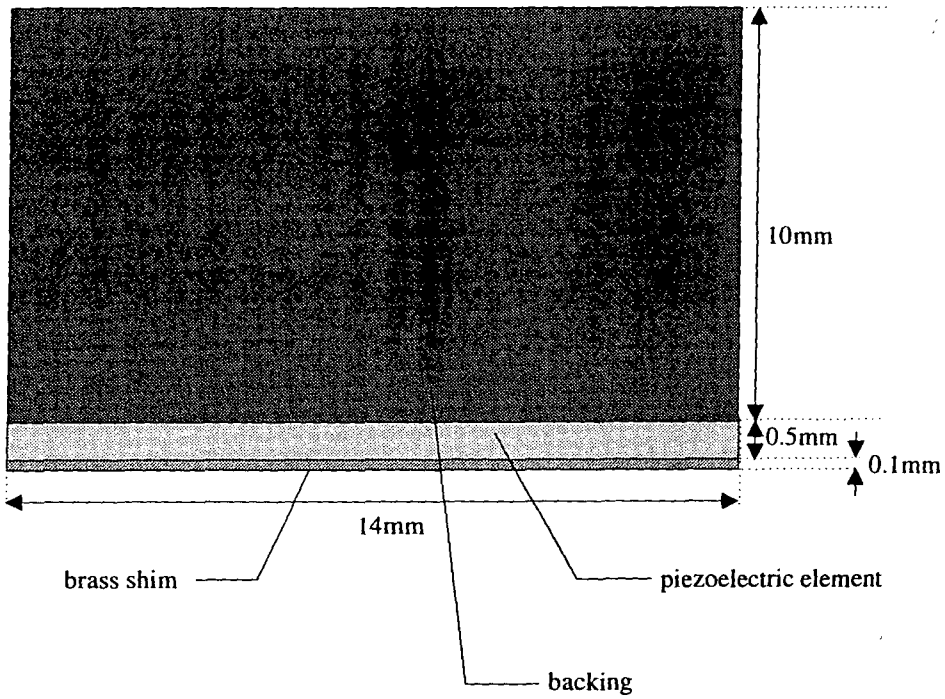


Fig.7.24 Schematic of a transducer with backing showing dimensions used for FE model

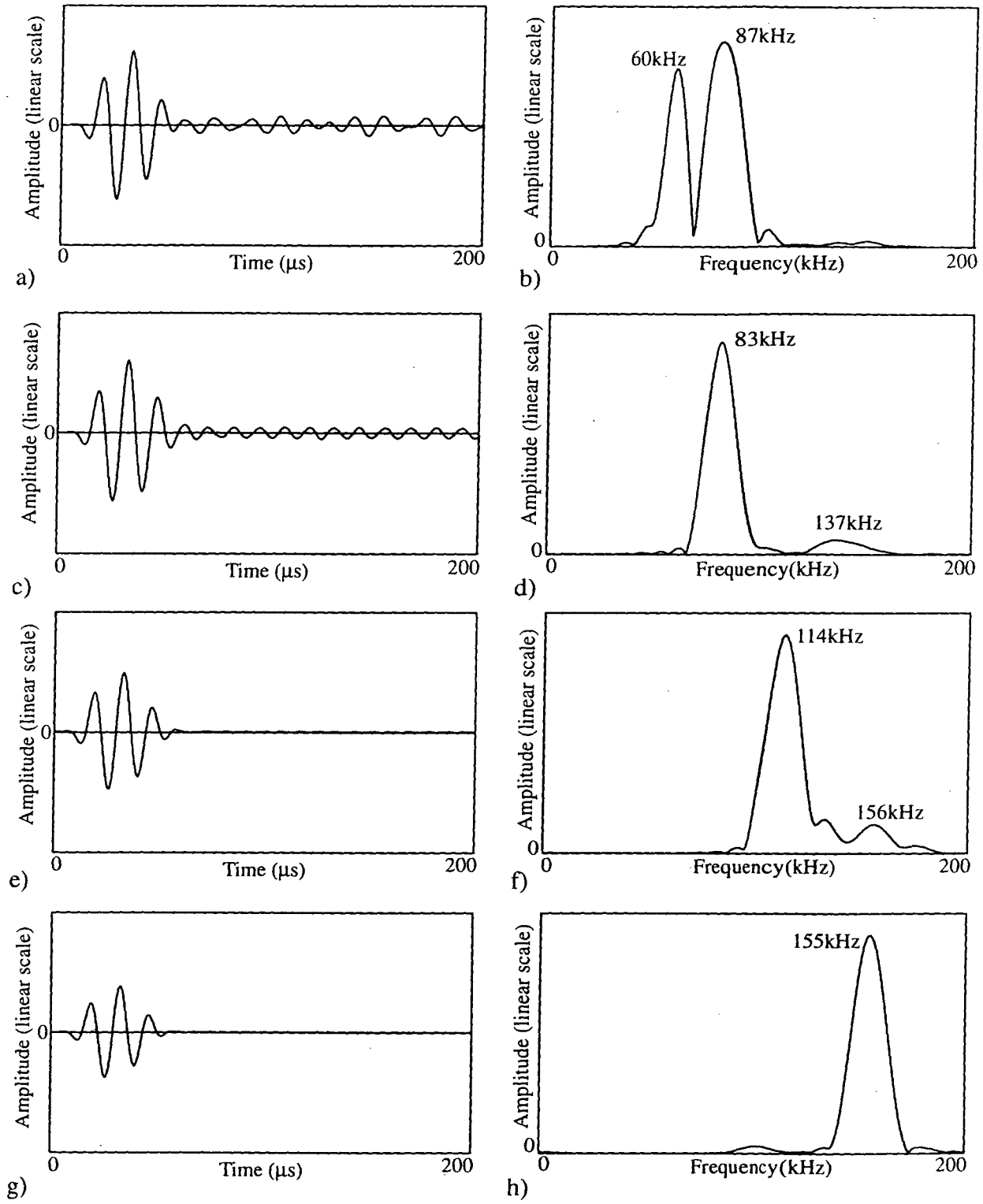


Fig.7.25 Responses of transducer edge with various backings. a) Time domain response with tungsten epoxy backing; b) Frequency spectrum of ringing in a); c) Time domain response with PZT backing; d) Frequency spectrum of ringing in c); e) Time domain response with brass backing; f) Frequency spectrum of ringing in e); g) Time domain response with steel backing; h) Frequency spectrum of ringing in e)

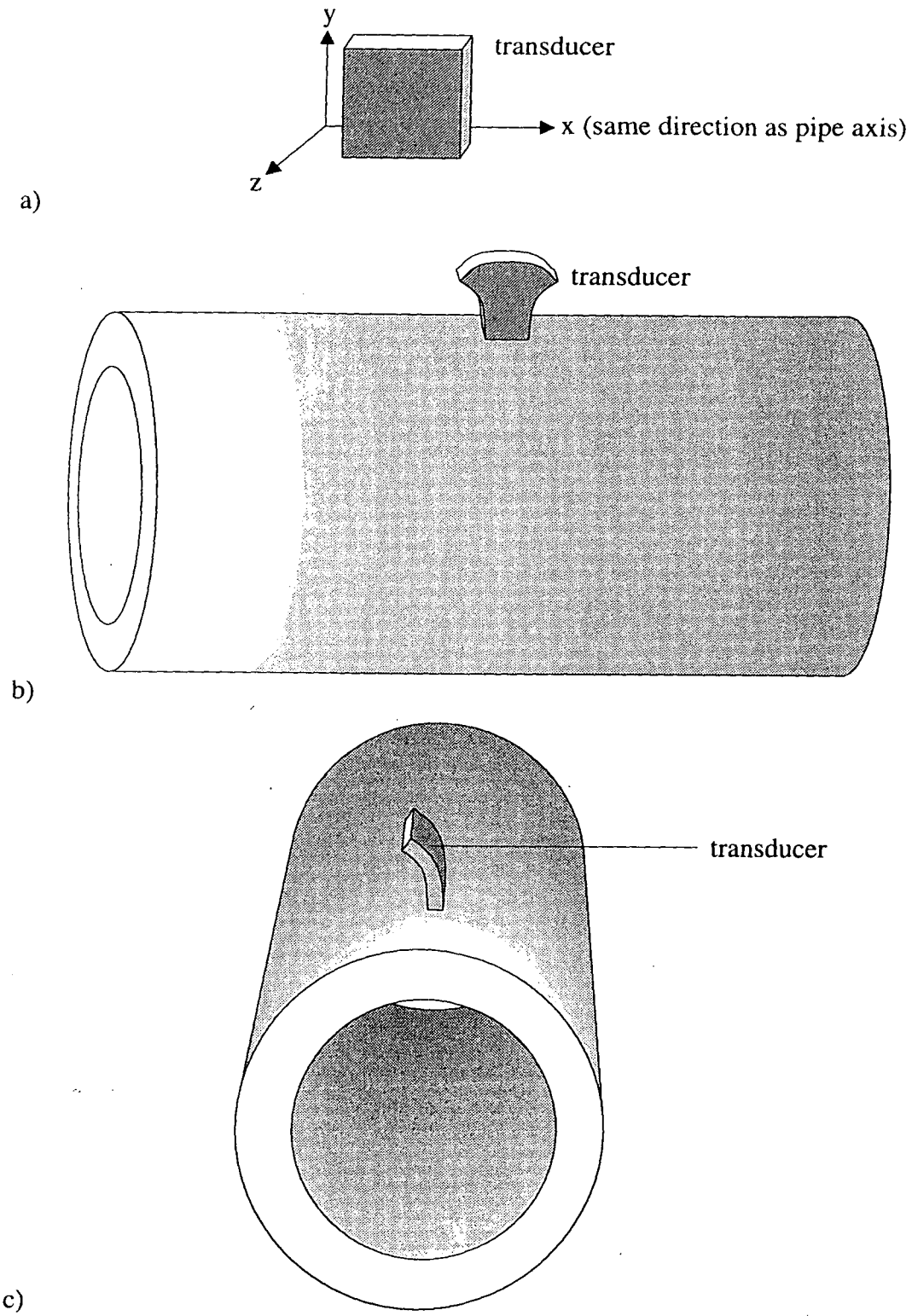


Fig.7.26 Bending modes of a transducer. a) coordinate system for transducer; b) a longitudinal bending mode; c) a lateral bending mode.

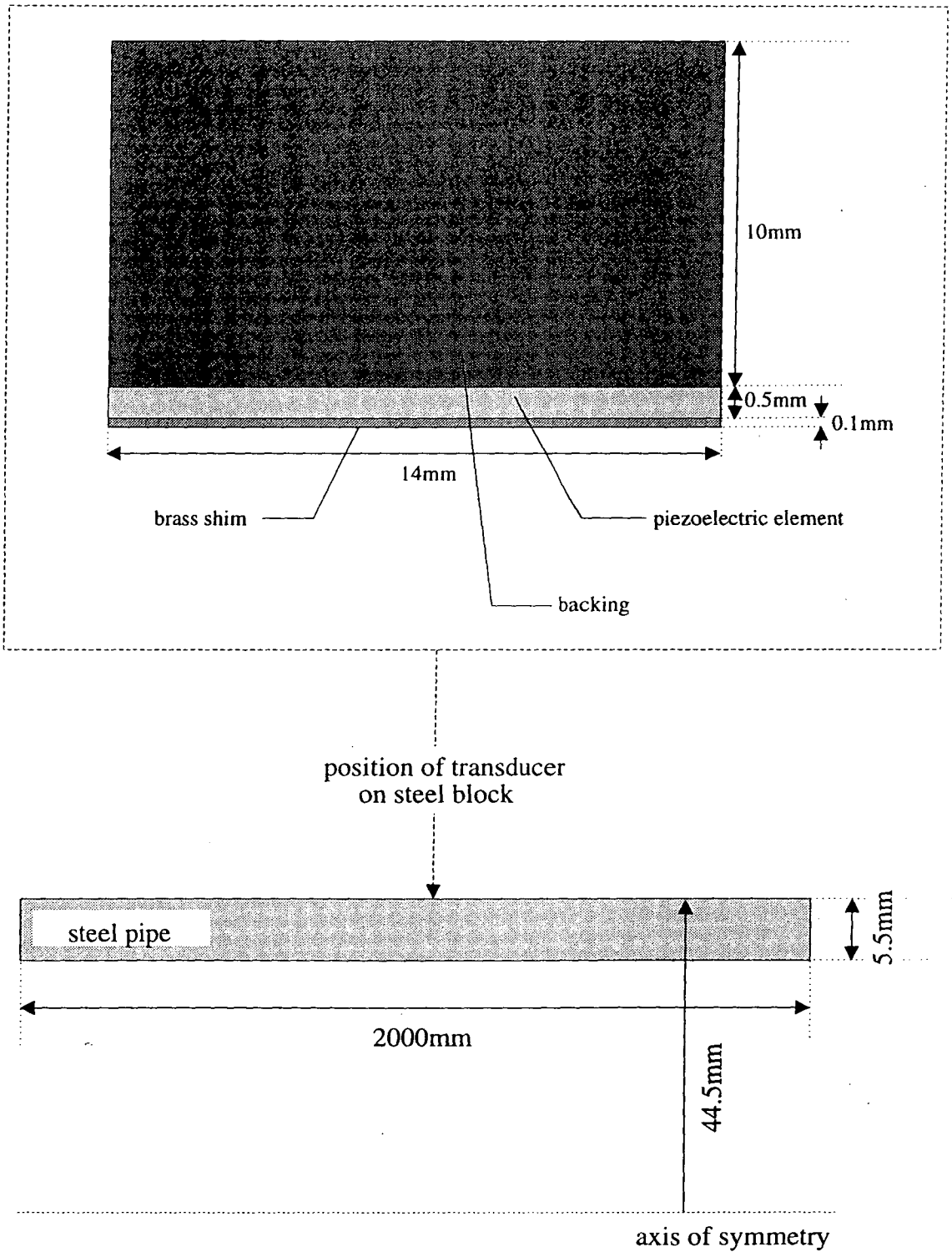


Fig.7.27 Schematic showing outline of FE model of backed transducer on a steel pipe

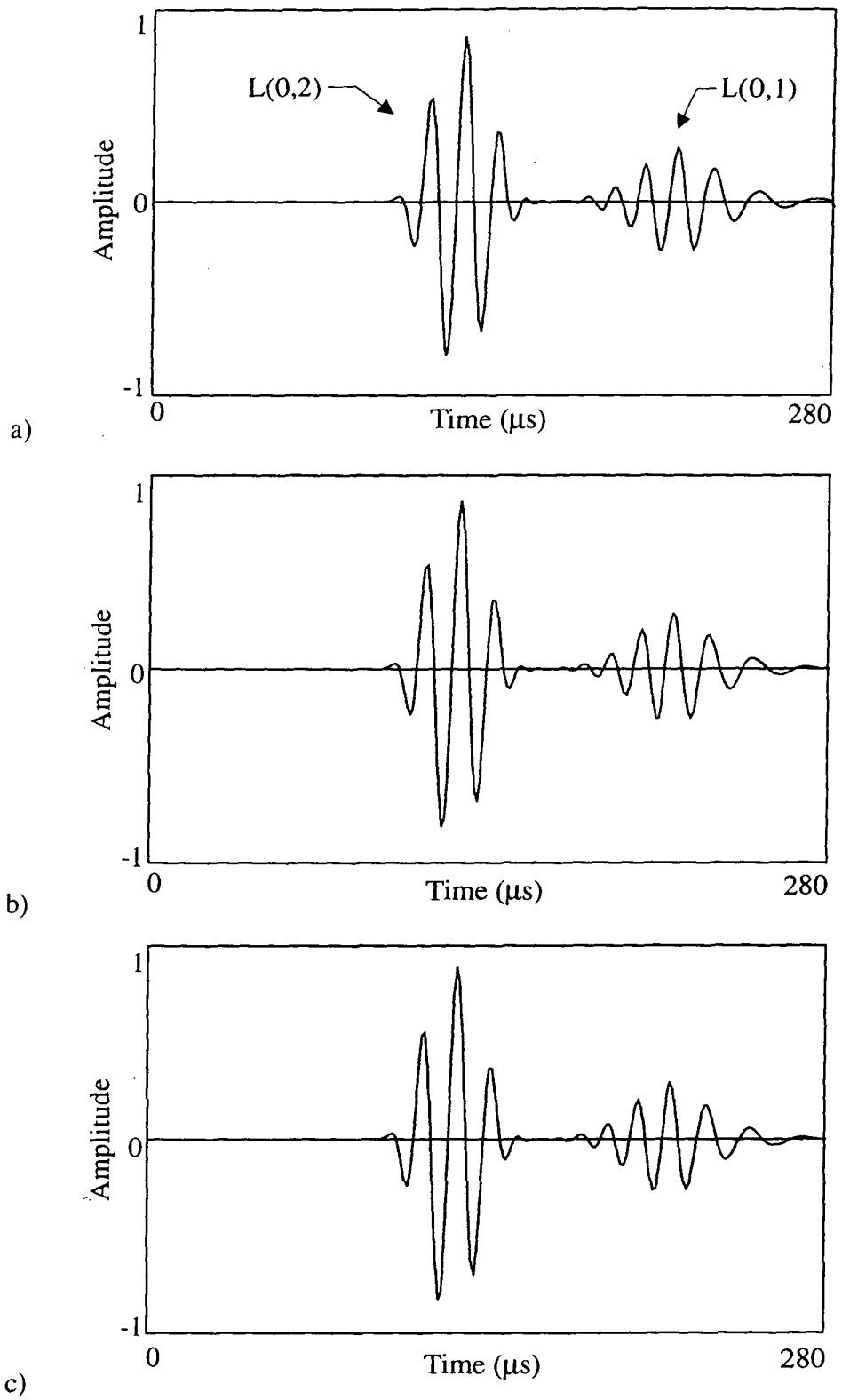


Fig.7.28 Time domain responses for various backing thicknesses on an expansional transducer. Thickness is a) 10mm; b) 8mm; c) 6mm

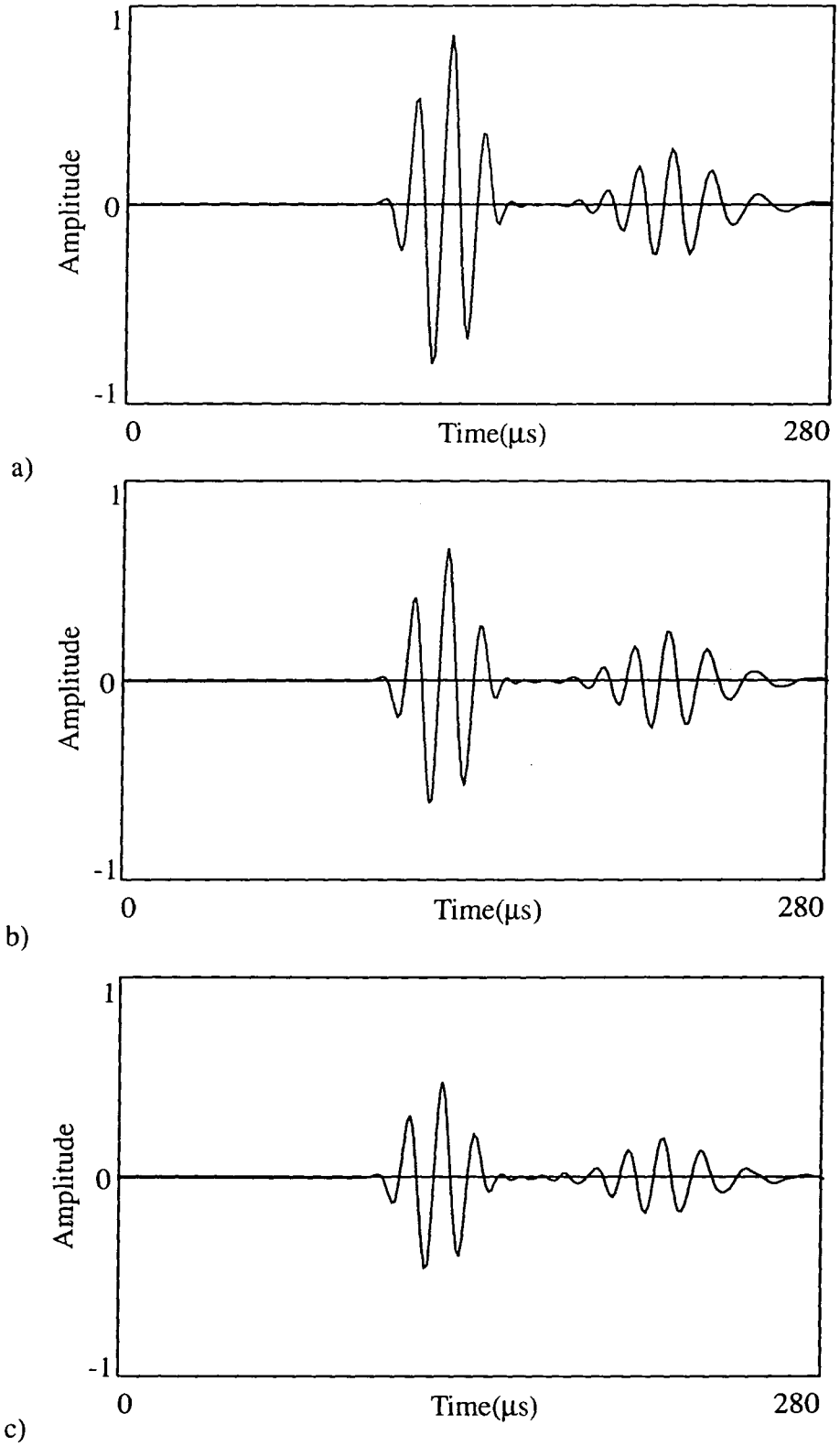


Fig.7.29 Time domain responses on steel pipe using expansional transducers with various shim thicknesses. a) 0.1mm; b) 1mm; c) 2mm

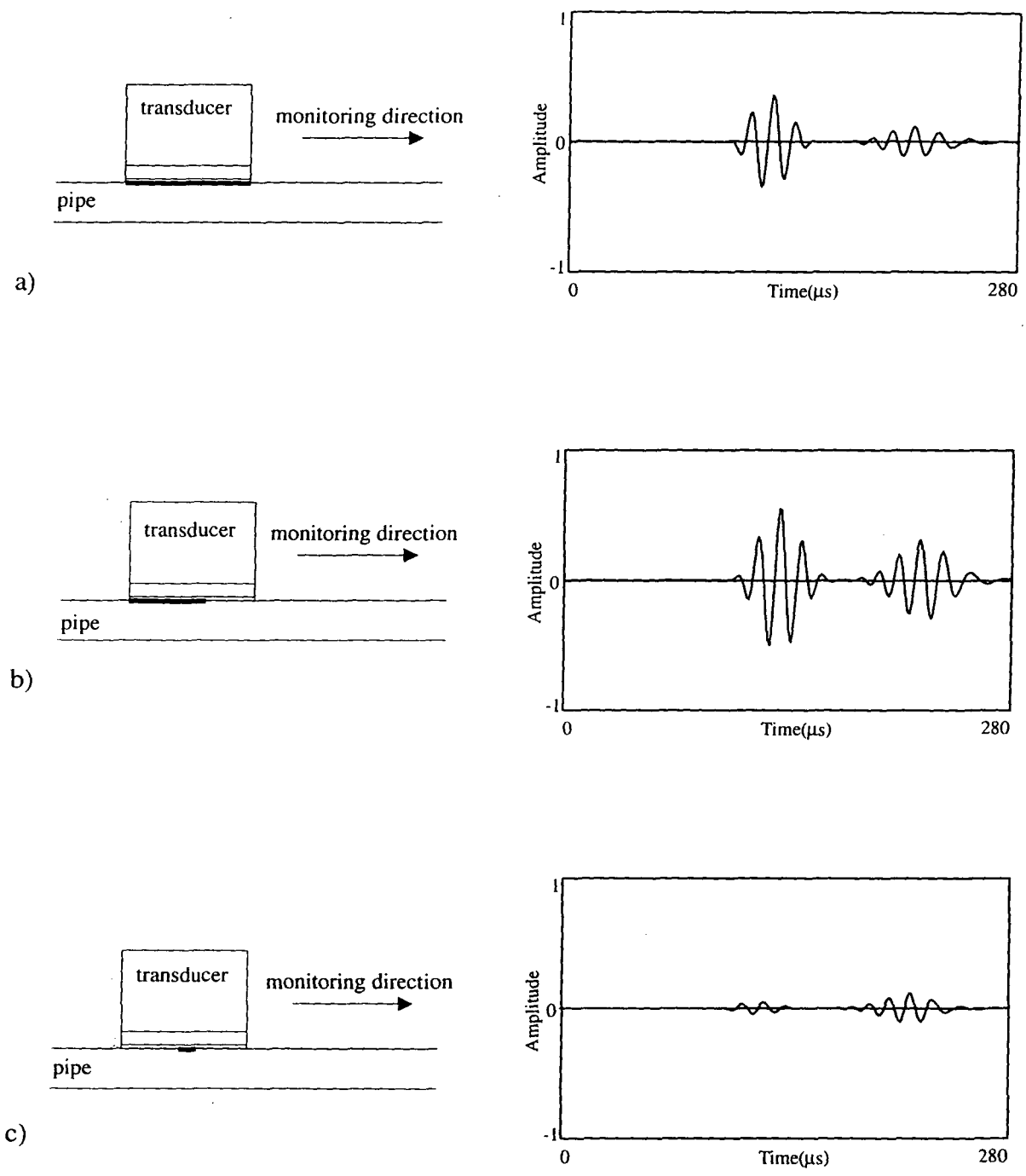


Fig.7.30 Time domain responses on steel pipe using expansional transducers for different contact areas

——— area of contact

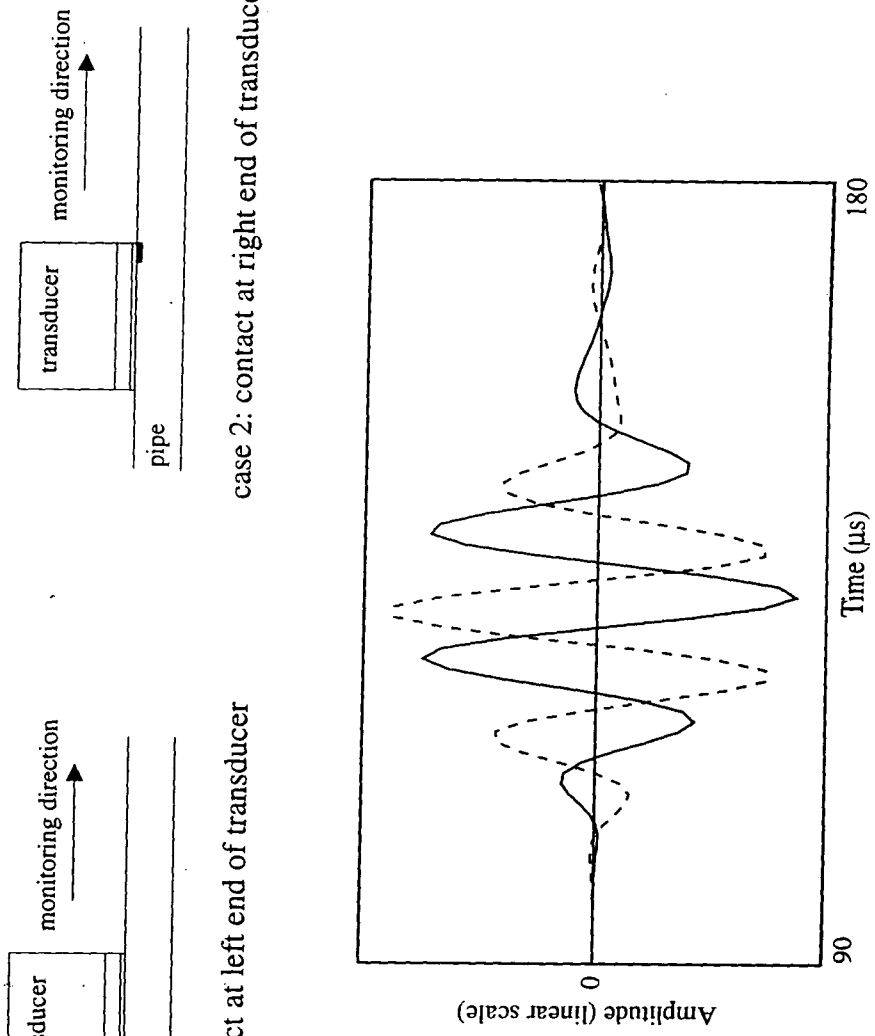


Fig.7.31 Time domain responses showing the phase shift when either end of the expansional transducer contacts the pipe.
——— case 1
..... case 2

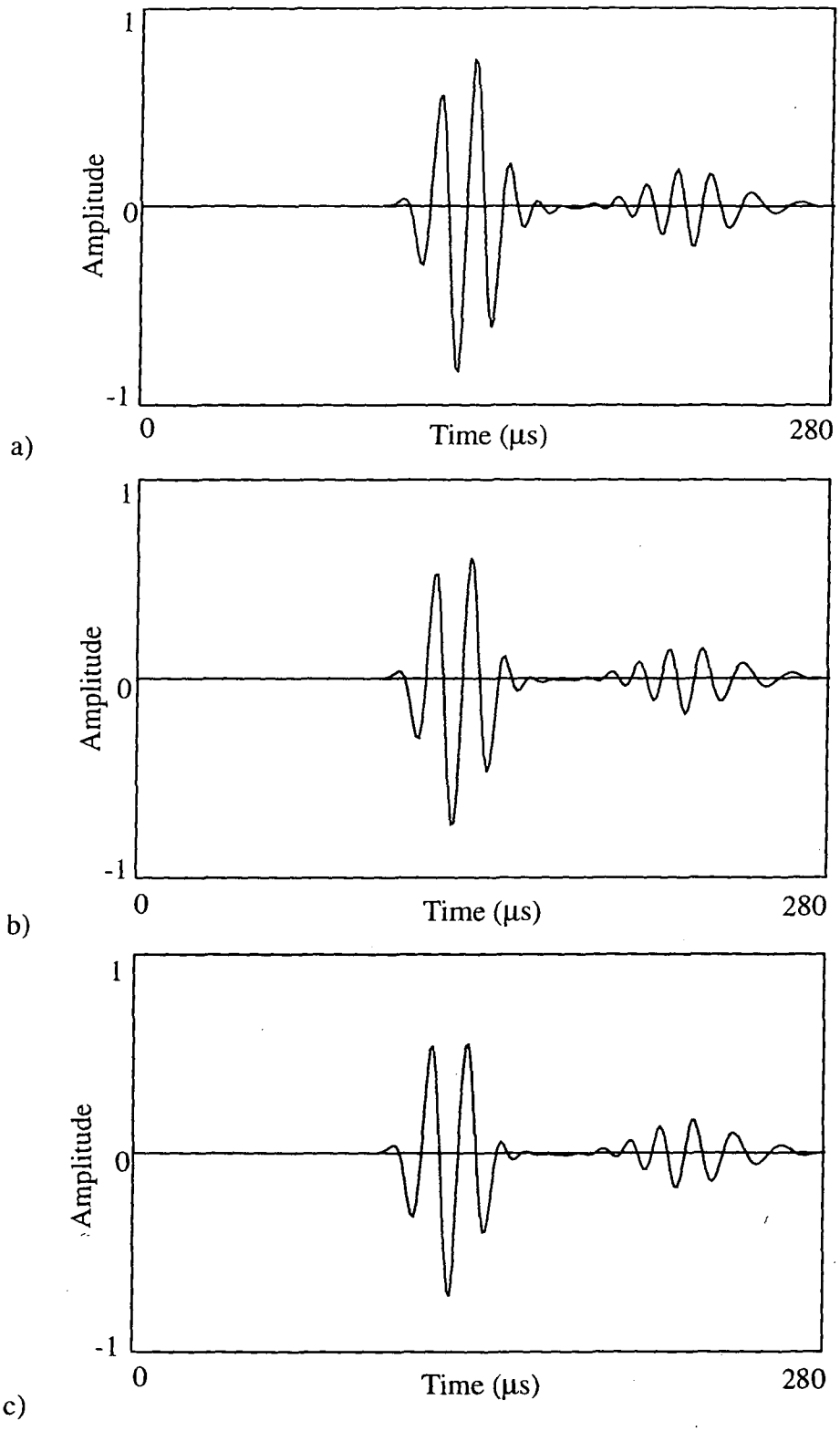


Fig.7.32 Time domain responses on pipe using shear transducers for various backing thicknesses. a) 10mm; b) 8mm; c) 6mm

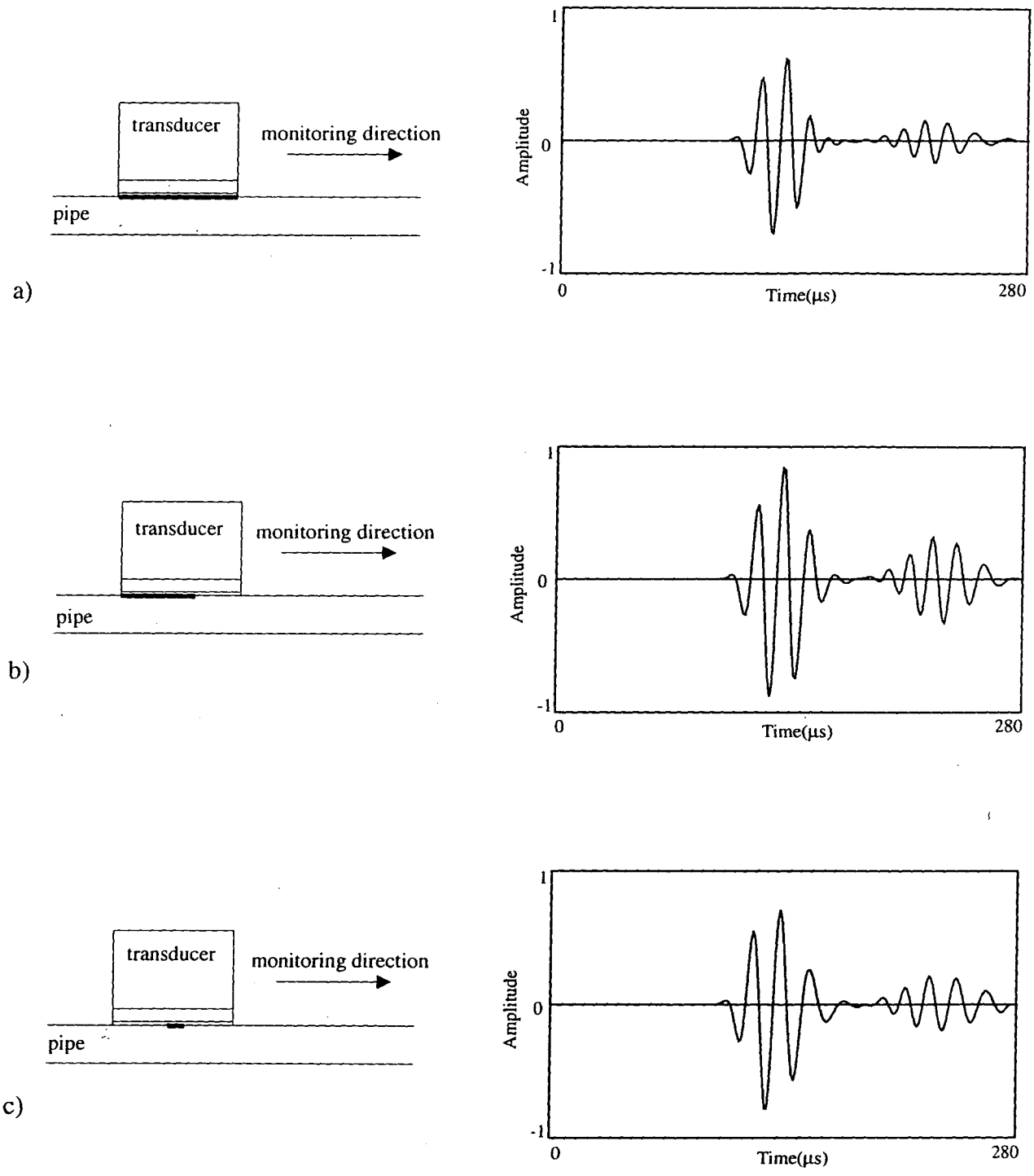


Fig.7.33 Time domain response on steel pipe using shear transducers for different contact areas. a) full contact; b) 4/7 contact; c) 1/7 middle contact

—— area of contact

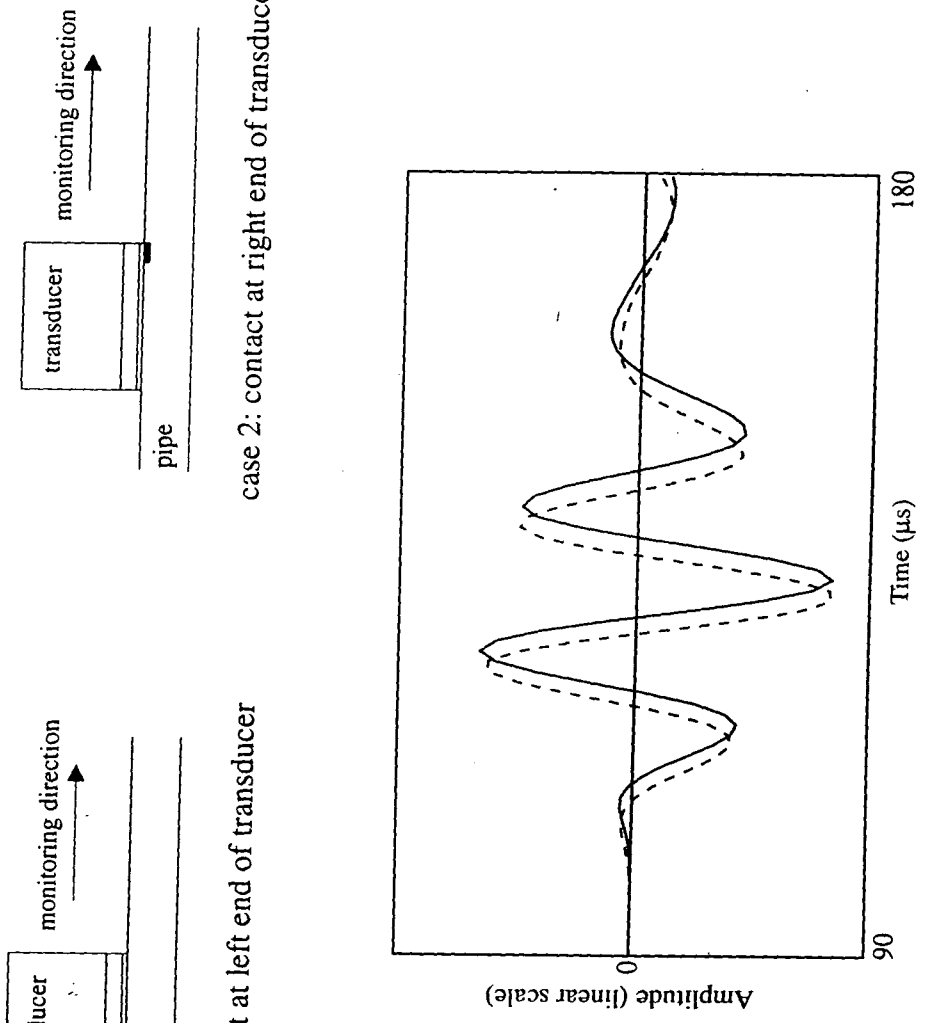


Fig.7.34 Time domain responses showing no phase shift when either end of the shear transducer contacts the pipe.
——— case 1
..... case 2

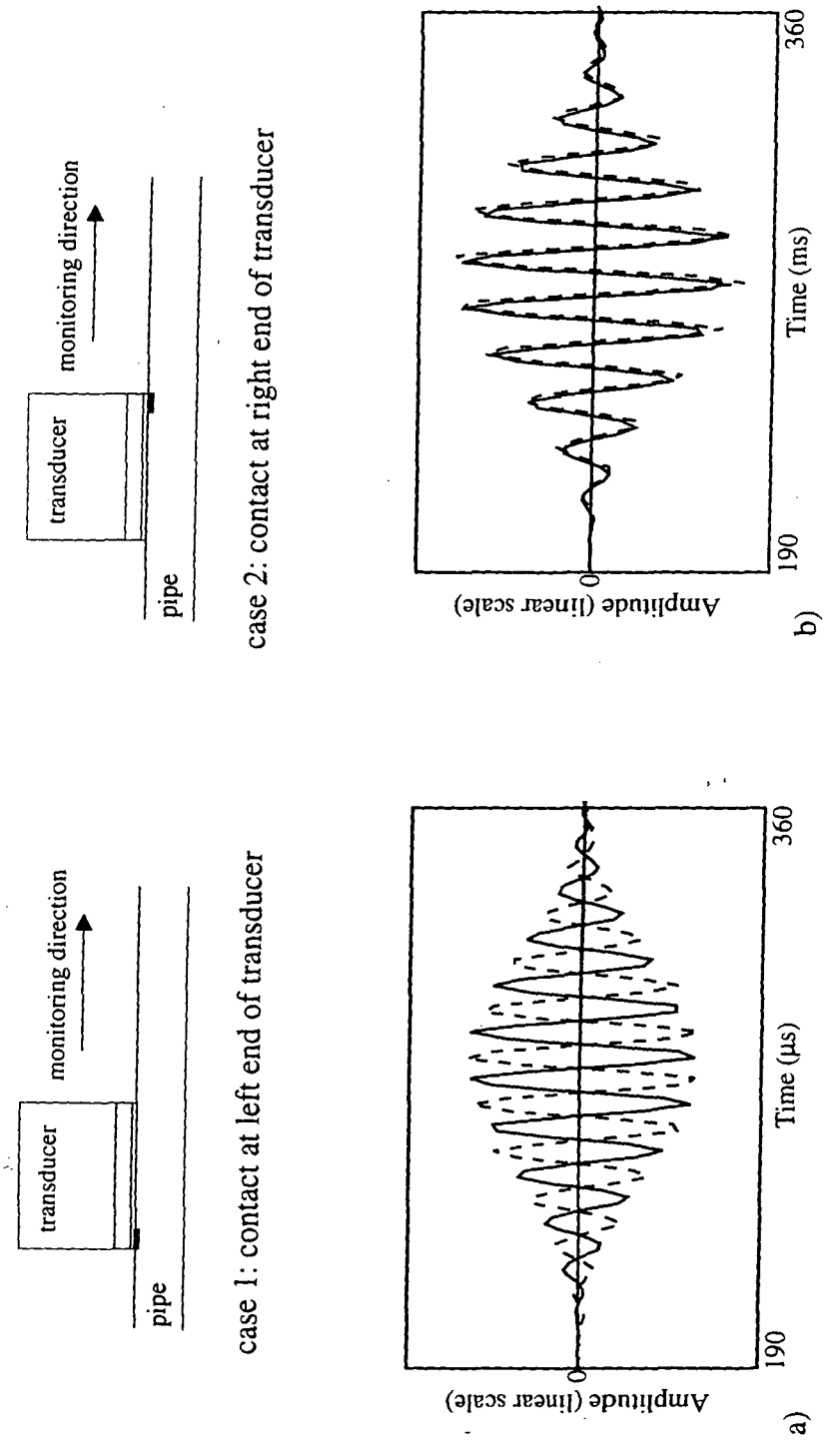


Fig.7.35 Experimental results showing effect of contact position on generated Lamb mode L(0,2). a) Time domain response showing phase shift of L(0,2) when transducer contact is made at alternate ends for an expansional transducer; b) Time domain response showing very little phase shift of L(0,2) mode when transducer contact is made at alternate ends for a shear transducer

——— case 1 - - - - - - - - - - case 2

CHAPTER 8

The Detectability of Butt-Fusion Weld Defects Using Lamb Waves

8.1 Introduction

The usual method of inspecting a welded metal joint makes use of angle-probes (Krautkramer and Krautkramer (1983)) and involves a two dimensional scan (along the length of the pipe and around the circumference of the pipe). The angle of the probe is usually chosen such that the longitudinal wave becomes inhomogeneous and hence only the shear wave propagates into the weld. The size of the defect can be determined by measuring the time of flight of reflected waves (Bernard (1986), Silk (1987)). The technique of using shear waves has not been applied to polyethylene butt-fusion welds. A similar technique has been employed where longitudinal waves are used because shear waves are too strongly attenuated (McClinton (1986), Munns and Georgiou (1995)). Frequencies in the range 1-2MHz are most commonly used ((Ben'kovskii (1991))). Although this method works reasonably well, the main drawback is that it is a slow method due to the necessity for bi-directional scanning which is required in order to detect the defect. The Lamb wave technique is a potentially attractive alternative given that scanning is reduced to a single direction (circumferential) because the whole thickness of the pipe is interrogated. Also, the orientation of the defect in butt-fusion welds (which is normal to the axis of the pipe ((Ben'kovskii (1991))) is favourable to the incident Lamb wave. Given such advantages of using Lamb waves, this technique is investigated in this chapter.

In Chapter 6, we identified the existence of low attenuation modes which could be used in polyethylenes. The next step is to look at whether such modes could be used for defect detection in the same materials. We saw in the same chapter that probably the most useful of these modes, by virtue of its low attenuation and high group velocity, was the s_2 mode when excited at a frequency-thickness corresponding to its maximum group velocity. We will focus on using this mode for the defect detection studies. In this chapter, we will look at the response of the s_2 mode when it comes into contact with a defect. The defects used in this work are slots machined into the polyethylene plates at different depths to simulate different sizes of defect. The investigation of the interaction between the Lamb wave and the slots can be carried out in several ways. We could use a pulse-echo set-up where the amplitude of the

reflection of the s_2 mode from the slots would be measured so that the reflection coefficient could be calculated. Alternatively, we could opt for a transmit-receive method where the transmitted signal across the slot is measured. The choice of method will be very dependent on the equipment available and it will be shown that only transmission coefficient measurements were possible given the equipment available at the time. Therefore, transmission coefficient results are presented. These measured results are then compared to results calculated from a finite element analysis of the same system. The finite element method is also used to obtain reflection coefficients. The results are discussed in the light of the critical defect sizes obtained in Chapter 2. At the end of this chapter, conclusions are drawn on whether the Lamb mode selected could be used effectively for defect detection in polyethylene pipes.

8.2 Choice of Configuration

The amount of TUB 124 HPPE (as used in Chapter 6) and Rigidex 002-50 MDPE material available was very limited. However, an alternative MDPE grade was available and this material was consequently used for the reflection/transmission coefficient measurements. This material was not identical to the Rigidex 002-50, for which acoustic property measurements had already been made. Therefore, the bulk properties of this particular grade had to be measured so that the dispersion curves could be obtained from which the s_2 mode could be located. Table 8.1 shows the results. If we compare these values to those of Rigidex 002-50, also shown in Table 8.1, we can see that the two materials have very similar velocities but the attenuation of Rigidex 002-50 is higher. Figs.8.1a, 8.1b and 8.1c show the phase velocity, group velocity and attenuation dispersion curves for the MDPE material. It can be seen from the group velocity dispersion curve that in order to excite the mode at its maximum group velocity, we need to use a frequency-thickness of 1.536MHzmm. This means a frequency of 240kHz for a 6.4mm thick plate. From the phase velocity dispersion curve, the angle of inclination of the transducers was calculated to be 28 degrees (the excitation set-up is the same as that used in Chapter 6). A 20 cycle tone burst in a Hanning window was used for the input signal.

Initially, the experiment was set up to operate in transmit-receive mode in order to obtain group velocity and attenuation measurements for the s_2 mode. Fig.8.2a shows the configuration used. Figs.8.2b and 8.2c show the time domain responses of the receiver at the two positions shown in Fig.8.2a (position 1 and position 2); the separation distance was 67mm.

Property	Current MDPE	Rigidex 002-50
C_L (m/s)	2273	2308
C_S(m/s)	840	853
α_L (Np/wavelength)	0.044	0.081
α_S(Np/wavelength)	0.293	0.404

Table 8.1 Bulk property measurements for MDPE grade used in defect studies

The results obtained looked promising, with a single mode propagating. Using the same method described in Chapter 6, the group velocity and attenuation were measured and are presented in Table 8.2. The difference in the group velocities is about 10%. This unexpectedly large error could be due to the fact that the attenuation is high enough for the predicted group velocity to be no longer adequately described by the derivative of the frequency with respect to wavenumber. The underlying assumption in the definition of group velocity is that the material has no damping. In Chapter 6, we showed that the predicted group velocity of the s_2 mode correlated well with the measured value indicating that the level of attenuation was low enough for the predicted group velocity to be valid. In the present case, the attenuation is almost twice the value in Chapter 6 and may be large enough to account for the difference in the group velocity. A more apt parameter to describe the propagation of the wave envelope in attenuative media is the energy velocity (Ditri (1995)) and it can be shown that the energy velocity is equal to the group velocity in lossless media (Auld (1990)). However, this was not implemented in the dispersion curve software.

	Predicted	Measured
Group velocity (m/s)	1223	1124±5%
Attenuation (Np/m)	18.6	18.5±20%

Table 8.2 Comparison of predicted and measured group velocities and attenuation of s_2 mode

The next configuration that was investigated was based on the pulse-echo technique using two transducers, one to excite and the other to receive (Fig.8.3a). The aim of the experiment was to propagate the s_2 mode towards the edge of the plate where it would be reflected and then to measure the amplitude of the same mode back at the receiver. The time domain history of the received signal is shown in Fig.8.3b. It can be seen that the time trace is fairly complicated with at least two signals appearing to overlap. The first signal occurs very early on and by noting the arrival time of this signal we

can deduce that it is an s_2 mode which has propagated directly from the transmitter to the receiver. This may seem surprising given that the receiver is not the at correct angle to receive the directly transmitted s_2 mode. One possible explanation for this signal is that there is sufficient beam spreading of the transducer so that some energy hits the side of the transducer holder and is reflected onto the plate at a angle which allows backward propagating modes to be excited (Fig.8.4a). The slower second signal is possibly due to a wave which has hit the plate at the intended angle, been reflected from the plate onto the transducer holder at an angle of 90 degrees, and then reflected from the holder back onto the plate at an angle suitable for exciting backwards propagating modes (Fig.8.4b). The predicted position in time for the arrival of the reflected wave from the edge is indicated in Fig.8.3b. We can clearly see that if such a reflection exists, it cannot be resolved from the rest of the signals and hence a pulse-echo technique based on two transducers will not work given the current set-up.

The third configuration is once again based on pulse-echo but this time only using a single transducer. A schematic of the set-up is shown in Fig.8.5a. The time domain response of the transducer is shown in Fig.8.5b. The reflection from the edge has been marked on the figure. All the signals which occur before the arrival of the edge reflection are due to ringing of the transducer. We can see that the ringing continues for some time and as a result, interferes with the reflected signal from the edge. It is possible to increase the distance between the transducer and the edge in order to improve the resolution. However, this is at the expense of signal amplitude of the reflected wave because for the extra distance required, the amplitude of the reflected signal becomes too small for any realistic measurements to be made. If more highly damped transducers were available, this technique would be very feasible and given the convenience of a single transducer it is also the most attractive. However, with the present equipment available, the first configuration (transmit-receive) was found to be the most practical and therefore this technique will be used for looking at the transmission of the s_2 mode across slot defects.

8.3 Transmission Coefficient Measurements and FE Predictions.

Transmission coefficient measurements were conducted on slots machined into the polyethylene plates. The slots depths were 1/6, 2/6, 3/6 and 4/6 the thickness of the plate. Fig.8.6a shows the relative positions of the transmitter, receiver and slot. A reference signal was first obtained by capturing the signal from a slot-free plate (Fig.8.6b). The received signal in the presence of a slot was then captured for the

different slot depths (Fig.8.6c shows such a signal for a half through thickness slot). Transmission coefficients were then calculated by dividing the peak amplitude of the signal transmitted across the slot by the peak amplitude of the reference signal. The results are plotted in Fig.8.7. It can be seen that the sensitivity of the transmission coefficient to the depth of the slot looks reasonable with the amplitude dropping to less than 0.2 when the slot is half way through the plate wall.

In order to verify the experimental results, FE analysis was used to calculate the transmission coefficients. In addition, it was possible to predict reflection coefficients which was not feasible experimentally. Given that the FE software used did not have the ability to model the damping inherent in the polyethylenes, the model was limited to an elastic plate. This is valid given that the transmission coefficients measured experimentally were not dependent on attenuation (these were cancelled out when the signal transmitted across the slot was divided by the reference signal, the propagation distance between transmitter and receiver being the same in both cases).

When we compare the phase velocity (Fig.8.8a) or group velocity (Fig.8.8b) dispersion curves of the s_2 mode for the case of an MDPE plate with that for the same plate but without attenuation, we can see that there is a slight difference in the position of the maximum group velocity. If we compare the displacement mode shapes at the position of maximum group velocity for each case (Fig.8.8c), we find that they are very similar. Therefore, in the FE model, we have used the frequency-thickness corresponding to the maximum of the group velocity of the s_2 mode (1.487Hzmm) in an elastic MDPE plate (i.e. an elastic plate with the density and bulk velocities of MDPE). Figs.8.8d and 8.8e show the stress and strain energy density mode shapes respectively.

A schematic of the FE model used is shown in Fig.8.9a. The plate used was 1mm thick which meant that the input frequency into the model had to be 1.487MHz. The excitation input consisted of 10 cycles and was applied at the left end of the plate. In order to excite a single mode, each frequency component in the excitation signal applied to a node had to be convolved with the mode shape amplitudes of the s_2 mode at that node, at the same frequency. In this way, at each frequency, the input will be sufficient to only excite the s_2 mode we require. Exciting using a uniform amplitude in-plane signal at the end of the plate was not effective because the s_1 and s_0 modes were also excited. This was not a problem in Chapter 5 because only one symmetric mode (s_0) could exist at low frequency-thickness.

Fig.8.9b shows the time domain response of a monitoring point situated 6.3mm from the left edge of the plate and at the mid-plane through the thickness. The monitoring direction was in-plane (this will be explained shortly). Only the outgoing signal has been shown. Fig.8.9c shows the wavenumber spectrum of this outgoing mode at the same frequency as the centre frequency of the input signal. It can be seen that a pure mode is generated. On reaching the slot, the s_2 mode may undergo mode conversion into any of the modes that can exist at 1.487MHzmm. These are the s_0, a_0, s_1, a_1 and a_2 modes. This was found to present a problem when we tried to identify the reflected and transmitted modes using a 2D FFT (see Chapter 6) when we monitored at the top surface of the plate. The problem was that when we looked at the wavenumber spectrum, the wavenumber spectrum of the a_2 mode was too close to that of the s_2 mode. As a result the two peaks could not be separated and hence the amplitudes could not be obtained with much confidence. In order to resolve this, monitoring was redirected to the mid-plane of the plate with the monitoring direction being in-plane. In this way, asymmetric modes would not be detected simply because there is a node in the in-plane displacement mode shape of such modes.

Fig.8.9d shows the time domain response of the reflected waves of the same monitored point used for Fig.8.9b. Note that a longer time history than that shown in Fig.8.9d was obtained; the time history in Fig.8.9d has simply been chopped at 40μs. Fig.8.9e shows the wavenumber spectrum of the reflected modes. We can see that there are three symmetric modes and that asymmetric modes have not been detected.

Fig.8.9f shows the time domain response of modes transmitted across a half depth slot (the monitoring point was located 13.6mm from the right edge of the plate). Fig.8.9g shows the corresponding wavenumber spectrum. We can see that mode conversion is very evident. In an elastic plate, these extra mode converted modes would be very problematic. Fortunately, in an attenuating plate, the amplitudes of the s_1 and s_0 modes would be greatly diminished due to their high attenuation.

Fig.8.10a shows a plot of the transmission coefficient of the s_2 mode. Plotted on the same figure are the experimental data points obtained earlier. The correlation between theory and experiment looks reasonable. However, there were not enough experimental data points to identify the peaks and troughs and more points are needed for conclusive verification of the finite element results. The trend of the predicted transmission coefficient is rather complicated. The transmission coefficient plot has a distinctive local minimum at a depth ratio (the ratio of the depth of the slot to the plate thickness) of about 0.2. This is approximately the position where a local maximum

occurs in the strain energy density mode shape (Fig.8.8e). The results show that by the time the slot has reached half the thickness of the plate, the transmission coefficient is down to less than 0.1. After this, the transmission coefficient remains fairly low although it does undulate. Fig.8.10b shows the predicted reflection coefficients. By the time the defect reaches half the wall thickness, the reflection coefficient has increased to about 0.85. After this point, the reflection ratio oscillates gradually and rises to about 0.95 when the slot is at full thickness depth.

8.4 Discussion of Results

We shall initially discuss the results with respect to edge cracks. This is simply done so that we can make assumptions that will then be used to look at the circular defect.

From the fracture mechanics analysis conducted in Chapter 2, we found that the critical defect size based on an edge crack (i.e. the same type as the slots used in this chapter) was 1.1mm for a 7.1mm thick plate (i.e. a depth ratio of 0.15). From Fig.8.10a, we can see that this corresponds to a transmission coefficient of 0.66, so the presence of such a crack would result in a drop in amplitude of the received signal by 34%. Such a crack would be readily detectable. If a reflection configuration is used, this would result in a reflection coefficient of 0.33 which should easily be detectable.

In reality, the defect may not start in the same position as the slots but may be located anywhere through the thickness of the plate. The effect that this has on the transmission/reflection coefficients will be dependent on the size of the defect to be detected. To demonstrate this point, FE predictions of the reflection coefficient from slots were made whereby the starting position of the slots was varied through the depth (Fig.8.11). Three starting depths were chosen for the slots: 0.14, 0.27, and 0.41 times the plate thickness. Two sizes of slot were chosen: 0.18 and 0.45 times the plate thickness. Table 8.3 shows the results.

Starting depth of slot (as a fraction of plate thickness)	Refl. coeff. for small slot (0.18 plate thickness)	Refl. coeff. for large slot (0.45 plate thickness)
0	0.44	0.81
0.14	0.43	0.82
0.27	0.77	0.86
0.41	0.70	0.82

Table 8.3 Effect of slot starting position on the reflection coefficient from slots

The reflection coefficient for the smaller slot varies significantly with the starting depth of the slot and is seen to increase as the slot moves towards the centre of the plate. We have seen in Chapter 5 that for delaminations, the stress component governing the reflectivity from delaminations was shear. In the current system, the defects are normal to the axis of the pipe and we would therefore expect the reflectivity to be dependent on the in-plane stress component. Therefore, when the in-plane stress is low, as it is at the surface, the reflection coefficient is low and the closer the defect is to the middle of the plate the larger the reflection coefficient. Note that this is only strictly true for very small defects where the in-plane stress across the defect can be assumed to be constant. For the larger defect, the reflection coefficient is fairly constant. This can be attributed to the fact that the in-plane stress (which is not constant across the defect) is being averaged over the area of the defect. We can hence deduce from these results that the reflection coefficient will increase (and the transmission coefficient decrease) as the starting position of the slot moves towards the centre of the plate.

Therefore the transmission and reflection coefficients of 0.66 and 0.33 obtained with the defect at the edge of the plate can be taken as the maximum and minimum values respectively for a defect whose depth ratio is 0.15 and whose width is infinite (see Fig.2.7a).

The final task is to determine the reflection and transmission coefficients for the circular defect which was chosen as the minimum defect size required to be detectable. The critical value was found to be 5.7mm in diameter for a 7.1mm thick plate (i.e. a diameter to thickness ratio of 0.8). Therefore, the corresponding diameter for the 6.4mm plate would be 5.1mm. To simplify the analysis, we can convert the circular defect to a square one of the same area. This gives a depth of 4.5mm. If such a defect was 4.5mm deep but infinitely wide (in reality, infinitely wide would mean that the width of the defect is larger than the width of the insonifying beam (Lamb wave) in the plate (Fig.8.12a)), the corresponding transmission coefficient would be 0.11. However, the width of the defect is finite (Fig.8.12b). This means that the transmission coefficient is actually larger than that for the infinite width defect. To take this into account, we can assume that when the defect width is infinite, the transmission coefficient is 0.11 and when the width is zero, the transmission coefficient is 1, and that for intermediate widths, the transmission coefficient will be linearly proportional to the ratio of the width within the insonifying beam not occupied by the defect to the width of the insonifying beam. Therefore if the width of the defect is half the width of the insonifying beam, then the transmission coefficient

is 0.11+(1-0.5)x(1-0.11)=0.56. If we assume that the insonifying beam width is 25mm (i.e. the diameter of a typical low frequency piezoelectric transducer ignoring beam spreading), then the transmission coefficient would be 0.11+((1-(4.5/25))x(1-0.11))=0.90. So the transmission coefficient for the minimum defect size which has to be detected is 0.90. Such a value may be difficult to detect in practice and it would therefore be more useful to employ a reflection approach where the reflection coefficient is 0.17.

The technique suggested for the inspection of butt-fusion welds involves one dimensional scanning around the circumference of the pipe. A method based on the use of pipe modes is also possible which would avoid any scanning. This technique would involve exciting a mode such as L(0,2) (see Chapter 7) using a set of dry coupled transducers attached around the circumference of the pipe. A pipe wave is excited and is able to probe the entire cross section of the pipe (in the plate wave case, the area is limited to the beam width of the exciting transducers and hence scanning around the circumference is required to interrogate the whole cross section of the pipe). However, given that the area of the insonifying beam for a pipe wave is relatively large (i.e. the cross section of pipe) in comparison with the sizes of defect that are being sought, the reflection coefficients would be relatively small. Defect sensitivity studies have been reported by Alleyne et al (1996) and the results showed that for notch like defects, the reflection coefficient of the L(0,2) mode was approximately linearly related to the proportion of the circumference of the pipe covered by the notch. Therefore, if we assume this relationship holds for all zero harmonic pipe modes and also that the equivalent mode to s_2 in a pipe has the same modeshape (L(0,5) has a very similar modeshape to s_2), then using the same analysis as for the plate, the corresponding reflection coefficient would be 1%, which should be just detectable. If a transmission configuration is used, the problem would be that the change in transmission coefficient in the presence of a small defect will be so small as to render the change practically unmeasurable.

8.5 Conclusions

Experimental and numerical studies have been conducted on polyethylene to determine the effect of defects on the transmission and reflection coefficients of a low attenuation Lamb mode with the aim of using such a mode on butt-fusion welds. Comparison between experiment and theory was relatively good. The transmission and reflection coefficients were related to the critical defect sizes which were obtained in Chapter 2 and the results showed that for the minimum defect size required to be

detectable, a reflection technique would be the most appropriate given. This is because the changes in the transmission coefficient in the presence of a critical defect were quite small and detecting these changes in practice may be difficult. Moreover, a reflection technique is always preferable given that it is much more sensitive to detecting the existence of a defect (i.e. when there is no defect, we do not get a reflected signal from the weld; when there is a defect, we do receive a reflected signal).

The Lamb wave technique can be applied in two main ways. If relatively large reflections are sought and scanning time is not too important, then a scanning arrangement is recommended, with the Lamb waves behaving essentially as plate waves. Excitation using a single transducer will enable this to be achieved. If scanning is not the preferred method, pipe waves could be used where numerous transducers are clamped onto the pipe (Alleyne and Cawley (1996)) but this will be at the expense of having to measure small changes. The Lamb wave technique may be preferable to the commonly used angle probe technique because of the speed of inspection.

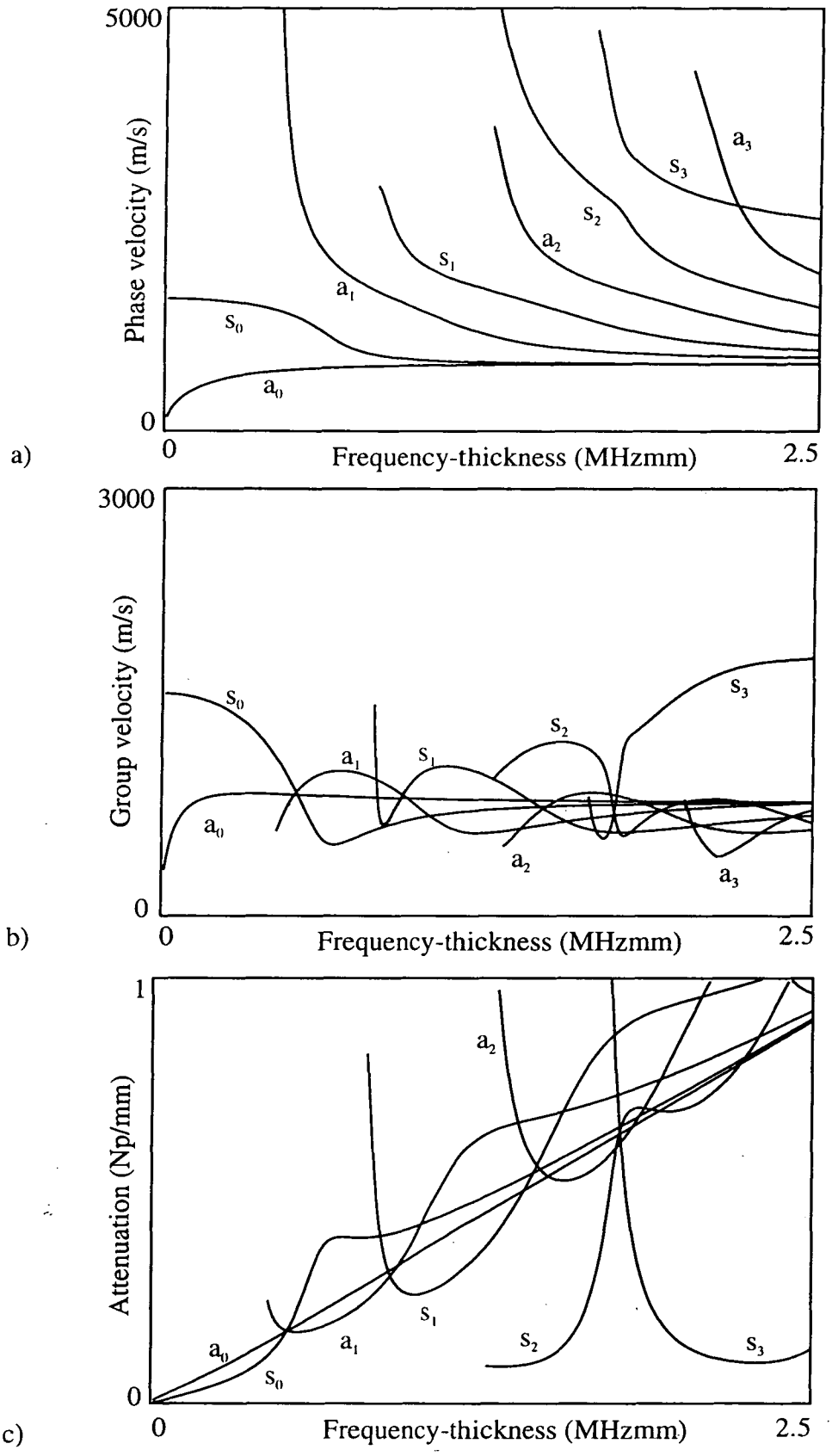
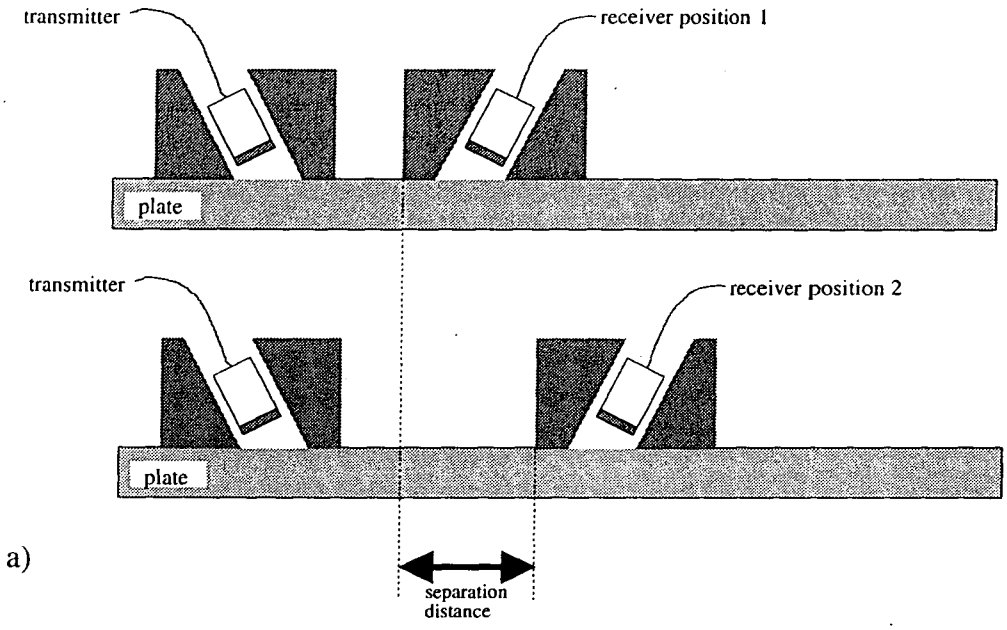
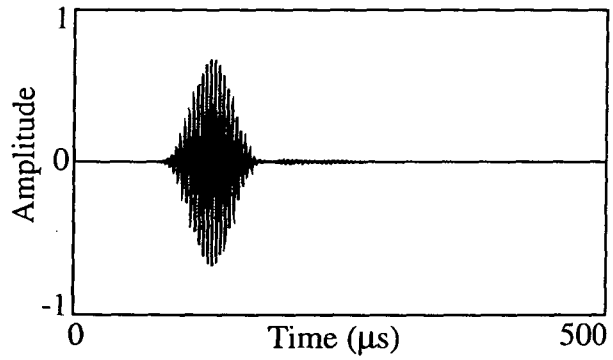


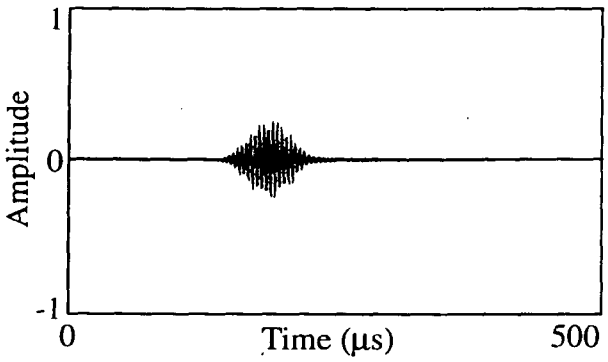
Fig.8.1 Dispersion curves for MDPE. a) Phase velocity; b) Group velocity; c) Attenuation



a)

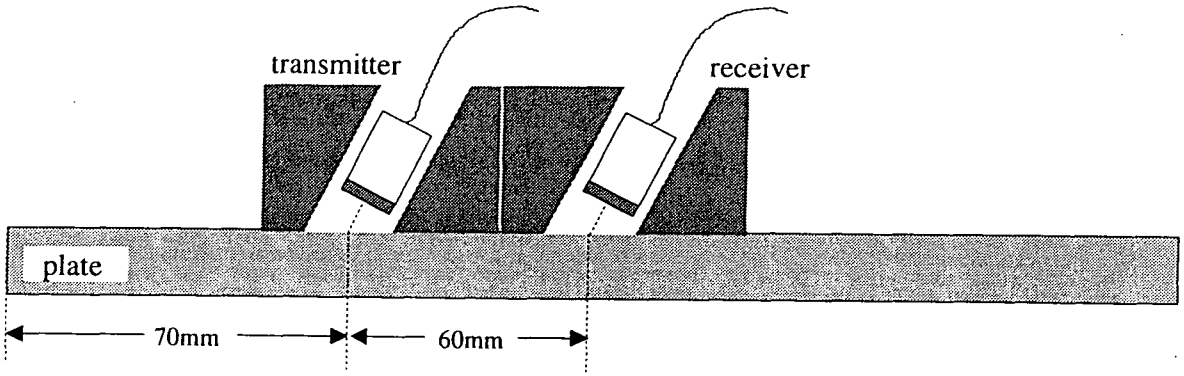


b)

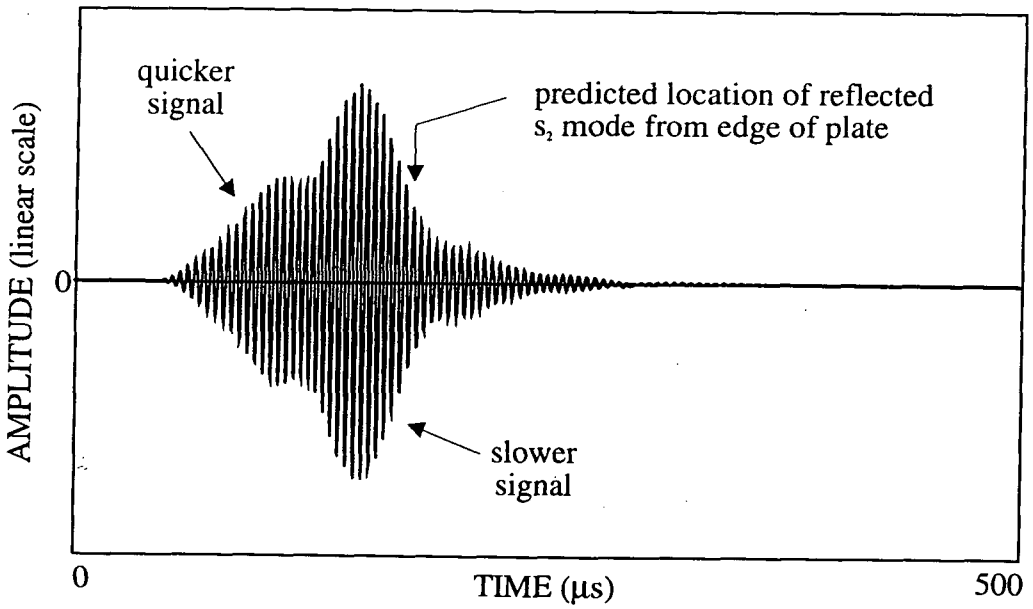


c)

Fig.8.2 Measurement sequence for monitoring Lamb waves along an MDPE plate. a) Schematic showing measurement sequence; b) Time domain response at receiver position 1; c) Time domain response at receiver position 2.

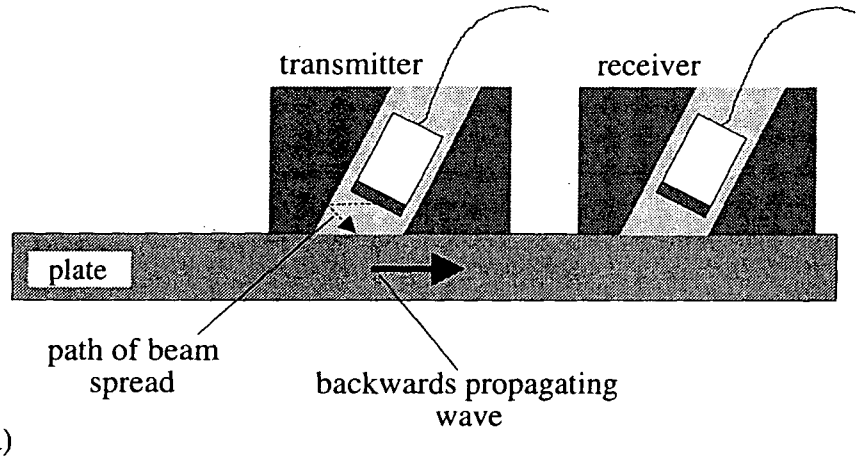


a)

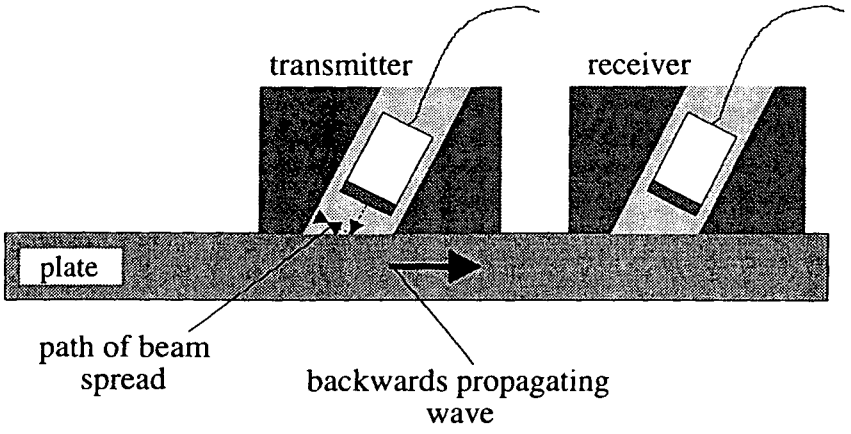


b)

Fig.8.3 Reflection measurement using two transducers. a) Diagram showing positions of transducers relative to the MDPE plate used for demonstrating reflection of s_2 mode from the end of a plate; b) Time history of received signals

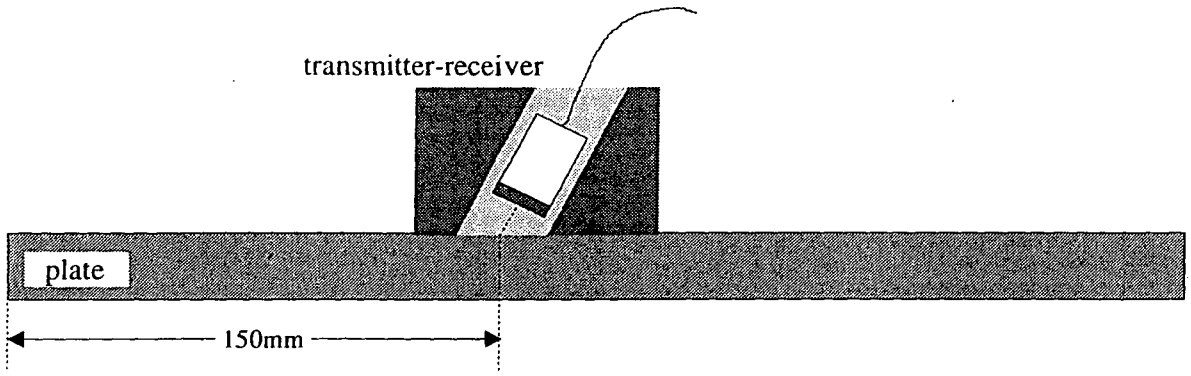


a)

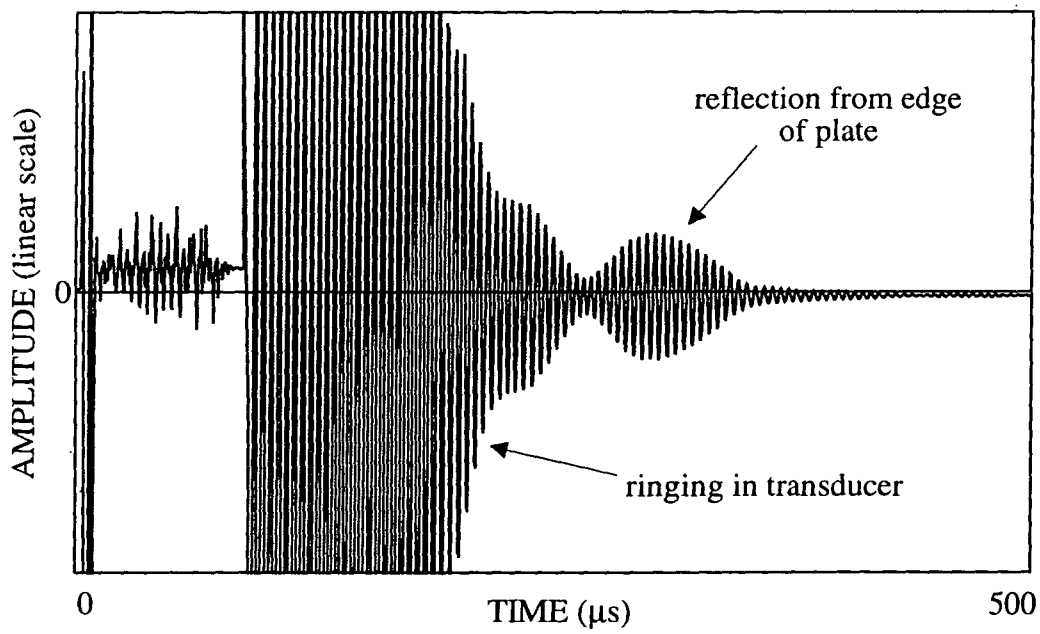


b)

Fig.8.4 Possible ray paths for backwards propagating waves. a) earliest arrival; b) later arrival

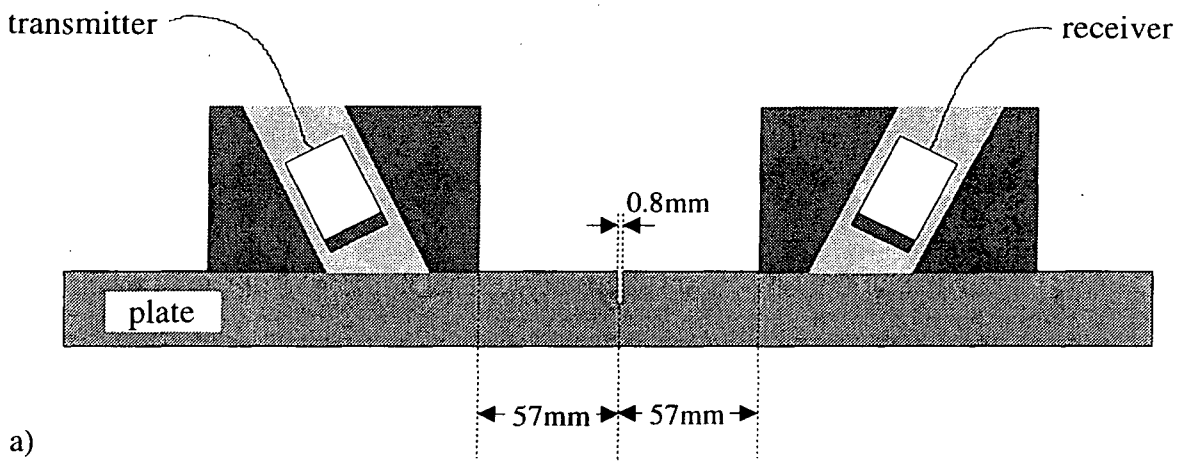


a)

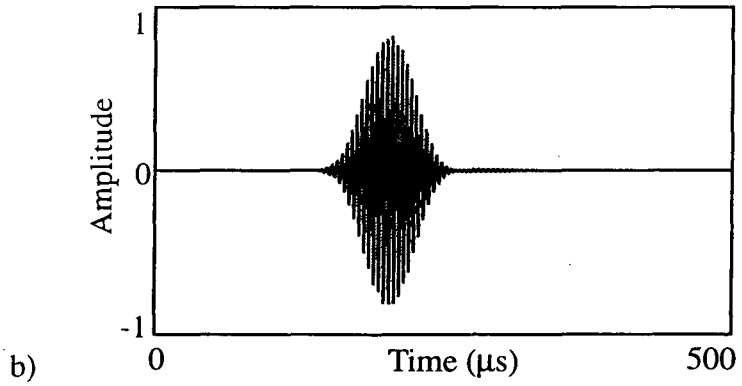


b)

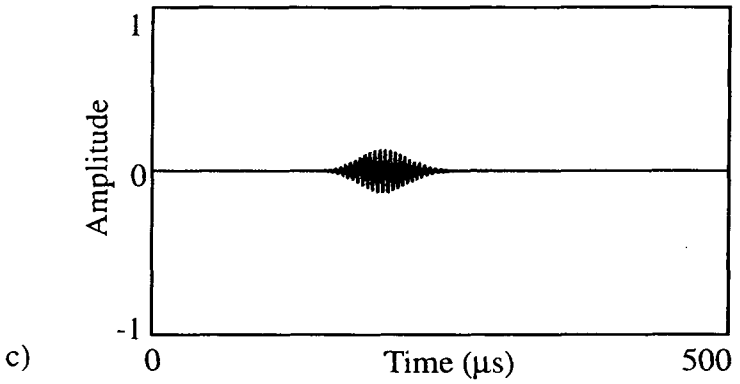
Fig.8.5 Reflection measurement using a single transducer. a) Diagram showing positions of transducers relative to the MDPE plate used for demonstrating reflection of s_2 mode from the end of a plate; b) Time history of received signals



a)



b)



c)

Fig.8.6 Transmission coefficient measurements of slotted plates. a) Schematic of set-up used for transmission coefficient measurements; b) Time domain response of reference signal (i.e. from a slot-free plate); c) Time domain response of received signal from a half through thickness slot

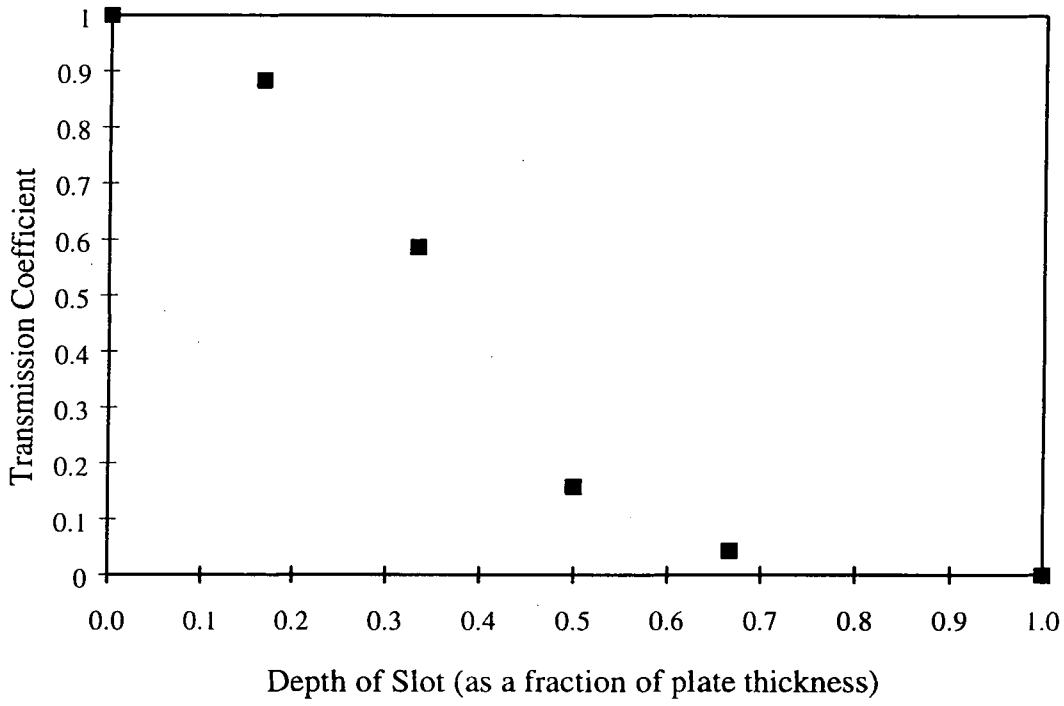
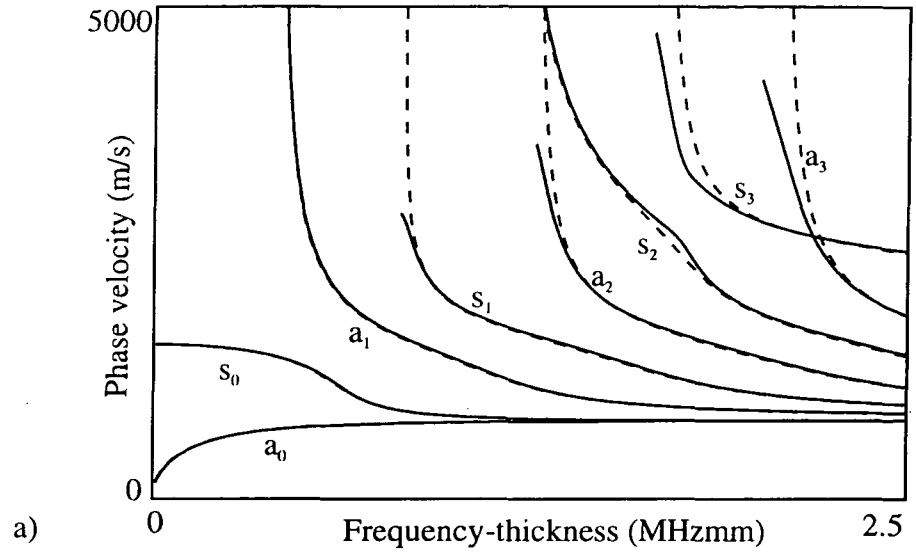
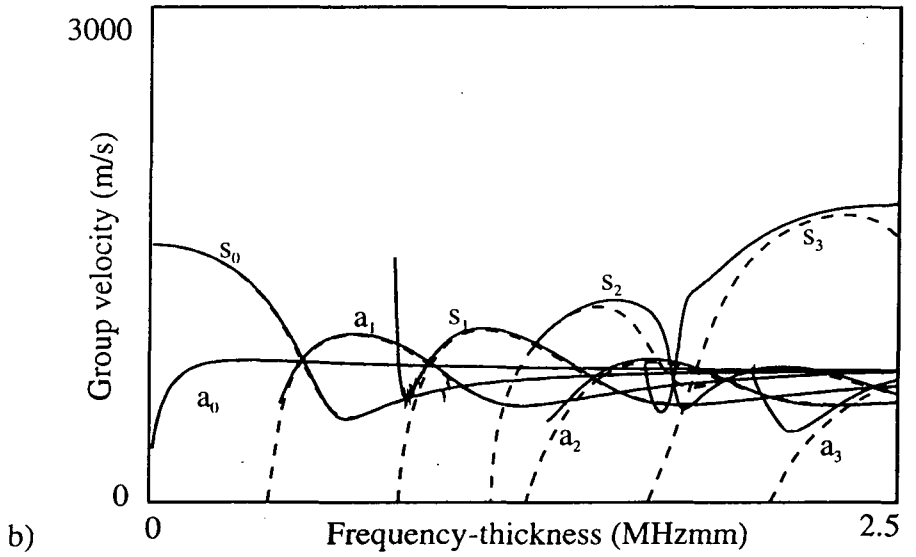


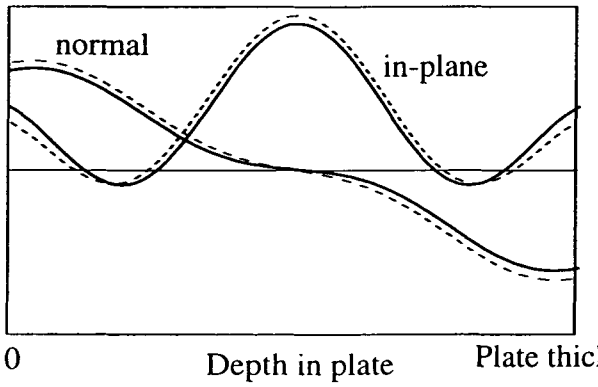
Fig.8.7 Measured transmission coefficient variation with depth of slot



a)

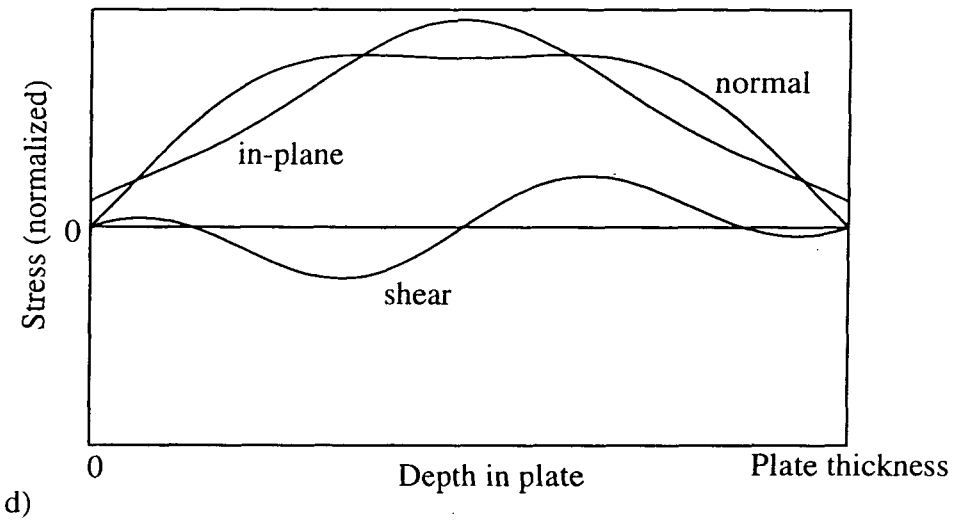


b)

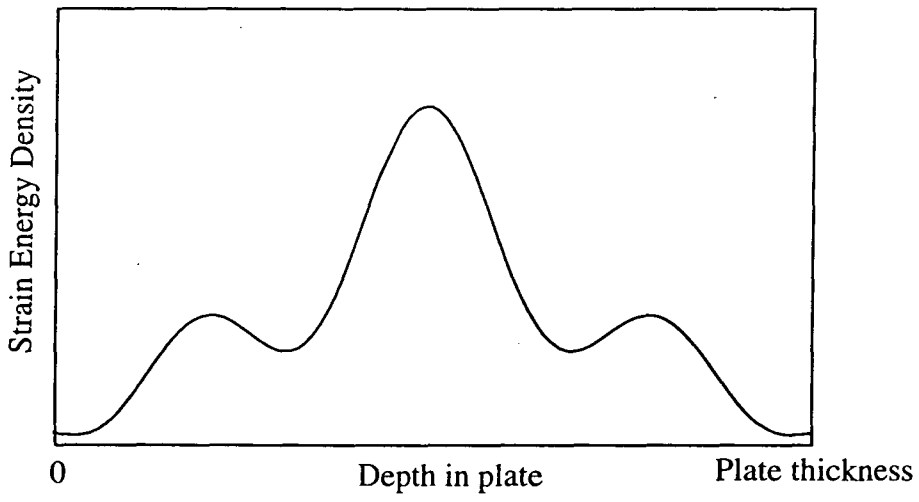


c)

Fig.8.8 Dispersion curves and mode shapes for s_2 mode. a) Phase velocity dispersion curves for MDPE plate, with attenuation (full lines) and without attenuation (dotted lines); Group velocity dispersion curves for MDPE plate, with attenuation (full lines) and without attenuation (dotted lines); c) Displacement mode shapes of s_2 mode at the point of maximum group velocity in an MDPE plate, with attenuation (full lines) and without attenuation (dotted lines)



d)



e)

Fig.8.8 d) Stress mode shape of s_2 mode in an elastic MDPE plate; e) Strain energy density mode shape of s_2 mode in an elastic MDPE plate

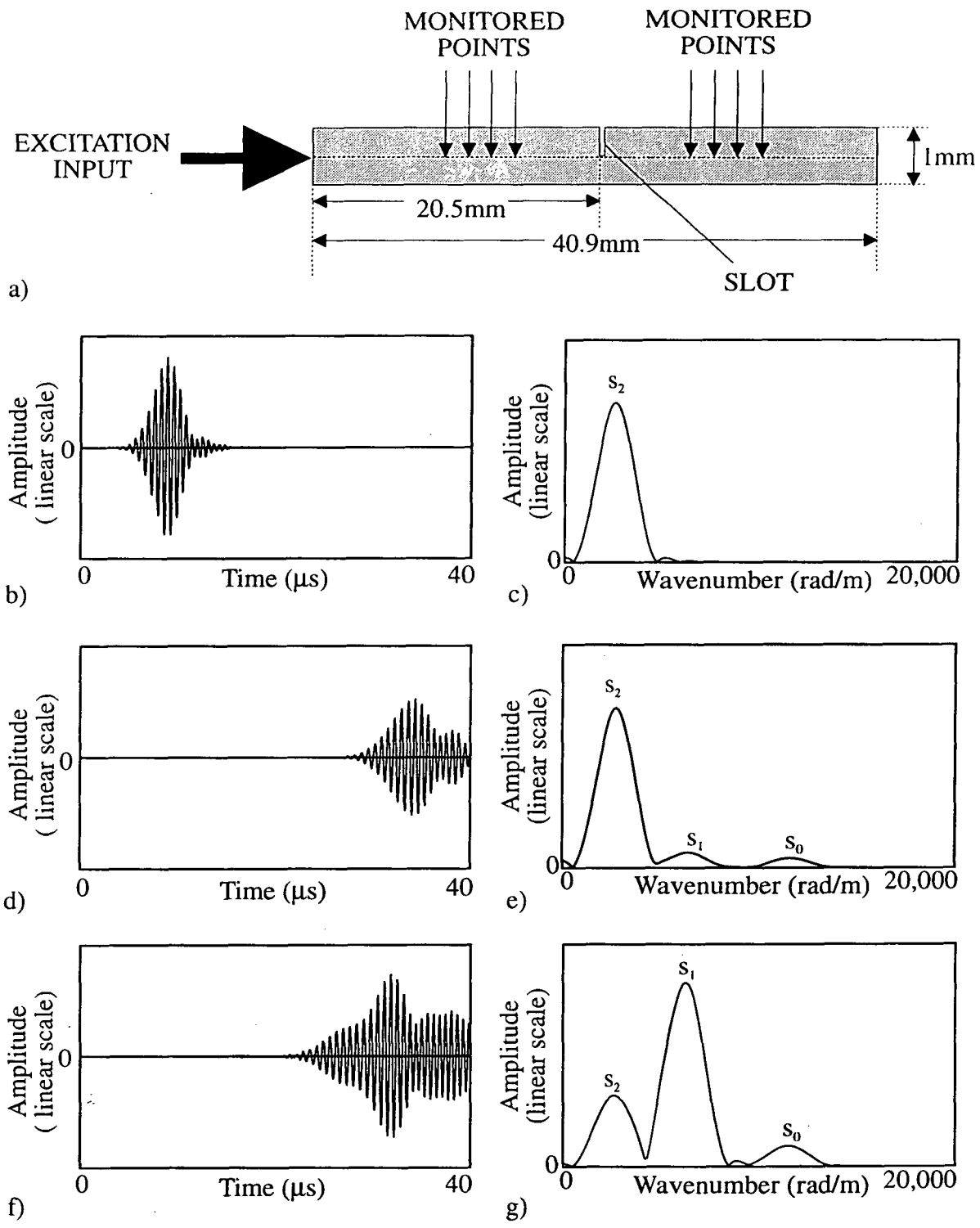
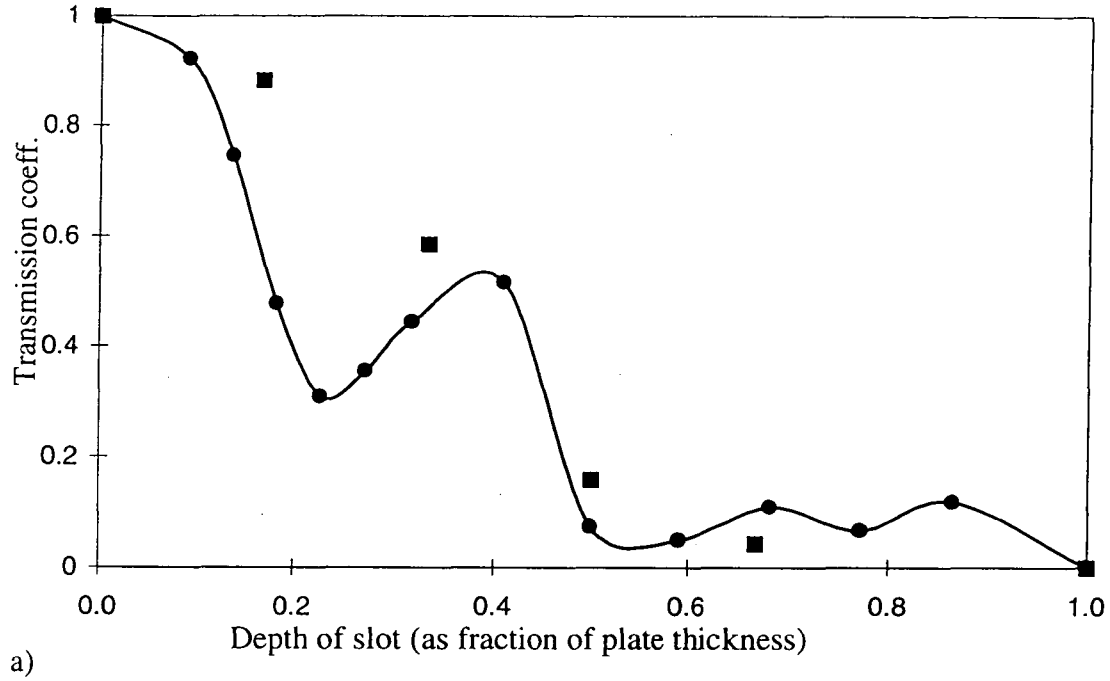
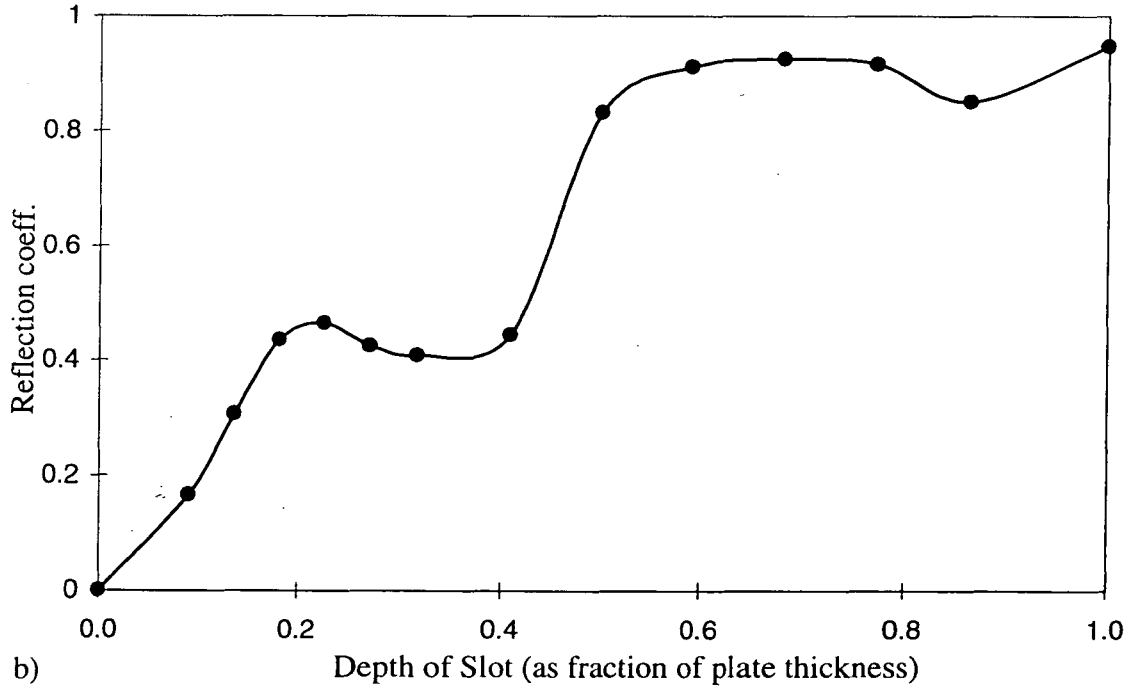


Fig.8.9 FE analysis of slots in plate. a) Schematic showing dimensions of model used for FE analysis; b) Time domain response of monitored point 6.3mm from left edge of plate showing outgoing signal only; c) Wavenumber spectrum of outgoing signal; d) Time domain response of monitored point 6.3mm from left edge of plate showing reflected signals only; e) Wavenumber spectrum of reflected signals; f) Time domain response of monitored point 13.6mm from right edge of plate showing signals transmitted across the slot; g) Wavenumber spectrum of transmitted signals



a)



b)

Fig.8.10 FE results for transmission and reflection coefficients. a) Transmission coefficient (large black squares= experimental results); b) Reflection coefficient.

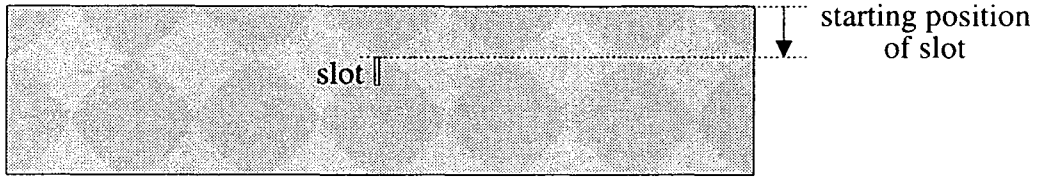
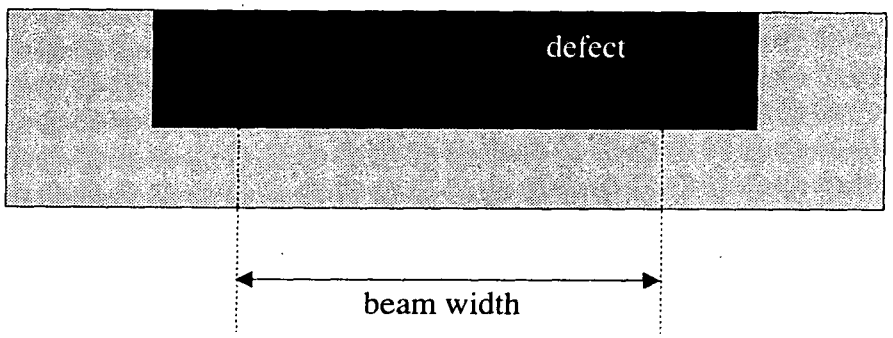
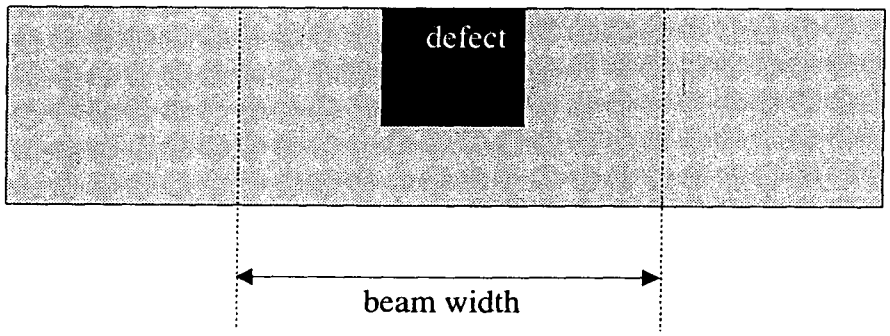


Fig.8.11 Starting positions for slots in plate



a)



b)

Fig.8.12 Cross sectional views of a) an infinite and b) a finite defect in a plate

CHAPTER 9

Conclusions

9.1 Review of Thesis

The lack of a nondestructive testing technique for inspecting welds in plastic water pipes means that pipes with imperfect joints are put into the ground. Many of the defects which lie in the weld can be internal and therefore cannot be detected visually. Slow crack growth failure is recognised as the dominant failure mechanism for water pipes under low loads. Hydrostatic tests are carried out on newly made welds. However, these tests can only identify joints which have not been welded to the prescribed specifications. A nondestructive inspection technique is clearly desirable and forms the basis of this thesis.

Two types of weld are investigated, these being butt-fusion and electrofusion. The major difference between the two types is the likely orientation of defects in the weld. In the electrofusion weld, the plane of the defects is parallel to the axis of the pipe whereas for the butt-fusion weld it is normal to the axis.

Out of all the nondestructive techniques available for use in plastics, ultrasonics has been chosen for the investigation. This particular technique was chosen on the basis that no other techniques would work sufficiently well on electrofusion welds. For butt fusion welds, ultrasonics would be an alternative to X-rays.

Given the geometry difference between the two weld types, a different ultrasonic technique is required for each one. For the electrofusion weld, two techniques have been assessed. One involves the use of conventional normal incidence scanning; the other uses Lamb waves. For the butt-fusion weld, the investigation is restricted to Lamb waves.

Critical Defect Size

In order to conduct any feasibility studies, it is necessary to first establish a defect size which will form a minimum detection limit for a nondestructive testing technique. Slow crack growth is most conveniently modelled using fracture mechanics, in particular linear elastic fracture mechanics. In Chapter 2, the critical defect size for a

50 year lifetime of the welds is calculated. The value was found to be 5.7mm for the smallest thickness pipe. This value was calculated specifically for butt-fusion welds where the loading was assumed to be mode I. For electrofusion welds, this value is expected to be considerably higher because of the larger fracture toughness for defects under mode II loading. However, in the first instance, the value of 5.7mm was also used. It was decided that if such a defect size was problematic to detect in an electrofusion joint, then a more thorough analysis would have to be conducted. Therefore, for both welds, the limit for a minimum detectable defect size was set at 5.7mm

Acoustic Properties of Polyethylene

The next task was to obtain the properties of bulk waves in the polyethylenes used in this project. These are the bulk velocities and the bulk attenuations. These properties were required for work in later chapters and the results are presented in Chapter 3. The bulk acoustic properties of longitudinal and shear waves were measured experimentally for the two grades of polyethylene used in this project (TUB 124 HPPE and Rigidex 002-40). The bulk longitudinal wave velocity was found to be 2.5-3 times larger than that of bulk shear waves. It was also found that the shear wave attenuation was approximately five to six times larger than that of longitudinal waves. The implication of this is that any method which involves the use of shear waves would not be practical given the high losses associated with such waves. The variation of attenuation with frequency was found to be approximately linear which meant that the attenuation could be considered constant per wavelength. The effect of the weld region on the propagation of ultrasound was also investigated and the results showed that the weld material could be assumed to be the same as the parent pipe material.

Electrofusion Welds

In Chapter 4, the normal incidence technique for an electrofusion joint was assessed. Scans were conducted on a variety of joints with artificial defects, with the aim of determining the influence of the frequency and spot size of the focused transducers used. Normal incidence inspection of electrofusion welds proved to be successful with critical size defects being easily detectable although the method is slow. The inspection could be performed from inside or outside of the pipe. There is a slight advantage of scanning from the inside because the surface is relatively smooth and the scanned image is not hindered by the presence of the copper wires found within the coupler. Scanning from the outside is feasible provided the wire pitch is not too small

9.2 Recommendations

Feasibilty studies have been carried out on several techniques for inspecting the integrity of welds in plastic pipes. For the electrofusion weld, conventional normal incidence scanning is the recommended method. Although this method is slow, it was found to work extremely well, being able to detect defects which are smaller than the critical defect sizes for 50 years calculated using fracture mechanics. The specification for the transducers to be used for the scanning will be pipe size dependent. However, particularly if scanning is to be performed from the outside, the higher the frequency, the better the detectability. The limit to how high the frequency can be will be determined by the attenuation and the thickness of the coupler. The scanning pitch will be dependent on the required resolution of the scan but if the scan is conducted from the outside, a scan pitch of 0.5mm should be sufficient. (0.5mm is the minimum wire pitch in the weld). From the inside, the scan pitch could be increased to speed up inspection. The practical implementation of this technique on-site has not been explored due to the time constraints of the project. However, commercial scanning systems do exist which could perform the task satisfactorily with the appropriate transducers.

For the butt-fusion weld, the recommended technique is Lamb waves. This technique is recommended over the angle probe technique simply because of the potential saving in inspection time. An appropriate mode to use is the s_2 mode excited at its maximum group velocity. The practical implementation of this technique is similar to that of normal incidence scanning except that the transducers are no longer normal to the pipe surface and scanning is required only along one direction (circumferential). This technique is based on exciting a plate wave in the pipe and would involve scanning around the circumference of the pipe. If this is a significant drawback, further development work could be carried out on an quicker alternative. One such alternative is to use dry coupled probes which are placed around the circumference of the pipe. This would result in the generation of pipe waves which can then be used to interrogate the entire cross section of the pipe. This implementation would require no scanning and hence there is potential for rapid inspection but does mean that reflection amplitudes will be smaller then for the plate wave case. The design of possible transducers to excite pipe waves in steel has been looked at in some detail and the results obtained were very promising. If a pipe wave technique is preferable, such transducers could be used on plastic pipes.

APPENDIX I

Derivation of the FFT program 'FAST'

The following derivation shows how the two dimensional Fourier Transform for a series of transducers arranged around the pipe can be obtained. A simple expression is obtained which can then be evaluated on a computer.

Let the force P at any time t be a function of two variables θ and x, where θ represents the angle around a pipe and x the axial position along the pipe as shown in Fig.A.1.

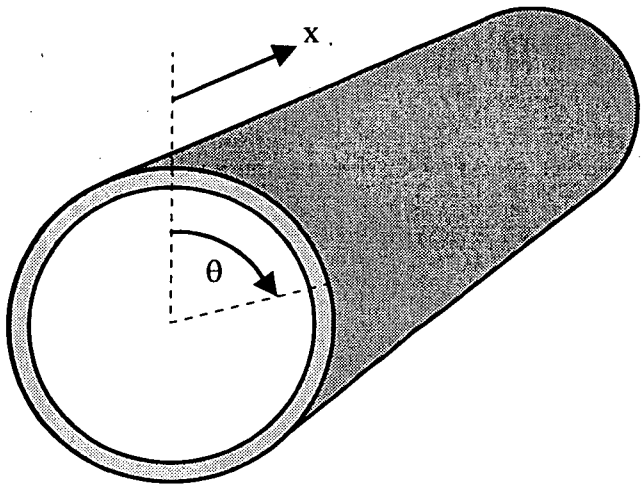


Fig.A.1 Co-ordinate system on pipe

In other words,

$$P = P(\theta,x)$$

then the Two Dimensional Fourier Transform of this function can then be written as

$$F(n,k) = \iint P(\theta,x)\, e^{-ikx}\, e^{-in\theta}\, dx\, d\theta$$

where n represents the harmonic number around the pipe and k the axial wavenumber. Physically, F(n,k) would represent the amplitude of excitation of a Lamb wave of harmonic number n and axial wavenumber k in the pipe.

If $P(\theta,x)$ consists entirely of Dirac Delta functions then $P(\theta,x)$ can be rewritten as

$$P(\theta,x) = P(\theta_1,x_1) + P(\theta_2,x_2) + P(\theta_3,x_3) + \ldots\ldots\ldots + P(\theta_N,x_N)$$

where each term represents a separate Dirac delta function and N is the total number of such functions.

The integral then becomes

$$F(n,k) = \iint P(\theta_1,x_1)\, e^{-ikx}\, e^{-in\theta}\, dx\, d\theta + \iint P(\theta_2,x_2)\, e^{-ikx}\, e^{-in\theta}\, dx\, d\theta + \ldots\ldots\ldots\ldots + \iint P(\theta_N,x_N)\, e^{-ikx}\, e^{-in\theta}\, dx\, d\theta$$

Now, $P(\theta_n,x_n) = \delta(\theta-\Theta_n, x-X_n)$ where δ is the Dirac delta function such that $\delta=1$ when $\theta = \Theta_n$ and $x = X_n$; 0 otherwise.

Therefore,

$$F(n,k) = \iint \delta(\theta-\Theta_1, x-X_1)\, e^{-ikx}\, e^{-in\theta}\, dx\, d\theta + \iint \delta(\theta-\Theta_2, x-X_2)\, e^{-ikx}\, e^{-in\theta}\, dx\, d\theta + \ldots\ldots + \iint \delta(\theta-\Theta_N, x-X_N)\, e^{-ikx}\, e^{-in\theta}\, dx\, d\theta$$

Let us now use the substitution $\varnothing = \theta-\Theta$ and $z = x-X$ so that by rearranging and differentiating we arrive at

$$\theta = \varnothing + \Theta, \qquad x = z + X$$
$$d\varnothing = d\theta, \qquad dz = dx$$

So, by substituting these into the integral we obtain

$$F(n,k) = \iint \delta(\varnothing, z)\, e^{-ik(z+X_1)}\, e^{-in(\varnothing + \Theta_1)}\, dz\, d\varnothing + \iint \delta(\varnothing, z)\, e^{-ik(z+X_2)}\, e^{-in(\varnothing + \Theta_2)}\, dz\, d\varnothing + \ldots\ldots + \iint \delta(\varnothing, z)\, e^{-ik(z+X_N)}\, e^{-in(\varnothing + \Theta_N)}\, dz\, d\varnothing$$

$$= \iint e^{-i(kX_1+n\Theta_1)}\, \delta(\varnothing, z)\, e^{-i(kz+n\varnothing)}\, dz\, d\varnothing + \ldots\ldots$$

$$= e^{-i(kX_1+n\Theta_1)} \iint \delta(\varnothing, z)\, e^{-i(kz+n\varnothing)}\, dz\, d\varnothing + \ldots\ldots$$

Now, $\iint \delta(\varnothing, z)\, e^{-i(kz+n\varnothing)}\, dz\, d\varnothing = 1$, so,

$$F(n,k) = e^{-i(kX_1+n\Theta_1)} + e^{-i(kX_2+n\Theta_2)} + \ldots\ldots\ldots + e^{-i(kX_N+n\Theta_N)}$$

$$= \sum_{r=1}^{N} e^{-i(kX_r+n\Theta_r)}$$

Therefore, the Fourier Transform for a given k and n can be obtained by a simple summation which takes into account the axial and circumferential position of each transducer on the pipe. This means that we can now determine the amplitude of excitation of a wave of harmonic number n and axial wavenumber k in a pipe.

References

Alleyne, D. N. (1991). *The nondestructive testing of plates using ultrasonic Lamb waves.* PhD thesis, University of London.

Alleyne, D. N. and Cawley, P. (1991). *A two-dimensional Fourier transform method for the quantitative measurement of Lamb modes.* Review of Progress in Quantitative NDE, pp 201-208.

Alleyne, D. N. and Cawley, P. (1992). *The interaction of Lamb waves with defects.* IEEE Transactions on Ultrasonics, Ferroelectrics and Frequency control, Vol.39, 3, pp 381-397.

Alleyne, D. N. and Cawley, P. (1992). *Optimization of Lamb wave inspection techniques.* NDT and E International, Vol.25, pp 11-22.

Alleyne, D. N., Lowe, M. and Cawley, P. (1996). *The inspection of chemical plant pipework using Lamb waves: defect sensitivity and field experience.* Review of Progress in Quantitative NDE (in press).

Alleyne, D. N. and Cawley, P. (1996). *The excitation of Lamb waves in pipes using dry coupled piezoelectric transducers.* Journal of Nondestructive Evaluation (in press).

Al-Nassar, Y. N., Datta, S. K. and Shah, A. H. (1991). *Scattering of Lamb waves by a normal rectangular strip weldment.* Ultrasonics, Vol.29, pp 125-132.

Alsop, L. (1970). *The leaky-mode period equation - a plane-wave approach.* Bulletin of the Seismological Society, Vol.6, 6, pp 1989-1998.

ASTM. (1965). *Fracture toughness testing and its applications.* No. ASTM STP 381.

Auld, B. A. (1990). *Acoustic fields and waves in solids.* Vol.1, 2nd ed., Kreiger, Malabar, FL.

Barker, M. B., Bowman, J., et al. (1983). *The performance and causes of failure of polyethylene pipes subjected to constant and fluctuating internal pressure loadings.* Journal of Materials Science, Vol.18, pp 1095-1118.

Barrett, J. D. and Foschi, R. O. (1977). *Mode II stress-intensity factors for cracked wood beams.* Engineering Fracture Mechanics, Vol.9, pp 371-378.

Ben'kovskii, V. V. (1991). *Inspecting the quality of heated-tool butt fusion joints in polyethylene pipes.* Technical Diagnostics and NDT, Vol.3, 4, pp 280-282.

Bernard, L. (1986). *Time of flight ultrasonics. July*, ASTM Standardization News, pp 56-58.

Broek, D. (1974). *Elementary engineering fracture mechanics.* Noordhoff, Leydon.

Brown, N. and Bhattacharya, S. K. (1985). *The initiation of slow crack growth in linear polyethylene under single edge notch tension and plane strain.* Journal of Materials Science, Vol.20, pp 4553-4560.

Bryant, E. L. and McIntire, P. (1985). *Nondestructive testing handbook:- Vol.3: Radiography and radiation testing.* American Society for Nondestructive Testing.

Castaings, M. and Hosten, B. (1994). *Delta operator technique to improve the Thomson-Haskell method stability for propagation in multilayered anisotropic absorbing plates.* Journal of the Acoustical Society of America, Vol.95, 4, pp 1931-1941.

Chan, M. K. V. (1982). *Fracture toughness testing and slow crack growth in polyethylenes.* PhD thesis, University of London 1982.

Chan, M. K. V. and Williams, J. G. (1983). *Slow stable crack growth in high density polyethylenes.* Polymer, Vol.24, pp 234-244.

Chimenti, D. E. and Nayfeh, A. H. (1985). *Leaky Lamb waves in fibrous composite laminates.* Journal of Applied Physics, Vol.58, pp 4531-4538.

Chung, W. N. (1991). *Fracture toughness and creep fracture studies of polyethylenes.* PhD thesis, University of London.

Cremer, L. (1942). *Theorie der schalldammung dunner wande bei schragem einfall.* Akustische Zeitschrifte, Vol.7, pp 81-104.

Ditri, J. J. (1995). *Phase and energy velocities of cylindrically crested guided waves.* Journal of the Acoustical Society of America, Vol.97, 1, pp 98-107.

Drinkwater, B. W. (1995). *The use of dry coupling in ultrasonic nondestructive testing.* PhD thesis, University of London.

Dugdale, D. S. (1960). *Yielding of steel sheets containing slits.* Journal of the Mechanics & Physics of Solids, Vol.8, pp 100-104.

Ewalds, H. L. (1986). *Fracture mechanics.* Edward Arnold/Delftse Uitgevers Maatschappij.

Firestone, F. A. and Ling, D. S. (1951). *Methods and means of generating and utilizing vibrational waves in plates.* U.S. Pat. 2,536,128.

Gazis, D. C. (1959). *Three dimensional investigation of the propagation of waves in hollow circular cylinders.* Journal of the Acoustical Society of America, Vol.31, 5, pp 568-573.

Gimmler, E. A., Farrage, R., et al. (1994). *Manual for polyethylene pipe systems for water supply applications.* Section 8 - Installation: Testing and Commissioning. Copyright WRc.

Gray, A., Mallinson, J. N., et al. (1981). *Fracture behaviour of polyethylene pipes.* Plastics and Rubber Processing and Applications, Vol.1, pp 51-53.

Greig, J. M. (1981). *Specification and testing of polyethylene gas distribution systems for a minimum 50-year operational life.* Plastics and Rubber Processing and Applications, Vol.1, pp 43-49.

Griffith, A. A. (1920). *The phenomenon of rupture and flow in solids.* Phil. Trans. Roy. Soc., Vol.221, pp 163-198.

Guo, N. and Cawley, P. (1993). *The interaction of Lamb waves with delaminations in composite laminates.* Journal of the Acoustical Society of America, Vol.94, 4, pp 2240-2246.

Guo, N. and Cawley, P. (1994). *Lamb wave reflection for the quick NDE of large composite laminates.* Materials Evaluation, Vol.52, pp 404-411.

Haagensen, P. J., Slind, T. and Orjasaeter, O. (1988). *Size effects in machine components and welded joints.* Proceedings of the International Offshore Mechanics and Arctic Engineering Symposium, Vol.3, pp 367-377.

Hitchings, D. (1987). *FE77 User Manual.* Imperial College internal report.

Inglis, C. E. (1913). *Stresses in a plate due to the presence of cracks and sharp corners.* Trans. Inst. Naval Architects, Vol.60, pp 219-241.

Irwin, G. R. (1948). *Fracture dynamics, fracturing of metals.* American Soc. of Metals, pp 147-166.

Irwin, G. R. (1957). *Analysis of stresses and strains near the end of a crack traversing a plate.* Journal of Applied Mechanics, 24, pp 361-364.

Irwin, G. R. (1960). *Fracture mode transition for a crack traversing a plate.* Journal of Basic Engineering, Vol.82, pp 417-425.

Kino, G. S. (1987). *Acoustic waves: devices, imaging and analogue signal processing.* Prentice-Hall Inc, New Jersey.

Kinsler, L. E. and Frey, A. R. (1982). *Fundamentals of acoustics.* John Wiley and Sons Inc., New York.

Koshiba, M., Karakida, S. and Suzuki, M. (1984). *Finite-element analysis of Lamb waves scattering in an elastic plate waveguide.* IEEE Trans. Sonics. Ultrason., pp 18-25.

Krautkramer, J. (1959). *Fehlergrossenermittlung mit Ultraschall.* Arch. F. D. Eisenhuttenwesen, Vol.30, pp 693-703.

Krautkramer, J. and Krautkramer, H. (1983). *Ultrasonic testing of materials.* Springer-Verlag, New York.

Lamb, H. (1917). *On waves in an elastic plate.* Conference of the Royal Society, pp 114-128.

Larsson, S. G. and Carlsson, A. J. (1973). *Influence of non-singular stress terms and specimen geometry on small scale yielding at crack tips in elastic-plastic materials.* Journal of the Mechanics and Physics of Solids, Vol.21, pp 263-277.

Lazan, B. J. (1968). *Damping of materials and members in structural mechanics.* Pergamon Press, London.

Lehfeldt, E. and Holler, P. (1967). *Lamb waves and lamination detection. Ultrasonics*, Vol.5, pp 255-257.

Lockett, T. K. (1973). *Lamb and torsional waves and their use in flaw detection in tubes.* Ultrasonics, pp 31-37.

Lowe, M. J. S. (1993). *Plate waves for the NDT of diffusion bonded titanium.* PhD thesis, University of London.

Lustiger, A. and Corneliussen, R. D. (1987). *The role of crazes in the crack growth of polyethylene.* Journal of Materials Science, Vol.22, pp 2470-2476.

Malvern, L. E. (1969). *Introduction to the mechanics of a continuous medium.* Prentice-Hall, New Jersey.

Mandell, J. F., Roberts, D. R., et al. (1983). *Plane strain fracture toughness of polyethylene materials.* Polymer Engineering and Science, Vol.23, pp 404-411.

Marshall, G. P. (1982). *Design for toughness in polymers. 1-Fracture mechanics.* Plastics and Rubber Processing and Applications, Vol.2, 2, pp 169-182.

Marshall, G. P., Taylor, M. D., et al. (1982). *Assessment of the influence of processing on medium-high density PE pressure pipes.* Plastic Pipes V, pp 7.1-7.9.

Marshall, G. P., Ingham, E., et al. (1995). *The crack growth resis*tance of PVC and PE. Plastic Pipes IX, pp 77-86.

McClinton, M. (1986). *How to detect defects in PE pipe butt fusion joints.* Pipe Line Industry.

Meeker, T. R. and Meitzler, A. H. (1964). *Guided wave propagation in elongated cylinders and plates.* Physical Acoustics Principles and Applications, Vol.1, Academic Press, London, pp 111-167.

Mindlin, R. D. (1960). *Waves and vibrations in isotropic, elastic plates.* Proceedings of the first symposium on naval structural mechanics, pp 199-232.

Munns, I. J. and Georgiou, G. A. (1995). *Ultrasonic and radiographic NDT of butt fusion welds in polyethylene pipe.* Plastic Pipes IX, pp 551-560.

Nkemzi, D. (1993). *The Rayleigh-Lamb dispersion equations for a viscoelastic plate.* Mechanics Research Communications, Vol.20, 3, pp 215-222.

Pialucha, T., Guyott, C. C. H., et al. (1989). *Amplitude spectrum method for the measurement of phase velocity.* Ultrasonics, Vol.27, pp 270-279.

Pialucha, T. P. (1992). *The reflection coefficient from interface layers in NDT of adhesive joints.* PhD thesis, University of London.

Poette, C. and Albaladejo, S. (1991). *Stress intensity factors and influence functions for circumferential surface cracks in pipes.* Engineering Fracture Mechanics, Vol.39, 4, pp 641-650.

Qian, R., Lu, X., et al. (1989). *Investigating the existence of a threshold stress intensity for slow crack growth in high-density polyethylene.* Journal of Materials Science, Vol.24, pp 2467-2472.

Rajab, M. D. and Zahoor, A. (1990). *Fracture analysis for pipes containing full circumference internal part-throughwall flaw.* International Journal of Pressure Vessels and Piping, Vol.41, 1, pp 11-23.

Redwood, M. (1960). *Mechanical waveguides.* Pergamon Press, Oxford.

Redwood, M. (1963). *Ultrasonic waveguides - a physical approach.* Ultrasonics, Vol.1, pp 99-105.

Rice, J. R. (1968). *A path independent integral and the approximate analysis of strain concentration by notches and cracks.* Journal of Applied Mechanics, Vol.35, pp 379-386.

Rice, J. R. (1974). *Limitations to the small scale yielding approximation for crack tip plasticity.* Journal of the Mechanics and Physics of Solids, Vol.22, pp 17-26.

Rokhlin, S. I. (1979). *Interaction of Lamb waves with elongated delaminations in thin sheets.* Internation Advances in Nondestructive Testing, Vol.6, pp 263-285.

Rokhlin, S. I. (1980). *Diffraction of Lamb waves by a finite crack in an elastic layer.* Journal of the Acoustical Society of America, Vol.67, pp 1157-1165.

Rokhlin, S. I. (1981). *Resonance phenomena of Lamb waves scattering by a finite crack in a solid layer.* Journal of the Acoustical Society of America, Vol.69, pp 922-928.

Rooke, D. D. and Cartwright, D. J. (1975). *Compendium of stress intensity factors.* HMSO.

Sabbagh, H. A. and Krile, T. F. (1973). *Finite element analysis of elastic wave scattering from discontinuities.* Ultrason. Symp. Proc. IEEE, pp.216-219.

Sachse, W. and Pao, Y. H. (1978). *On the determination of phase and group velocities of dispersive waves in solids.* Journal of Applied Physics, Vol.49, 8, pp 4320-4327.

Sandilands, G. and Bowman, J. (1986). *An examination of the role of flaw size and material toughness in the brittle fracture of polyethylene pipes.* Journal of Materials Science, Vol.21, pp 2881-2888.

Silk, M. G. and Bainton, K. F. (1979). *The propagation in metal tubing of ultrasonic wave modes equivalent to Lamb waves.* Ultrasonics, pp 11-19.

Silk, M. G. (1984). *Ultrasonic Transducers for Nondestructive Testing.* Adam Hilger, Bristol.

Silk, M. G. (1987). *Changes in ultrasonic defect location and sizing.* NDT International, Vol.20, 1, pp 9-14.

Szelazek, J. (1989). *Flaw sizing with distance, probe displacement, size (DGS) diagrams.* NDT International, Vol.22, 1, pp 26-30.

Tada, H., Paris, P. C., et al. (1985). *The stress analysis of cracks handbook.* Paris Productions Incorp/Del Research Corp.

Taylor, M. D. (1983). *An investigation into the fracture mechanics of polymers used in engineering applications.* PhD thesis, Manchester Polytechnic.

Uberall, H., Hosten, B., et al. (1994). *Repulsion of phase-velocity dispersion curves and the nature of plate vibrations.* Journal of the Acoustical Society of America, Vol.96, 2, pp 908-917.

Vancrombrugge, R. (1982). *Fracture propagation in plastic pipes.* Plastic Pipes V, pp 11.1-11.5.

Vavilov, V. P. and Taylor, R. (1982). *Research techniques in nondestructive testing.* Vol.5, Ed. R. S. Sharpe, Academic Press, pp 239-279.

Viktorov, I. A. (1970). *Rayleigh and Lamb waves.* Plenum Press, New York.

WAA Sewers and Water Mains Committee: Materials and Standards. (1987). *Specification for blue polyethylene (PE) pressure pipe for cold potable water (nominal sizes 90 to 1000 for underground or protected use).* No. IGN 4-32-03.

Watson, T. H. (1972). *A real frequency complex wave-number analysis of leaking modes.* Bulletin of the Seismological Society of America, Vol.62, 1, pp 369-384.

Wells, A. A. (1961). *Unstable crack propagation in metals - cleavage and fast fracture.* The Crack Propagation Symposium, pp 210-230.

Westergaard, H. M. (1939). *Bearing pressures and cracks.* Journal of Applied Mechanics, 61, pp A49-A53.

Williams, J. G. and Marshall, G. P. (1975). *Environmental crack and craze growth phenomena in polymers.* Proc. R. Soc. Lond., Vol.A342, pp 55-77.

Williams, J. G. (1978). *Applications of linear fracture mechanics.* Springer-Verlag, Berlin.

Williams, J. G. (1984). *Fracture mechanics of polymers.* Ellis Horwood.

Williams, J. G. (1987). *Fracture mechanics of polymers and adhesives.* Fracture of non-metallic materials, pp 227-255.

Worlton, D. C. (1957). *Ultrasonic testing with Lamb waves.* Non-destructive testing, Vol.15, pp 218-222.

Xu, P. C. and Mal, A. K. (1987). *Calculation of the inplane Green's functions for a layered viscoelastic solid.* Bulletin of the Seismological Society of America, Vol.77, pp 1823-1837.

Yapura, C. L. and Kinra, V. K. (1995). *Guided waves in a fluid-solid bilayer.* Wave motion, Vol.21, pp 35-46.

Zemanek, J. (1972). *An experimental and theoretical investigation of elastic wave propagation in a cylinder.* Journal of the Acoustical Society of America, Vol.51, 1, pp 265-283.

BIBL. LONDIN. UNIV.